A Comprehensive Study of Double Pion Photoproduction and Meson Spectroscopy

Nadine Hammoud

Department of Theory of Structure of Matter
The Henryk Niewodniczański Institute of Nuclear Physics Polish Academy of Sciences Kraków, Poland

Thesis submitted for the Degree of Doctor of Philosophy in Physics
prepared under the supervision of

Dr hab. Robert Kamiński

Dr Łukasz Bibrzycki

September 23, 2023

Acknowledgement

I seize this moment to extend my profound appreciation to the remarkable individuals whose constant support and guidance have illuminated my path throughout the challenging journey of completing my thesis. Your contributions have been a source of inspiration, and I hold immense gratitude for your invaluable assistance.

Foremost among those deserving my heartfelt acknowledgment are my esteemed PhD mentors, Dr. Robert Kamiński and Dr. Łukasz Bibrzycki. Their consistent mentorship, wise counsel, and unflagging encouragement have been invaluable from the outset of my research journey until the final submission of my thesis. Their expertise in the realm of physics, coupled with their skilled guidance and profound insights, have played a central role in shaping my academic growth. It is with great fortune that I have had the privilege of being mentored by such distinguished academics, especially given their exceptional efforts in affording me the incredible opportunity to participate in numerous international conferences and by opening doors to valuable connections in the academic world.

From my second year onward, I was honored to become an affiliated member of the esteemed JPAC collaboration, an experience that has enriched my academic journey immeasurably. Prof. Adam Szczepaniak, Prof. Vincent Mathieu, Dr. Łukasz Bibrzycki, and Dr. Robert J. Perry have my deepest gratitude for their warm embrace of my presence within their group. Their unwavering support, patience in listening to my thoughts, motivational influence, invaluable critiques, and sharp insights have been a wellspring of growth. Our biweekly meetings not only served as vial milestone in my academic trajectory but also offered abundant encouragement. To all the members of the JPAC group, I extend my heartfelt appreciation for affording me the opportunity to engage in collaborative projects and participate in various publications.

A special note of gratitude goes out to my collaborator, Dr. Robert Perry. I am indebted for the time and effort he invested, his patience in addressing my naive questions, and his willingness to correct my errors. His presence served as a constant motivator during challenging times, reminding me that every academic journey, regardless of its elevation, encounters its share of obstacles and setbacks.

Lastly, I extend my deepest gratitude to my family, whose constant belief in my capabilities and support have been a cornerstone of my achievements. To my mother, I offer my profound appreciation for the sacrifices made and the fervent prayers that sustained me on this path.

I would be negligent not to express my gratitude to my circle of friends and relatives, whose support and encouragement propelled me towards my goals. Your presence has been a source of strength, and I am profoundly grateful for your unwavering faith in my endeavors.

Contents

List of Tables

List of Figures

Abstract

In the intricate realm of hadron spectroscopy, this thesis embarks on an insightful intellectual journey intricately connected to the exploration of meson resonances. The heart of this work lies in meticulous analyses of photoproduction processes and inelasticity phenomena, aimed at shedding light on the enigmatic complexities inherent in these remarkable occurrences.

The whole thesis consists of two parts, the first segment delves deeply into the domain of two-pion photoproduction, offering profound insights into comprehending meson resonances within the $\pi\pi$ system. Guided by the Regge formalism and the Drell-Söding-Deck approach, the model seamlessly integrates the established "Deck Mechanism" background, with a particular emphasis on the pivotal $\rho(770)$ resonance. This resonance encapsulates the P-wave contribution, driven by the interplay of pomeron and f_2 exchanges. Extending the model's scope, scalar mesons σ and $f_0(980)$ impact the S-wave behavior. Additionally, non-resonant P and S components are introduced. Consequently, model fitting against a subset of moments precedes the comparison of predictions with experimental data from CLAS.

Moreover, the second part of the thesis focuses around identifying $J^{PC} = 1^{--}$ excited ρ resonances, delving into the ongoing discourse surrounding $\rho(1250)$ versus $\rho(1450)$. Additionally, a forward-looking perspective is taken by forecasting insights within the $\pi\omega$ channel. The analysis embarks on a journey through elastic P-wave $\pi\pi$ phase shifts and inelasticities, reaching up to 2 GeV. This study utilizes a sophisticated approach based on a unitary and analytic three-channel S matrix, skillfully aligned with complex-energy pole positions. Notably, the enforcement of maximum crossing symmetry is facilitated through once-subtracted dispersion relations known as GKPY equations. The channels considered for these analyses encompass $\pi\pi$, $\rho 2\pi$, and $\rho\rho$.

The thesis concludes by addressing predictions within the $\omega\pi$ channel. Theoretical amplitudes are forecasted while analyzing their mass distributions. These forecasts span the domains of $\pi\pi$, $\rho\rho$, and $\omega\pi$ interactions. The analytical strategy presented draws strength from a flexible separable potential method for three coupled channels, finely adjusted through the dynamic interplay of both non-relativistic and relativistic propagators. This study is undertaken by considering varying positions of the $\rho(1450)$ meson within the $\omega\pi$ interactions, extending insights into the broader particle dynamics.

Overview

The following sections outline the structure and content of the thesis, presenting a road map for the subsequent chapters:

- **Chapter1: Introduction and Historical Review**
  This chapter provides a comprehensive introduction to the theory of strong interactions and hadrons, which lays the necessary foundation for comprehending the detailed analyses presented in this thesis. Commencing with an exploration of the fundamental principles of the Standard Model, including the quark model for mesons and baryons, the chapter establishes the fundamental concepts of Quantum Chromodynamics (QCD). Furthermore, it provides an in-depth examination of mesons and their distinctive characteristics. The chapter concludes by elucidating the motivations behind the present work. This chapter provides information at a popular science level.

- **Chapter 2: Theoretical Background**
  Given the central focus on resonances in this thesis, Chapter 2 establishes the scattering framework by briefly introducing the scattering S-matrix formalism in the context of quantum field theory. Special emphasis is placed on the dispersion theory framework, which harnesses the fundamental laws of physics to enable the non-perturbative evaluation of hadronic processes. Additionally, the chapter highlights the indispensable theory in photoproduction research, namely Regge theory. This includes an exploration of Regge amplitudes, Regge trajectories, and a concise introduction to the pomeron.

- **Part I - Photoproduction of Light Mesons**
  The first part of this thesis delves into the phenomenological studies of meson photoproduction, with a specific focus on $2 \to 3$ processes. Accordingly, this section provides a concise review of meson photoproduction, encompassing both pseudoscalar and vector meson photoproduction.

  - **Chapter 3: Double Pion Photoproduction** This chapter delves into a comprehensive investigation of the intriguing double pion photoproduction process, focusing specifically on scenarios involving virtual pion exchange within the Deck Mechanism [1]. In this pursuit, classic relations have been carefully adapted to enhance the precision of the analysis.

    Section 3.1 provides a concise overview of the employed model, presenting two primary components and describing the kinematics and notations adopted throughout the study.

    Section 3.2 initiates with the non-resonant component (Deck) model, establishing the gauge-invariant Deck amplitude. Subsequently, the virtual pion-proton scattering amplitude ($\pi^{\pm *}p$) is presented in section 3.2.1, accompanied by a study of the partial wave behavior at the threshold for a virtual pion. The necessity of a correction factor is thoroughly examined, ultimately determining that such an addition is unnecessary.

In Section 3.3, the research introduces two preferred frames of reference, each accompanied by its corresponding kinematics, further enriching the study.

Section 3.4 introduces the second component of the model, presenting the amplitude for the vector resonance (i.e., ρ meson) contributing to the P-wave through both pomeron ($\mathcal{P}$) and f_2 exchanges in section 3.4.1. Additionally, the section explores scalar resonances (i.e., $f_0(500)$ and $f_0(980)$) governing the S-wave contribution in section 3.4.2.

The chapter concludes with a brief summary, setting the stage for the subsequent chapter.

- **Chapter 4: Cross Section and Angular Distribution**
  This chapter offers insights into the experimental aspects related to the data source, primarily focusing on the CLAS experiment conducted at the Thomas Jefferson National Accelerator Facility (Jefferson Lab, also known as "JLab") in Newport News, Virginia.

  In Section 4.1, a detailed presentation of the formulation for the differential cross section, with a particular emphasis on deriving the projected P-wave differential cross section is provided.

  Section 4.2 introduces various approaches to computing angular momentum moments, while Section 4.3 delves into the methods used for exploring these moments. The outcomes following the establishment of the necessary framework and the introduction of fundamental concepts essential for moment calculations are provided.

  Moving on to Section 4.4, the methodology employed for the initial fit below 1 GeV is examined. The section presents the results, including the fitted parameters obtained during this process.

  Section 4.5 explores the incorporation of non-resonant contributions, which arise from the partial waves associated with the process under study.

  Finally, Section 4.6 provides insights into the moments resulting from the final fit, which encompasses all the aforementioned components. Variations in the fitted parameters are also analyzed and discussed.

  The chapter wraps up by summarizing key insights and conclusions gleaned from the study, all while acknowledging the ever-evolving nature of research within this domain.

- **Part II - Spectroscopy of Light Vector Mesons**
  The second part of this thesis focuses on the comprehensive evaluation of the light vector meson spectroscopy. The experimental status of the mesonic resonances below 2 GeV is carefully assessed, with particular attention given to the contentious ρ' within the Particle Data Group (PDG). The relationship between the S matrix and the phase shift is elucidated, along with the definition of various pole structures. Notably, the primary focus of this section revolves around the general formalism of the S matrix for the N-coupled channel scenario.

– **Chapter 5: Multichannel Elastic Scattering Analysis**
This chapter conducts an extensive investigation of elastic P-wave $\pi\pi$ phase shifts and inelasticities up to 2 GeV, aiming to unveil the associated $J^{PC} = 1^{--}$ excited ρ resonances and address the $\rho(1250)$ versus $\rho(1450)$ conflict. In section 5.1.1, the selection criteria used to identify the three effective channels that predominantly manifest ρ excitations are explained. These channels include $\pi\pi$, $\rho 2\pi$, and $\rho\rho$. Section 5.2 delves into an enhanced parametrization approach, utilizing a unitary and analytic three-channel S matrix with complex-energy pole locations, thereby achieving a more robust framework. The fitting procedures are extensively described in section 5.2. Section 5.3 presents and comprehensively discusses the outcomes of the fits. Finally, this chapter concludes with a concise summary in section 5.4, emphasizing the significance of $\rho(1250)$ and its inclusion in the PDG tables.

– **Chapter 6: Predictions for the $\omega\pi$ Channel**
Chapter 6 delves into forecasting insights within the $\pi\omega$ channel. Through the adept application of theoretical frameworks and precise analytical techniques, this chapter advances the understanding of particle dynamics, carrying implications beyond the boundaries of this channel's context.
Section 6.1 introduces the central theme of the chapter, outlining the objective of predicting intricate interactions in the $\pi\omega$ channel. This involves exploring untested theoretical aspects of $\omega\pi$ interactions and closely scrutinizing mass distributions, while considering varying positions of the $\rho(1450)$ meson.
Section 6.2 presents a comprehensive model that captures the interplay among $\pi\pi$, $\omega\pi$, and $\rho\rho$ channels. This theoretical foundation serves as a cornerstone for subsequent analytical inquiries.
In Section 6.3, an elaborate methodology is disclosed, meticulously designed to decipher complex interactions. Moreover, it dissects fitting procedures with precision, seamlessly aligning theoretical concepts with empirical data as outlined in 6.3.1. Finally, in 6.3.2, the fruits of this analytical endeavor are unveiled, revealing the attained outcomes.

Chapter 1

Introduction and Historical Review

The journey to unravel the fundamental structure of matter has ancient roots, dating back over 2500 years to ancient Greece. This enduring quest in particle physics continues to be driven by the pursuit of ever more precise theories that lay the foundation for comprehending a vast spectrum of physical phenomena. These phenomena span from the intricate behaviors of atomic nuclei to the dynamics governing the entire cosmos.

In the present day, our comprehension of the physical universe rests on two distinct pillars: Einstein's General Relativity, which offers insight into the behavior of gravity on cosmic scales, and the Standard Model of particle physics. The Standard Model, a quantum field theory, provides a comprehensive framework for understanding the microscopic and subatomic realms. It stands as a testament to human ingenuity, granting us profound insights into the fundamental laws governing the natural world.

1.1 Standard Model

The Standard Model (SM) classifies matter into twelve elementary particles, categorized into three groups: spin-1/2 quarks (up, down, charm, strange, top, bottom) and leptons (electron, electron neutrino, muon, muon neutrino, tau, tau neutrino), and spin-1 gauge bosons (gluon, photon, W, Z). This arrangement is illustrated in Figure 1.1.

According to this model, the electromagnetic, weak nuclear, and strong nuclear interactions govern the dynamics of these recognized subatomic particles. The electromagnetic force is responsible for the binding of atoms and molecules, mediated by the exchange of photons. The strong force holds quarks together within protons and neutrons, as well as attracting protons and neutrons within atomic nuclei, and is conveyed through the exchange of gluons. The weak force is responsible for certain types of radioactive decays, such as beta radiation, and it is mediated by the massive vector bosons W^+, W^-, and Z.

A notable extension of the Standard Model was the Higgs boson, introduced by physicist Peter Higgs to elucidate particle mass origins. Initially, particles were massless, but the Higgs boson's detection in 2012 by the ATLAS [2] and CMS [3] collaborations unveiled the mechanism responsible for imparting mass to particles.

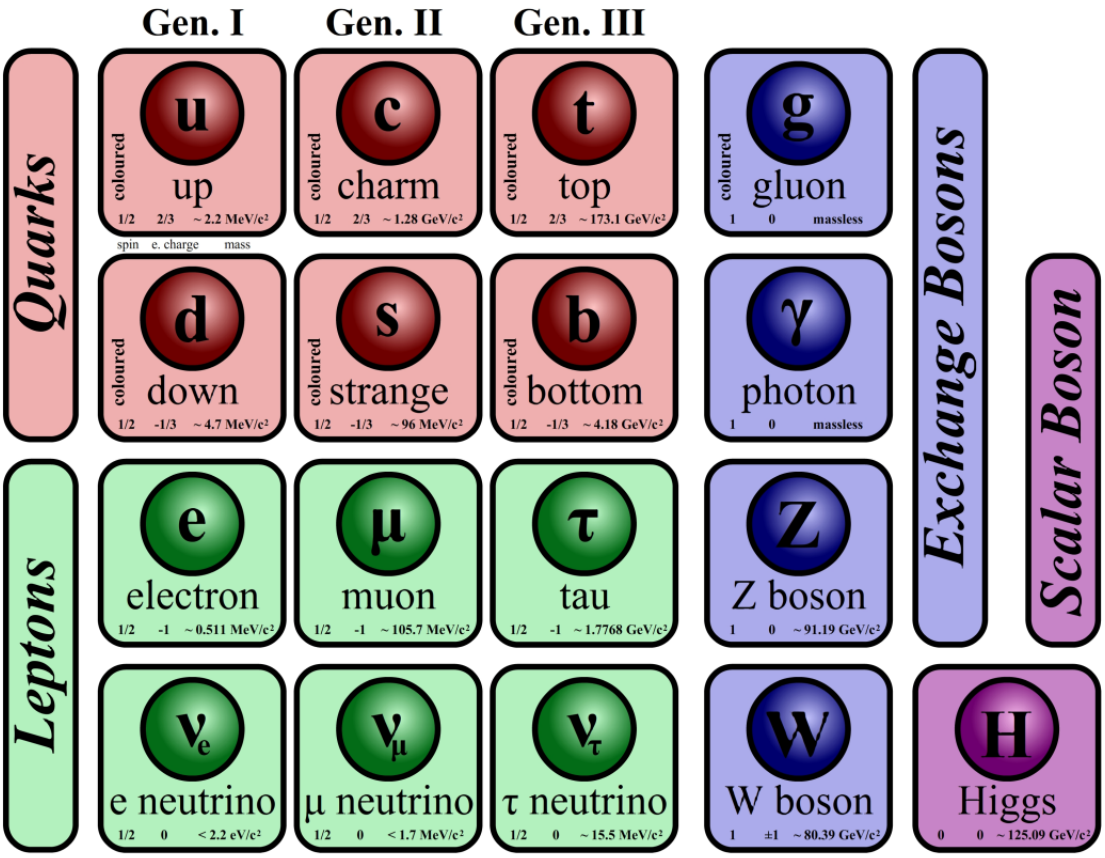

Figure 1.1: The Standard Model of Particle Physics. Figure adapted from [4].

In essence, the Standard Model represents the amalgamation of two separate theories: Quantum Chromodynamics (QCD), which describes the strong force, and the Electroweak theory, which unifies the electromagnetic and weak forces, accounting for a wide range of everyday physical phenomena.

1.1.1 Quark Model

The quark model, independently developed by Murray Gell-Mann and George Zweig [5, 6, 7, 8], provided valuable insights into the nature of hadrons. According to this model, hadrons are composite particles composed of quarks. The quark model categorizes hadrons into two types: mesons, which consist of a quark and an antiquark, and baryons, composed of three quarks each. Baryons and mesons naturally organize into multiplets, which contain hadrons with comparable properties and degenerate masses. This approximate flavor symmetry is the consequence of these multiplets, as depicted in Figure 1.2. The need for an additional quantum number specific to the strong interaction was addressed by the quark model, leading to the introduction of a "color charge" by O.W. Greenberg [9]. This hypothesis postulates

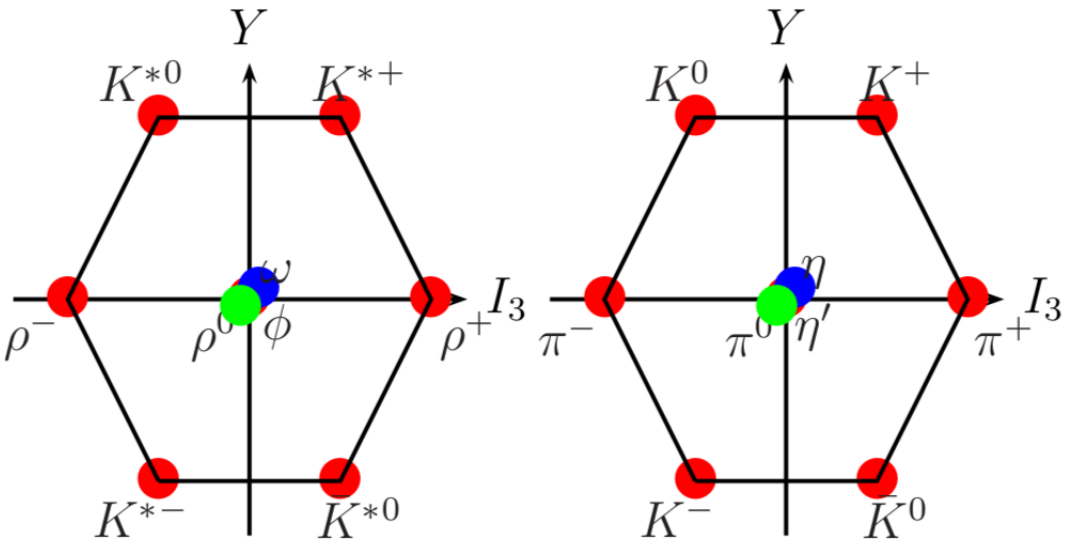

Figure 1.2: Vector and pseudoscalar meson nonets (left and right). The labels Y and I represent the hypercharge and isospin quantum numbers. All these particles have masses less than 1 GeV, with fluctuations of a few hundred MeV within each nonet.
Figure adapted from [10].

that quarks possess a color charge, which comes in three variations, and is entirely symmetric across all three colors, despite the different masses of various quarks. This color symmetry is described by the Lie group SU(3). The inclusion of color charges distinguishes quarks from other particles, enabling them to participate in strong interactions as well as weak and electromagnetic interactions with other fermions.

However, the quark model fails to explain the absence of free quarks in the natural world or the binding mechanism that holds quarks together. These limitations were overcome with the development of Quantum Chromodynamics (QCD), a quantum field theory that describes the strong interactions between quarks and gluons (the carriers of the strong force) [11, 12].

Hypercharge: In the context of the Standard Model of particle physics, hypercharge is a quantum number that characterizes the strong and weak forces acting on a particle. It is related to the third component of weak isospin and the electric charge of the particle. The hypercharge (Y) is defined as:

$$Y = 2(Q - I_3), \tag{1.1}$$

where Q is the electric charge and I_3 is the third component of weak isospin. The hypercharge of a particle determines its interactions via the strong and weak forces. While hypercharge is conserved in all strong and electromagnetic interactions, it is not conserved in weak interactions.

1.1.2 Quantum Chromodynamics

Quantum Chromodynamics (QCD) is a theory aimed at comprehending the properties and interactions of protons and neutrons, originating from nuclear physics [11]. QCD is an extension of Quantum Electrodynamics (QED), which describes the interaction between charged particles through the exchange of photons [13]. In QED, physical processes are computed using Feynman diagrams.

QCD Lagrangian

The complete QCD Lagrangian is given by:

$$\begin{aligned}\mathcal{L}_{QCD} = &\bar{\psi}[i\partial\!\!\!/ - m]\psi - \frac{1}{4}[\partial_\mu A^b_\nu - \partial_\nu A^b_\mu][^\mu A^\nu_b - \partial^\nu A^\mu_b] - \frac{1}{2a}\partial^\mu A^b_\mu \partial^\nu A^b_\nu \\ &+ \frac{g}{2}\bar{\psi}\lambda^a\gamma^\mu A^a_\mu\psi - \frac{g}{4}[\partial_\mu A^a_\nu - \partial_\nu A^a_\mu]f^{abc}A^\mu_b A^\nu_c - \frac{g^2}{4}f^{abc}f^{ade}A^a_\mu A^b_\nu A^\mu_d A^\nu_e \\ &- \partial^\mu c^{-a}\partial_\mu c^a + g f^{abc}A^c_\mu \partial^\mu c^{-a} c^b\,,\end{aligned} \tag{1.2}$$

where f_{abc} is the structure constant of the SU(3) algebra. The Lagrangian in Eq. (1.2) can be interpreted as follows:

- The first term represents the quark field i.e. can be used to derive the quark propagator.
- The second and third terms can be used to derive the gluon propagator defined by eight four-potentials A^b_μ.
- The fourth term represents the interaction between quark and gluon fields.
- The fifth term represents an interaction between three gluon fields.
- The sixth term represents an interaction between four gluon fields.
- The seventh term can be used to derive the ghost propagator,
- while the eighth term represents an interaction between ghost and gluon fields, where $c^{a,b}$ represents the ghost field and $c^{-a,-b}$ represents the antighost field.

It is important to note that the gauge-fixing Lagrangian in Eq. (1.2) is not gauge invariant. Details of the Lagrangian are described in [14, 15].
Quantum chromodynamics (QCD) provides an explanation for two intriguing properties of quarks, namely "asymptotic freedom" and "confinement."

The concepts of asymptotic freedom and confinement are fundamental in the field of quantum chromodynamics (QCD) [16, 17, 18, 19]. Asymptotic freedom refers to the phenomenon where the strength of the interactions between quarks diminishes at short distances. This occurs because static quarks emit virtual gluons, causing their color charges to spread into the surrounding vacuum. Consequently, the color force between quarks weakens as the distance between them decreases. On the other hand, confinement refers to the persistence

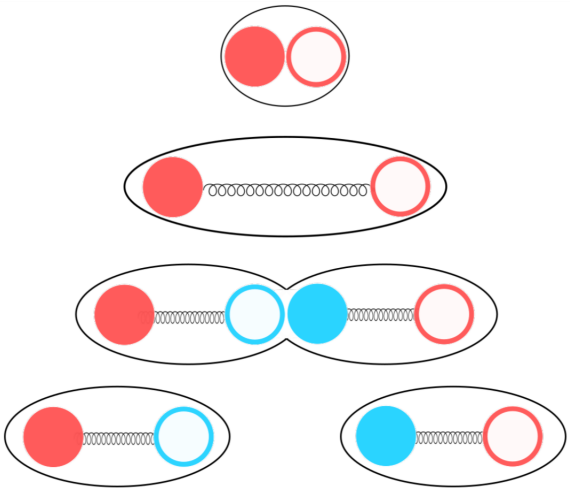

Figure 1.3: An illustration demonstrating color confinement in a meson. Figure adapted from [20]

of strong force between quarks even as they are separated. This leads to the formation of bound states, known as hadrons, composed of either a quark and an antiquark (mesons) or three quarks (baryons). Confinement, which arises from the strong interaction at long distances, explains the inability to observe free quarks. Although confinement lacks analytical proof, it is widely accepted due to its simple representation in lattice QCD.

To illustrate the concept of confinement, consider Figure 1.3, which depicts the confinement of color charges in a meson.

1.2 The World of Mesons

Mesons, a subset of hadrons, are composed of one quark and one antiquark. The confirmation of the existence of mesons came with the discovery of the π meson (pion) by English physicist Cecil Frank Powell and his research team in 1947. This discovery validated the initial theoretical work by Japanese physicist Yukawa Hideki in 1935, who had postulated the existence of mesons. Mesons exhibit a wide range of masses and typically have relatively short lifetimes, ranging from 10^{-8} to less than 10^{-22} seconds. The more massive mesons tend to be less stable than their lower mass counterparts, making the latter more suitable for study in cosmic ray experiments and particle accelerators.

Mesons are notable for their participation in both weak and strong interactions, with charged mesons additionally engaging in electromagnetic interactions. They generally have lower masses compared to baryons, making them more accessible for experimental creation and increasing the chances of observing high-energy phenomena. Consequently, mesons serve as valuable tools for investigating quark interactions, gaining insights into the role of gluons, and delving into the mechanisms of color confinement.

1.2.1 Groups and Symmetries

Isospin

The concept of isospin plays a fundamental role in the study of hadronic states, representing a symmetry arising from the compatibility between the two lightest quarks. This symmetry corresponds to the SU(2) group and leads to a distinct arrangement of hadronic states. Isospin was initially introduced to explain the nearly identical masses of the proton and neutron, which are indistinguishable under the influence of the nuclear force. The isospin quantum number I measures the strength of the strong interaction between nucleons and is projected onto the z-direction as $I_3 = +1/2$ and $-1/2$ for the proton and neutron, respectively. In the case of mesons, the isospin quantum number I assumes a value of 1, while the z-component I_3 can take on values of -1, 0, or 1, corresponding to the π^-, π^0, and π^+ mesons, respectively.

Parity, Charge-Conjugation, G-Parity

In the realm of meson classification, a comprehensive understanding hinges on multiple facets, including quark content, total angular momentum (J), parity (P), and other discerning properties like charge parity (C) and G-parity. The magnitude of the total angular momentum (J) serves as a fundamental descriptor, encompassing both orbital and spin angular momentum contributions. It spans a range from $|l - s|$ to $|l + s|$.

In this classification framework, discrete finite symmetry groups come into play, each having eigenvalues of ± 1. Three fundamental symmetries, namely Parity (P), Charge Conjugation (C), and G-parity, assume pivotal roles in characterizing mesons and their behavior:

- Parity (P): The P operator represents a spatial mirror reversal, a transformation preserved under both strong and electromagnetic interactions. Its action is elegantly captured by the expression:
$$P = (-1)^{l+1}\,. \tag{1.3}$$

- Charge Conjugation (C): C involves the intriguing transformation of a particle into its corresponding antiparticle by flipping the sign of its charge and magnetic moments ($q \to \bar{q}$ and vice versa). This transformation is encoded in the form:
$$C = (-1)^{l+s}\,. \tag{1.4}$$

- G-Parity (G): The G-parity, a more intricate symmetry, combines charge conjugation with a 180-degree rotation around the second axis of the isospin vector I_2. Its behavior is intricately expressed as:
$$G = (-1)^{I+l+s}\,. \tag{1.5}$$

These above equations encapsulate the relationships between these essential symmetries, angular momentum, and spin, providing a foundational framework for the systematic classification of mesons in the vibrant landscape of particle physics. The spin configuration of a

$q\bar{q}$ system can be either 0 or 1 for anti-parallel or parallel quarks, respectively. Mesons are categorized into different types based on their spin configuration, as presented in Table 1.1. These classifications offer insights into the dynamics of mesons by shedding light on the behavior and interactions of quarks.

State	s	l	J	P	C	J^{PC}	Mesons	Type
$^1S_0$	0	0	0	$-$	$+$	0^{-+}	$\pi \ \ \eta \ \ \eta' \ \ K$	pseudo-scalar
$^3S_1$	1	0	0	$-$	$-$	1^{--}	$\rho \ \ \omega \ \ \phi \ \ K^*$	vector
$^1P_1$	0	1	1	$+$	$-$	1^{+-}	$b_1 \ \ h_1 \ \ h_1' \ \ K_1$	pseudo-vector
$^3P_0$	1	1	0	$+$	$+$	0^{++}	$a_0 \ \ f_0 \ \ f_0' \ \ K_0^*$	scalar
$^3P_1$	1	1	1	$+$	$+$	1^{++}	$a_1 \ \ f_1 \ \ f_1' \ \ K_1$	axial vector
$^3P_2$	1	1	2	$+$	$+$	2^{++}	$a_2 \ \ f_2 \ \ f_2' \ \ K_2^*$	tensor

Table 1.1: The mesons states as a function of l, s and J and their corresponding meson types.

The lightest mesons, known as pseudo-scalar mesons, weakly decay into lepton pairs or electromagnetically into two photons [21]. Additionally, if their mass is sufficient, they can undergo strong interaction-induced disintegration into hadrons. Vector mesons, despite having a greater mass, have a shorter average lifespan compared to pseudo-scalar mesons due to their predominantly strong interaction-mediated decay.

1.2.2 Hybrids

Quantum Chromodynamics allows for the existence of meson states that possess unconventional quantum numbers, such as 0^{+-}, 1^{-+}, and 2^{+-}, as depicted in Figures 1.4 and 1.5. These spin-exotic states suggest the presence of particles comprising more than two quarks or gluonic excitations. Topics related to such states predominantly include hybrids, glueballs, or multi-quark states like tetraquarks and pentaquarks [22, 23, 24], as well as mesonic molecules and hadrocharmonium, which are commonly referred to as exotics, as illustrated in Figures 1.4, 1.5, and 1.6.

According to QCD, "glueballs," which consist solely of gluons, are predicted to exist as additional isoscalar mesons. Lattice gauge theories indicate that the ground state glueball is 0^{++}, with a mass of $(1730 \pm 80$ MeV/c$^2)$, while the first excited state is 2^{++}, with a mass of $(2400 \pm 120$ MeV/c$^2)$ [25, 26]. Hybrid states, believed to be mesons formed by binding excited gluons to $q\bar{q}$ pairs, are expected to fall within the mass range of 1.9 GeV. The lightest hybrid, an exotic 1^{-+} state, with a mass ranging from 1.8 to 1.9 GeV, is also predicted by lattice QCD [27],[28].

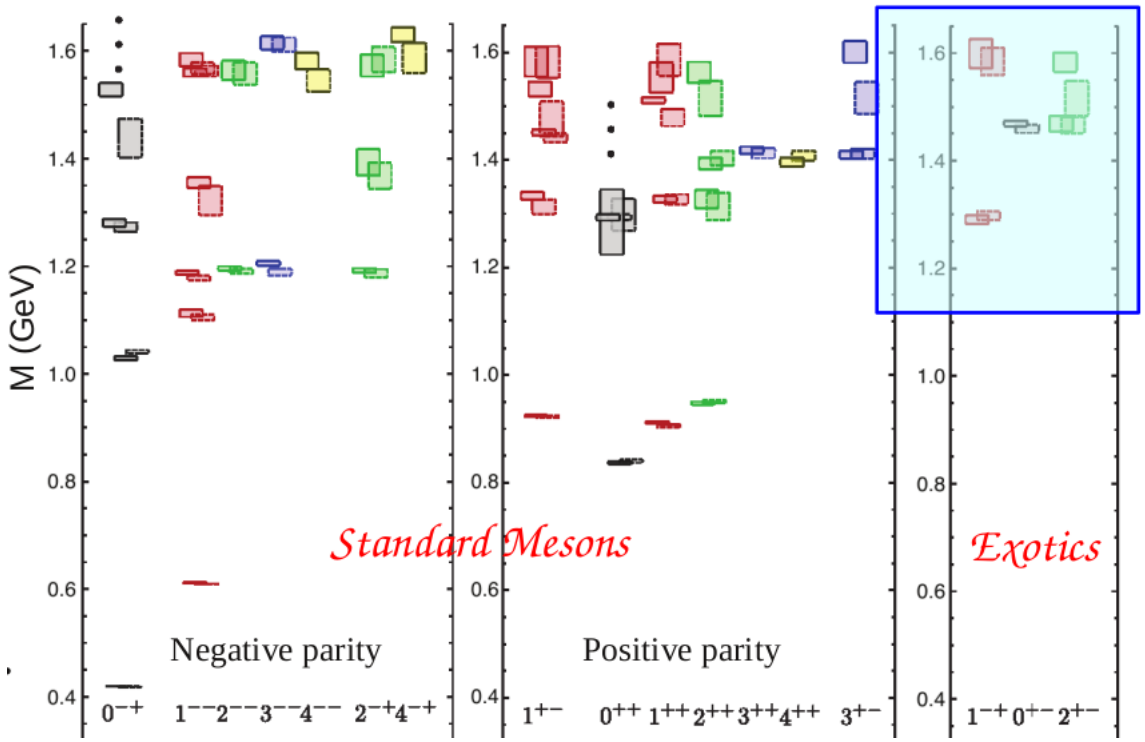

Figure 1.4: Isovector meson spectrum obtained from Lattice QCD. Figure from [29]

1.3 Motivation

The intricate domain of quantum chromodynamics (QCD) continues to grapple with a multitude of unresolved intricacies, encompassing the enigmatic nature of the strong interaction binding quarks and gluons, the elusive internal structure of hadrons, and the perplexing phenomenon of confinement. Within this context, the study of light meson spectroscopy assumes paramount importance, as it serves as a linchpin for unraveling the enigmatic low-energy structure of QCD, wherein the existence of gluonic excitations represents a captivating facet.

Recent experimental breakthroughs, exemplified by the manifestation of structural diversity and multiquark states [30, 31, 32, 33] observed at particle colliders, have bestowed upon us the tantalizing prospect of unearthing further exotic hadrons, particularly those bearing explicit gluonic content [34]. These unconventional hadrons furnish a unique vantage point from which to glean insights into the intricate characteristics of gluons, the mechanisms governing color confinement, and the dynamics of the strong interaction, thus rendering them an indispensable subject of scholarly pursuit.

Photoproduction processes emerge as a fertile realm for the creation of exotic mesons, and unraveling the underlying mechanisms governing non-exotic meson photoproduction serves as an auspicious springboard for exploring and comprehending the phenomenology surrounding "exotic hybrid states" engendered by such processes. It is noteworthy that

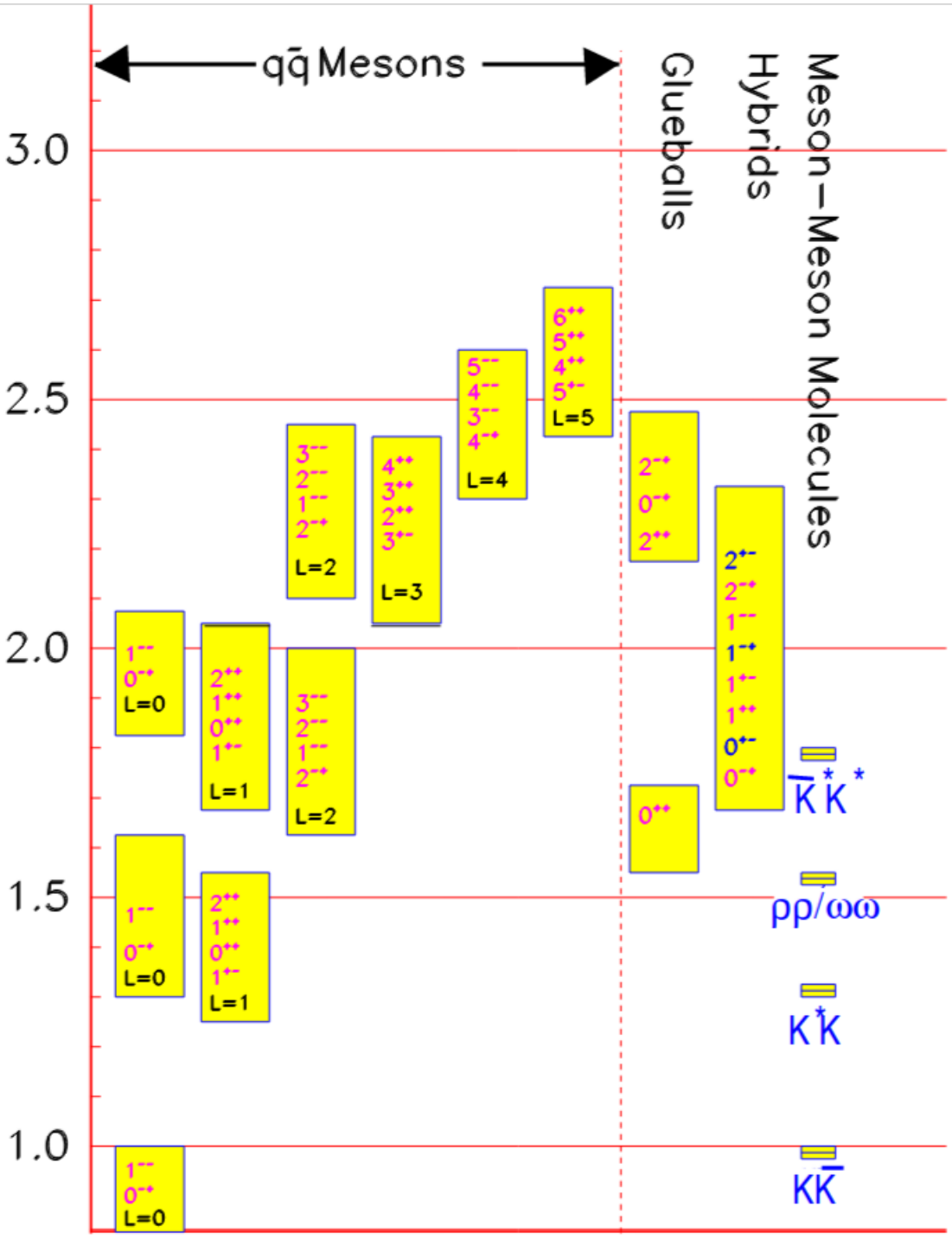

Figure 1.5: Expected meson spectrum. Figure from [35]

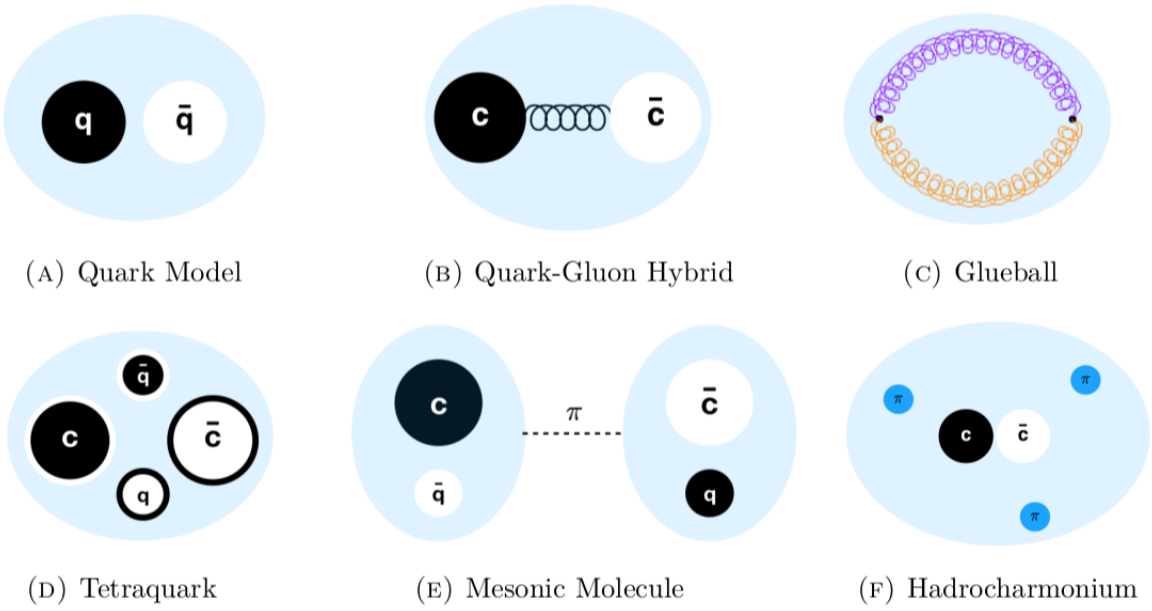

(A) Quark Model (B) Quark-Gluon Hybrid (C) Glueball

(D) Tetraquark (E) Mesonic Molecule (F) Hadrocharmonium

Figure 1.6: Illustration of meson substructure models, with black and white colors representing particles and antiparticles, respectively. Figure adapted from [36]

these photoproduction-induced exotic hybrid states, typified by $\eta\pi$ and $\omega\pi$ photoproductions, assume particular significance within the confines of Jefferson Laboratory (JLab). These processes occupy a paramount position in the quest for detecting exotic states at JLab, their comprehensive study proving pivotal in shedding light on the nuanced characteristics of gluons, the mechanisms orchestrating color confinement, and the tenets of the strong interaction.

Amongst photoproduction channels, $\pi\pi$ photoproduction reigns supreme as the most prominent process, rendering it the optimal "non-exotic" candidate for delving into the multifaceted features pervading the meson resonance spectrum. However, the intricacies of the production mechanism underpinning larger momentum transfers remain shrouded in ambiguity. Moreover, a contentious debate persists regarding the true nature of the pomeron, thereby endowing this avenue of inquiry with a tantalizing allure.

In concert with the photoproduction process, the arena of final-state interactions assumes great significance, wherein a meticulous examination of resonance properties encompassing phase shifts, widths, and inelasticities can facilitate the identification of latent exotic manifestations.

While antecedent research has addressed resonances within the $\pi\pi$ channel, attaining precise results has been impeded by the unfavorable phase shift behavior observed at the $\pi\pi$ threshold, primarily attributable to the lack of crossing symmetry. Consequently, this investigation endeavors to analyze P-wave resonances employing a coupled channel separable potential approach, thereby proffering projections pertaining to $\pi\omega$ characteristics. Accu-

rate measurements of scattering amplitudes bestowed by this study hold immense potential for advancing analyses at JLab, where the subtle repercussions of predicted exotic states necessitate the precise estimation of amplitudes.

Notational Convensions

In this thesis, the following notations will be used:
The general contravariant four-vector in the Bjorken and Drell notation:

$$p^{\mu} : (p^0, p^1, p^2, p^3), . \tag{1.6}$$

With the metric tensor convention:

$$g^{\mu\nu} = \begin{pmatrix} 1 & 0 & 0 & 0 \\ 0 & -1 & 0 & 0 \\ 0 & 0 & -1 & 0 \\ 0 & 0 & 0 & -1 \end{pmatrix}, \tag{1.7}$$

the covariant four vector reads:

$$p_{\mu} : (p^0, -p^1, -p^2, -p^3) = g_{\mu\nu} p^{\mu}, . \tag{1.8}$$

The notation $\not{p} = \gamma^{\mu} p_{\mu}$ is used, where γ^{μ} represents the Dirac matrices (See Appendix A).
The thesis calculations will utilize the following mass and width values, measured in GeV/c^2, while adhering to the convention of setting $\hbar$ and c to unity:

$$m_p = 0.93827\,, \tag{1.9}$$
$$m_{\pi} = 0.13957\,, \tag{1.10}$$
$$m_{\rho} = 0.775\,, \tag{1.11}$$
$$m_{\sigma} = 0.5\,, \tag{1.12}$$
$$m_{f_0} = 0.98\,, \tag{1.13}$$
$$\Gamma_{\rho} = 0.149\,, \tag{1.14}$$
$$\Gamma_{\sigma} = 0.5\,, \tag{1.15}$$
$$\Gamma_{f_0} = 0.1\,. \tag{1.16}$$

where $m_{\rm p}$, m_{π}, m_{ρ} , m_{σ}, m_{f_0} are the proton, pion, ρ meson, $\sigma \equiv f_0(500)$, $f_0(980)$ masses respectively, with $e = \sqrt{\frac{4\pi}{137}}$ as the electric charge. Also, "pomeron" exchange will be included within the study and it will be defined in 2.2.

Chapter 2

Theoretical Background

Scattering theory serves as a fundamental framework for analyzing particle reactions without requiring a specific definition of the underlying particle interaction. Rooted in fundamental principles such as probability conservation, unitarity, and causality, it enables the construction of amplitude models that can be analytically extended to extract the underlying physics of the reaction. This chapter elucidates the concept of the S-matrix and its intrinsic characteristics, along with dispersion relations that establish connections between the overall transition amplitude and its discontinuities. Additionally, it explores resonances within the complex plane and delves into Regge theory, encompassing trajectories and poles.

2.1 The S Matrix

The scattering process can be delineated into three stages: the pre- and post-collision phases, where particles can be described in terms of their free states, and an intermediate stage characterized by particle interactions. The notion of the S-matrix, first proposed by Wheeler [37] in 1937, encapsulates an operator that transforms an initial state into a final state. Subsequently, in 1942, Heisenberg postulated that this matrix encompassed all the requisite information for calculating physical observables, including cross sections and bound state energies [38].

Even today, S-matrix theory remains a potent tool in hadronic physics, particularly for probing meson-meson interactions. This formalism yields model-independent, robust, and accurate results while maintaining simplicity of implementation.

The construction of the S-matrix is founded upon essential principles governing the nature of the underlying interaction. These principles encompass relativistic covariance, Lorentz invariance, and the unitarity condition.

Relativistic covariance guarantees that theoretically computed observables yield consistent results, irrespective of the chosen inertial frame of reference. It serves as a broader concept encompassing the preservation of physical laws under various transformations in relativistic physics. In contrast, Lorentz invariance specifically focuses on preserving equations under Lorentz transformations within the framework of special relativity.

Conversely, the unitarity condition is a crucial requirement for probability conservation. It ensures that the total probability remains constant at one, representing the likelihood of all potential outcomes in an interaction.

As previously mentioned, the S-matrix describes the transition from asymptotic initial states $|i\rangle$ to asymptotic final states $|f\rangle$, allowing for the definition of the matrix element $\langle f|\, S\, |i\rangle$. These matrix elements must be scalars, given that S is expected to be Lorentz invariant[1]. Consequently, if particles are described solely by their 4-momentum, the amplitude will depend solely on scalar variables such as $p_i^{\mu} p_{j\mu}$.

The S matrix finds its concise representation in two distinct terms:

$$S = \mathbb{I} + iT\,. \tag{2.1}$$

In this formulation, the identity matrix, denoted as $\mathbb{I}$, signifies the state of non-interacting particles. On the other hand, the T-matrix encapsulates the intricacies of the interaction process and can be articulated as:

$$\langle f|\, T\, |i\rangle = i(2\pi)^4 \delta^4(p_i - p_f) T_{fi}\,. \tag{2.2}$$

In Eq. (2.2) $\delta^4(p_i - p_f)$ established the four-momentum conservation $p_i = p_f$ with $p_i = p_1 + p_2$ and $p_f = p_3 + p_4$.

In the realms of nuclear, atomic, and particle physics, the differential and total scattering cross sections stand as paramount observables. They serve as a means to describe the likelihood of a particular scattering event occurring. These cross sections encapsulate the essence of two-body scattering measurements and play a crucial role in understanding the intricacies of hadronic physics, as resonances often manifest as distinctive peaks or bumps within these cross sections. With dimensions of an area, the total cross section for the $12 \to 34$ scattering process can be defined as:

$$\sigma_{12} = \frac{1}{4|p_1|\sqrt{s}} \sum_j (2\pi)^4 \delta^4(p_f - p_i) |\langle f|\, T\, |i\rangle|^2\,, \tag{2.3}$$

Here, the sum over "j" represents the summation over all possible final states 'j" that are consistent with the initial state "i" and the scattering process.

In this thesis, the S-matrix formalism plays a prominent role in investigating resonance properties in meson-meson scattering processes, encompassing phase shifts and inelasticities. The $\pi\pi$ and $\pi\omega$ channels will be the primary focus, with detailed discussions in Chapters 5 and 6.

[1]The Lorentz invariance of the S matrix stems from the Lorentz invariance of the scattering amplitudes, which are themselves Lorentz invariant quantities. The S matrix, which describes the probability of a scattering process occurring, remains unchanged in all inertial reference frames related by Lorentz transformations. This property arises from the fundamental symmetry of the laws of physics under Lorentz transformations.

2.1.1 Unitarity

The principle of unitarity ensures the conservation of particle flux, implying that the total probability of all possible final states must sum up to one:

$$\sum_n P_n = 1, \tag{2.4}$$

where P_{if} represents the transition probability from an initial state $|i\rangle$ to a final state $|f\rangle$, given by:

$$P_{if} = \left| \langle f| \hat{S} |i\rangle \right|^2. \tag{2.5}$$

Rearranging Eq. (2.4) using the completeness identity $\sum_n |n\rangle \langle n| = \mathbb{I}$ yields:

$$\sum_n |\langle n| S |i\rangle|^2 = 1. \tag{2.6}$$

Further manipulation, employing algebraic transformations, leads to the unitarity conditions:

$$S^\dagger S = S S^\dagger = \mathbb{I}, \tag{2.7}$$

$$T - T^\dagger = iT^\dagger T = iTT^\dagger\,. \tag{2.8}$$

By substituting Eq. (2.2) into (2.8), we obtain:

$$\langle f| T |i\rangle - \langle f| T^\dagger |i\rangle = (2\pi)^4 \delta^4(p_f - p_i)(T_{fi} - T^*_{if})\,. \tag{2.9}$$

Due to the time reversal symmetry in strong interactions, i.e., $T_{fi} = T_{if}$, Eq. (2.9) can be expressed as:

$$\mathrm{Im}\, T_{fi} = \frac{T_{fi} - T^*_{if}}{2i}\,. \tag{2.10}$$

The unitarity condition for the transition amplitude is expressed as follows:

$$2\,\mathrm{Im}\, T_{fi} = (2\pi)^4 \sum_N \delta^4(p_n - p_i) T_{fn} T^*_{in}, \tag{2.11}$$

Here, the summation $\sum_N$ represents both a phase-space integral and a sum over all potential intermediate states. This summation is defined as:

$$\sum_N = \sum_n \int \prod_{j=1}^{n} \frac{d^3 p_j}{(2\pi)^3 2E_j}\,. \tag{2.12}$$

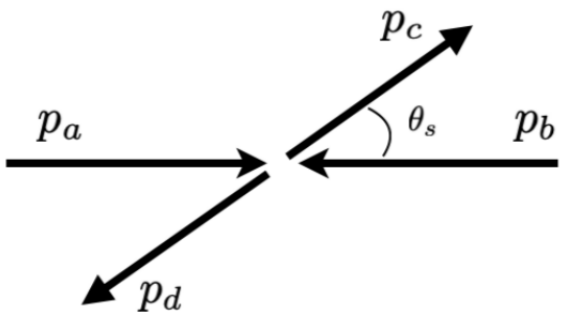

Figure 2.1: Representation of the $AB \to CD$ scattering process in the center of mass frame. Figure from [36]

2.1.2 Crossing Symmetry

Consider a scattering process $A(p_a, m_a)+B(p_b, m_b) \to C(p_c, m_c)+D(p_d, m_d)$, where $p_i = (E_i, \vec{p_i})$. In this context, one can establish the following relationships:

$$\sum_i p_i^\mu = 0 \Rightarrow p_a + p_b = p_c + p_d \quad \text{conservation of 4-momentum,} \tag{2.13}$$

$$p_i^2 = m_i^2 \quad \text{on-shell condition.} \tag{2.14}$$

To conveniently describe the scattering process, the Mandelstam variables, which are Lorentz invariant kinematic variables can be introduced as:

$$\begin{aligned} s &= (p_a + p_b)^2 = (p_c + p_d)^2 \,, \\ t &= (p_a - p_c)^2 = (p_b - p_d)^2 \,, \\ u &= (p_a - p_d)^2 = (p_b - p_c)^2 \,. \end{aligned} \tag{2.15}$$

Using Eqs.(2.13),(2.14), and (2.15), one can derive the following relation:

$$s + t + u = \sum_{i=1}^{4} m_i^2 \,. \tag{2.16}$$

It is important to note that the Mandelstam variables in Eq.(2.16) are not independent. Therefore, one of them can be expressed in terms of the other two, meaning that two independent kinematic variables are sufficient to describe the two-body scattering process. Specifically, in the s-channel center of mass frame of the initial particles (as depicted in Fig.2.1), thus the Mandelstam variables can be expressed as:

$$\begin{aligned} s &= m_a^2 + m_b^2 + 2(E_a E_b - |\vec{p_a}||\vec{p_b}| \cos\pi) \,, \\ t &= m_a^2 + m_c^2 - 2(E_a E_c - |\vec{p_a}||\vec{p_c}| \cos(\pi - \theta_s)) \,, \\ u &= m_a^2 + m_d^2 - 2(E_a E_d - |\vec{p_a}||\vec{p_d}| \cos\theta_s) \,. \end{aligned} \tag{2.17}$$

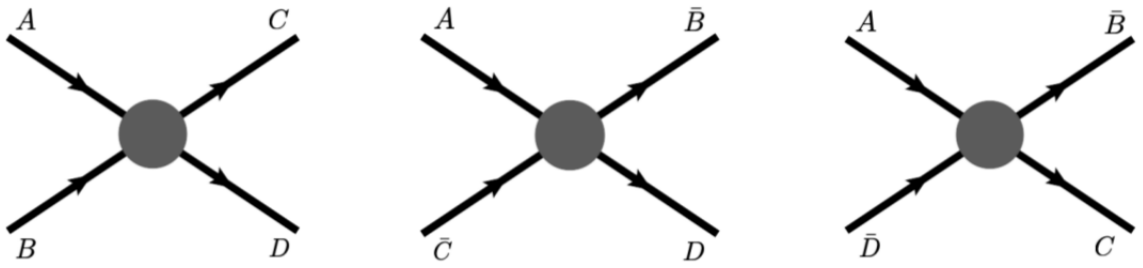

(A) s-channel (B) t-channel (C) u-channel

Figure 2.2: The crossing channels of the $AB \to CD$ scattering process. Figure from [36]

The momenta in the center of mass frame can be expressed as:

$$|\vec{p_a}|^2 = |\vec{p_b}|^2 = \frac{\lambda(s, m_a^2, m_b^2)}{4s} = \frac{(s-(m_a+m_b)^2)(s-(m_a+m_b)^2)}{4s}\,, \tag{2.18}$$

$$|\vec{p_c}|^2 = |\vec{p_d}|^2 = \frac{\lambda(s, m_c^2, m_d^2)}{4s} = \frac{(s-(m_c+m_d)^2)(s-(m_c+m_d)^2)}{4s}\,, \tag{2.19}$$

where $\lambda(a, b, c)$ is the Källen function defined as:

$$\lambda(a, b, c) = a^2 + b^2 + c^2 - 2(ab + bc + ca)\,. \tag{2.20}$$

By expressing the energies in terms of the three-momenta, $E_i^2 = |\vec{p_i}|^2 + m_i^2$, the energies in the center of mass frame can be determined as:

$$E_a = \frac{s + m_a^2 - m_b^2}{2\sqrt{s}} \quad , \quad E_b = \frac{s + m_b^2 - m_a^2}{2\sqrt{s}}\,, \tag{2.21}$$

$$E_c = \frac{s + m_c^2 - m_d^2}{2\sqrt{s}} \quad , \quad E_d = \frac{s + m_d^2 - m_c^2}{2\sqrt{s}}\,. \tag{2.22}$$

From Eqs.(4.12),(2.19),(2.21), and (2.22), it is evident that s alone determines the energies and momenta of the particles in the center of mass frame. The scattering angle θ_s, which is the angle between the directions of motion of particles C and D (see Fig. 2.1), can be expressed as:

$$\cos\theta_s = \frac{s(t-u) + (m_a^2 - m_b^2)(m_c^2 - m_d^2)}{4sp_ap_c}\,. \tag{2.23}$$

The crossing channels of the process, as shown in Fig. 2.2, are represented by the following analytic expressions:

$$s-\text{channel}: \quad A(p_a)+B(p_b)\to C(p_c)+D(p_d)\,, \tag{2.24}$$
$$t-\text{channel}: \quad A(p_a)+\bar{C}(-p_c)\to \bar{B}(-p_b)+D(p_d)\,, \tag{2.25}$$
$$u-\text{channel}: \quad A(p_a)+\bar{D}(-p_d)\to \bar{B}(-p_b)+D(p_d)\,. \tag{2.26}$$

The antiparticles of B, C, and D are represented by $\bar{B}$, $\bar{C}$, and $\bar{D}$, respectively, with reverse 4-momentum compared to the s-channel kinematics. The concept of crossing symmetry asserts that the amplitude characterizing the scattering in the s-channel is related to the amplitudes of the t-channel and the u-channel. By exchanging the kinematic variables, the scattering amplitudes in the s-, t-, and u-channels can be obtained through the same analytical function. Therefore, for an elastic scattering process with equal masses, the following relations can be defined:

$$T(s,t,u)=\begin{cases} T_s & \equiv T(s,t,u) \quad s_{\text{th}}\geq 4m^2, \quad t\leq 0, \quad u\leq 0\,, \\ T_t & \equiv T(t,s,u) \quad t_{\text{th}}\geq 4m^2, \quad s\leq 0, \quad u\leq 0\,, \\ T_u & \equiv T(u,t,s) \quad u_{\text{th}}\geq 4m^2, \quad t\leq 0, \quad s\leq 0\,. \end{cases} \tag{2.27}$$

Here, the subscript (th) represents the threshold energy, i.e., the minimum energy needed for the scattering process to be allowed. The relations in Eq. (2.27) are referred to as the Mandelstam hypothesis [39, 40], which is essential in describing hadronic processes.

2.1.3 Partial Wave Expansion

The preservation of total angular momentum in all scattering processes is a fundamental requirement for maintaining rotational invariance. As a consequence, the amplitudes can be decomposed into a series of scalar functions with well-defined angular momentum, commonly known as partial waves. These partial waves play a crucial role in the analysis of resonances, as resonant behavior is typically associated with specific partial waves. This underscores the significance of performing a partial wave analysis to extract valuable information about resonance parameters.

For a spinless amplitude, the partial wave expansion can be expressed as:

$$T(s,t,u)=16\pi N(2l+1)f_l(s)P_l(\cos\theta_s)\,. \tag{2.28}$$

Here, N takes the value of 2 when dealing with scattering of identical particles, and 1 otherwise. The term $P_l(\cos\theta_s)$ corresponds to the Legendre polynomials of the first kind, which satisfy the following orthogonality condition:

$$\int_{-1}^{+1} P_l(x)P_{l'}(x)dx=\frac{2}{2l+1}\delta_{ll'}\,. \tag{2.29}$$

By utilizing the orthogonality property described in Eq. (2.29), the partial waves $f_l(s)$, which depend solely on the variable s, can be determined as follows:

$$f_l(s) = \frac{1}{32\pi N} \int_{-1}^{+1} dz_s P_l(z_s) T(s,t,u); \tag{2.30}$$

In this equation, $z_s = \cos\theta_s$ represents the cosine of the scattering angle within the physical region. It is important to note that this approach can be applied to other channels, such as the t- and u-channels, in a similar manner.

2.1.4 Analyticity and Dispersion Relation

The fundamental property of analyticity in the S-matrix asserts that the scattering amplitude remains an analytic function of the kinematic variables when continued into the complex plane. This property is of utmost importance for maintaining the validity of crossing symmetry. To facilitate analytical continuation, a small imaginary part, denoted as $i\epsilon$, is introduced to the kinematic variables, which are originally real. It is noteworthy that the original physical amplitude can be retrieved by taking the limit as ϵ approaches zero, as expressed by:

$$f_l(s) = \lim_{\epsilon \to 0^+} f_l(s + i\epsilon)\,. \tag{2.31}$$

The unitarity relation, as presented in Eq. (2.11), indicates the existence of a non-zero imaginary component beyond the initial threshold, which occurs at $s = (m_1 + m_2)^2$ in the case of unequal masses. Furthermore, the opening of new intermediate inelastic channels may generate additional imaginary parts, each associated with their respective inelastic thresholds. It is important to note that the Mandelstam hypothesis suggests that the imaginary components of the crossed channels will also manifest in the s-channel when shifting the variables from the s-channel physical region to the t- or u-channel physical regions. For the case of two unequal masses, the expression in Eq.(2.16) can be written as:

$$s + t + u = 2(m_1^2 + m_2^2)\,. \tag{2.32}$$

A noteworthy observation arising from the preceding discussion is that the imaginary parts persist from $(m_1 + m_2)^2$ to ∞ due to the presence of the s-channel cut, as well as from $(m_1 - m_2)^2 - t$ to $-\infty$ due to the u-channel cut. Consequently, the amplitude is real on the real axis between these two thresholds.

The Cauchy theorem provides a dispersion relation that illuminates the analytic properties of the scattering amplitude, and it can be expressed as the Cauchy representation for $f(s)$[2]:

$$f(s) = \frac{1}{2\pi i} \oint_C ds' \frac{f(s')}{s' - s}\,. \tag{2.33}$$

[2]For simplicity, the orbital angular momentum index will be omitted

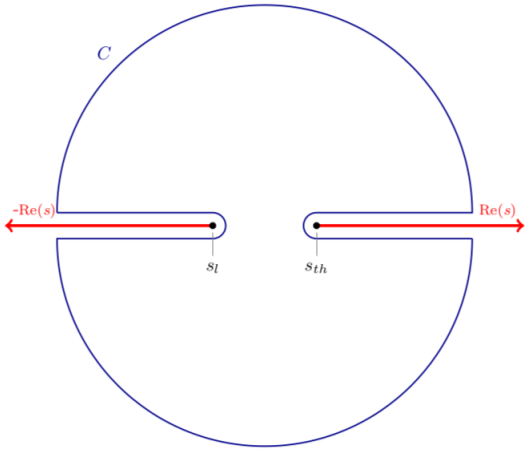

Figure 2.3: Integration contour in the s-plane, where the real-axis is indicated in red and the first left- and right-hand cut are labeled as s_l and s_{th} respectively. Figure from [36]

To simplify the analysis, the amplitude tends to zero as s approaches infinity, and the curved portion of the circular contour shown in Figure 2.3 becomes negligible as the radius R goes to infinity. Consequently, the contribution from the circular paths becomes insignificant. Hence, Eq. (2.33) can be simplified to:

$$f(s) = \frac{1}{2\pi i}\left[\int_{-\infty}^{s_l} ds' \frac{f(s'+i\epsilon) - f(s'-i\epsilon)}{s'-s} + \int_{s_{th}}^{\infty} ds' \frac{f(s'+i\epsilon) - f(s'-i\epsilon)}{s'-s}\right]. \tag{2.34}$$

The Schwarz reflection principle, a significant theorem in complex analysis, states that an analytic function $f(z)$ defined in a domain C in the complex plane, with real values in a segment of C, can be extended analytically to the entire complex plane:

$$f(z^*) = f^*(z)\,. \tag{2.35}$$

Consequently, the imaginary part of the amplitude can be related to its discontinuity as:

$$\mathrm{Im}\, f(s) = \frac{f(s+i\epsilon) - f(s-i\epsilon)}{2i}\,, \tag{2.36}$$

where $\epsilon \to 0$ and is positive. Thus, Eq.(2.34) can be expressed in terms of the imaginary part of the amplitude as:

$$f(s) = \frac{1}{\pi}\left[\int_{-\infty}^{s_l} ds' \frac{\mathrm{Im}\, f(s')}{s'-s-i\epsilon} + \int_{s_{th}}^{\infty} ds' \frac{\mathrm{Im}\, f(s')}{s'-s-i\epsilon}\right]. \tag{2.37}$$

In case where the amplitude does not satisfy the condition $\lim_{s\to\infty} f(s) = 0$, then the convergence of the dispersion relation can be maintained through subtraction:

$$f(s) = \frac{1}{\pi}\int ds' \frac{\operatorname{Im} f(s')}{s'-s}\frac{(s'-s)+(s-s_0)}{s'-s_0}\,, \tag{2.38}$$

$$f(s) = f(s_0) + \frac{s-s_0}{\pi}\int \frac{ds'}{(s'-s_0)}\frac{\operatorname{Im} f(s')}{(s'-s)}\,. \tag{2.39}$$

The first equation represents the unsubtracted dispersion relation, also known as the Kramers-Kronig relation. The second equation corresponds to the once-subtracted dispersion relation, which is obtained by subtracting the pole contribution at $s = s_0$ from the unsubtracted dispersion relation. Here, $f(s_0)$ is determined as:

$$f(s_0) = \frac{1}{\pi}\int \frac{ds'}{(s'-s_0)} \operatorname{Im} f(s')\,. \tag{2.40}$$

The incorporation of subtractions into dispersion relations is an effective approach to improving convergence at high energies (s); however, it requires the determination of additional parameters $f_i(s_0)$, either from the final observable or by matching them to other theories such as Chiral Perturbation Theory (ChPT). It should be noted that dispersion relations may contain more subtractions than the minimum necessary for convergence (i.e., over-subtracted), which reduces sensitivity to the high-energy region and can be rectified.

In summary, this section has demonstrated the power of dispersion relations in reconstructing the total amplitude from the S-matrix's discontinuities by leveraging its analyticity, unitarity, and crossing symmetry.

2.1.5 Resonances

Understanding the profound implications of line shapes within experimental data poses an exceedingly intricate challenge in the realm of particle physics. Observable features, such as peaks, bumps, and dips, serve as signatures of underlying physical processes. These distinctive structures can manifest in two distinct forms: as consequences of scattering kinematics or as manifestations of particle states, including resonances or bound states.

Bound states, also recognized as hadronic molecules, materialize as poles situated along the real axis of the primary physical Riemann sheet, positioned just below the first threshold. Within the confines of unitarity and causality, the first Riemann sheet admits only branch cuts and bound states. In contrast, a pole residing on the second unphysical Riemann sheet characterizes a resonance, characterized by a negative imaginary component beyond the threshold. Refer to Fig. 2.4 for a visual representation.

To encapsulate their behavior, resonances are commonly described by the Breit-Wigner (BW) propagator, an amplitude representation widely employed in particle physics. Specifically, for P-wave resonances, the BW propagator can be elegantly expressed as:

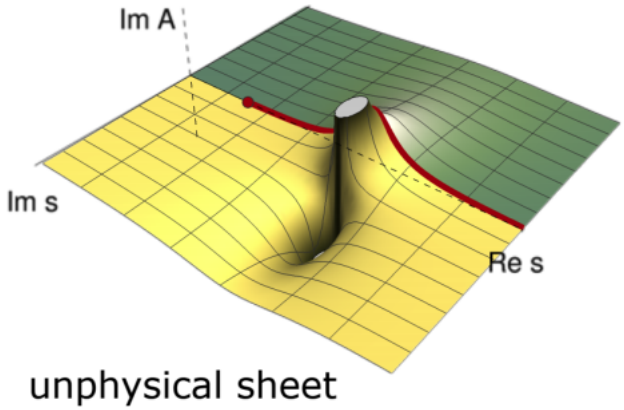

Figure 2.4: The complex plane where a single resonance generates a pole in the unphysical Riemann sheet (yellow plane). The proximity of the pole to the physical region (red line in the green plane) reflects the extent of its influence on the physical sheet. Figure adapted from [41].

$$BW(s) = \frac{1}{m_\rho^2 - s_{\pi\pi} - i m_\rho \Gamma} \,. \tag{2.41}$$

In this equation, m_ρ denotes the mass of the ρ meson, $s_{\pi\pi}$ represents the squared energy of the pion-pion system ($s_{\pi\pi} = m_{\pi\pi}^2$), and Γ signifies the decay width, which exhibits an inverse proportionality to the resonance's lifetime, denoted by τ. The decay width governs the sharpness of the resonance's peak and its positioning along the real axis, thereby indicating its proximity to the physical region.

Introducing an energy-dependent decay width $\Gamma(s)$ within the Breit-Wigner propagator necessitates comprehensive knowledge of all alternative decay channels and their corresponding coupling constants. This, however, introduces a level of model dependency to the representation of the Breit-Wigner function.

To thoroughly investigate the impact of P-wave contributions within the current model (as expounded further in Chapter 3), a meticulous analysis was conducted on the Breit-Wigner amplitude for ρ meson production. Both energy-dependent and energy-independent widths were considered in this examination. Remarkably, the adoption of an energy-dependent width, as visually depicted in Fig. 2.5, elicited a noticeable shift in the resonance peak towards lower values of $s_{\pi\pi}$. Consequently, this intensified the Breit-Wigner response to the left of $s_{\pi\pi} = m_\rho^2$, ultimately resulting in a diminution of the amplitude. Incorporating this approach substantially enhanced the overall model.

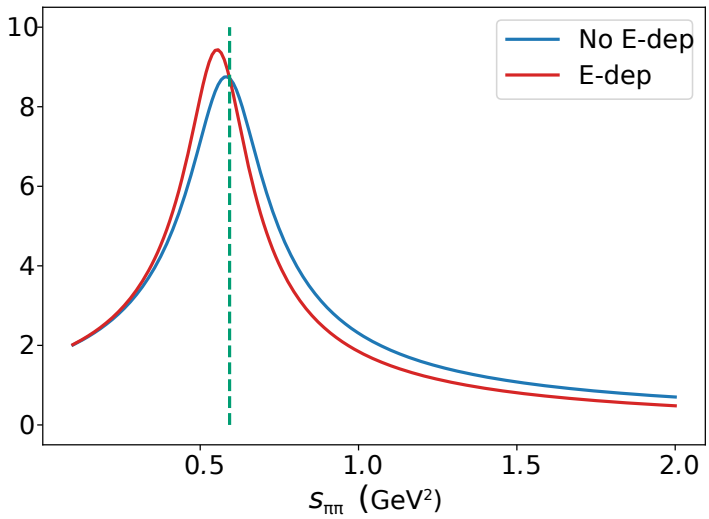

Figure 2.5: Comparison of the P-wave Breit-Wigner amplitude with energy-dependent and energy-independent widths as a function of $s_{\pi\pi}$.

2.2 Regge Theory

Regge theory, named after Tullio Regge [42, 43], provides a theoretical framework for characterizing hadronic cross-sections based on fundamental assumptions in scattering theory. Developed in the 1950s and 1960s prior to quantum chromodynamics (QCD), Regge theory posits that strong forces are mediated by the correlated exchange of entire hadron families, known as orbital excitations, over extended distances, rather than individual hadrons. These exchanges are described by interpolating between resonances in the complex angular momentum and mass plane, referred to as Regge trajectories.

2.2.1 Scattering Amplitude in the Regge Limit

In the physical region ($s > 0$ and $t < 0$), the scattering amplitude can be expanded as a series of Legendre polynomials $P_\ell(\cos\theta)$, where θ represents the scattering angle in the center-of-mass frame and depends on s and t through $\cos\theta = 1 + \frac{2t}{s}$. For the process $a + c \to b + d$, the scattering amplitude takes the form:

$$A(s,t) = \sum_{\ell=0}^{\infty} (2\ell+1) f_\ell(s) P_\ell(1 + \frac{2t}{s}) \,. \tag{2.42}$$

Here, the partial wave amplitudes $f_\ell(s)$ are used to expand the scattering amplitude in terms of Legendre polynomials $P_\ell(\cos\theta)$ in the physical region. By considering the t-channel and utilizing crossing symmetry, the amplitude in Eq. (2.42) can be expressed as:

$$A(s,t) = \sum_{\ell=0}^{\infty} (2\ell+1) f_\ell(t) P_\ell(1 + \frac{2s}{t}) \,. \tag{2.43}$$

Applying the Sommerfeld-Watson transformation [44], Eq. (2.43) can be reformulated as a contour integral in the complex l-plane:

$$A(s,t) = \frac{(-1)^\ell}{2i} \oint_{\mathbb{C}} dl \frac{(2\ell+1)}{\sin \pi\ell} f_\ell(t) P_\ell(1 + \frac{2s}{t}) \,. \tag{2.44}$$

In Eq. (2.44), the functions $f_\ell(t)$ and $P_\ell(1 + \frac{2s}{t})$ represent the analytically continued partial wave and Legendre polynomial functions, respectively. This equation captures the contributions from the poles on the real l-axis through integration along the contour $\mathbb{C}$.

2.2.2 Regge Trajectories

Most hadrons are phenomenologically organized into linear Regge trajectories, which can be parameterized as:

$$\alpha_{\mathbb{R}}(t) = \alpha_{\mathbb{R}}(0) + \alpha'_{\mathbb{R}} t \,. \tag{2.45}$$

Here, $\alpha_{\mathbb{R}}(t)$ is the trajectory for a specific hadron family $\mathbb{R}$, and $\alpha'_{\mathbb{R}}$ (GeV^{-2}) is the slope for the Regge trajectory $\mathbb{R}$. The Regge trajectory intercept $\alpha_{\mathbb{R}}(0)$ is the value of $\alpha_{\mathbb{R}}(t)$ at $t = 0$ and determines the mass of the lowest-lying hadron on the trajectory. The leading Regge trajectories in Regge theory include the Pomeron ($\mathcal{P}$), the ρ trajectory ($\mathbb{R} = \rho$), and the ω trajectory ($\mathbb{R} = \omega$), among others.

Regge trajectories are believed to exhibit degeneracy, implying the absence of a shared dispersive characteristic among them, thereby establishing clear distinctions between each trajectory. For a thorough and informative exploration of Regge theory, please refer to the sources [45, 46, 47].

2.2.3 Reggeization

Reggeization stands as a fundamental concept within Regge theory, particularly concerning certain hadronic amplitudes. It postulates that scattering amplitudes associated with exchange processes occurring in the t-channel, encompassing particles of varying spin, can be effectively described through the exchange of a Regge trajectory. This essential property facilitates the development of Regge-like amplitudes even for particles possessing higher spin values. Consequently, it plays a pivotal role in the extension of Regge theory to encompass processes involving particles beyond those with spin 1.

2.2.4 Regge Pole

In Regge theory, a Regge pole signifies a singularity within the scattering amplitude located in the complex angular momentum plane. These poles give rise to specific terms, known as pole terms, in the partial wave amplitudes denoted as $f_\ell(t)$ in Eq. (2.44). The position of a Regge pole is indicative of both the intercept and slope of the associated Regge trajectory. Simultaneously, the residue at the pole serves as a determinant of the coupling strength between the relevant particle and the exchanged trajectory.

2.2.5 Regge Factorization

In Regge theory, Regge factorization is a fundamental property of scattering amplitudes that facilitates the disentanglement of a process into distinct kinematic and dynamical components. This property asserts that the scattering amplitude can be effectively split into two parts:

1. A kinematical factor, contingent upon the Mandelstam variables s, t, and u.
2. A dynamical factor, reliant on the Regge trajectory and the particles' coupling to that trajectory.

Regge factorization streamlines the analysis of high-energy scattering events, enabling the extraction of valuable physical insights from experimental data.

2.2.6 Applications

Regge theory has proven its utility across a spectrum of scientific domains, including particle physics, nuclear physics, and high-energy physics. Its versatility shines in its applications to hadron-hadron scattering, meson spectroscopy, diffractive scattering, total cross-section measurements, and the behavior of scattering amplitudes at elevated energies. Moreover, Regge theory has catalyzed the emergence of advanced theoretical frameworks like the dual resonance models and string theory.

Overall, Regge theory furnishes a valuable tool for unraveling the dynamics of strong interactions. It complements the more fundamental description furnished by QCD, fostering deeper insights into the strong force and its manifestations in particle physics. Researchers continue to rely on its concepts and techniques, expanding their use to further our grasp of these fundamental phenomena.

2.2.7 The Pomeron Phenomenon

At high energies, hadronic cross-sections exhibit an intriguing consistency that hints at the involvement of a distinct mechanism. This phenomenon prompted the introduction of the concept of Reggeon exchange, necessitating a Regge trajectory with an intercept surpassing unity. However, none of the known hadronic families met this requirement. As a result, a new trajectory, termed the pomeron trajectory ($\mathcal{P}$), was postulated to elucidate the dynamics at high energies. The term "pomeron" is a tribute to the physicist Isaak Pomeranchuk [48]. Donnachie and Landshoff derived the standard parameters for the pomeron trajectory by analyzing scattering cross-sections in proton-proton and proton-antiproton interactions [49, 50]. Their analysis yielded the following trajectory form:

$$\alpha_{\mathcal{P}}^{\mathrm{DL}} = 1.0808 + 0.25\ \mathrm{t}\,. \tag{2.46}$$

It is important to note that slight variations in the parameters were considered in subsequent calculations [51], leading to the following representation:

$$\alpha_{\mathcal{P}} = 1.08 + 0.2\ \mathrm{t}\,. \tag{2.47}$$

Beyond its intercept and slope, the pomeron possesses distinguishing characteristics, including:

- The pomeron trajectory relates to color-singlet states that exhibit negligible isospin effects.
- Parity and charge conjugation transformations are applicable to the pomeron.
- The cross-sections for particle-particle and particle-antiparticle exchanges involving the pomeron exhibit remarkable equality, highlighting its phenomenological implications.

Incorporating the pomeron trajectory into the framework of Quantum Chromodynamics (QCD) holds great appeal, as it represents a manifestation of the strong interaction. One possible avenue involves establishing a connection between the pomeron trajectory in the resonance zone and glueballs [52]. While experimental evidence for glueballs remains scarce, their mass spectra can be determined through lattice QCD calculations [53] or classical potential model techniques [54, 55].

In this thesis, Regge theory, which includes Reggeon exchanges, is employed to examine the contributions of P-wave amplitudes in the $\pi N \to \pi N$ process, as described in Chapter 3.

PART I Photoproduction of Light Mesons

Preface

The realm of photoproduction, where photons interact with hadrons, offers a unique avenue for exploring the structural and spectroscopic characteristics of these particles. This phenomenon provides insights into the quantum properties of photons as they traverse the proton's field, undergoing transformations into quark-antiquark pairs. The intricate dynamics of this process are governed by a delicate interplay among factors such as the energy of the incident photon, the momentum transferred to the proton, and the quantum attributes of the resulting meson.

In the domain of photoproduction, two fundamental scenarios come into play. In the first scenario, the incident photon can be absorbed by a meson, leading to the creation of a final-state meson—an event known as the "t-channel process." Alternatively, the incident photon can induce the radiative excitation of the target proton into a baryon resonance, which subsequently decays into a meson and a proton. This sequence of events is termed the "s-channel process."

This preface outlines the following explorations:

1. Pseudoscalar Meson Photoproduction: The dynamics of pseudoscalar meson photoproduction are captured through a scattering matrix comprising four complex amplitudes. While cross-section measurements provide information about these amplitudes, understanding phase details and interference effects arising from overlapping processes necessitates knowledge of the eight real parameters that characterize these four complex amplitudes. Polarization observables offer a means to decipher the angular distribution of decay particles resulting from either a polarized photon beam or a polarized target.

2. Vector Meson Photoproduction: The involvement of additional spin components in vector meson photoproduction gives rise to a plethora of amplitudes. An effective approach involves treating the quantum system as an ensemble of states described by a density matrix, which, in fact, is constructed using these numerous amplitudes. This approach allows for the determination of "spin density matrix elements"

(SDMEs) for spin polarization states. Schilling [56] extensively discusses the application of this method in the study of vector meson photoproduction. The Vector Meson Dominance (VMD) model, proposed by Sakurai [58] prior to the advent of Quantum Chromodynamics (QCD), remains widely accepted in this domain. According to this model, the incident photon can become a vector meson, subsequently participating in diffractive scattering off the proton through Pomeron exchange [59]. The photon and vector mesons share identical quantum properties, including spin, parity, and charge conjugation. Within this framework, the photon is portrayed as a superposition of light vector mesons [60].

In the past, hadron beams were the predominant method for investigating exotic mesons. However, the advantages of using photoproduction for studying these resonances have become increasingly apparent, primarily because of its broader cross-section [61]. Recent research, carried out through $\eta\pi$ photoproduction experiments utilizing the CLAS facility at Jefferson Lab, has achieved successful detection of exotic mesons [62].

Chapter 3

Double Pion Photoproduction

Hadronic photoproduction serves as a valuable avenue for experimental observations that yield crucial insights into the spectroscopic and structural properties of hadrons in quantum chromodynamics (QCD). By employing protons as target hadrons, researchers can analyze the spectrum of excited nucleons at low energies. Meanwhile, at higher energies, the dominance of t-channel Reggeon exchanges, as predicted by Regge theory, allows for the exploration of the process and extraction of information about the exchanged Reggeons.

This chapter presents a comprehensive exploration of the intriguing phenomenon of double pion photoproduction, denoted as $\gamma p \to \pi^+\pi^- p$. The investigation involves the utilization of the model, which incorporates the Drell-Söding-Deck Mechanism [1]. Section 3.1 introduces the kinematic notations used throughout the analysis. In Section 3.3, two different frames of reference are introduced, providing alternative approaches to construct the photoproduction amplitude. Furthermore, the construction of both the background amplitude (Deck) in Section 3.2 and the signal in Section 3.4 are meticulously discussed. These sections particularly emphasize the creation of various resonances, with the dominant ρ meson contributing to the P-wave, and the scalar resonances σ and $f_0(980)$ influencing the S-wave through a Regge t-channel exchange mechanism (Sections 3.4.1 and 3.4.2, respectively).

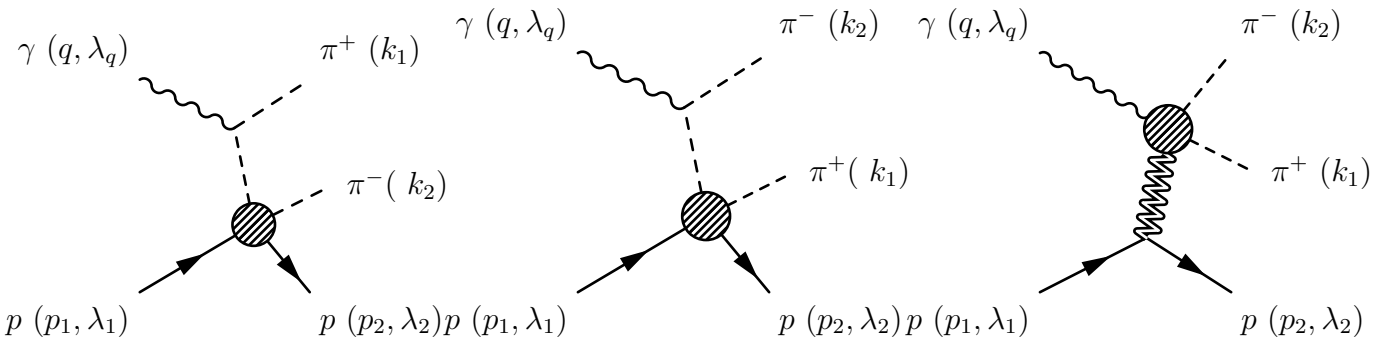

Figure 3.1: The Deck Mechanism for two pion photoproduction.

3.1 Model Description

The theoretical framework employed in this study is based on the renowned Drell-Söding-Deck approach, which was initially proposed by Drell [63] and later extended by Deck [1] to describe hadroproduction. Building upon these foundations, Söding [64] further developed the model by incorporating the resonant contribution of the $\rho(770)$ meson, which dominates at small invariant masses, into the continuous component. Consequently, a combined approach emerged, often referred to as the "Drell-Söding Mechanism" or "Deck Mechanism", that effectively captures the essential aspects of the angular moments.

In accordance with the Deck mechanism [1], the double pion photoproduction process can be conceptualized as a dynamic interplay between two distinct processes, as illustrated in Figure 3.1. The first two diagrams, denoting the continuum (Deck), and the final diagram, representing resonant contributions, collectively describe this intricate phenomenon. In this framework, the Deck contribution arises from the complementary processes involved in the diffractive dissociation of the photon off the nucleon target. These processes are primarily governed by long-range interactions, such as one-pion exchange.
Furthermore, in this work the virtuality of the exchanged pion is fully taken into account. To yield a parameter-free representation of the non-resonant continuous background within the $2 \to 3$ process of double pion photoproduction, the Deck Mechanism establishes a linkage to πN elastic scattering. When a photon encounters a proton, resulting in the generation of two pions, a multifaceted set of processes unfolds. Among these processes is the excitation of the ρ meson, which can subsequently undergo decay into two pions. Consequently, this allows for the adoption of a conventional Breit-Wigner parameterization for the resonant production component, encompassing the ρ resonance.

Kinematics

The four components of the helicity-dependent nucleon Dirac spinors are defined as follows:

$$u(p) = \sqrt{E_p + m_\mathrm{p}} \begin{pmatrix} 1 \\ \frac{\vec{\sigma}\cdot\vec{p_i}}{E_p + m_\mathrm{p}} \end{pmatrix} \otimes \chi_\lambda(\theta, \varphi)\,, \tag{3.1}$$

where E_p represents the proton energy, θ and φ denote the spherical angles of the 3-momenta vector, and $\vec{\sigma}$ stands for the Pauli matrices (see Appendix A).

The two-component Pauli spinors χ_λ, corresponding to an arbitrary direction θ and ϕ, can be explicitly expressed as:

$$\chi_{1/2}(\theta, \varphi) = \begin{pmatrix} \cos(\theta/2) \\ e^{i\varphi}\sin(\theta/2) \end{pmatrix} \;,\; \chi_{-1/2}(\theta, \varphi) = \begin{pmatrix} -e^{i\varphi}\sin(\theta/2) \\ \cos(\theta/2) \end{pmatrix}. \tag{3.2}$$

Furthermore, the z-projection of the Pauli matrices is given by:

$$\chi_{1/2}(0) = \begin{pmatrix} 0 \\ 1 \end{pmatrix} \;,\; \chi_{-1/2}(0) = \begin{pmatrix} 0 \\ 1 \end{pmatrix}. \tag{3.3}$$

It is important to note that these nucleon spinors satisfy the orthogonality and completeness conditions. The following notations will be utilized in the description of the studied process:

- The incoming photon γ:
  1. Four-vector momentum q^μ, with $q^\mu : (E_\gamma, \vec{q})$,
  2. Helicity λ_q, where $\lambda_q = \pm 1$,
  3. Polarization vector ϵ_q:

$$\epsilon_q = -\frac{\lambda_q}{\sqrt{2}}(\cos\theta_q, i\lambda_q \sin\theta_q). \tag{3.4}$$

     It is noteworthy that the polarization vector must adhere to the transversity condition:

$$q_\mu \epsilon^\mu = 0. \tag{3.5}$$

- The target proton p_1:
  1. Four-vector momentum $p_1^\mu : (E_1, \vec{p_1})$,
  2. Helicity $\lambda_1 = \pm 1/2$.
- The recoiling proton p_2:
  1. Four-vector momentum $p_2^\mu : (E_2, \vec{p_2})$,
  2. Helicity $\lambda_2 = \pm 1/2$.
- The final pions:
  1. Four-vector momentum of π^+ denoted as $k_1^\mu : (E_{k_1}, \vec{k_1})$,
  2. Four-vector momentum of π^- denoted as $k_2^\mu : (E_{k_2}, \vec{k_2})$,
- The intermediate exchanged virtual pion denoted as $\pi^{*\pm}$.
- The pion virtuality denoted as t_π.

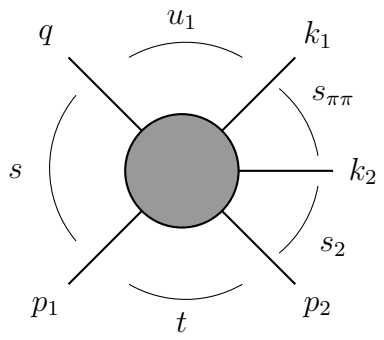

Figure 3.2: Some of the double pion photoproduction relevant invariants

The relevant set of invariants for the photoproduction process depicted in Fig. 3.2 can be defined based on the general description of the Mandelstam variables s, t, and u discussed in Chapter 2:

$$s = (p_1 + q)^2 = (p_2 + k_1 + k_2)^2 \,, \tag{3.6}$$
$$t = (p_1 - p_2)^2 = (k_1 + k_2 - q)^2 \,, \tag{3.7}$$
$$u = (q - p_2)^2 = (p_1 - k_1 - k_2)^2 \,, \tag{3.8}$$
$$s_1 = (p_2 + k_1)^2 \,, \tag{3.9}$$
$$t_1 = (p_1 - k_1)^2 \,, \tag{3.10}$$
$$u_1 = (q - k_1)^2 = (p_1 - k_2 - p_2)^2 \,, \tag{3.11}$$
$$s_2 = (p_2 + k_2)^2 \,, \tag{3.12}$$
$$t_2 = (p_1 - k_2)^2 \,, \tag{3.13}$$
$$u_2 = (q - k_2)^2 = (p_1 - k_1 - p_2)^2 \,, \tag{3.14}$$
$$s_{\pi\pi} = (k_1 + k_2)^2 = (p_1 - p_2 + q)^2 \,. \tag{3.15}$$

Here, s represents the total center-of-mass energy squared, t denotes the total four-momentum transfer, and $s_{\pi\pi}$ is the invariant mass of the $\pi\pi$ system squared. Moreover, s_1, t_1, u_1, s_2, t_2, and u_2 are the invariants corresponding to the $\pi^{*+}N \to \pi^+ N$ and $\pi^{*-}N \to \pi^- N$ scattering processes, respectively.

3.2 Deck Model

The objective of this section is to offer a comprehensive explanation of the two-pion photoproduction process within the framework of the Deck Mechanism. In the realm of hadronic physics, the Deck Mechanism serves as a theoretical model designed to elucidate the diffractive disintegration of a photon when it interacts with a nucleon target. This model primarily revolves around long-range interactions, particularly one-pion exchange. Its principal utility

lies in providing a description of the continuous, non-resonant background in certain scattering phenomena, such as double pion photoproduction, without the need for additional parameters.

At its core, the Deck Mechanism establishes a link between the initial interaction of the photon with the proton and the subsequent generation of two pions. This often entails the intermediate excitation and subsequent decay of the ρ meson, a resonance particle.

To provide a deeper insight into the Deck Mechanism, it can be envisioned as a two-step process. Initially, the incoming photon undergoes decay, resulting in the creation of two pions, with one of them being off-shell. Subsequently, this off-shell pion elastically recoils towards the nucleon target, leading to the formation of the $\pi\pi N$ final state. Despite the off-shell nature of the involved pion, it is reasonable to approximate its amplitude with the physical πN scattering amplitude, especially in cases of small pion virtuality. This approximation establishes a connection between the $2 \to 3$ process and πN elastic scattering, ultimately offering an effective and parameter-free representation of the non-resonant continuous background.

The Deck amplitude was initially introduced in [1], where the pion pole was identified as a consequence of the nearest singularity at low t_π. One-pion exchange amplitudes in double pion photoproduction may not satisfy current conservation due to potential violations of gauge invariance. To rectify this, "gauge invariance restoring terms" are introduced, ensuring the preservation of current conservation principles in electromagnetic interactions. These additional terms are crucial for accurately calculating the double pion photoproduction amplitude while adhering to the laws of physics. Gauge invariance was subsequently established by adjusting the pion pole in [65].

To derive the gauge invariant Deck amplitude, follow this procedure:

$$\begin{aligned}\mathcal{M}^{\text{Deck}}_{\lambda_1\lambda_2\lambda_q}(s,t,s_{\pi\pi},\Omega) = e\Bigg[&- \frac{\epsilon(q,\lambda_q)\cdot k_2}{q\cdot k_2}\mathcal{M}^{+}_{\lambda_1\lambda_2}(s_1,t) \\ &+ \frac{\epsilon(q,\lambda_q)\cdot k_1}{q\cdot k_1}\mathcal{M}^{-}_{\lambda_1\lambda_2}(s_2,t)\Bigg].\end{aligned} \tag{3.16}$$

Here, $\mathcal{M}^{\pm}_{\lambda_1\lambda_2}$ represents the scattering amplitude for the process $p + \pi^{*\pm} \to p + \pi^{\pm}$. The relative minus sign between the two terms arises from the photon's coupling to both positive and negative charged pion states. It is important to note that this binary amplitude depends on three kinematic invariants due to the virtuality of the initial pion. In the limit where $t_\pi \to m_\pi^2$, these amplitudes can be related to elastic $\pi^{\pm}p$ scattering, for which there exists abundant experimental data. However, it should be emphasized that the amplitudes presented here are given in the charge basis and should not be mistaken for the t-channel isospin basis of elastic πN scattering, which will be discussed in Sec.3.2.1. Furthermore, the amplitude given in Eq.(3.16) does not satisfy gauge invariance. Gauge invariance, defined by the Ward-Takahashi identity, requires the amplitude to vanish upon the substitution $\epsilon \to q$, i.e., $\epsilon(q,\lambda_q)\cdot q = 0$. However, this assertion does not hold true. To address this limitation, a methodology developed by Pumplin [65], which has been in use for decades, is employed. This methodology introduces a contact term $\epsilon(q,\lambda_q)\cdot V$ into the matrix element. To ensure the comprehensive nature of V^μ, the most general form is utilized:

$$V^\mu = a p_1^\mu + b q^\mu + c p_2^\mu + d k_1^\mu + e k_2^\mu, \tag{3.17}$$

where the coefficients a, b, c, d, and e are functions of the five independent kinematic variables. It is important to note that the electromagnetic interaction of the pion has been already included in Eq.(3.16), thus the gauge invariance restoring term lacks four-vectors for the charged pions. Furthermore, the dependence on q can be disregarded, as it is unrelated to the physical amplitude. Hence, the expression simplifies to:

$$V^\mu = a p_1^\mu + c p_2^\mu. \tag{3.18}$$

To satisfy the conservation of total momentum ($p_1 - p_2 = k_1 + k_2 - q$), the coefficients a and b are subject to a single constraint. Pumplin's choice is to adopt:

$$V^\mu = (p_1 + p_2)^\mu v, \tag{3.19}$$

where v is a scalar function of the five independent kinematic variables. With this modification, the gauge invariant Deck amplitude can be defined as:

$$\begin{aligned}\mathcal{M}^{\text{Deck,GI}}_{\lambda_1\lambda_2\lambda_q}(s,t,s_{\pi\pi},\Omega) = e\Bigg[&- \frac{\epsilon(q,\lambda_q)\cdot k_2}{q\cdot k_2}\beta(t_{\pi 2})\mathcal{M}^{+}_{\lambda_1\lambda_2}(s_1,t) \\ &+ \frac{\epsilon\cdot k_1}{q\cdot k_1}\beta(t_{\pi 1})\mathcal{M}^{-}_{\lambda_1\lambda_2}(s_2,t) + \epsilon(q,\lambda_q)\cdot(p_1+p_2)v\Bigg],\end{aligned} \tag{3.20}$$

where $\beta(t_{\pi_i}) = \exp\big((t_{\pi_i} - t^{\min}_{\pi_i})/\Lambda^2_\pi\big)$, where $t_{\pi_i} = (q - k_i)$, represents the hadronic form factors with $\Lambda_\pi = 0.9$ GeV, which are introduced to suppress the Born Term pion propagator for one-pion exchange at large t_{π_i}. The minimum pion virtuality is defined as:

$$t^{\min}_{\pi_1} = m^2_\pi - \frac{1}{2s}\Bigg[(s - m^2_p)(s - s_2 + m^2_\pi) - \lambda^{1/2}(s,0,m^2_p)\lambda^{1/2}(s,s_2,m^2_\pi)\Bigg], \tag{3.21}$$

$$t^{\min}_{\pi_2} = m^2_\pi - \frac{1}{2s}\Bigg[(s - m^2_p)(s - s_1 + m^2_\pi) - \lambda^{1/2}(s,0,m^2_p)\lambda^{1/2}(s,s_1,m^2_\pi)\Bigg]. \tag{3.22}$$

By applying gauge invariance, the scalar function v can be expressed as:

$$v = \frac{\mathcal{M}^{+}_{\lambda_1\lambda_2}(s_1,t) - \mathcal{M}^{-}_{\lambda_1\lambda_2}(s_2,t)}{q\cdot(p_1+p_2)}, \tag{3.23}$$

where $q\cdot(p_1+p_2)$ can be written in terms of s and u as $q\cdot(p_1+p_2) = \frac{1}{2}(s-u)$. Notably, for the given conditions $s > 0$ and $u < 0$, this term does not contribute to a pole. Consequently, the gauge invariant Deck amplitude can be written as:

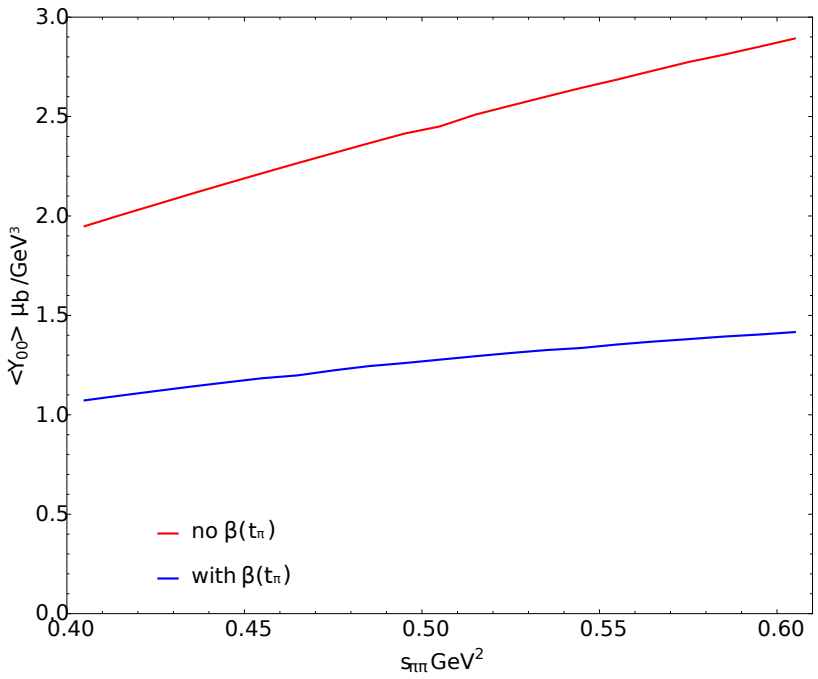

Figure 3.3: Effect of $\beta(t_\pi)$ on the moments $\langle Y_0^0 \rangle$ for the Deck amplitude.

$$\begin{aligned}\mathcal{M}^{\text{Deck,GI}}_{\lambda_1\lambda_2\lambda_q}(s,t,s_{\pi\pi},\Omega) = \sqrt{4\pi\alpha} \\ \times \left[\left(\frac{\epsilon(q,\lambda_q)\cdot k_1}{q\cdot k_1} - \frac{\epsilon(q,\lambda_q)\cdot(p_1+p_2)}{q\cdot(p_1+p_2)}\right)\beta(t_{\pi_1})\mathcal{M}^{-}_{\lambda_1\lambda_2}(s_2,t)\right. \\ \left. - \left(\frac{\epsilon(q,\lambda_q)\cdot k_2}{q\cdot k_2} - \frac{\epsilon(q,\lambda_q)\cdot(p_1+p_2)}{q\cdot(p_1+p_2)}\right)\beta(t_{\pi_2})\mathcal{M}^{+}_{\lambda_1\lambda_2}(s_1,t)\right],\end{aligned} \tag{3.24}$$

with $\alpha = e^2/4\pi$. The impact of the introduced factor $\beta(t_\pi)$ on the moment $\langle Y_0^0 \rangle$[1] of the Deck amplitude is depicted in Figure 3.3. These calculations were conducted for specific values of the beam energy ($E_\gamma = 3.4$ GeV) and momentum transfer ($t = -0.45$ GeV^2). The CLAS detector utilized in this study detected photons with energies ranging from 3.2 GeV to 3.8 GeV and momentum transfers ranging from $t = -0.45$ to $t = -0.95$ GeV^2 in increments of -0.1 GeV^2. This additional term was incorporated to enhance the model's agreement with experimental data, and further discussions on it will be presented in subsequent sections.

In the following section, the πN elastic amplitude will be presented to complete the specification of the continuum model.

[1]The moments will be discussed deeply in Chapter 4, Sec. 4.2

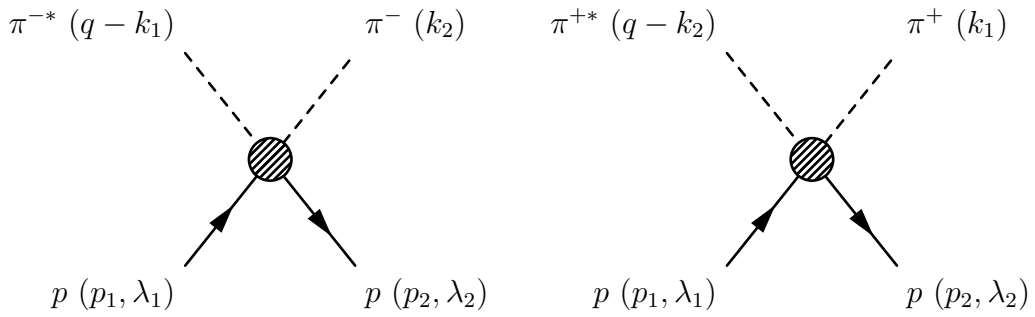

Figure 3.4: Pictorial representation of $\pi^{-*}p \to \pi^- p$ (left) and $\pi^{+*}p \to \pi^+ p$ (right).

3.2.1 Scattering Amplitude of Pion-Proton Interaction

The process of πN scattering has been extensively studied, including the study of multiple meson production. This section focuses on the scattering between an intermediate pion and a proton, resulting in a final state with two pions. The standard parametrization of the $\pi^{\pm}N$ scattering amplitude, expressed in terms of scalar functions A and B [66], is given by:

$$\mathcal{M}_{\lambda_1\lambda_2} = \bar{u}(\lambda_2, p_2)\left[A + \frac{1}{2}(\not{k}_2 + \not{k}_1)^{\mu} B\right] u(\lambda_1, p_1)\,. \tag{3.25}$$

It is important to emphasize that this equation applies exclusively to real exchanged pions. In scenarios involving virtual exchanged pions, Eq. (3.25) can still be utilized; however, certain adjustments are required to accommodate the virtual nature of the exchanged pion.

Upon adapting the equation to the conditions of the study, the scattering amplitude for virtual pion-proton interaction can be expressed as follows:

$$\mathcal{M}^{\pm}_{\lambda_1\lambda_2}(s_j, t, t_{\pi_i}) = \overline{u}(p_2, \lambda_2)\left[A^{\pm}(s_j, t; t_{\pi_i}) + \frac{1}{2}(\not{q} - \not{K}_i + \not{k}_j)B^{\pm}(s_j, t; t_{\pi_i})\right] u(p_1, \lambda_1)\,. \tag{3.26}$$

Here, i and j take values of 1 and 2, where $i \neq j$. It is noteworthy that as the pion virtuality t_{π_i} approaches m_π^2, the amplitude of virtual pion-proton scattering converges to the on-shell scattering amplitude.

In particular, the amplitude for $\pi^- p$ and $\pi^+ p$, as depicted in Fig. 3.4, can be written as:

$$\mathcal{M}^{-}_{\lambda_1\lambda_2}(s_2, t, t_{\pi_2}) = \overline{u}(p_2, \lambda_2)\left[A^{-}(s_2, t; t_{\pi_2}) + \frac{1}{2}\gamma_\mu(q - k_1 + k_2)B^{-}(s_2, t; t_{\pi_2})\right] u(p_1, \lambda_1)\,, \tag{3.27}$$

$$\mathcal{M}^{+}_{\lambda_1\lambda_2}(s_1, t, t_{\pi_1}) = \overline{u}(p_2, \lambda_2)\left[A^{+}(s_1, t; t_{\pi_1}) + \frac{1}{2}\gamma_\mu(q - k_2 + k_1)B^{+}(s_1, t; t_{\pi_1})\right] u(p_1, \lambda_1)\,. \tag{3.28}$$

Here, the pion virtualities are defined as $t_{\pi_1} = (q - k_1)^2$ and $t_{\pi_2} = (q - k_2)^2$ for negative and positive virtual pions, respectively.

In the given approach, the scattering amplitudes for the $\pi N \to \pi N$ process are expressed in terms of isospin amplitudes in the s-channel and t-channel. The isospin amplitudes in the s-channel are denoted by $A^{(1/2)}$ and $A^{(3/2)}$ for isospin $I = 1/2$ and $I = 3/2$, respectively. In the t-channel, the isospin amplitudes are denoted by $A^{(+)}$ and $A^{(-)}$ for isospin $I = 0$ and $I = 1$, respectively.

The relationship between the isospin amplitudes in the two channels is given by:

$$A^{ji}_{ba}(s,t) = \delta_{ba}\delta^{ji}A^{(+)} + i\epsilon_{abc}(\tau_c)^{ji}A^{(-)}\,, \tag{3.29}$$

where δ_{ba} and δ^{ji} are Kronecker delta symbols, and ϵ_{abc} is the Levi-Civita symbol. Here, a, b, i, and j represent isospin indices.

Using this relation, the isospin amplitudes in the s-channel can be expressed in terms of the amplitudes in the t-channel as follows:

$$A^{(1/2)} = A^{(+)} + 2A^{(-)}\,, \tag{3.30}$$

$$A^{(3/2)} = A^{(+)} - A^{(-)}\,. \tag{3.31}$$

Similarly, the scalar amplitude B can be decomposed in terms of isospin amplitudes in the same way.

In the t-channel, the isospin amplitudes are further decomposed into reduced helicity amplitudes $f_1^{\pm}$ and $f_2^{\pm}$. These are related to the isospin amplitudes as follows:

$$\frac{1}{4\pi}A^{\pm} = \frac{\sqrt{s} + m_p}{Z_1^+ Z_2^+}f_1^{\pm} - \frac{\sqrt{s} - m_p}{Z_1^- Z_2^-}f_2^{\pm}\,, \tag{3.32}$$

$$\frac{1}{4\pi}B^{\pm} = \frac{1}{Z_1^+ Z_2^+}f_1^{\pm} - \frac{1}{Z_1^- Z_2^-}f_2^{\pm}\,, \tag{3.33}$$

where m_p is the proton mass, $Z_i^{\pm} = \sqrt{E_i^{\mathrm{CM}} \pm m_p}$, and E_i^{CM} is the nucleon energy in the s-channel center-of-mass frame.

The reduced helicity amplitudes $f_1^{\pm}$ and $f_2^{\pm}$ are expanded [67] in terms of Legendre polynomials, and they depend on the scattering energy s and the scattering angle $z = \cos(\theta_s)$ in the s-channel:

$$f_1^{\pm} = \frac{1}{\sqrt{|\mathbf{p}_1^{\mathrm{CM}}||\mathbf{p}_2^{\mathrm{CM}}|}}\sum_{l=0}^{\infty} f_{l+}^{\pm}(s)P'_{l+1}(z) - \frac{1}{\sqrt{|\mathbf{p}_1^{\mathrm{CM}}||\mathbf{p}_2^{\mathrm{CM}}|}}\sum_{l=2}^{\infty} f_{l-}^{\pm}(s)P'_{l-1}(z)\,, \tag{3.34}$$

$$f_2^{\pm} = \frac{1}{\sqrt{|\mathbf{p}_1^{\mathrm{CM}}||\mathbf{p}_2^{\mathrm{CM}}|}}\sum_{l=1}^{\infty} \left[f_{l-}^{\pm}(s) - f_{l+}^{\pm}(s)\right] P'_l(z)\,. \tag{3.35}$$

Where $\mathbf{p}_1^{\mathrm{CM}}$ and $\mathbf{p}_2^{\mathrm{CM}}$ are the momenta of the two particles in the s-channel center-of-mass frame, $P_l(z)$ are Legendre polynomials, and $P'_l(z)$ represents the first derivative of the Legendre polynomials with respect to z. The partial wave amplitudes $f_{l\pm}(s)$ are SAID amplitudes [68] with parity $(-1)^{l+1}$ and total angular momentum $J = l \pm 1/2$.

3.2.2 $\pi^* N$ Kinematics

In the pion proton center of mass frame the energies and scattering angle corresponding to $\pi^* N$ are:

$$E_1^{\mathrm{CM}} = \frac{s + m_p^2 - t_i}{2\sqrt{s_i}}\,, \tag{3.36}$$

$$E_2^{\mathrm{CM}} = \frac{s - s_{\pi\pi} + m_p^2}{2\sqrt{s_i}}\,, \tag{3.37}$$

$$E_{k_1}^{\mathrm{CM}} = E_{k_2}^{\mathrm{CM}} = \frac{\sqrt{s_{\pi\pi}}}{2}\,, \tag{3.38}$$

$$\cos(\theta_s) = \frac{2s_i(t - 2m_p^2) + (s_i - t_i + m_p^2)(s_i - m_\pi^2 + m_p^2)}{\sqrt{\lambda(s_i, t_i, m_p^2)}\sqrt{\lambda(s_i, m_\pi^2, m_p^2)}}\,. \tag{3.39}$$

The momenta can be calculated using $E^2 = |\vec{p}|^2 + m^2$ as follows, where E_1^{CM} and E_2^{CM} represent the energies of the initial and recoiling protons, respectively, and $E_{k_1}^{\mathrm{CM}}$ and $E_{k_2}^{\mathrm{CM}}$ represent the energies of the two final pions. Hereby, the momenta can be expressed as:

$$p_1 = \sqrt{\frac{\lambda(s_i, t_i, m_p^2)}{4s_i}}\,, \tag{3.40}$$

$$p_2 = \sqrt{\frac{\lambda(s_i, m_\pi^2, m_p^2)}{4s_i}}\,, \tag{3.41}$$

$$k_1 = k_2 = \frac{\sqrt{s_{\pi\pi} - 4m_\pi^2}}{2}\,. \tag{3.42}$$

3.2.3 Investigating Partial Waves

An important consideration in the analysis of πN scattering is the behavior of scattering amplitudes in the on-shell limit ($t_\pi = m_\pi^2$), where constraints can be applied based on known on-shell πN scattering data. However, beyond this limit, the form of the scattering amplitudes remains unknown. In a broader context, the cosine of the scattering angle, denoted as z, can be expressed as:

$$z = \cos\theta_s = \frac{t - 2m_N^2 + 2E_1E_2}{2|\mathbf{p}_1||\mathbf{p}_2|}\,. \tag{3.43}$$

For the case where $|\mathbf{p}_1| = |\mathbf{p}_2| = p$, a relation can be simplified as:

$$z = 1 + \frac{t}{2p^2}\,. \tag{3.44}$$

As the scattering energy approaches the threshold value $s_{\mathrm{th}} = (m_N + m_\pi)^2$, the momentum $p(s)$ approaches zero. Consequently, z exhibits a singularity since it scales as $1/p^2$.

However, in the physical region, z remains within the range $[-1, 1]$ as it represents the physical scattering angle. Therefore, it is expected that the partial wave amplitudes exhibit a similar behavior near the threshold to ensure finiteness.

To further investigate the behavior of the partial waves, let's consider the Legendre polynomial $P_l(z)$. It's important to note that $P_l(z)$ diverges for large values of z. Specifically, z^l behaves as $1/q^{2l}$, with the most singular term represented by $P_l'(z) \sim z^{l-1} \sim (q^2)^{1-l}$. To ensure the scattering angle equation remains finite when extended to the off-shell limit near the threshold, a correction factor must be introduced and applied to the partial wave amplitude.

Two threshold adjustment factors have been proposed. The first one, referred to as R_1, is defined as:

$$R_1 = \left(\frac{|\mathbf{p}_1|^{\text{off-shell}}}{|\mathbf{p}_1|^{\text{on-shell}}} \right)^l , \tag{3.45}$$

here l represents the orbital angular momentum. The second choice, denoted as R_2, is based on the partial wave expansion presented in Hoehler's Appendix [69], which takes the form:

$$\text{Re}\, f_{l\pm}(s) = a_\pm^0 q^{2l} + a_\pm^2 q^{2l+2} + \dots \tag{3.46}$$

$$\text{Im}\, f_{l\pm}(s) = b_\pm^0 q^{4l} + b_\pm^2 q^{4l+2} + \dots \tag{3.47}$$

Therefore:

$$f_{l_\pm}^{(\pm)}(s) \sim a q^{2l+1} . \tag{3.48}$$

Using these factors, the amplitudes A and B for different waves, such as $L = 0, 1, 2$, and 3, were computed for the pure on-shell case, the pure off-shell case, and the off-shell case with both threshold factors included. The results are shown in Figures 3.5 and 3.6.

Upon examining the real and imaginary parts of the P-wave amplitudes A^+ and A^- at $t = -0.1\ \text{GeV}^2$, depicted in Figures 3.5 and 3.6, it is evident that applying R_2 as a correction factor to the off-shell amplitudes significantly reduces the discrepancies between the off-shell and on-shell results compared to R_1.

However, it is noteworthy that the amplitudes do not exhibit any divergences near the threshold in the pure off-shell scenario, raising questions about the necessity of a correction factor in the first place.

After extensive investigations and studies, it has been concluded that the calculations can proceed without the addition of any correction term to the partial waves.

It is important to note that the study will consider a pure off-shell case without the inclusion of any corrective terms.

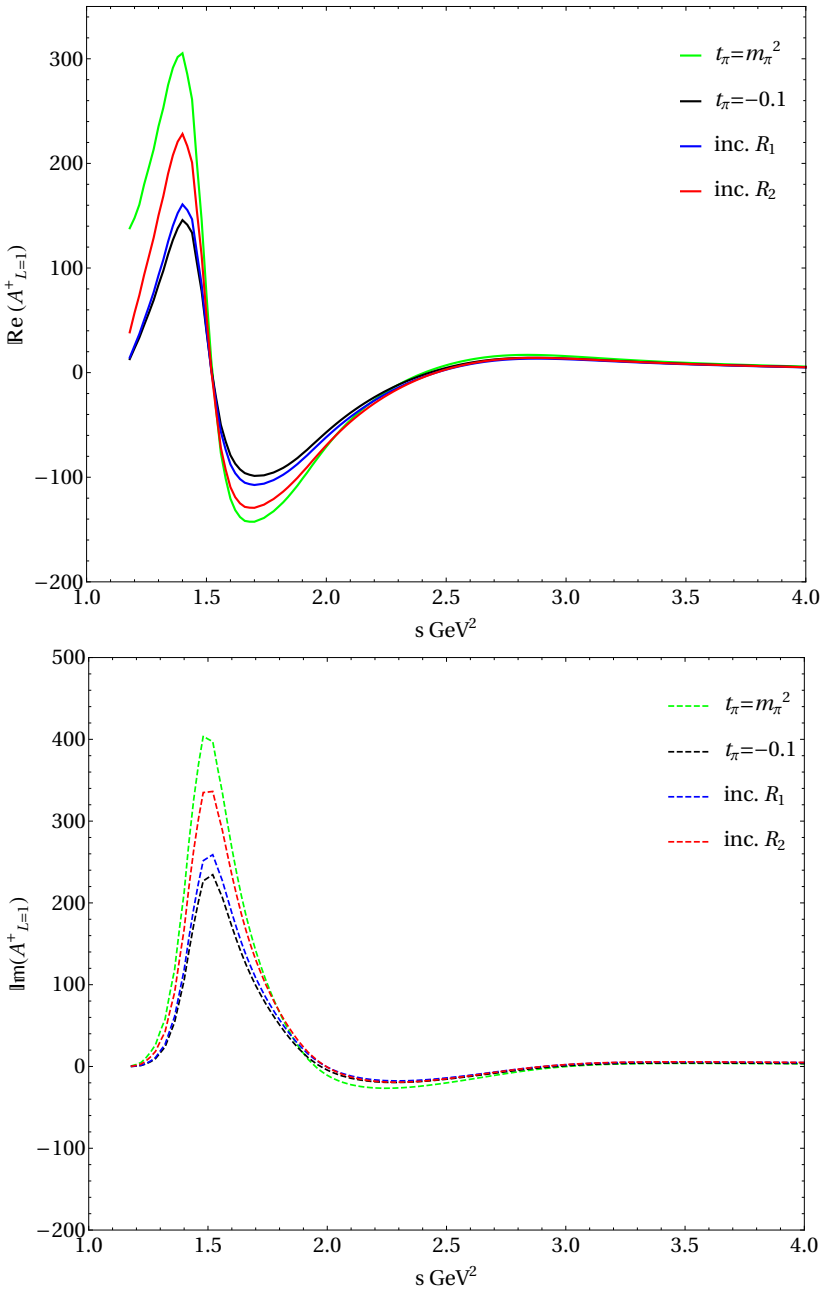

Figure 3.5: The Real (upper figure) and Imaginary (lower figure) values of A^+ amplitude for $L = 1$ and at $t = -0.1$ GeV^2

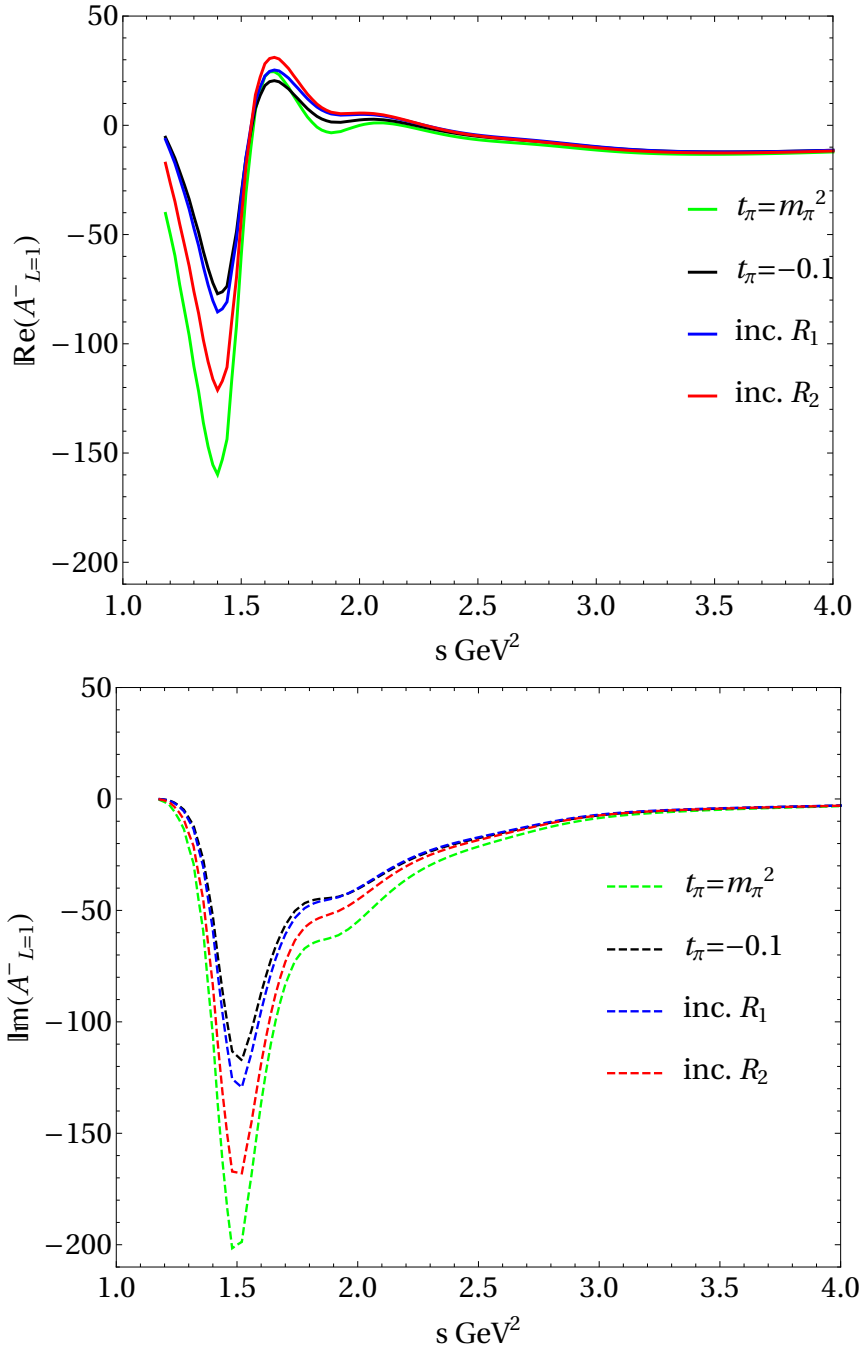

Figure 3.6: The Real (upper figure) and Imaginary (lower figure) values of A^- amplitude for $L = 1$ and at $t = -0.1$ GeV^2

3.3 Photoproduction frames

In the $\pi\pi$ channel, two distinct reference frames are of interest, namely the s-channel helicity frame and the Gottfried-Jackson frame. The subscripts H and GJ will be utilized to differentiate between the two frames.

3.3.1 Helicity Frame

In the helicity frame, the direction of the recoiling proton (p_2) defines the negative z-axis as follows:

$$\hat{\boldsymbol{z}} = \frac{-\vec{\boldsymbol{p_2}}}{|\vec{\boldsymbol{p_2}}|}\,, \tag{3.49}$$

$$\hat{\boldsymbol{y}} = \frac{\vec{\boldsymbol{p_2}} \times \vec{\boldsymbol{q}}}{\vec{\boldsymbol{p_2}} \times \vec{\boldsymbol{q}}}, \tag{3.50}$$

$$\hat{\boldsymbol{x}} = \hat{\boldsymbol{y}} \times \hat{\boldsymbol{z}}\,. \tag{3.51}$$

The three aforementioned invariants (s, t and $s_{\pi\pi}$) as well as the two angles $\Omega_{\mathrm{H}} = (\theta_{\mathrm{H}}, \phi_{\mathrm{H}})$ of the π^+ in the $(\pi^+\pi^-)$ rest frame can be used. The momenta three vectors are written as:

$$\boldsymbol{p_1}^H = |\vec{\boldsymbol{p_1}}|(\sin\theta_1, 0, \cos\theta_1)\,, \tag{3.52}$$

$$\boldsymbol{p_2}^H = |\vec{\boldsymbol{p_2}}|(0, 0, -1)\,, \tag{3.53}$$

$$\boldsymbol{k_1}^H = |\vec{\boldsymbol{k_1}}|(\sin\theta_H\cos\phi_H, \sin\theta_H\sin\phi_H, \cos\theta_H) = -\vec{\boldsymbol{k_2}}^{\,H}\,, \tag{3.54}$$

$$\boldsymbol{q}^H = |\vec{\boldsymbol{q}}|(-\sin\theta_q, 0, \cos\theta_q)\,. \tag{3.55}$$

With:

$$\cos(\theta_q) = \frac{E_1^2 - E_2^2 - E_q^2}{2qp_2}\,, \tag{3.56}$$

$$\cos(\theta_1) = \frac{2m_p^2 - 2E_1E_2 - t}{2p_1p_2}\,, \tag{3.57}$$

$$\sin(\theta_q) = \sqrt{1 - \cos(\theta_q)^2}\,, \tag{3.58}$$

$$\sin(\theta_1) = \sqrt{1 - \cos(\theta_1)^2}\,. \tag{3.59}$$

3.3.2 Gottfried-Jackson Frame:

In the Gottfried-Jackson frame, the same invariants as in the helicity frame can be used, along with $\Omega_{\mathrm{GJ}} = (\theta_{\mathrm{GJ}}, \phi_{\mathrm{GJ}})$ as the angles of the π^+ in the $(\pi^+\pi^-)$ rest frame. The direction of the photon is parallel to the z-axis in the GJ frame, and thus the production plane can

be defined as:

$$\hat{\boldsymbol{z}} = \frac{\vec{\boldsymbol{q}}}{|\vec{\boldsymbol{q}}|}\,, \tag{3.60}$$

$$\hat{\boldsymbol{y}} = \frac{\vec{\boldsymbol{p_2}} \times \vec{\boldsymbol{q}}}{\vec{\boldsymbol{p_2}} \times \vec{\boldsymbol{q}}}, \tag{3.61}$$

$$\hat{\boldsymbol{x}} = \hat{\boldsymbol{y}} \times \hat{\boldsymbol{z}}\,. \tag{3.62}$$

Consequently, the three momentum vectors can be expressed as follows

$$\boldsymbol{p_1}^{GJ} = |\vec{\boldsymbol{p_1}}|(-\sin\theta_1, 0, \cos\theta_1)\,, \tag{3.63}$$

$$\boldsymbol{p_2}^{GJ} = |\vec{\boldsymbol{p_2}}|(-\sin\theta_2, 0, \cos\theta_2)\,, \tag{3.64}$$

$$\boldsymbol{k_1}^{GJ} = |\vec{\boldsymbol{k_1}}|(\sin\theta_{GJ}\cos\phi_{GJ}, \sin\theta_{GJ}\sin\phi_{GJ}, \cos\theta_{GJ}) = -\vec{\boldsymbol{k_2}}^{\,GJ}\,, \tag{3.65}$$

$$\boldsymbol{q}^{GJ} = |\vec{\boldsymbol{q}}|(0, 0, 1)\,. \tag{3.66}$$

Where:

$$\cos(\theta_2) = \frac{2s_{\pi\pi}(s_{\pi\pi} - s - t + m_p^2) + (s_{\pi\pi} - t)(s - s_{\pi\pi} - m_p^2)}{(s_{\pi\pi} - t)\sqrt{\lambda(s, s_{\pi\pi}, m_p^2)}}\,, \tag{3.67}$$

$$\sin(\theta_2) = \sqrt{1 - \cos(\theta_2)^2}\,. \tag{3.68}$$

The corresponding energies in both frames are expressed as:

$$E_1 = \frac{s + t - m_p^2}{2\sqrt{s_{\pi\pi}}}\,, \tag{3.69}$$

$$E_2 = \frac{s - s_{\pi\pi} - m_p^2}{2\sqrt{s_{\pi\pi}}}\,, \tag{3.70}$$

$$E_q = q = \frac{s_{\pi\pi} - t}{2\sqrt{s_{\pi\pi}}}\,, \tag{3.71}$$

$$E_{k_1} = E_{k_2} = \frac{\sqrt{s_{\pi\pi}}}{2}\,. \tag{3.72}$$

3.4 Resonance production

To accurately describe the threshold behavior in resonance processes, an energy-dependent width Breit-Wigner function for each upcoming resonance has been employed. This method follows the parameterization provided by the Particle Data Group (PDG) [70]. The energy-dependent Breit-Wigner function is defined as follows:

$$\mathrm{BW}^{\mathrm{dep}}(s, l) = \frac{n(s)}{m_{\mathrm{BW}}^2 - s - i m_{\mathrm{BW}}\Gamma_{\mathrm{tot}}(s)}\,, \tag{3.73}$$

where

$$n(s) = \left(\frac{q}{q_0}\right)^l F_l(q, q_0)\,, \tag{3.74}$$

with l being the angular momentum of the resonance and Γ_{tot} denotes the total width, given by the sum of partial widths Γ_b.

For example, in the specific case of the exclusive process involving the decay of a ρ meson into a $\pi\pi$ system, where $l = 1$ and $b = \pi\pi$, the energy-dependent Breit-Wigner function can be expressed as:

$$\text{BW}^{\text{dep}}(s_{\pi\pi}, 1) = \left(\frac{q}{q_0}\right) F_1(q, q_0) \frac{1}{m_\rho^2 - s_{\pi\pi} - i m_\rho \Gamma_{\pi\pi}(s_{\pi\pi})}, \tag{3.75}$$

here, $F_1(q, q_0)$ represents a phenomenological form factor known as the Blatt-Weisskopf form factor. The momentum q of the pion in the $\pi\pi$ system is given by:

$$q = q(s_{\pi\pi}) = \frac{1}{2}\sqrt{s_{\pi\pi} - 4m_\pi^2}, \tag{3.76}$$

while q_0 is defined as:

$$q_0 = q(m_\rho^2) = \frac{1}{2}\sqrt{m_\rho^2 - 4m_\pi^2}. \tag{3.77}$$

The width $\Gamma_{\pi\pi}$ of the $\pi\pi$ system in the ρ decay is given by:

$$\Gamma_{\pi\pi}(s_{\pi\pi}) = \Gamma_0 \left(\frac{m_\rho^2}{s_{\pi\pi}}\right)^{1/2} \frac{\sqrt{s_{\pi\pi} - 4m_\pi^2}}{\sqrt{m_\rho^2 - 4m_\pi^2}} \left[\left(\frac{q}{q_R}\right) \frac{F_1(q, q_0)}{F_1(q_R, q_0)}\right]^2, \tag{3.78}$$

where Γ_0 is a constant and $q_R = q_0$. Simplifying the expression for $\Gamma_{\pi\pi}$ when $q_R = q_0$, thus:

$$\text{BW}^{\text{dep}}(s_{\pi\pi}, 1) = \left(\frac{s_{\pi\pi} - 4m_\pi^2}{m_\rho^2 - 4m_\pi^2}\right)^{1/2} F_1(q, q_0) \frac{1}{m_\rho^2 - s_{\pi\pi} - i m_\rho \Gamma_{\pi\pi}(s_{\pi\pi})}, \tag{3.79}$$

with

$$\Gamma_{\pi\pi}(s_{\pi\pi}) = \Gamma_0 \left(\frac{m_\rho^2}{s_{\pi\pi}}\right)^{1/2} \left[\frac{s_{\pi\pi} - 4m_\pi^2}{m_\rho^2 - 4m_\pi^2}\right]^{3/2} \left[\frac{F_1(q, q_0)}{F_1(q_0, q_0)}\right]^2. \tag{3.80}$$

Using the property of the Blatt-Weisskopf form factor, specifically $F_1(z) = \sqrt{\frac{1}{1+z}}$ with $z = q/q_0$, it can be derived that $F_1(1) = 1/\sqrt{2}$. Thus, the complete expression for $\Gamma_{\pi\pi}$ is:

$$\Gamma_{\pi\pi}(s_{\pi\pi}) = \Gamma_0 \left(\frac{m_\rho^2}{s_{\pi\pi}}\right)^{1/2} \left[\frac{s_{\pi\pi} - 4m_\pi^2}{m_\rho^2 - 4m_\pi^2}\right]^{3/2} 2 \left[\frac{\sqrt{m_\rho^2 - 4m_\pi^2}}{\sqrt{m_\rho^2 - 4m_\pi^2} + \sqrt{s_{\pi\pi} - 4m_\pi^2}}\right] \tag{3.81}$$

Furthermore, the energy-dependent Breit-Wigner function can be written as:

$$\mathrm{BW}^{\mathrm{dep}}(s, l=1) = \left(\frac{s_{\pi\pi} - 4m_\pi^2}{m_\rho^2 - 4m_\pi^2}\right)^{1/2} \left[\frac{2\sqrt{m_\rho^2 - 4m_\pi^2}}{\sqrt{m_\rho^2 - 4m_\pi^2} + \sqrt{s_{\pi\pi} - 4m_\pi^2}}\right]^{1/2} \times \left[\frac{1}{m_\rho^2 - s_{\pi\pi} - i m_\rho \Gamma_{\pi\pi}(s_{\pi\pi})}\right]. \tag{3.82}$$

It is important to note that the Regge propagator describes the resonance production on the proton, while the Breit-Wigner represents the description of the resonance propagation and decay.

3.4.1 Vector Resonance (*P*-wave contribution):

The prevailing intermediate state in $\pi^+\pi^-$ photoproduction is the ρ meson. This resonance primarily decays into $\pi^+\pi^-$ pairs, sharing a similar quark composition with pions but distinguished by its spin-1 characteristics. The principal mechanism responsible for this production is the pomeron exchange, exhibiting vector-like behavior at low momentum transfer, $t \sim 0$, with its trajectory passing through $J = 1$ [71, 72]. However, it is anticipated to shift to $J = 2$ as t becomes larger and positive, a transition that might be linked to the tensor glueball[73, 74]. Additionally, it has been suggested in [75] that an additional contribution from f exchange may exist, particularly noteworthy due to its matching quantum numbers with the pomeron. To account for the P-wave amplitude, both pomeron exchange, denoted by $\mathcal{P}$, and f_2 exchange are considered, as depicted in Fig. 3.7.

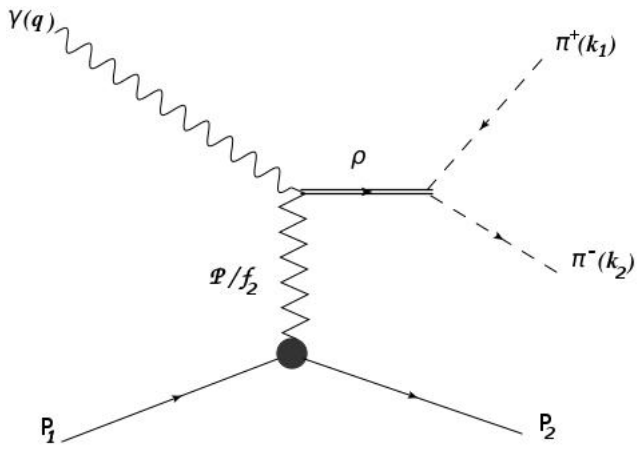

Figure 3.7: Pictorial representation for ρ meson production via pomeron i.e. $\mathcal{P}$ and f_2 exchanges.

3.4.1.1 Production Model:

Following the P-wave amplitude definition from [76] one can write:

$$\mathcal{A}^{\mathrm{P}}_{\lambda,\lambda_1,\lambda_2} = \bar{u}(p_2,\lambda_2)\gamma^\mu u(p_1,\lambda_1)\nu^\lambda_\mu\,, \tag{3.83}$$

where

$$\nu^\lambda_\mu = k_\mu \epsilon^\lambda \cdot (k_1 - k_2) - q \cdot (k_1 - k_2)\epsilon^\lambda_\mu\,. \tag{3.84}$$

The objective is to evaluate Eq. (3.83) in the s-channel frame and investigate its behavior in the high-energy limit for comparison with the normalization demonstrated in [77]. The s-channel reference plane can be defined with respect to different momentum vectors, as depicted in Fig. 3.8. Within this context, the momentum of the ρ meson aligns with the z-axis. Following the labelling from Eq.(3.52)-to-(3.59), the center of mass momenta can be

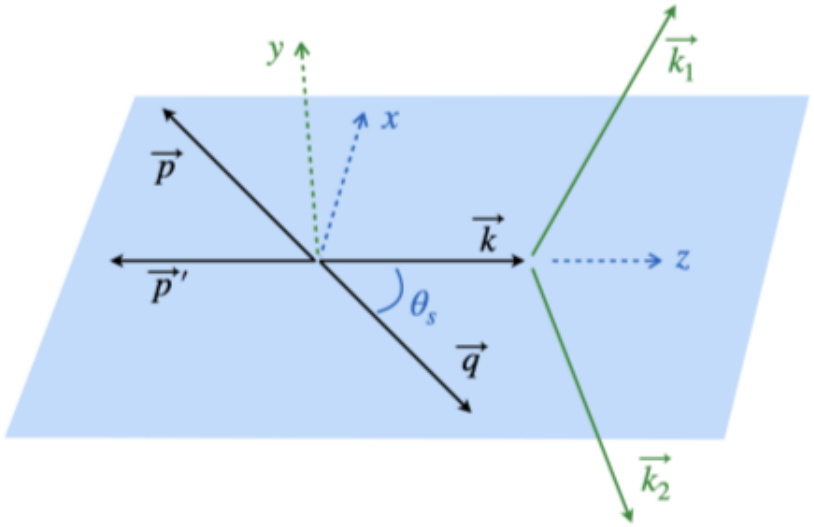

Figure 3.8: s-channel reference plane.

expressed as:

$$q^\mu = q_s(1, -\sin\theta_s, 0, \cos\theta_s)\,, \tag{3.85}$$

$$k^\mu = (E_s, 0, 0, p_s)\,, \tag{3.86}$$

$$\epsilon^\mu = \frac{-\lambda}{2}(0, \cos\theta_s, i\lambda, \sin\theta_s)\,. \tag{3.87}$$

Here, the subscript $(_s)$ denotes the s-channel kinematics. Expanding Eq. (3.83), the expression becomes:

$$\mathcal{A}^{\mathrm{P}}_{\lambda,\lambda_1,\lambda_2} = \bar{u}(p_2,\lambda_2)\gamma^0\nu^0_\lambda u(p_1,\lambda_1) - \bar{u}(p_2,\lambda_2)\vec{\gamma}\vec{\nu}_\lambda u(p_1,\lambda_1) \tag{3.88}$$

$$\text{where} \quad \nu^0_\lambda = -E_s\vec{\epsilon_\lambda}\cdot(\vec{k_1} - \vec{k_2})\,, \tag{3.89}$$

$$\text{and} \quad \vec{\nu} = \vec{k}\;\vec{\epsilon}_\lambda \cdot (\vec{k_1} - \vec{k_2}) - q\cdot(\vec{k_1} - \vec{k_2})\vec{\epsilon}_\lambda\,. \tag{3.90}$$

Modeling the decay of ρ into $\pi\pi$ ($\rho \to \pi\pi$) involves constructing the following expression:

$$\langle \rho | \pi\pi \rangle = 2gkD^{1*}_m(\Omega) = 2gk\sqrt{\frac{4\pi}{3}}Y^1_M(\Omega)\,, \tag{3.91}$$

where D is the Wigner D-matrix (see Appendix B). The amplitude for pomeron exchange is defined in [77] as:

$$\mathcal{M}^{\lambda,M/\mathcal{P}}_{\lambda_1,\lambda_2} = -i\frac{s}{s_0}\beta^{\gamma\rho}_{\mathcal{P}}e^{\beta_{\mathcal{P}}t}\delta_{\lambda,M}\delta_{\lambda_1,\lambda_2}\,. \tag{3.92}$$

Combining the equations (3.91) and (3.92) results in:

$$\mathcal{M}^{\lambda,M/\mathcal{P}}_{\lambda_1,\lambda_2} = -i\frac{s}{s_0}\beta^{\gamma\rho}_{\mathcal{P}}e^{\beta_{\mathcal{P}}t}\delta_{\lambda_1,\lambda_2}\sum_{M=-1,1}\delta_{\lambda,M}2k\sqrt{\frac{4\pi}{3}}Y^1_M(\Omega)\,. \tag{3.93}$$

Finally, after applying an appropriate normalization and restoring the Regge propagator, the complete model for ρ production, represented by the P-wave amplitude, is defined as:

$$\mathcal{M}^{\mathbb{N}}_{\lambda,\lambda_1,\lambda_2} = \frac{-1}{s}g_{\rho\pi}\beta^{\gamma\rho}_{\mathbb{N}}e^{\beta_{\mathbb{N}}t}BW(s)R(s,t)\bar{u}(p_2,\lambda_2)\gamma^{\mu}u(p_1,\lambda_1)\nu^{\lambda}_{\mu}\,, \tag{3.94}$$

where the subscript ($_{\mathbb{N}}$) represents the Natural Reggeon exchange, which can be either pomeron i.e. $\mathcal{P}$ or f_2 exchanges.

3.4.1.2 Regge Propagator:

The Regge propagator can be expressed as follows:

$$R(s,t) = \frac{\alpha_{\mathbb{N}}(t)}{\alpha_{\mathbb{N}}(0)}\frac{1+e^{i\pi\alpha_{\mathbb{N}}(t)}}{\sin(\pi\alpha(t))}\left(\frac{s}{s_0}\right)^{\alpha_{\mathbb{N}}(t)}\,, \tag{3.95}$$

where $\alpha_{\mathbb{N}}(t)$ denotes the linear trajectory for both pomeron and f_2 exchanges, as previously determined in [51, 77]. Specifically, the trajectory equations are given by:

$$\alpha_{\mathcal{P}}(t) = 1.08 + 0.25\ \mathrm{t}\,, \tag{3.96}$$

$$\alpha_{f_2}(t) = 0.5 + 0.9\ \mathrm{t}\,. \tag{3.97}$$

3.4.1.3 Couplings:

This section introduces the relevant couplings along with their corresponding values, derived from prior analyses in [77]:

- The decay coupling $g_{\rho\pi} = 5.96$ encapsulates information pertaining to resonance widths and the branching ratio corresponds to $\rho \to \pi\pi$.
- The Reggeon-photon-resonance couplings, obtained from the CLAS analysis, are defined as follows:

- $\beta_{\mathcal{P}}^{\gamma\rho} = 2.506$ [77], signifying the coupling between the pomeron ($\mathcal{P}$), photon, and proton ($\mathcal{P}$-γ-p coupling).
- $\beta_{f_2}^{\gamma\rho} = 2.47$ [77], representing the coupling between the f_2 meson, photon, and proton (f_2-γ-p coupling).

- The proton-proton-Reggeon couplings, obtained via factorization from other reactions, are defined as:
  - $\beta_{\mathcal{P}} = 3.6$ [77], indicating the coupling between protons (p-p) and the pomeron ($\mathcal{P}$).
  - $\beta_{f_2} = 0.55$ [77], representing the coupling between protons (p-p) and the f_2 meson.
- The scaling parameter s_0 is assigned a value of 1 GeV^2.

By integrating these couplings with the Regge propagator, a comprehensive model can be developed to investigate the production process of the ρ meson.

3.4.2 Scalar Resonances (*S*-wave contribution):

In the realm of double pion photoproduction, two scalar resonances, namely the σ meson or $f_0(500)$ and the $f_0(980)$, play a central role.

In this section, the computational analysis of the $\gamma + p \to p + (S \to \pi + \pi)$ process is conducted within a one-particle exchange model, with the primary focus on exploring the properties of the scalar resonance. Within this process, two crucial vertices are encountered: the VVS vertex, representing interactions involving the vector boson γ, the Reggeon (assumed to exhibit vector characteristics, denoted as $\mathcal{P}$), and the scalar resonance, including entities like σ, $f_0(980)$, and more. Additionally, the SPP vertex describes interactions between the scalar resonance and the two pseudoscalar pions, with its strength characterized by a coupling constant.

In a manner analogous to the Reggeized formulation of the vector resonance amplitude discussed in the previous section, the Reggeized amplitude for the scalar resonances can be expressed as follows:

$$i\mathcal{M}_S = gR(s,t)BW(s)\overline{u}(p_2,\lambda_2)\gamma^\mu u(p_1,\lambda_1)v_\mu(\lambda_\gamma)\,. \tag{3.98}$$

The parameter g governs the strength of the interaction and will be treated as a free parameter, subject to fitting with the data in the subsequent chapter. $R(s,t)$ represents the Regge propagator, while $BW(s_{\pi\pi})$ denotes the Breit-Wigner distribution defined in Eq. (3.82). The interaction term $v_\mu(\lambda_\gamma)$ is given by:

$$v_\mu(\lambda_\gamma) = q_\mu\epsilon\cdot(p_1-p_2) - q\cdot(p_1-p_2)\epsilon_\mu\,. \tag{3.99}$$

Starting from Eqs.(1) and (2), and considering $l = 0$, taking into account the phenomenological form factor $F_0(z) = 1$[70], the Breit-Wigner formula for scalar resonances representing the S-wave contribution can be expressed as follows:

$$\mathrm{BW}^{\mathrm{dep}}(s, l = 0) = \frac{1}{m_{f_0}^2 - s - i m_{f_0} \Gamma_{\pi\pi}(s_{\pi\pi})}\,, \tag{3.100}$$

where the total decay width is given by:

$$\Gamma_{\pi\pi}(s_{\pi\pi}) = \Gamma_0 \left[\frac{s_{\pi\pi} - 4m_\pi^2}{m_{f_0}^2 - 4m_\pi^2}\right]^{1/2}\,. \tag{3.101}$$

The Regge propagator used for these scalar resonances is taken from [78] and is expressed as:

$$R(s,t) = \left(\frac{s}{s_0}\right)^{\alpha_S(t)-1} \frac{\pi\alpha'_S}{\sin\pi\alpha_S(t)} \frac{-1 + e^{-i\pi\alpha_S(t)}}{2} \frac{1}{\Gamma(\alpha_S(t))}\,, \tag{3.102}$$

where $\alpha(t)$ is the Regge trajectory, and s_0 is the scale parameter taken to be 1. To describe the trajectory of both resonances, the ρ Regge trajectory given in [78] was used:

$$\alpha_\sigma \sim \alpha_{f(980)} \sim \alpha_\rho = 0.55 + 0.8\ \mathrm{t}\,. \tag{3.103}$$

3.5 Summary

In this chapter, an extensive examination is conducted on double pion photoproduction, denoted as $\gamma p \to \pi^+\pi^-$. The primary objective is to comprehensively analyze the intricate dynamics and underlying physics governing this reaction.

To achieve this goal, a well-established model is adopted, which encompasses the Drell-Söding-Deck Mechanism. This model incorporates partial wave contributions, particularly focusing on the S and P-waves, elucidating the production and participation of resonances such as σ, $f_0(980)$, and ρ. Regarding the Deck component, while it contributes minimally to the overall cross section and is considered a background, it offers two notable advantages. Firstly, it serves as the foundation for intriguing interference effects. Secondly, its strong dependence on available data bolsters its reliability and practicality.

As this chapter concludes, the study stands at the threshold of the next phase. The subsequent chapter will introduce fundamental quantities such as the cross section and moments of angular distribution. These essential measures will facilitate a more rigorous analysis of the photoproduction process, allowing for deeper insights into its intricate dynamics.

Moreover, the following chapter will detail the fitting methodology employed in the model, followed by the presentation of the fitted results at each step of the analysis. Armed with these rigorous techniques and insights, the concealed intricacies of double pion photoproduction will be unveiled, advancing the understanding of strong interactions in the realm of subatomic physics.

Chapter 4

Cross Section and Angular Distribution

In the previous chapter, a comprehensive model was developed to describe double pion photoproduction, encompassing both P and S wave contributions. This chapter represents a continuation of the investigation, focusing on the analysis of data from the CEBAF Large Acceptance Spectrometer, specifically the CLAS and GlueX experiments at the Thomas Jefferson National Accelerator Facility in Newport News, Virginia.

The CLAS experiment involved the scattering of an electron beam with an energy range of 0.5 to 12 GeV on nuclei targets (protons and neutrons) positioned at the center of CLAS. CLAS is well-suited for meson spectroscopy, allowing the measurement of exclusive reaction channels and the determination of the J^{PC} quantum numbers of generated states through partial wave analysis (PWA).

On the other hand, the GlueX experiment employs photoproduction, where a real photon with an energy of 12 GeV scatters on a nucleon to produce mesonic states. Its primary mission is to gain a deeper understanding of confinement in quantum chromodynamics (QCD), with a focus on identifying a spectrum of hybrid and exotic mesons resulting from the excitation of the gluonic field binding the quarks, as discussed in section 1.2.2.

To elucidate recent advancements in the investigations carried out by CLAS and GlueX, this analysis begins in section 4.1 by emphasizing the formalism of the cross-section. It includes a comparison between the expected distribution, particularly for the well-established variable t ($d\sigma/dt$), and the model's predictions. Section 4.2 provides conventions for computing angular momentum moments, followed by section 4.3, which explains the methods used to probe these moments and presents the outcomes following the establishment of the necessary framework and key concepts for moment calculations.

Subsequently, section 4.4 delves into the methodology employed to perform the initial fit, particularly focusing on data below 1 GeV, and provides the results obtained, including the fitted parameters. In section 4.5, the incorporation of non-resonant contributions arising from the partial waves associated with the process is explored. Finally, section 4.6 offers insights into the moments resulting from the ultimate fit, which incorporates all the aforementioned components, along with variations in fitted parameters.

The chapter concludes with a concise summary, consolidating key findings and conclusions drawn from the study. It also acknowledges ongoing work in this field, highlighting the evolving nature of this research.

4.1 Cross Section

The differential cross section for double pion photoproduction processes plays a pivotal role in quantifying the probability of a photon's interaction with a target hadron, leading to the production of two pions. Additionally, the energy-dependent behavior of the cross section reveals resonant structures and threshold effects, shedding light on the underlying interaction dynamics.

The differential cross section, denoted by $d\sigma$, can be expressed as:

$$d\sigma = (2\pi)^4 \frac{1}{2(s-m_p^2)} d\Phi_3 \sum_{\lambda_q \lambda_1 \lambda_2} |\mathcal{M}_{\lambda_q \lambda_1 \lambda_2}(s,t,s_{\pi\pi},\Omega)|^2 \,, \tag{4.1}$$

where $d\Phi_3$ is the 3-body phase space, and it can be written as:

$$d\Phi_3 = \delta^4(p_1+q-p_2-k_1-k_2) \frac{d^3k_1}{(2\pi)^3}\frac{1}{2E_{\mathbf{k}_1}} \frac{d^3k_2}{(2\pi)^3}\frac{1}{2E_{\mathbf{k}_2}} \frac{d^3p_2}{(2\pi)^3}\frac{1}{2E_2} \,. \tag{4.2}$$

Consequently, the resulting four-fold differential cross section can be defined as:

$$\frac{d\sigma}{dt dm_{\pi\pi} d\Omega} = \frac{1}{2}(2\pi)\kappa \sum_{\lambda_q \lambda_1 \lambda_2} |\mathcal{M}_{\lambda_q \lambda_1 \lambda_2}(s,t,s_{\pi\pi},\Omega)|^2 \,, \tag{4.3}$$

with

$$\kappa = \frac{1}{(2\pi)^3}\frac{1}{4\pi}\frac{1}{2\pi}\frac{\lambda^{1/2}(s_{\pi\pi},m_\pi^2,m_\pi^2)}{16\sqrt{s_{\pi\pi}}(s-m_p^2)^2}\frac{1}{2} \,. \tag{4.4}$$

4.2 Moments of Angular Distribution

The investigation of moments of angular distributions in photoproduction processes holds paramount importance for several reasons. Firstly, these moments provide a model-independent analysis of the angular dependence, allowing for direct comparisons between theoretical predictions and experimental measurements. By quantifying the relative strengths of partial waves, they offer valuable insights into the underlying dynamics governing the photoproduction process. Additionally, moments of angular distributions enable the discrimination between different production mechanisms, thereby illuminating the specific contributions and their angular dependencies. These moments serve as critical guidelines for theoretical models, imposing constraints on resonance structures and driving the refinement of our understanding of the strong interaction at the subatomic level.

In the formalism introduced by Mathieu et al. [79], the most general expression for the differential cross section of the $\pi\pi$ system is given as follows:

$$\begin{aligned}\frac{d\sigma}{dtd\sqrt{s_{\pi\pi}}d\Omega d\Phi} &= I(\Omega,\Phi) \\ &= I^0(\Omega) - P_\gamma I^1(\Omega)\cos 2\Phi - P_\gamma I^2(\Omega)\sin 2\Phi\,, \end{aligned} \tag{4.5}$$

where $0 < P_\gamma < 1$ is the degree of linear polarization of the photon beam and Φ is the angle between the photon polarization vector and the production plane. $I(\Omega,\Phi) = (I^0, I^1, I^2)$ represents the intensity vector which can be expressed as:

$$I^0(\Omega) = \frac{\kappa}{2}\sum_{\lambda,\lambda_1,\lambda_2}\mathcal{M}_{\lambda;\lambda_1\lambda_2}(\Omega)\mathcal{M}^*_{\lambda;\lambda_1\lambda_2}(\Omega)\,, \tag{4.6}$$

$$I^1(\Omega) = \frac{\kappa}{2}\sum_{\lambda,\lambda_1,\lambda_2}\mathcal{M}_{-\lambda;\lambda_1\lambda_2}(\Omega)\mathcal{M}^*_{\lambda;\lambda_1\lambda_2}(\Omega)\,, \tag{4.7}$$

$$I^2(\Omega) = i\frac{\kappa}{2}\sum_{\lambda,\lambda_1,\lambda_2}\lambda\mathcal{M}_{-\lambda;\lambda_1\lambda_2}(\Omega)\mathcal{M}^*_{\lambda;\lambda_1\lambda_2}(\Omega)\,, \tag{4.8}$$

with the phase space factor κ given in (4.4).
The moments of angular distribution may be extracted from the experimental intensity $I(\Omega,\Phi)$, in which the dynamical dependency on the polarized angle in Eq. (2.2) with a linearly polarized beam enable us to define the unpolarized moment $H^0(LM)$ and the polarized moments $H^{1,2}(LM)$ as follows:

$$H^0(L,M) = \frac{1}{2\pi}\int_0^\pi\int_0^{2\pi}\int_0^{2\pi}\int_{-1}^1 I(\Omega,\Phi)d^L_{M0}(\theta)\cos M\phi d(\cos\theta)d\phi d\Phi\,, \tag{4.9}$$

$$H^1(L,M) = \frac{1}{P_\gamma\pi}\int_0^\pi\int_0^{2\pi}\int_0^{2\pi}\int_{-1}^1 I(\Omega,\Phi)d^L_{M0}(\theta)\cos M\phi\cos 2\Phi d(\cos\theta)d\phi d\Phi\,, \tag{4.10}$$

$$\mathfrak{Im}H^2(L,M) = \frac{1}{P_\gamma\pi}\int_0^\pi\int_0^{2\pi}\int_0^{2\pi}\int_{-1}^1 I(\Omega,\Phi)d^L_{M0}(\theta)\cos M\phi\sin 2\Phi d(\cos\theta)d\phi d\Phi\,. \tag{4.11}$$

Where L is the total angular momentum of the $\pi\pi$ system and M is its z-component, and the small Wigner-d function $d^L_{M0}(\theta)$ may be computed with the use of DDJMNB function from CERNLIB.

The unpolarized moment is of particular interest since it characterizes the cross section for an unpolarized beam. An alternative convention for computing the moments of angular distributions was introduced in [80] i.e.

$$\langle Y_{LM}\rangle(s,t,m_{\pi\pi}) = \sqrt{4\pi}\int d\Omega\,\frac{d\sigma}{dtdm_{\pi\pi}d\Omega}\mathfrak{Re}\,Y_{LM}(\Omega)\,, \tag{4.12}$$

this normalization ensures that

$$\langle Y_{00}\rangle(s,t,m_{\pi\pi}) = \frac{d\sigma}{dtdm_{\pi\pi}}\,. \tag{4.13}$$

Both moments represented in Eqs. (4.9) and (4.12) can be related according to the following relation:

$$\langle Y_{LM} \rangle = (2\pi)\sqrt{2L+1}H^0(LM)\,. \tag{4.14}$$

4.3 Fitting Procedure:

In this section, the fitting procedure employed in the study is outlined, involving a comprehensive analysis of the amplitudes within the model through a redefinition of their t-dependence. Building upon the discussions presented in the preceding chapter, expressions for the various amplitudes involved are introduced:

1. **Deck Amplitude:**

$$\begin{aligned}\mathcal{M}^{\text{Deck,GI}}_{\lambda_1\lambda_2\lambda_q}(s,t,s_{\pi\pi},\Omega) &= \sqrt{4\pi\alpha} \\ &\times \left[\left(\frac{\epsilon(q,\lambda_q)\cdot k_1}{q\cdot k_1} - \frac{\epsilon(q,\lambda_q)\cdot(p_1+p_2)}{q\cdot(p_1+p_2)}\right)\beta(t_{\pi_1})\mathcal{M}^{-}_{\lambda_1\lambda_2}(s_2,t;t_{\pi_1})\right. \\ &\left. - \left(\frac{\epsilon(q,\lambda_q)\cdot k_2}{q\cdot k_2} - \frac{\epsilon(q,\lambda_q)\cdot(p_1+p_2)}{q\cdot(p_1+p_2)}\right)\beta(t_{\pi_2})\mathcal{M}^{+}_{\lambda_1\lambda_2}(s_1,t;t_{\pi_2})\right].\end{aligned} \tag{4.15}$$

2. **ρ meson production amplitude via pomeron exchange:**

$$\mathcal{M}^{\mathcal{P}}_{\lambda_1\lambda_2\lambda_\gamma}(s,t,s_{\pi\pi},\Omega_{\text{H}}) = \frac{-1}{s}g_{\rho\pi}\beta^{\gamma\rho}_{\mathcal{P}}e^{\beta_{\mathcal{P}}t}BW(s)R_{\mathcal{P}}(s,t)\bar{u}(p_2,\lambda_2)\gamma^{\mu}u(p_1,\lambda_1)\nu^{\lambda}_{\mu}\,. \tag{4.16}$$

3. **ρ meson production amplitude via $\mathbf{f_2}$ exchange:**

$$\mathcal{M}^{f_2}_{\lambda_1\lambda_2\lambda_\gamma}(s,t,s_{\pi\pi},\Omega_{\text{H}}) = \frac{-1}{s}g_{\rho\pi}\beta^{\gamma\rho}_{f_2}e^{\beta_{f_2}t}BW(s)R_{f_2}(s,t)\bar{u}(p_2,\lambda_2)\gamma^{\alpha}u(p_1,\lambda_1)\nu^{\lambda}_{\alpha}\,. \tag{4.17}$$

4. **Scalar resonances i.e. $\boldsymbol{\sigma}$ and $\mathbf{f_0(980)}$ mesons production amplitudes:**

$$\mathcal{M}^{S}_{\lambda_1\lambda_2\lambda_\gamma}(s,t,s_{\pi\pi},\Omega_{\text{H}}) = \frac{1}{s}gR(s,t)BW(s)\overline{u}(p_2,\lambda_2)\gamma^{\mu}u(p_1,\lambda_1)v_{\mu}(\lambda_\gamma)\,. \tag{4.18}$$

The Regge propagators $R_{\mathcal{P}}(s,t)$ and $R_{f_2}(s,t)$ account for both pomeron and f_2 exchanges, as defined in Equations (3.95), (3.96), and (3.97), with further details regarding coupling constants available in Section 3.4.1. Whereas, $R(s,t)$ is associated with both σ and $f_0(980)$ and is detailed in Equation (3.103).

Summarily, the current model distinguishes itself as comprising two fundamental components. The first component, termed "Fixed," encapsulates elements such as the Deck amplitude, and the amplitude associated with ρ meson production via pomeron exchange. The second component, known as the "Free" component, introduces specific adjustments designed to effectively accommodate contributions arising from f_2 exchange, in addition to addressing the production of both σ and $f_0(980)$ mesons, as well as the non-resonant background components arising from both S and P-waves, which will be further discussed in Section 4.5.

4.3.1 Adjusting the Free components

As previously discussed, the "Free" components of the model encompass the ρ production amplitude via f_2 exchange, along with the two scalar meson production amplitudes. The term "Free" denotes that the t-dependence within these amplitudes will be redefined and treated as novel free parameters. Consequently, these adjusted parameters will serve as the new t-dependent couplings. Achieving this entails essential modifications to the amplitudes. Begining with the ρ production amplitude, the approach involves a representation of the four-vectors, which inherently exhibit t-dependence, through the lens of spherical harmonics corresponding to the distinct partial waves, namely $P+$, $P-$, and $P0$. More specifically, the relevant spherical harmonics are:

1. $P+$ (P-wave, $L = 1, M = +1$):

$$Y_{11}(\theta, \phi) = -\frac{1}{\sqrt{2}}\left(\frac{3}{4\pi}\right)^{1/2} \sin\theta(\cos\phi + i\sin\phi)\,, \tag{4.19}$$

2. $P-$ (P-wave, $L = 1, M = -1$):

$$Y_{1-1}(\theta, \phi) = \frac{1}{\sqrt{2}}\left(\frac{3}{4\pi}\right)^{1/2} \sin\theta(\cos\phi - i\sin\phi)\,, \tag{4.20}$$

3. $P0$(P-wave, $L = 1, M = 0$):

$$Y_{10}(\theta, \phi) = \left(\frac{3}{4\pi}\right)^{1/2} \cos\theta\,. \tag{4.21}$$

After performing some algebraic manipulations, one can obtain the following expression

$$Y_{1-1}(\theta, \phi) - Y_{11}(\theta, \phi) = \sqrt{2}\left(\frac{3}{4\pi}\right)^{1/2} \sin\theta\cos\phi\,, \tag{4.22}$$

$$Y_{1-1}(\theta, \phi) + Y_{11}(\theta, \phi) = -i\sqrt{2}\left(\frac{3}{4\pi}\right)^{1/2} \sin\theta\sin\phi\,. \tag{4.23}$$

This allows us to express $\sin\theta\cos\phi$, $\cos\theta$, and $\sin\theta\sin\phi$ in terms of these spherical harmonics as follows:

$$\sin\theta\cos\phi = \frac{1}{\sqrt{2}}\left(\frac{4\pi}{3}\right)^{1/2}\Big[Y_{1-1}(\theta, \phi) - Y_{11}(\theta, \phi)\Big]\,, \tag{4.24}$$

$$\cos\theta = \left(\frac{4\pi}{3}\right)^{1/2} Y_{10}(\theta, \phi)\,, \tag{4.25}$$

$$\sin\theta\sin\phi = \frac{i}{\sqrt{2}}\left(\frac{4\pi}{3}\right)^{1/2}\Big[Y_{1-1}(\theta, \phi) + Y_{11}(\theta, \phi)\Big]\,. \tag{4.26}$$

Now, consider the four-vector ν given by:

$$\nu^{\mu}(\lambda_q) = k^{\mu}\epsilon(q,\lambda)\cdot(k_1-k_2) - q\cdot(k_1-k_2)\epsilon^{\mu}(q,\lambda)\,, \tag{4.27}$$

$d' = (k_1 - k_2)$ represents the adjusted version of the pion momenta difference and can be expressed as:

$$\begin{aligned}
\mathbf{d}' &= 2\mathbf{k}_1^{\mathrm{H}} \\
&= 2|\mathbf{k}_1^{\mathrm{H}}|(\sin\theta_{\mathrm{H}}\cos\phi_{\mathrm{H}}, \sin\theta_{\mathrm{H}}\sin\phi_{\mathrm{H}}, \cos\theta_{\mathrm{H}}) \\
&= \sqrt{2}|\mathbf{k}_1^{\mathrm{H}}|\left(\frac{4\pi}{3}\right)^{1/2}\Bigg(Y_{1-1}(\theta_{\mathrm{H}},\phi_{\mathrm{H}}) - Y_{11}(\theta_{\mathrm{H}},\phi_{\mathrm{H}}), \\
&\quad iY_{1-1}(\theta_{\mathrm{H}},\phi_{\mathrm{H}}) + iY_{11}(\theta_{\mathrm{H}},\phi_{\mathrm{H}}), \sqrt{2}Y_{10}(\theta_{\mathrm{H}},\phi_{\mathrm{H}})\Bigg)\,.
\end{aligned} \tag{4.28}$$

After mathematical operations, a new three-vector $\mathbf{d}$ and the corresponding four-vector $D_{\lambda_q} = (0, \mathbf{d}_{\lambda_q})$ can be constructed. This allows the introduction of three independent couplings associated with the three helicity amplitudes. For $\lambda_q = +1$, $\lambda_q = -1$, and d_i representing the components of the original three-vector i.e. $(k_1 - k_2)$, the new formulations of $\mathbf{d}$ are as follows:

- For $\lambda_q = +1$:

$$\begin{aligned}
\mathbf{d}_+ = \Bigg(&\frac{1}{2}\big[a_+(t) + a_-(t)\big]d_1 + \frac{i}{2}\big[a_+(t) - a_-(t)\big]d_2, \\
&\frac{i}{2}\big[-a_+(t) + a_-(t)\big]d_1 + \frac{1}{2}\big[a_+(t) + a_-(t)\big]d_2, a_0(t)d_3\Bigg)\,,
\end{aligned} \tag{4.29}$$

- For $\lambda_q = -1$ we need to exchange the definitions of the plus and minus amplitudes so:

$$\begin{aligned}
\mathbf{d}_- = \Bigg(&\frac{1}{2}\big[a_-(t) + a_+(t)\big]d_1 + \frac{i}{2}\big[a_-(t) - a_+(t)\big]d_2, \\
&\frac{i}{2}\big[-a_-(t) + a_+(t)\big]d_1 + \frac{1}{2}\big[a_-(t) + a_+(t)\big]d_2, a_0(t)d_3\Bigg)\,.
\end{aligned} \tag{4.30}$$

This leads to the emergence of three t-dependent couplings: $a_+(t)$, $a_-(t)$, and $a_0(t)$, aligning with the $P+$, $P-$, and $P0$ waves, respectively. An important step of this fitting procedure entails the treatment of these free coupling parameters as complex entities, achieved by introducing an imaginary component to each $a_i(t)$, denoted as $a_i(t) + ib_i(t)$. The equations for $\omega_+^{\mu}(\lambda_q = 1)$ and $\omega_-^{\mu}(\lambda_q = -1)$ are updated accordingly:

- For $\lambda_q = +1$:

$${\omega_+}^{\mu}(\lambda_q = 1) = k^{\mu}\epsilon(q,\lambda_q = 1)\cdot D_+ - q\cdot d_+\epsilon^{\mu}(q,\lambda_q = 1)\,, \tag{4.31}$$

- For $\lambda_q = -1$:

$$\omega_-{}^{\mu}(\lambda_q = 1) = k^{\mu}\epsilon(q, \lambda_q = -1) \cdot D_- - q \cdot d_-\epsilon^{\mu}(q, \lambda_q = -1)\,. \tag{4.32}$$

Therefore, with the inclusion of complex coupling parameters, Eqs. (4.31) and (4.32) are adapted to accommodate these new complex quantities. Thus the modified formulation of the amplitude for f_2 exchange reads:

$$\mathcal{M}^{f_2,\text{Free}}_{\lambda_1\lambda_2\lambda_\gamma} = -\frac{1}{s}BW(s_{\pi\pi})R_{f_2}(s,t)\bar{u}(p_2,\lambda_2)\gamma_\mu\omega^\mu(\lambda_q)u(p_1,\lambda_1)\,. \tag{4.33}$$

Shifting the focus to another aspect of the "Free" component, attention is directed towards the contributions arising from S-wave scalar resonances. This involves a straightforward procedure for redefining the t dependence, where the strength coupling represented by g is replaced with a complex free parameter capable of accommodating this t dependency. Consequently, Eq. (3.98) undergoes a transformation, yielding the following formulation:

$$i\mathcal{M}_S = \frac{1}{s}(a_{s_j} + ib_{s_j})R(s,t)BW(s)\overline{u}(p_2,\lambda_2)\gamma^\mu u(p_1,\lambda_1)v_\mu(\lambda_\gamma)\,. \tag{4.34}$$

Notably, it's essential to highlight that an Energy-Independent decay width is employed in the Breit-Wigner distribution for the scalar resonances. Consequently, the overall model[1] can be expressed as:

$$\mathcal{M}^{\text{JPAC}}_{\lambda_1\lambda_2\lambda_\gamma}(s,t,s_{\pi\pi},\Omega^{\text{H}}) = \mathcal{M}^{\text{Fix}}_{\lambda_1\lambda_2\lambda_\gamma} + \mathcal{M}^{f_2,\text{Free}}_{\lambda_1\lambda_2\lambda_\gamma} + \mathcal{M}^{s_j,\text{Free}}_{\lambda_1\lambda_2\lambda_\gamma}\,, \tag{4.35}$$

where $\mathcal{M}^{\text{Fix}}_{\lambda_1\lambda_2\lambda_\gamma}$ encompasses both the Deck and ρ production via pomeron exchange components.

4.3.2 Analysis Method

This analysis entailed parameter adjustments to effectively align with the current experimental data acquired by the CLAS detector. The data were collected across various t bins, spanning from -0.45 GeV^2 to -0.95 GeV^2, with increments of -0.1 GeV^2. The primary emphasis was placed on moments strongly influenced by P-wave contributions, specifically $\langle Y_{00}\rangle$, $\langle Y_{20}\rangle$, $\langle Y_{21}\rangle$, $\langle Y_{22}\rangle$, alongside S-wave contributions, denoted by $\langle Y_{10}\rangle$ and $\langle Y_{11}\rangle$.

The parameter adjustment process involved employing the χ^2 test for individual moment components at specific fixed values of t. As an illustration, the χ^2 value for the moment $\langle Y_{00}\rangle$ at each selected t can be expressed as follows:

$$\chi^2_{\langle Y_{00}\rangle} = \Big(\frac{\langle Y_{00}\rangle^{th} - \langle Y_{00}\rangle^{exp}}{\Delta_{\langle Y_{00}\rangle}}\Big)^2\,. \tag{4.36}$$

[1]The model is denoted as the JPAC model in recognition of the collaborative research efforts with the Joint Physics Analysis Center (JPAC) group.

Here, the superscripts "th" and "exp" refer to the theoretical (calculated) moments and the experimental values obtained from CLAS, respectively, while $\Delta_{\langle Y \rangle}$ represents experimental errors. The overall χ^2 at each value of t is computed as the sum of these components, each corresponding to a specific moment in the angular distribution being analyzed. Therefore, χ^2_{Tot} is expressed as:

$$\chi^2_{\text{Tot}} = \sum_{L=0}^{L=2} \sum_{M=-L}^{M=L} \Big(\frac{\langle Y_{LM} \rangle^{th} - \langle Y_{LM} \rangle^{exp}}{\Delta_{\langle Y_{LM} \rangle}} \Big)^2 . \tag{4.37}$$

The total number of free parameters varied from one fit to another, depending on the specific contributions taken into account. The degrees of freedom were subsequently determined as:

$$\text{n.d.f} = \text{number of experimental data} - \text{number of free parameters} .$$

To compute the relevant moments for fitting, a dedicated FORTRAN program was developed based on the theoretical framework of the moment formalism, as detailed in Eq. (4.12). For the fitting process, this program made use of the CERN library program MINUIT, employing SIMPLEX and MIGRAD functions to locate the global minima of the χ^2_{Tot}.

4.4 Establishing the Initial Fit

The preliminary investigations covered the energy range below 1 GeV, encompassing contributions from both ρ and σ mesons. This initial fit involved 8 free parameters, with 6 corresponding to the $\rho(770)$ meson and the remaining 2 related to the σ meson, also known as the $f_0(500)$ meson. Subsequent fits focused on the energy range of $m_{\pi\pi} = [0.4 - 0.9]$ GeV, with each t bin analyzed individually, spanning t values from -0.45 to -0.95 GeV^2 in increments of -0.1 GeV^2. The photon energy utilized in this analysis was $E_\gamma = 3.3$ GeV. The principal aim of this study is to optimize concordance and faithfully represent the contours of the data within the stipulated fitting domain. Table 4.1 presents the derived values of all eight parameters resulting from the initial fit, while a graphical representation is available in Fig. 4.1.

The fitting outcomes are visually delineated in figures spanning from 4.2 to 4.7. These figures reveal that the model performs well for specific moments within certain t bins, demonstrating substantial alignment with the data within the fitting energy range. Nevertheless, it is essential to acknowledge noticeable disparities, which were expected due to the influence of other partial waves, particularly higher resonances (as elaborated in Appendix D), and the presence of background contributions beyond Deck in the data. These supplementary contributions primarily stem from non-resonant effects generated by various partial waves.

A closer examination reveals that the additional moments associated with the S-wave, specifically $\langle Y_{10} \rangle$ and $\langle Y_{11} \rangle$, exhibit promising characteristics that closely match the corresponding experimental data. Remarkably, $\langle Y_{10} \rangle$ exhibits excellent agreement with experimental results for $t = -0.55, -0.65, -0.95$ GeV^2 (as depicted in Figs. 4.3, 4.4, and 4.7). Even the outcomes for other t bins demonstrate noteworthy resemblance to the empirical data.

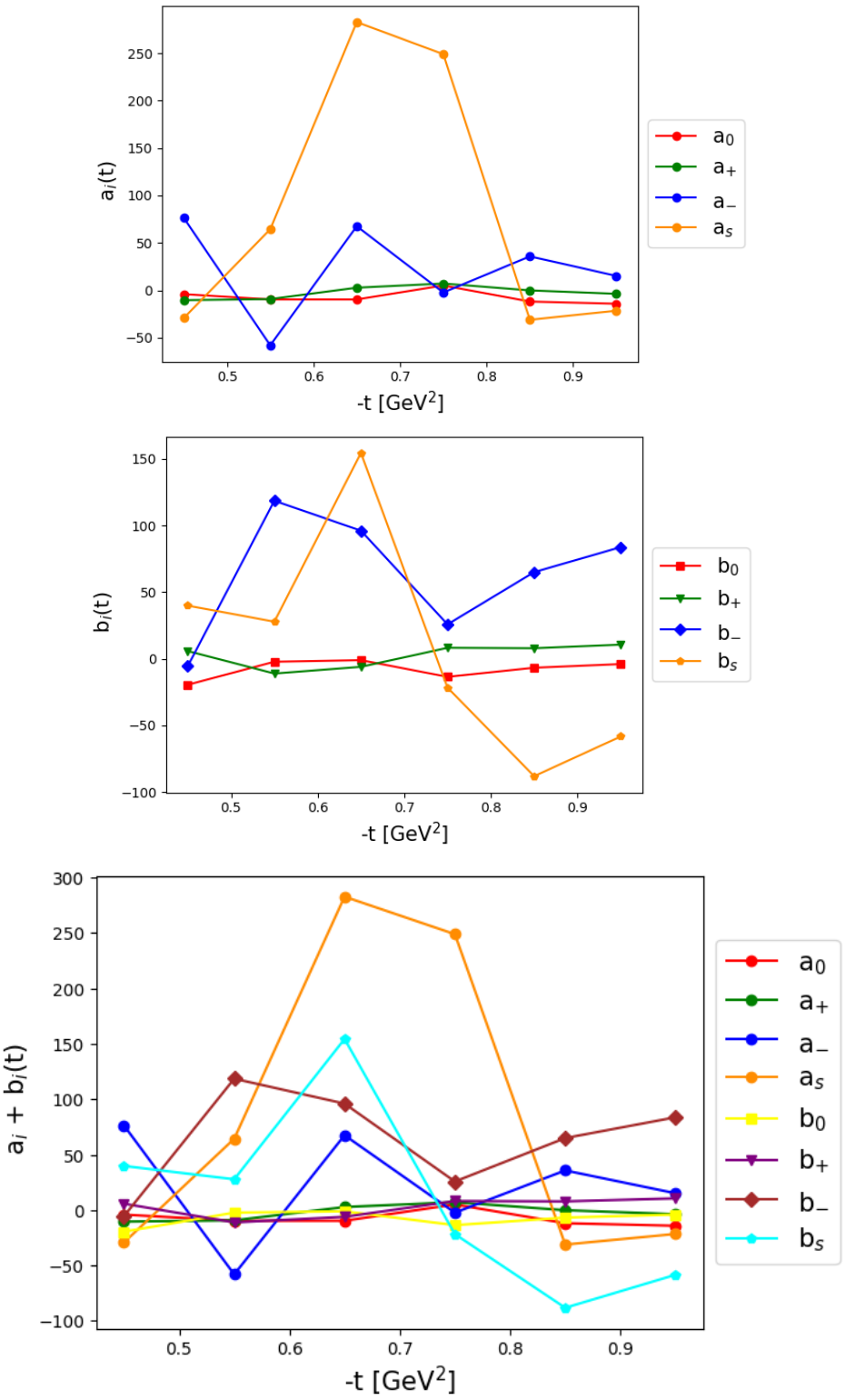

Figure 4.1: Variation of fitted parameters corresponding to the P-wave and σ meson contribution's as function of t bins at $E_\gamma = 3.3$ GeV.

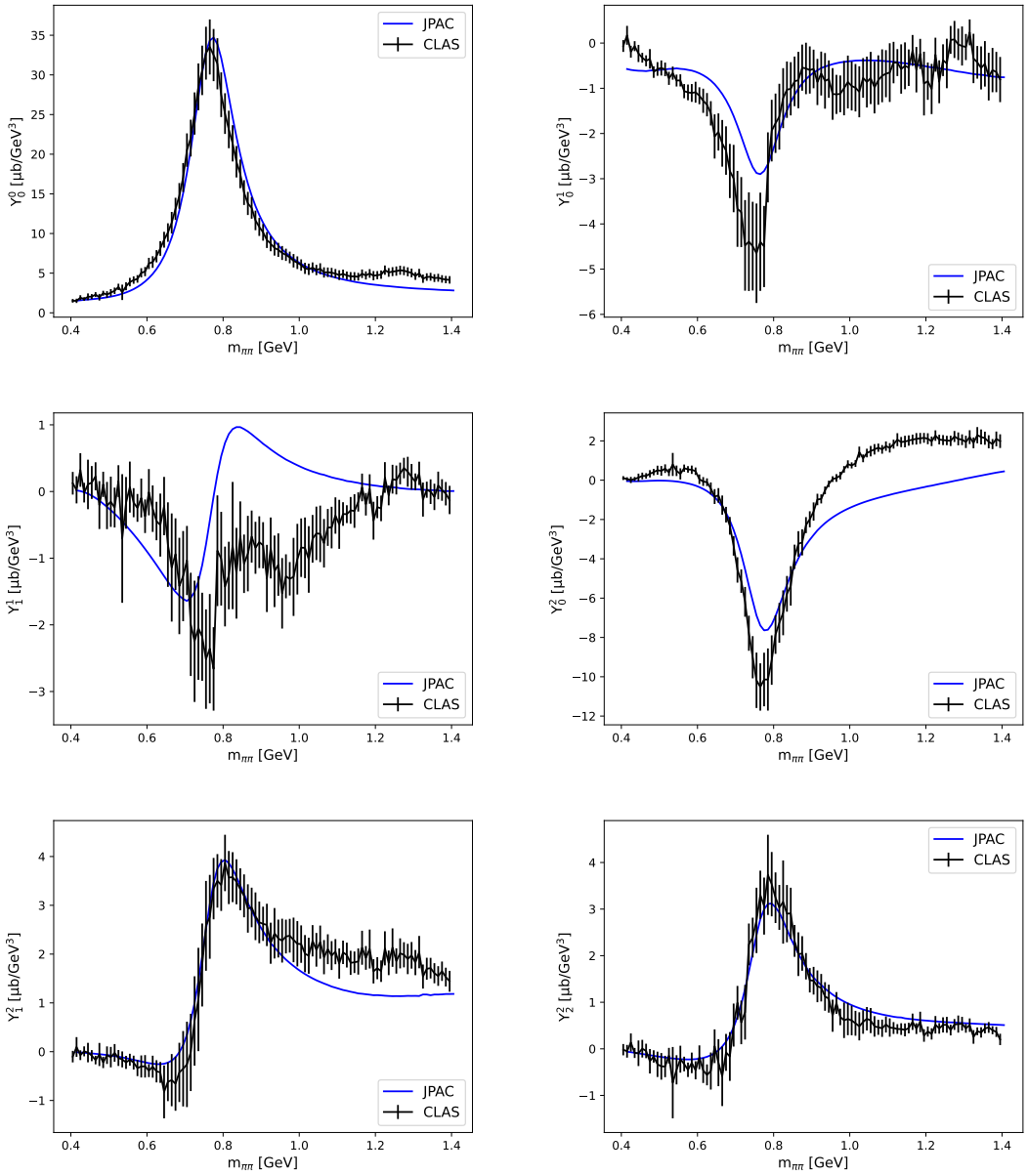

Figure 4.2: Fitted moments with Deck, ρ and σ contributions for $t = -0.45$ GeV^2 at $E_\gamma = 3.3$ GeV

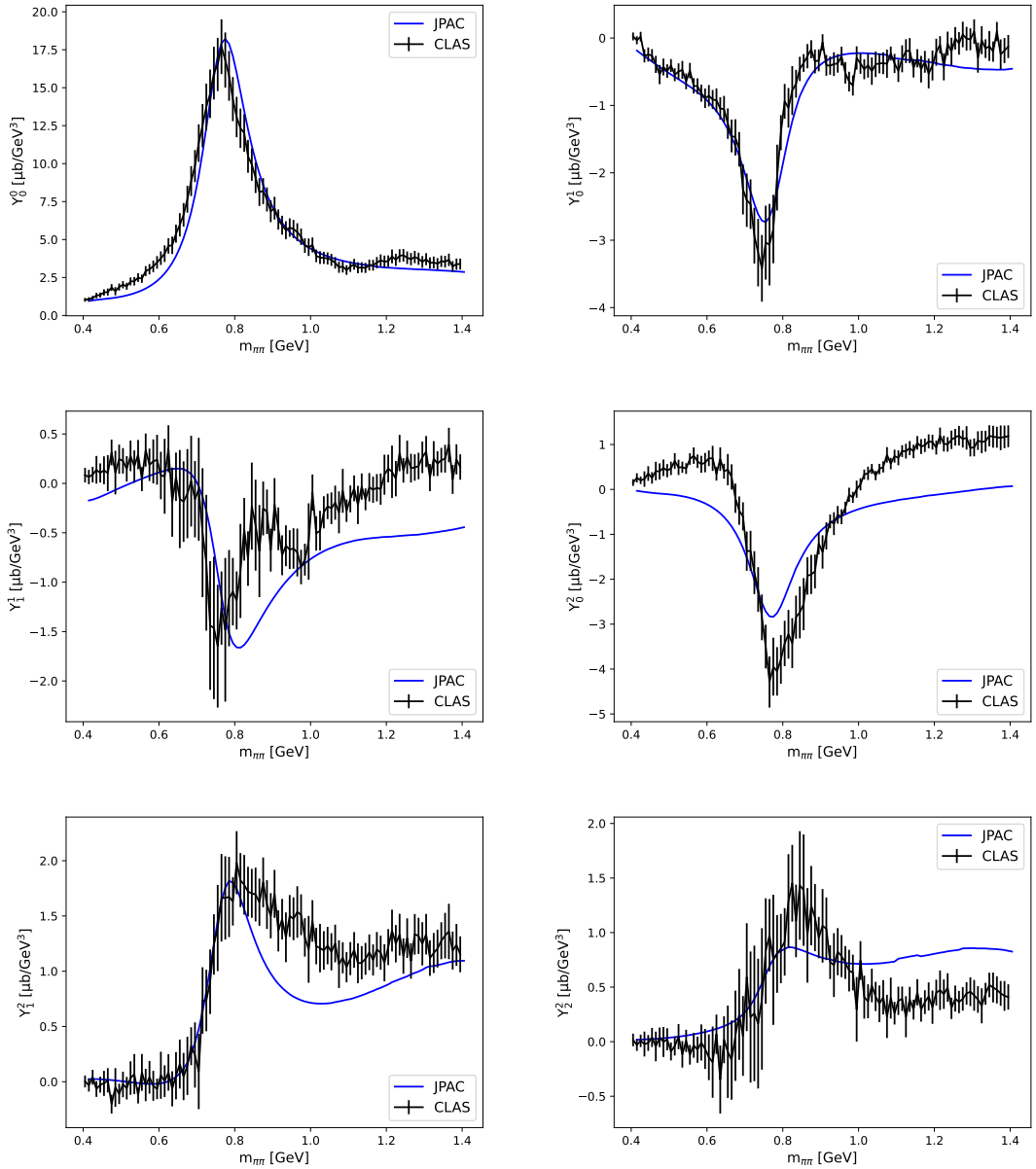

Figure 4.3: Fitted moments with Deck, ρ and σ contributions for $t = -0.55$ GeV^2 at $E_\gamma = 3.3$ GeV

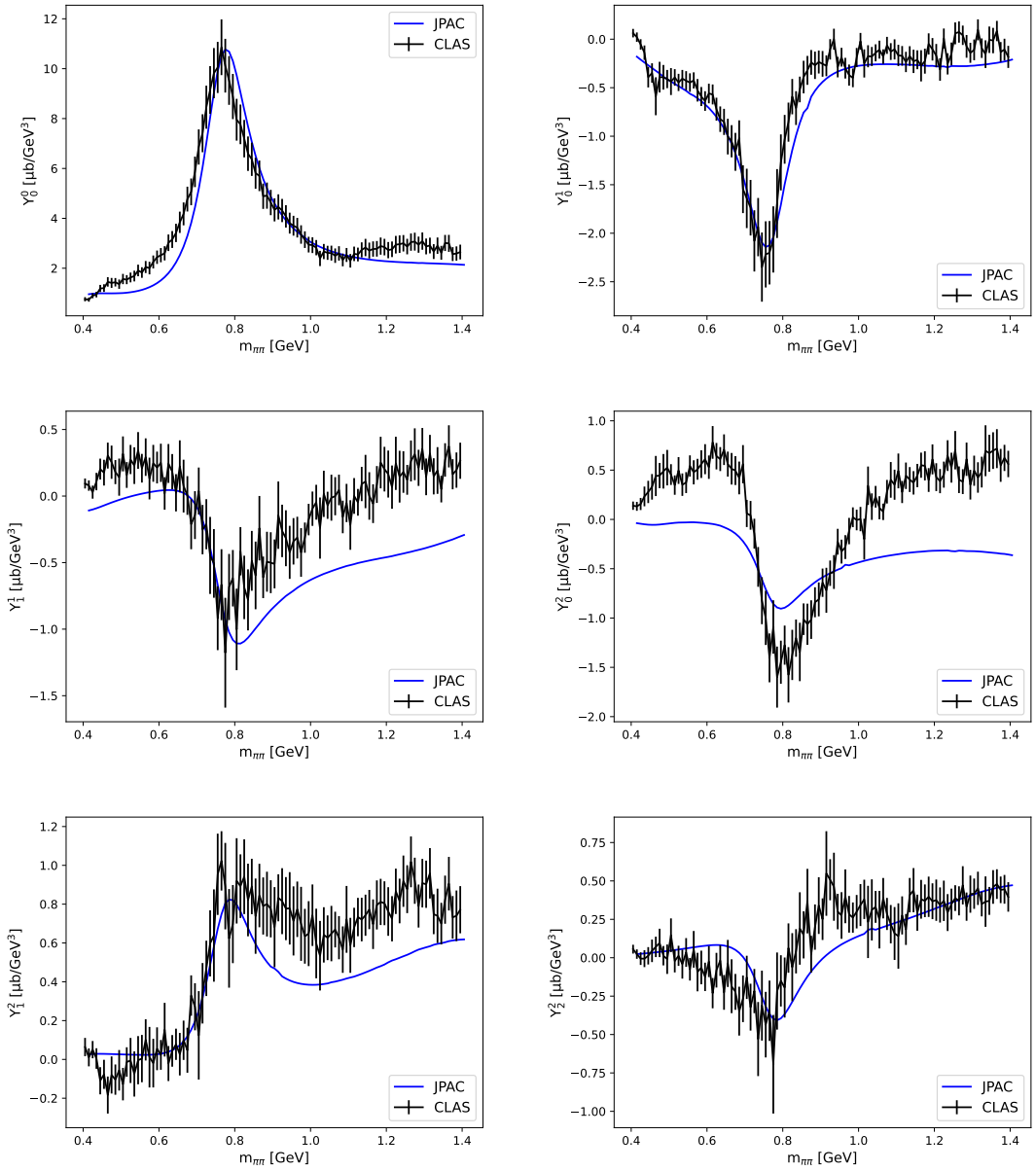

Figure 4.4: Fitted moments with Deck, ρ and σ contributions for $t = -0.65$ GeV^2 at $E_\gamma = 3.3$ GeV

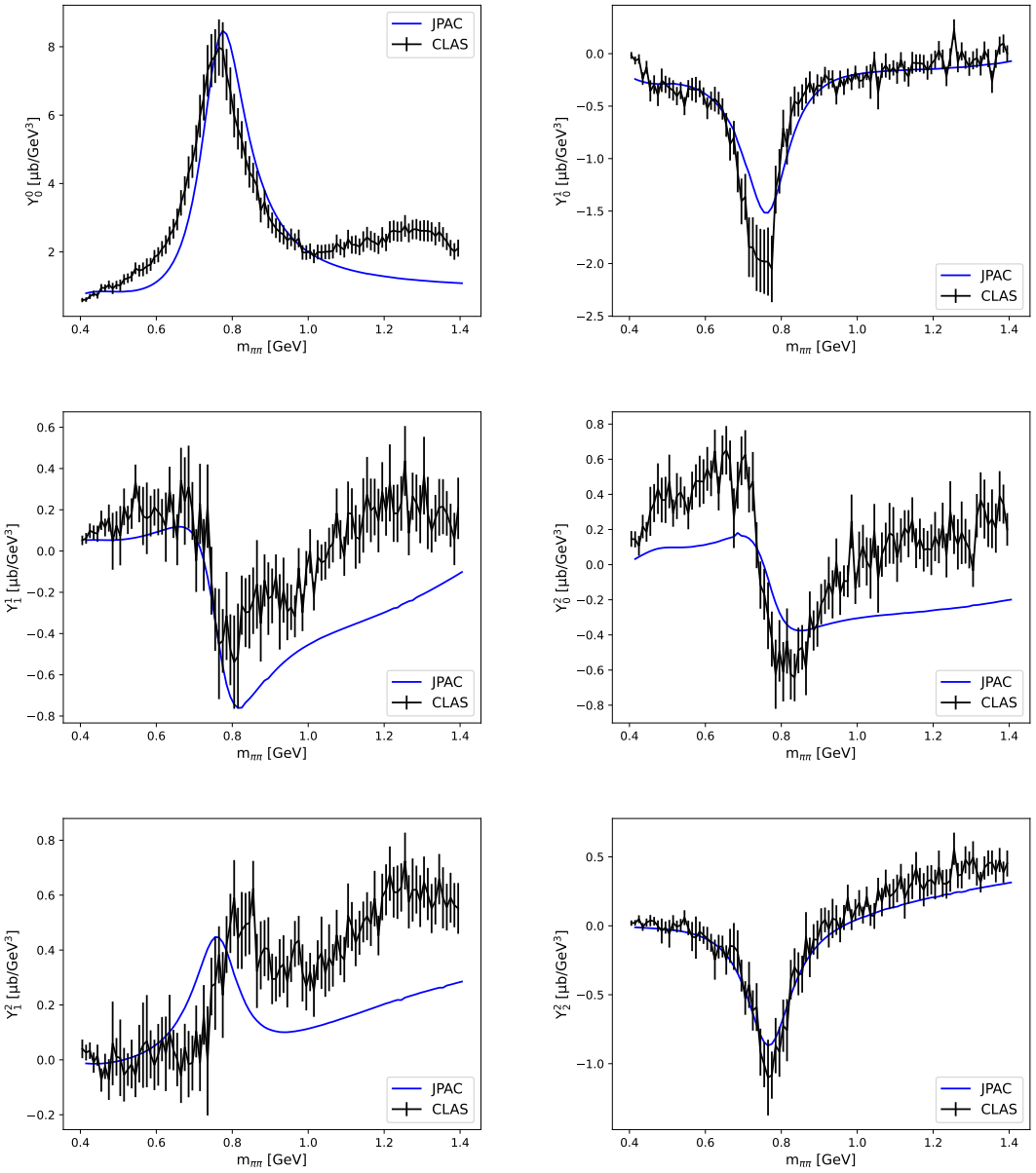

Figure 4.5: Fitted moments with Deck, ρ and σ contributions for $t = -0.75$ GeV^2 at $E_\gamma = 3.3$ GeV

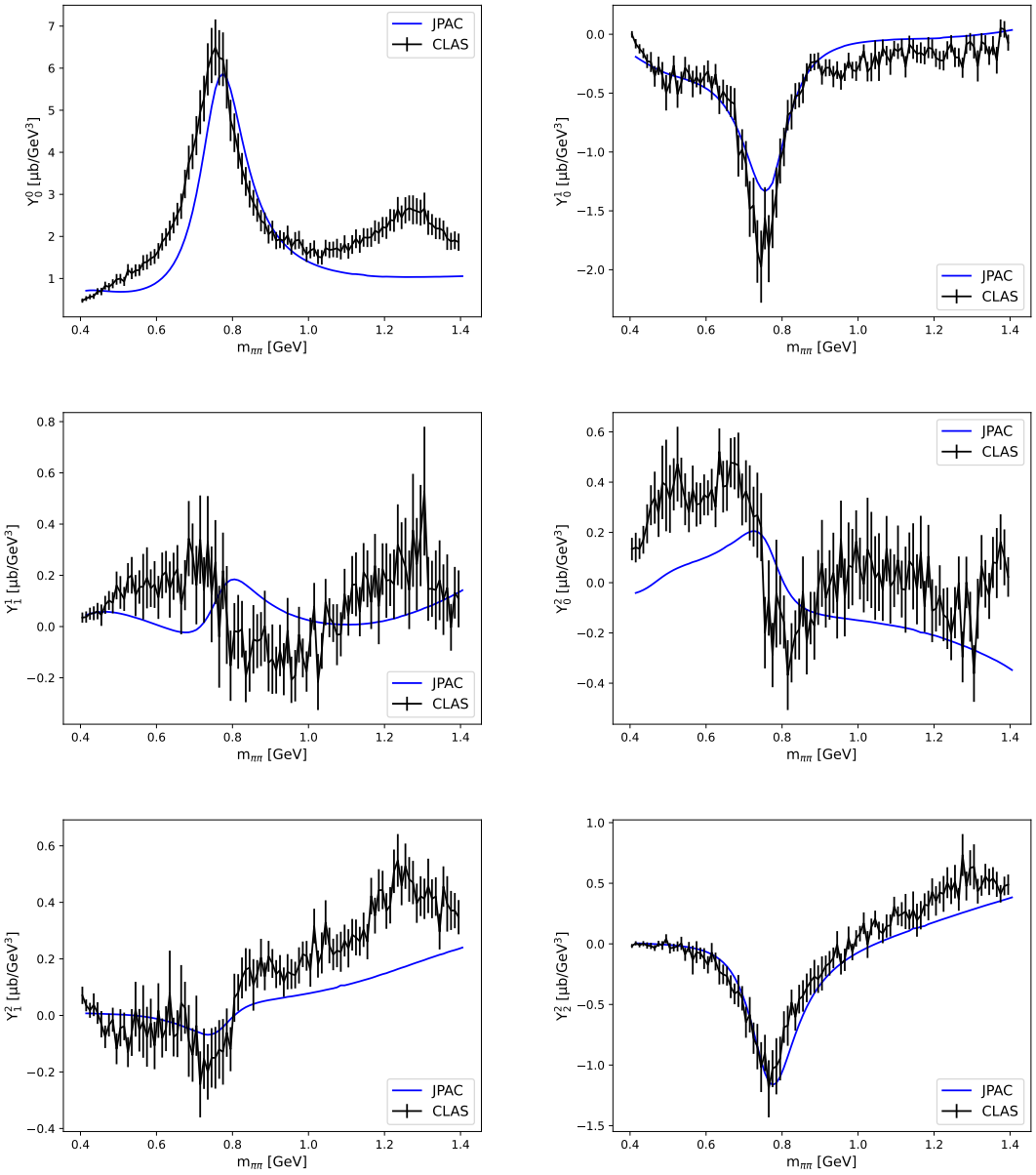

Figure 4.6: Fitted moments with Deck, ρ and σ contributions for $t = -0.85$ GeV^2 at $E_\gamma = 3.3$ GeV

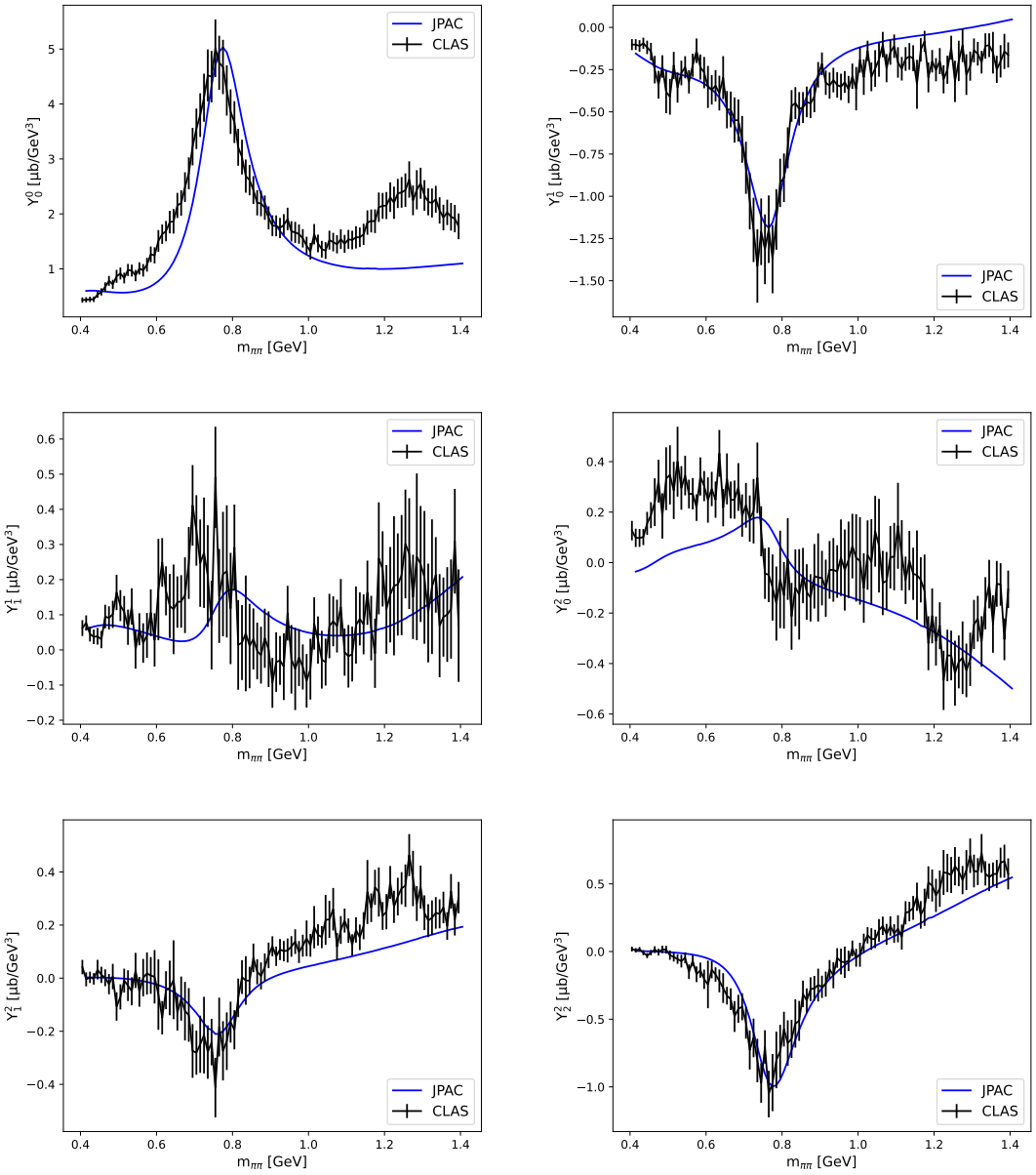

Figure 4.7: Fitted moments with Deck, ρ and σ contributions for $t = -0.95$ GeV^2 at $E_\gamma = 3.3$ GeV

t GeV^2	a_-	a_0	a_+	a_s	b_-	b_0	b_+	b_s
-0.45	76.436	-4.0476	-10.395	-29.298	-5.5655	-19.516	5.7729	39.824
-0.55	-57.939	-9.6181	-9.2397	64.357	118.50	-2.2659	-11.114	27.782
-0.65	67.519	-9.6406	2.7564	282.67	96.036	-1.0783	-6.0882	154.32
-0.75	-2.3078	5.0981	7.1335	248.83	25.771	-13.587	8.1905	-21.672
-0.85	35.782	-11.848	-0.095983	-31.082	64.949	-6.7605	7.8642	-88.109
-0.95	15.171	-14.134	-3.6972	-21.498	83.723	-4.0271	10.555	-58.334

Table 4.1: The eight fitted parameters of the moments with Deck, P-wave, and σ meson contributions for each t at $E_\gamma = 3.3$ GeV.

Furthermore, Appendix D elucidates that fitting $\langle Y_{20} \rangle$ poses significant challenges due to intricate wave interferences prevalent in the current modeling framework. Additionally, an examination of the $\langle Y_{11} \rangle$ and $\langle Y_{21} \rangle$ moments reveals prominent peaks within the $m_{\pi\pi}$ spectrum, notably in the intervals [0.9-1] and [1.2-1.4] GeV. These conspicuous features underscore the substantial influence of higher resonances, including the scalar $f_0(980)$, direct D-wave resonance (represented by the tangible tensor $f_2(1275)$), and the scalar $f_0(1370)$. Consequently, the inclusion of these resonances, coupled with meticulous consideration of additional background contributions, holds the potential for significant improvements in the fitted moments, ultimately resulting in a more profound alignment with empirical data.

4.5 Non-Resonance Background

In the context of modeling resonant and non-resonant contributions, it is common to encounter distinct features in the cross-section data. Resonances typically exhibit characteristic peak structures associated with their specific energies and decay widths. However, when dealing with non-resonant background contributions, the situation becomes more complex. To effectively account for these non-resonant backgrounds, arising from both P and S-wave contributions, a more versatile and generalized approach is required. This approach involves using a simplified parameterization with minimal parameters, allowing for a flexible description of the background behavior.
This parametrization can be expressed as follows:

$$F_{bkg}(s_{\pi\pi}) \equiv \left[(s_{\pi\pi}^{\text{th}} - s_{\pi\pi})(s_{\pi\pi}^{\max} - s_{\pi\pi})\right], \tag{4.38}$$

where

$$s_{\pi\pi}^{\rm th} = 4m_\pi^2 \tag{4.39}$$

$$s_{\pi\pi}^{\rm max} = s + m_p^2 - \frac{1}{2m_p^2}\left[(s+m_p^2)(2m_p^2 - t) - \lambda^{1/2}(s, m_p^2, 0)\lambda^{1/2}(t, m_p^2, m_p^2)\right]. \tag{4.40}$$

Consequently, the non-resonant component within the P-wave contribution is expressed as:

$$\mathcal{M}_{\mathbf{P}}^{\rm nr} = R_{f_2}(s,t)\frac{1}{s}F_{bkg}(s_{\pi\pi})\overline{u}(p_2,\lambda_2)\psi'(\lambda_\gamma)u(p_1,\lambda_1)\,, \tag{4.41}$$

where in the context of the non-resonant P amplitude, the associated parameters are designated as follows: $a_+^{\rm nr}(t)$, $a_-^{\rm nr}(t)$, and $a_0^{\rm nr}(t)$. Likewise, the non-resonant S-wave contribution can be formulated as follows:

$$\mathcal{M}_{\mathbf{S}}^{\rm nr} = \frac{1}{s}(a_{s_j}^{\rm nr} + ib_{s_j}^{\rm nr})R(s,t)[(s_{\pi\pi}^{\rm th} - s_{\pi\pi})(s_{\pi\pi}^{\rm max} - s_{\pi\pi})]\overline{u}(p_2,\lambda_2)\gamma^\mu u(p_1,\lambda_1)v_\mu(\lambda_\gamma)\,. \tag{4.42}$$

4.6 Full Energy Range Fit

In this section, the model is extended to include the second scalar meson ($f_0(980)$) and two non-resonant components stemming from both the analyzed contributions, namely the P and S waves. This expansion results in an increase in the number of free parameters from 8 to 18. These parameters can be categorized into 10 that represent the resonance contributions (6 for ρ and 4 for σ and $f_0(980)$, two for each), and 8 that represent the non-resonance contributions (6 for non-resonant P and 2 for non-resonant S denoted by NR_P and NR_S respectively).

The new fit covers the entire energy range, specifically $m_{\pi\pi} = [0.4 - 1.4]$ GeV. Similar to the previous fit, this study focuses on analyzing the moments within each t bin, ranging from -0.45 to -0.95 GeV^2 in increments of -0.1 GeV^2, all at the same photon energy of $E_\gamma = 3.3$ GeV.

The total χ^2 values for these fits at each t bin, as presented in Table 4.2, exhibit remarkable consistency. This consistency underscores the stability and reliability of the results obtained. Additionally, Tables 4.3 and 4.4 present the resulting parameters associated with the resonance contributions and non-resonant contributions, respectively. For a more comprehensive understanding, graphical representations are available in Figs. 4.8 and 4.9.

t GeV^2	-0.45	-0.55	-0.65	-0.75	-0.85	-0.95
$\chi^2_{\rm Tot}$	576	576	576	576	576	576
$\chi^2_{\rm Tot}$/n.d.f	1.0093	1.3279	1.3680	1.2580	1.1974	1.2017

Table 4.2: Values of total χ^2 for the fits of the full model at each t with $E_\gamma = 3.3$ GeV.

t GeV^2	a_-	a_0	a_+	a_{s_1}	a_{s_2}	b_-	b_0	b_+	b_{s_1}	b_{s_2}
-0.45	9.015	-0.158	-4.316	14.869	2.622	-12.539	-6.263	1.172	6.348	-13.377
-0.55	-0.531	0.101	-0.042	-12.121	-1.23	-2.93	-0.142	-0.0728	-12.752	-2.488
-0.65	-23.72	-3.237	-0.726	-16.433	1.655	24.01	1.985	0.473	-7.495	1.8134
-0.75	53.098	-4.074	2.558	-17.24	3.053	3.053	7.713	0.898	1.759	70.092
-0.85	73.594	0.1705	2.686	-14.354	2.969	-35.042	13.515	-1.525	10.393	-1.795
-0.95	35.299	-5.043	-5.27	-17.826	3.063	-84.181	16.67	-10.693	6.103	1.677

Table 4.3: The 10 fitted parameters representing $\rho(770)$, σ, and $f_0(980)$ resonances for each t at $E_\gamma = 3.3$ GeV.

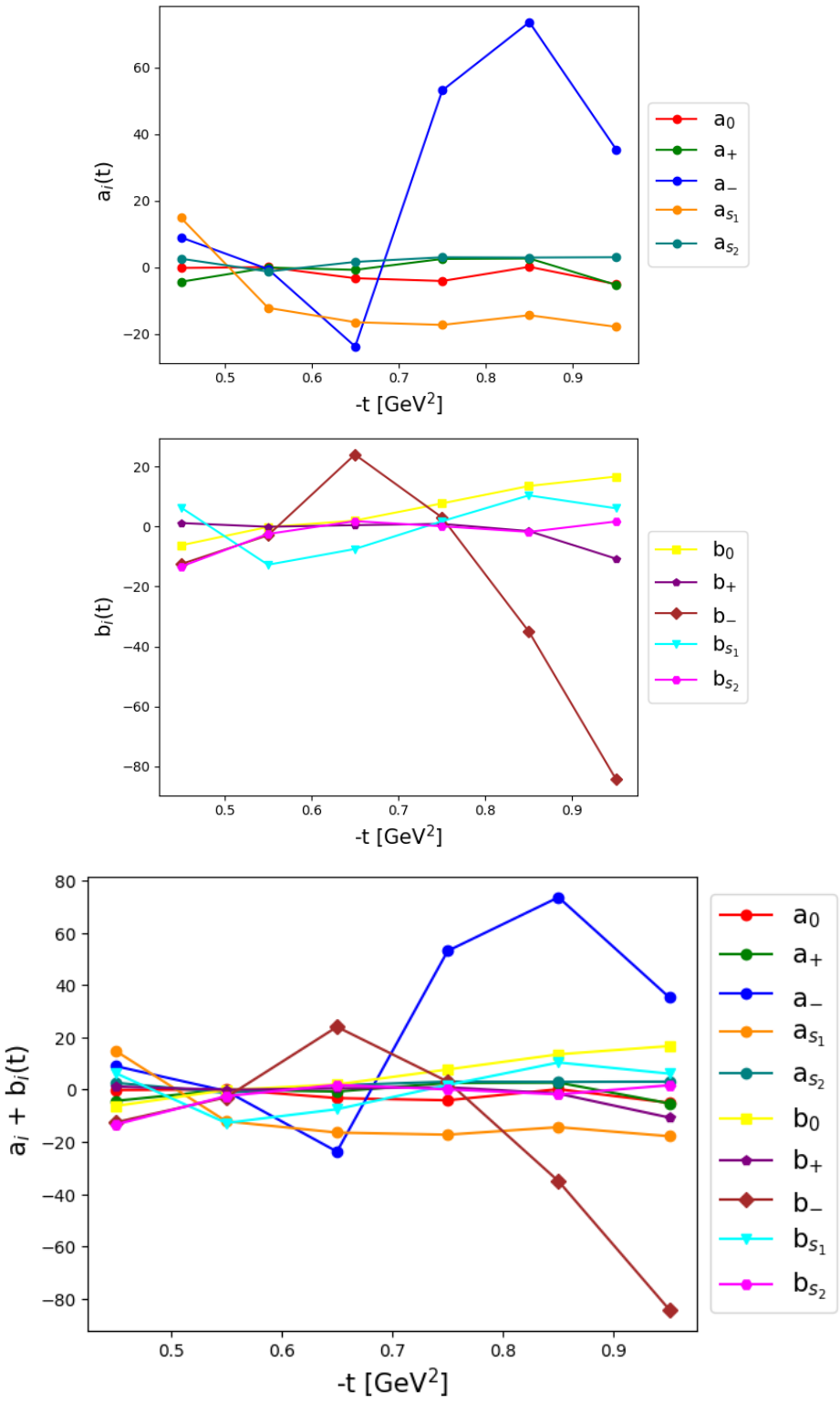

Figure 4.8: Variation of Fitted Parameters corresponding to the resonant pieces of the model as function of t bins at $E_\gamma = 3.3$ GeV.

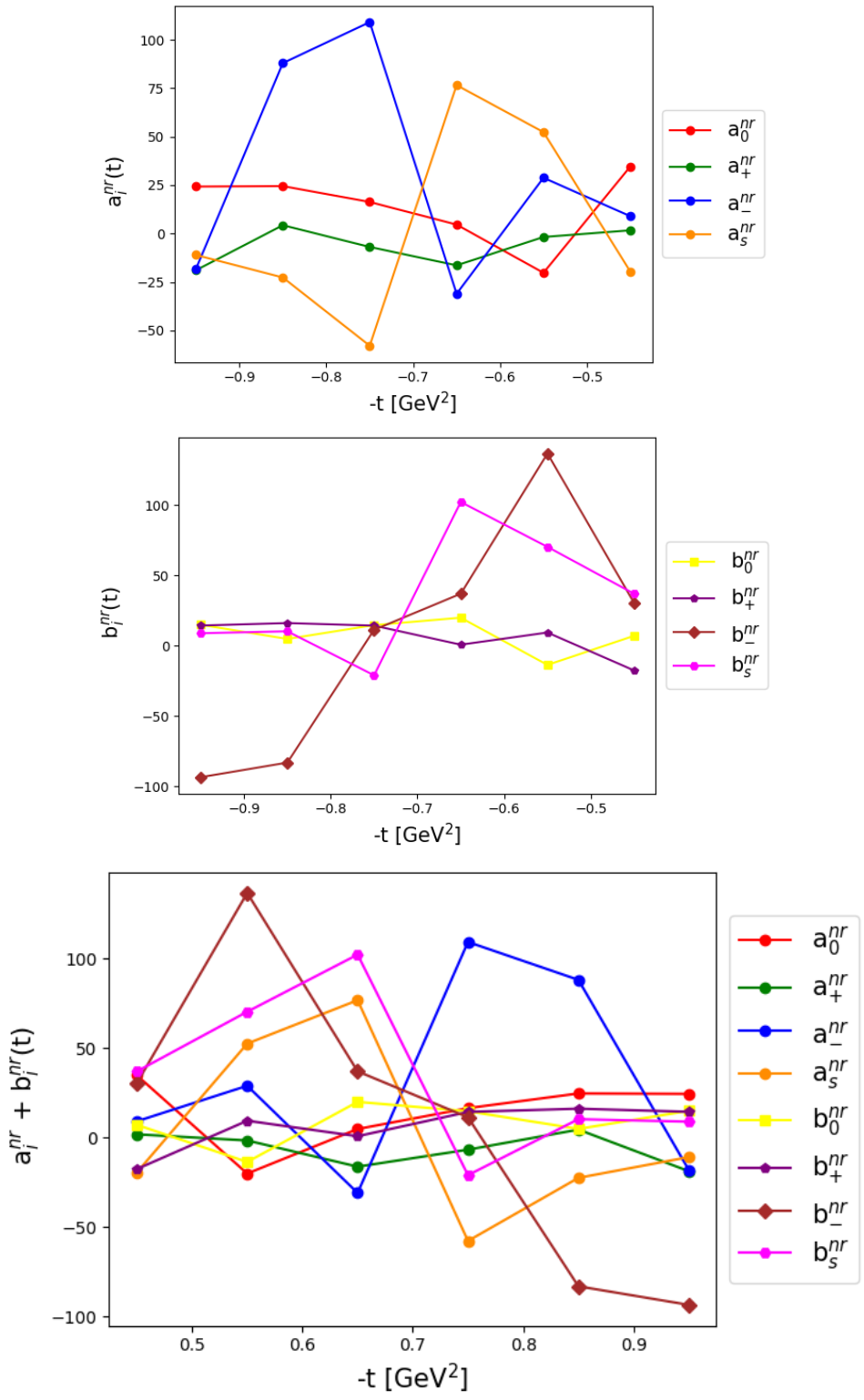

Figure 4.9: Variation of Fitted Parameters corresponding to the non-resonant pieces of the model as function of t bins at $E_\gamma = 3.3$ GeV.

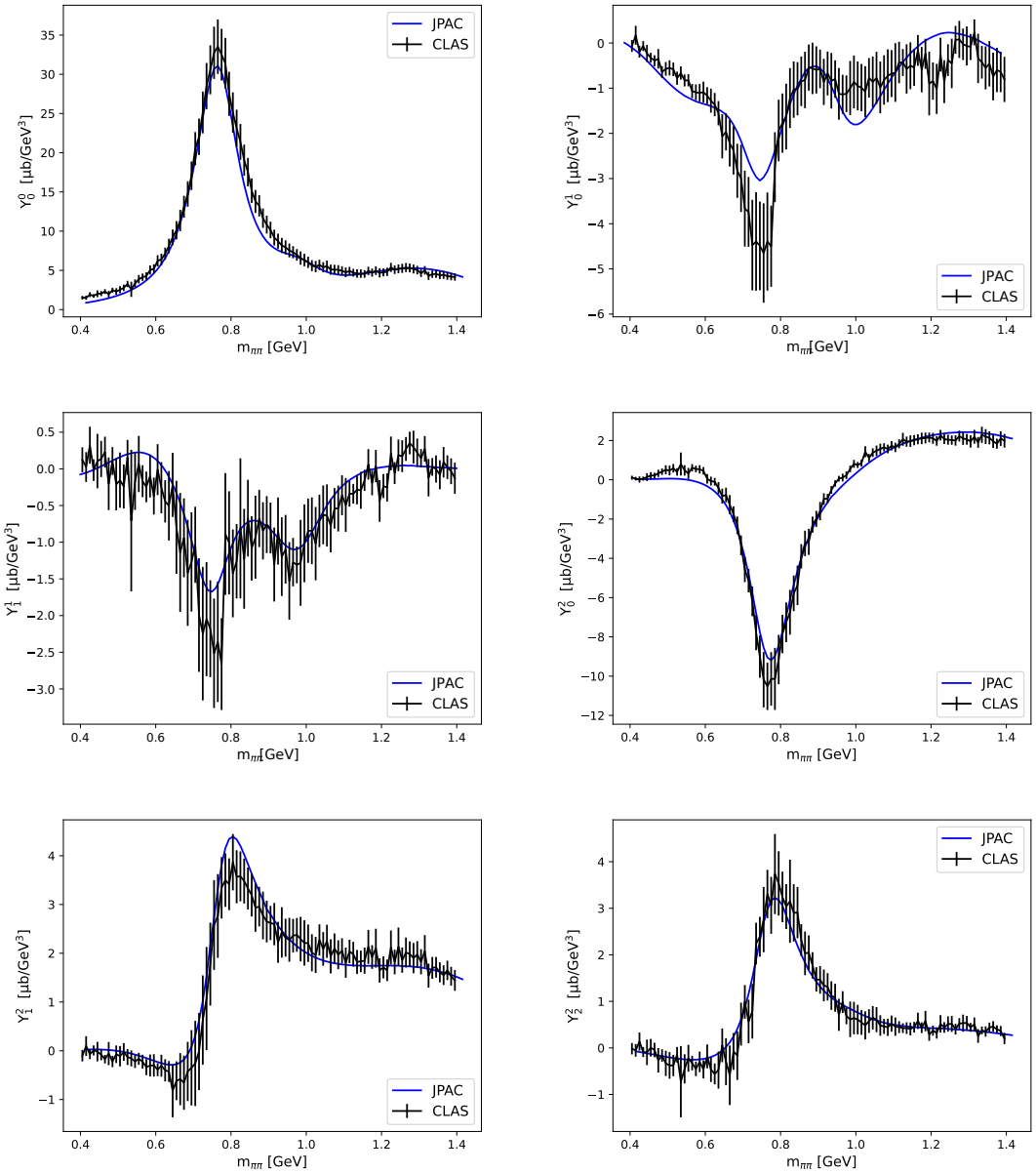

Figure 4.10: Fitted moments for model with Deck, P, S, NR_P and NR_S contributions for $t = -0.45$ GeV^2 at $E_\gamma = 3.3$ GeV

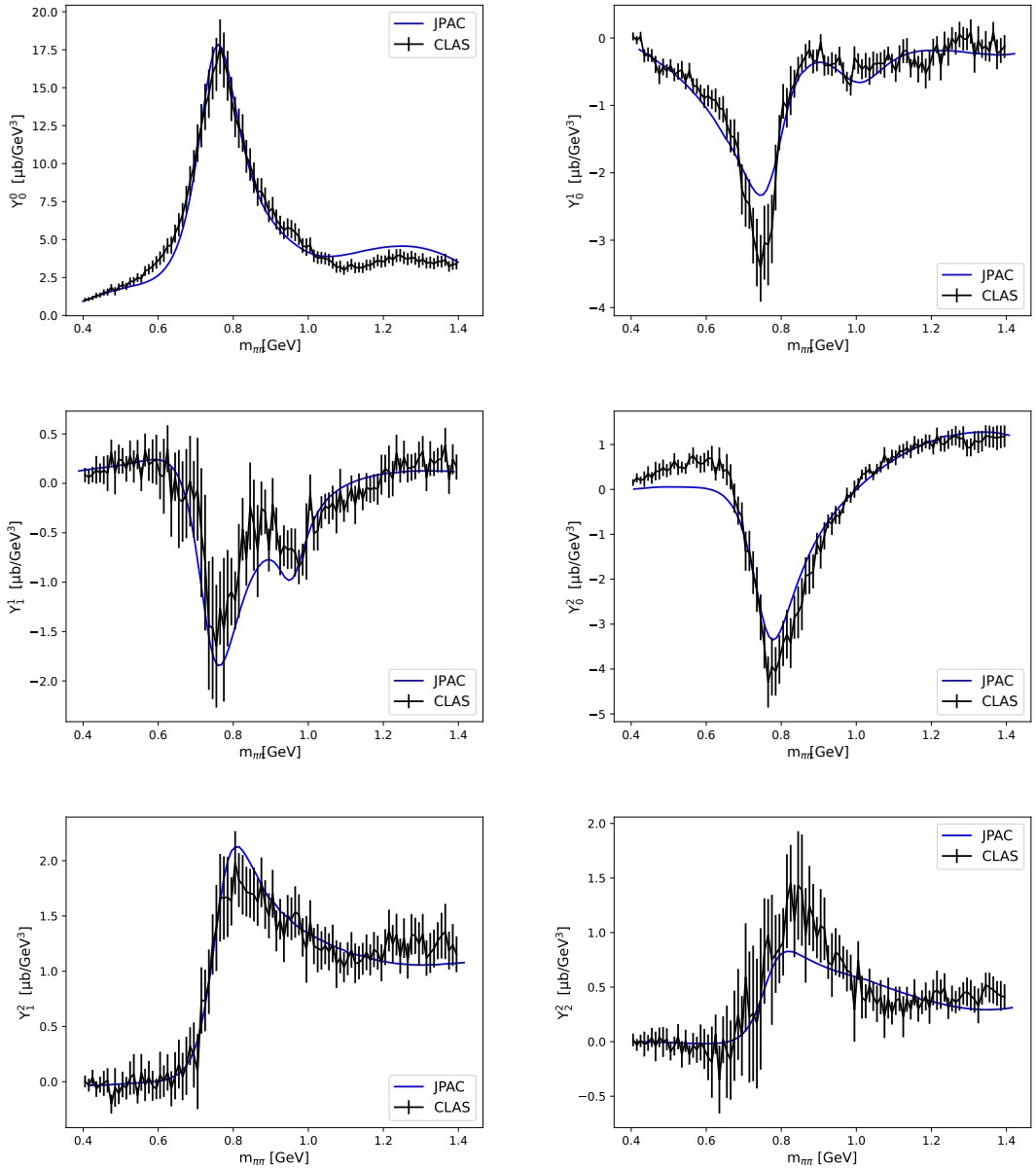

Figure 4.11: Fitted moments for model with Deck, P, S, NR_P and NR_S contributions for $t = -0.55$ GeV^2 at $E_\gamma = 3.3$ GeV

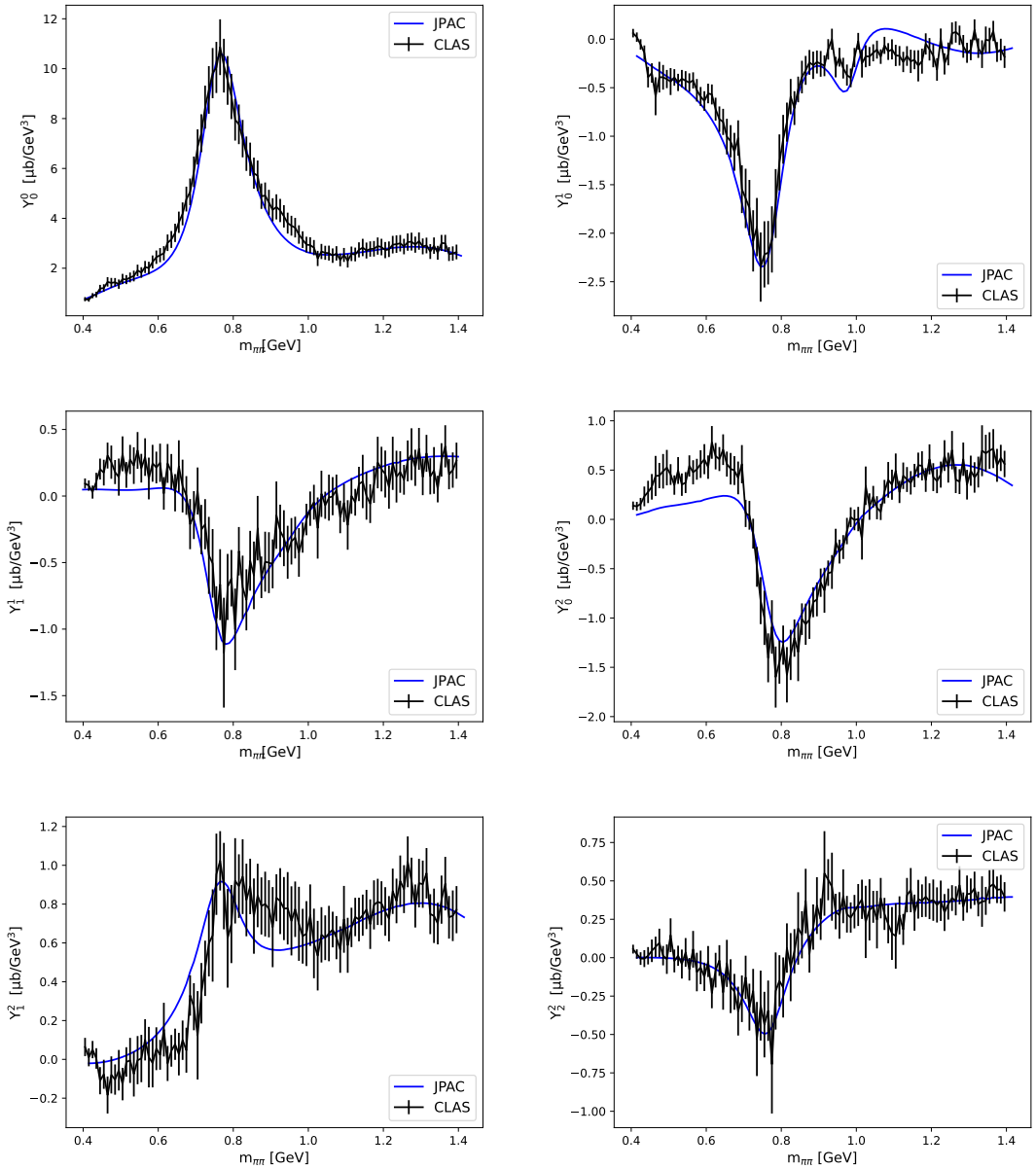

Figure 4.12: Fitted moments for model with Deck, P, S, NR_P and NR_S contributions for $t = -0.65$ GeV^2 at $E_\gamma = 3.3$ GeV

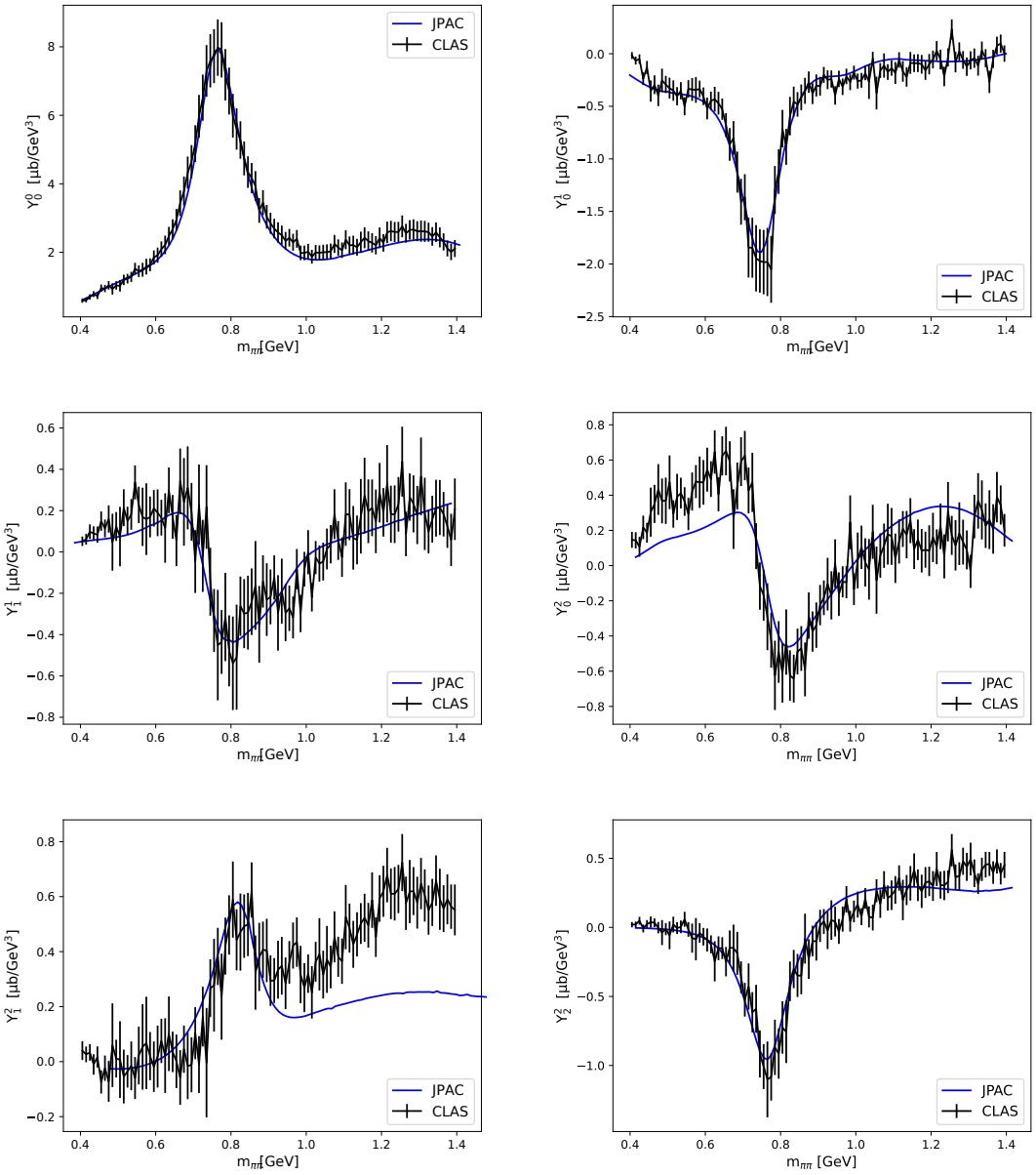

Figure 4.13: Fitted moments for model with Deck, P, S, NR_P and NR_S contributions for $t = -0.75$ GeV^2 at $E_\gamma = 3.3$ GeV

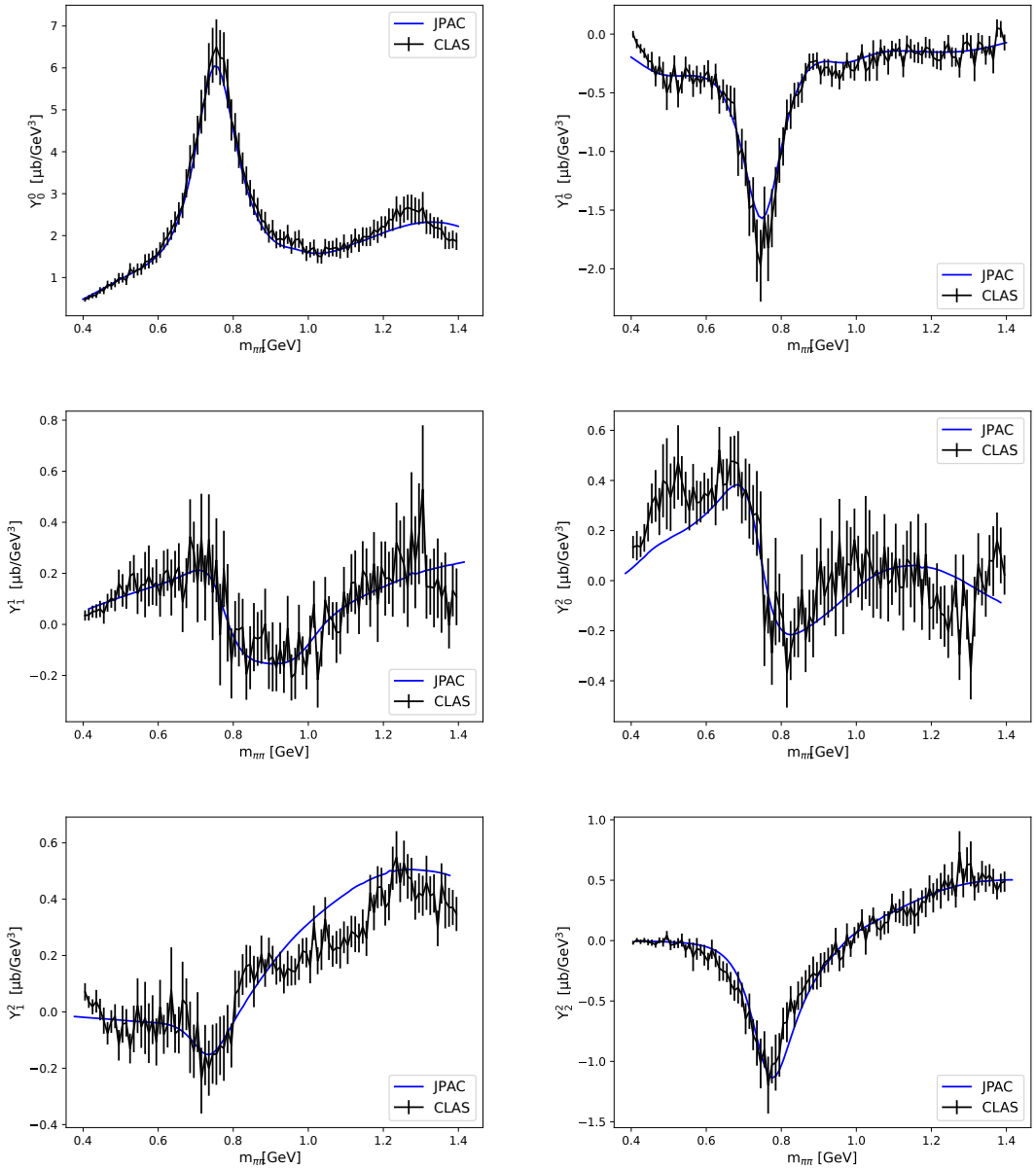

Figure 4.14: Fitted moments for model with Deck, P, S, NR_P and NR_S contributions for $t = -0.85$ GeV^2 at $E_\gamma = 3.3$ GeV

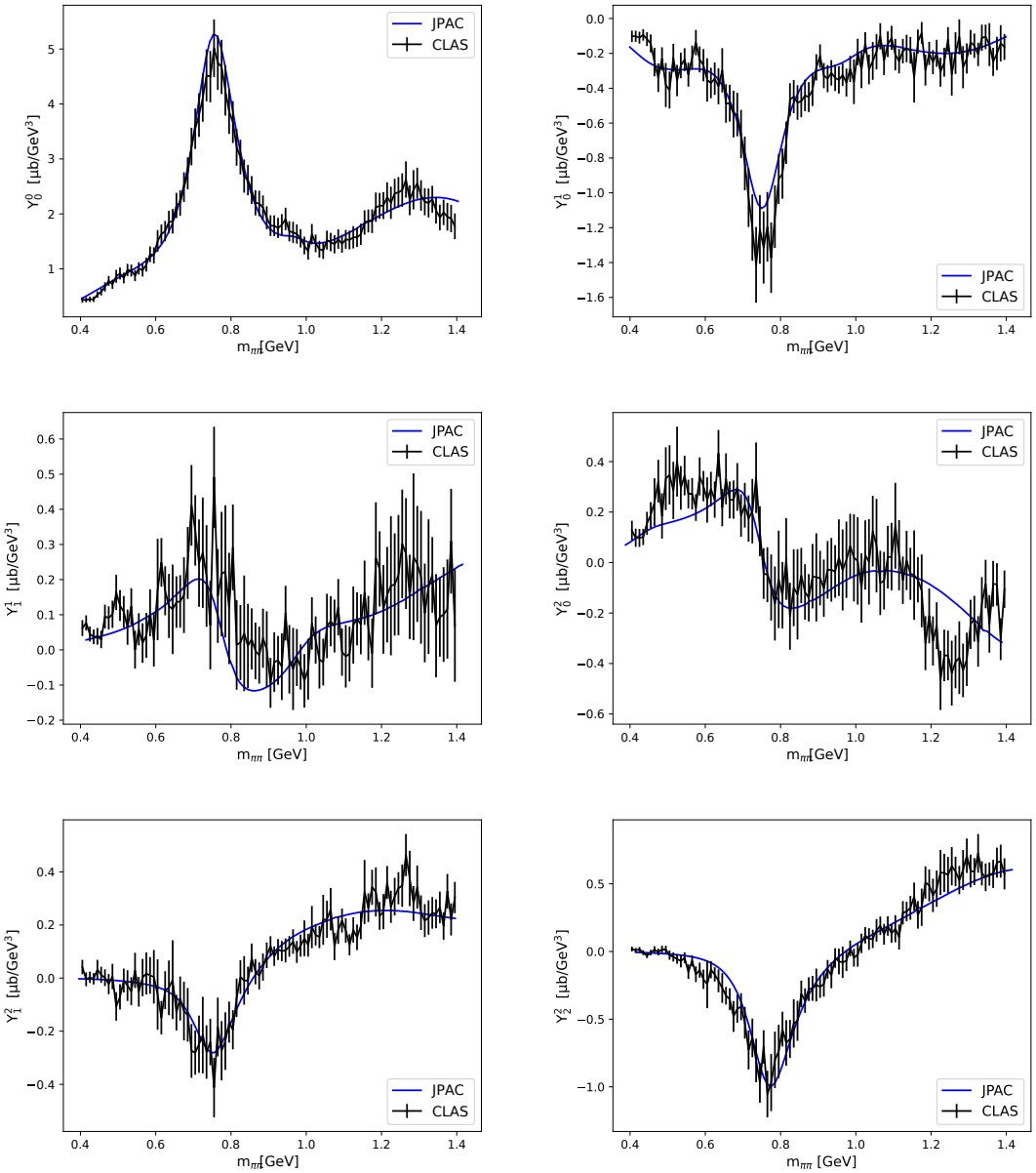

Figure 4.15: Fitted moments for model with Deck, P, S, NR_P and NR_S contributions for $t = -0.95$ GeV^2 at $E_\gamma = 3.3$ GeV

t GeV^2	$a_-^{\rm nr}$	$a_0^{\rm nr}$	$a_+^{\rm nr}$	$a_s^{\rm nr}$	$b_-^{\rm nr}$	$b_0^{\rm nr}$	$b_+^{\rm nr}$	$b_s^{\rm nr}$
-0.45	8.919	34.605	1.653	-19.672	30.202	6.934	-17.756	36.78
-0.55	28.754	-20.26	-1.79	52.303	136.432	-13.794	9.237	70.115
-0.65	31.1	4.605	-16.421	76.54	36.813	19.77	0.583	102.01
-0.75	109.062	6.27	-6.927	-57.883	11.149	14.51	14.155	-21.147
-0.85	87.911	24.463	4.29	-22.674	-83.216	4.670	15.97	10.101
-0.95	-18.24	24.23	-18.94	-11.067	-193.6	14.752	14.21	8.72

Table 4.4: The 8 fitted parameters representing the non-resonant contributions for each t at $E_\gamma = 3.3$ GeV.

4.6.1 Discussion of the results

The results presented in Figs. 4.10 to 4.15 are derived from the fitted model. An analysis of these results reveals the following key observations:

- Moment $\langle Y_{00}\rangle$:
  An examination of this moment, which represents the differential cross-section, demonstrates that the $\rho(770)$ meson contributes the most to the overall cross-section.

- $\langle Y_{10}\rangle$ and $\langle Y_{11}\rangle$:
  In the figures for $\langle Y_{10}\rangle$, the S-wave contributions begin to emerge. This is evident by a dip in the presence of the $\rho(770)$ resonance, indicating the scalar resonance σ. Additionally, a small bump around $m_{\pi\pi} \sim 0.98$ GeV signifies the scalar $f_0(980)$ meson. Regarding $\langle Y_{11}\rangle$, besides the presence of both scalar mesons σ and $f_0(980)$, a bump at $m_{\pi\pi} \sim 0.77$ GeV is observed. This feature results from the interference between the S-wave and the dominant $P+$ wave. The peak at $m_{\pi\pi} > 1.2$ GeV suggests the contribution of other resonances, primarily the tensor $f_2(1275)$ representing the D-wave and the scalar $f_0(1370)$. Consequently, the S-wave contribution is maximized in $\langle Y_{10}\rangle$ and $\langle Y_{11}\rangle$, influencing the interference with the P-wave.

- $\langle Y_{20}\rangle$,$\langle Y_{21}\rangle$, and $\langle Y_{22}\rangle$:
  In these moments, the interplay between the P-wave contribution and other wave components significantly shapes the results. At low t, scalar resonances may not be distinctly visible in the figures. However, they become more pronounced in $\langle Y_{21}\rangle$ and $\langle Y_{22}\rangle$ for $t = -0.55 \rightarrow -0.95$ GeV^2, along with contributions from $f_0(1370)$ and $f_2(1275)$.

A comparison of these fitting results with those presented in the previous section (Sec. 4.4) highlights substantial improvements in all moments across each t bin. Some moments even exhibit a striking resemblance to empirical data, approaching near-perfect alignment.

Nonetheless, it's crucial to acknowledge the remaining disparities. These differences can be attributed to contributions from other partial waves, indicating the presence of novel resonances and non-resonant components. Therefore, the inclusion of the remaining S-wave scalars, specifically $f_0(1370)$, and the D-wave tensor meson $f_2(1275)$ is highly likely to rectify these remaining discrepancies.

4.7 Summary

In summary, this chapter has provided valuable insights through a comprehensive examination of double pion photoproduction moments. By redefining the t-dependence within specific components of the full amplitude, including the Deck, scalar mesons σ and $f_0(980)$ production amplitudes representing the S-wave, as well as $\rho(770)$ production amplitudes via pomeron and f_2 exchanges, alongside backgrounds from both wave contributions, a comprehensive analysis was conducted. All moments $\langle Y_{LM} \rangle$ with $L, M \leq 2$ were fitted to experimental data, with results presented in Figs. 4.10→4.15 for $E_\gamma = 3.3$ GeV and fixed t: $0.45 \leq |t| \leq 0.95$ GeV^2. The stability of the χ^2_{Tot} value at 576 and the value χ^2_{Tot}/n.d.f close to 1 across all fits indicate the reliability of the obtained results, as evident in the figures, particularly for $m_{\pi\pi} < 1$ GeV. Notably, the P-wave contribution emerges as predominant, emphasizing its crucial role. This prominence was demonstrated through the thorough analysis of the moment $\langle Y_{00} \rangle$, as depicted in the mentioned figures, where the prominent $\rho(770)$ meson peak is evident. Furthermore, the classification of the Deck component as background has been clarified. A meticulous examination reveals that both Deck and S-wave contributions have minimal impacts on the model, underscoring their auxiliary roles. However, the presence of S-wave contributions is still discernible, particularly in moments $\langle Y_{10} \rangle$ and $\langle Y_{11} \rangle$, where peaks from the resonances σ and $f_0(980)$ are evident. Importantly, this study has shed light on the existence of other partial wave contributions, though not exhaustively discussed in this thesis, which significantly enrich the overall model. It is essential to recognize that these contributions collectively form a cohesive whole, emphasizing that none of them, regardless of their individual modesty, can be dismissed. Their intricate interplay and mutual influence are integral to achieving a comprehensive representation of experimental data.

As this thesis approaches its conclusion, the focus shifts towards the integration of additional components and refinement of the fitting process. These additions involve contributions from the $f_2(1275)$ tensor meson, representing the D-wave, and another scalar meson from the S-wave contribution, namely $f_2(1370)$. These new elements introduce 12 more free parameters (10 for $f_2(1275)$ and 2 for $f_2(1370)$), supplementing the 18 parameters discussed earlier in Tables 4.3 and 4.4, as depicted in Figures 4.8 and 4.9. Consequently, the model becomes overparametrized, necessitating an examination of their relationships with t to reduce their number. The ultimate goal is to return to the original amplitude form with fixed couplings. This phase represents the peak of the study, thoroughly exploring parameter interdependencies with the goal of simplification for fixed tt dependencies. This advancement enables the prediction of moments at higher CLAS energies, such as $E_\gamma = 8.5$ GeV.

PART II
Spectroscopy of Light Vector Mesons

Preface

According to the Particle Data Group (PDG), the experimental status of meson resonances with masses ranging from 1 to 2 GeV is relatively poor, as many states predicted by the quark model have yet to be seen [81]. Furthermore, several seemingly typical resonances reported in the PDG tables do not even fit into conventional quark theories, such as Godfrey and Isgur's (GI) relativized meson model [82]. Some of the most glaring inconsistencies were covered briefly in a previous work [83], such as the enormous number of observed f_2 states (with $J^{PC} = 2^{++}$) versus the much fewer expected in the GI model, as well as the very low mass of the strange vector meson $K^\star(1410)$, the first radial excitation of $K^\star(892)$, which is anticipated to be about 200 MeV greater in the GI and related quark models. The PDG lists ρ', the first radial excitation of $\rho(770)$, as $\rho(1450)$ [81], which is difficult to reconcile with a lighter $K^\star(1410)$, as the latter state includes one strange quark and one light quark rather than two light quarks. However, under the $\rho(1450)$ item in the PDG meson listings, one may find a wide range of experimental findings with masses ranging from 1208–1624 MeV, depending on the specific strong decay mode. In fact, there have been several indicators of a lighter ρ' in the range 1.25–1.3 GeV [81].

In this part of the thesis, a reexamination and attempt to resolve the ρ' meson paradox will be conducted in Chapter 5 by reanalyzing the elastic P-wave scattering data. The investigation will be extended in Chapter 6, where the three channels separable potential approach will be included to provide some predictions for the $\pi\omega$ channel phase shifts and inelasticities. The formalism and fundamental principles for the next study will be illustrated below.

S-matrix and phase shifts

The phase shift δ_ℓ is a fundamental quantity for characterizing the scattering amplitude, as has been established in various standard textbooks on quantum mechanics. Generally, the phase shift can be evaluated from measurable quantities such as the differential cross section $d\sigma/d\Omega$, or alternatively, through the formalism of the S-matrix. The scattering phase

shift encodes significant physical information, which can be utilized to investigate resonant phenomena in the data, leading to a deeper understanding of the underlying physical mechanisms of a given scattering process. Consequently, the determination of the phase shift (or amplitude) may yield additional insights into the kinetics of the scattering process, the properties of resonances, and related phenomena. In summary, the phase shift parameterization serves as a valuable tool for the analysis and interpretation of scattering data. Using the unitarity feature of the S- matrix, demonstrated in 2.1.1, one can relate each partial wave S_ℓ matrix element to the real phase shift δ_ℓ and inelasticity η_ℓ as:

$$S(k) = \eta_\ell(k) e^{2i\delta_\ell(k)} \,. \tag{4.43}$$

The invariant scattering amplitude can be represented using the phase shift parameterization as follows:

$$\mathcal{M}_\ell(k) = F(k) \left(\frac{1}{\cot \delta_\ell(k) - i} \right), \tag{4.44}$$

where the singularities in the denominator of $\mathcal{M}_\ell(k)$ provide information about the angular momentum of the intermediate states. $F(k)$ is a form factor that represents the internal structure of the scattering particles and their coupling to the external field[2]. These singularities, which are known as poles, can be categorized into resonant states, anti-resonant states, bound states, and anti-bound states (virtual) based on their positions in the momentum/energy complex planes, as shown in Fig. 4.16.

Pole Structures Illustrated in Fig. 4.16:

- *Permissible Poles:*
  - Bound States: These correspond to particles with poles situated on the real energy axis of the physical sheet, positioned below the threshold ($s = (m_1 + m_2)^2$) marked by the red circles.
  - Virtual Bound States or Anti-Bound States: poles on the real axis of the unphysical sheet, lying beneath the threshold. These are marked by $\triangle$ in Fig. 4.16.
  - Poles situated above the threshold but positioned away from the real axis of the unphysical sheet are indicative of both Resonant Poles and Zeroes. They are symbolized by $\circ$ (4th quadrant) and $\square$ (1st quadrant) respectively in Fig. 4.16, occurring as complex conjugate pairs. Our primary focus is on resonant poles, which correspond to resonances and hold significant importance in the analysis of resonance phenomena in scattering experiments.

[2]The specific form of $F(k)$ depends on the details of the scattering system and the interaction under consideration. In general, $F(k)$ is a complex function of the momentum transfer k, which can be experimentally determined from measurements of the differential cross section or other observables

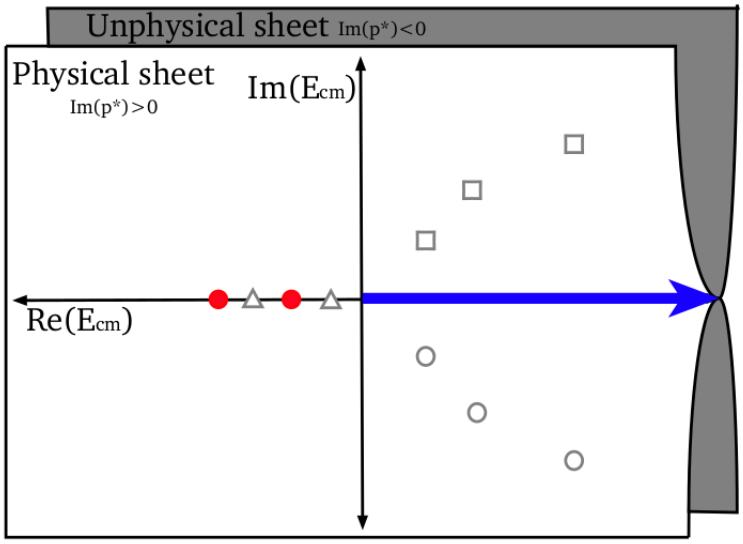

Figure 4.16: The different classifications of the S-matrix poles and their positions in the complex energy plane where the scattering states with real momentum and positive energy are shown by the blue solid arrows. The filled symbols represents the poles on the physical sheet. Figure from [84]

- *Prohibited Poles:*
  - Poles exceeding the threshold on the real axis of the physical sheet are disallowed due to their violation of unitarity.
  - Poles situated off the real axis of the physical sheet contravene causality and are therefore not permitted.

General form of the N-coupled channel S-matrix

The S-matrix element for a single channel can be expressed using the Jost function as

$$S(k) = e^{2i\delta_\ell(k)} = \frac{d(-k)}{d(k)}\,. \tag{4.45}$$

The S function can be parameterized in terms of poles at k_j and zeroes at $-k_j$ (which correspond to zeroes of $d(k)$ and $d(-k)$, respectively).

$$d(k) = \prod_{j=1}^{n}(k-k_j)(k+k_j^*) = \prod_{j=1}^{n}|d(k)|e^{i\alpha}e^{i\beta}\,, \tag{4.46}$$

$$d(-k) = \prod_{j=1}^{n}(k+k_j)(k-k_j^*) = \prod_{j=1}^{n}|d(k)|e^{i\gamma}e^{i\omega}\,. \tag{4.47}$$

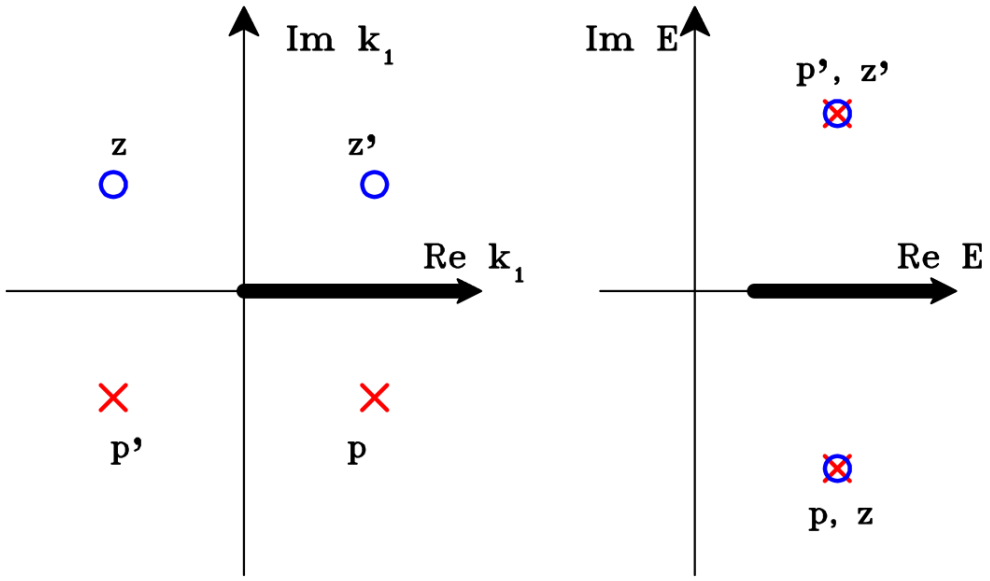

Figure 4.17: One channel poles i.e. p and p' and zeroes i.e. z and z' in both complex momentum and energy planes. Figure from [85]

In the above equations, the index j ranges from 1 to n, which corresponds to the number of poles being investigated. The second component of $d(\pm k)$ in Eq.(4.47) is introduced to satisfy the unitarity constraint of the S-matrix, which is why one resonance has two poles and two zeroes, as illustrated in Fig. 4.17. The phase shifts corresponding to the poles and zeroes may be easily calculated for $k_j = a + ib$ using angle $= \arctan\left(\frac{-b}{k-a}\right)$. Therefore, the total phase shift can be expressed as:

$$\delta = \left(\frac{-\alpha - \beta + \gamma + \omega}{2}\right), \tag{4.48}$$

due to the symmetry of poles and zeroes.

The Riemann sheets of the S-matrix are labeled with numbers corresponding to the imaginary sign of the channel momenta. In systems with N-coupled channels, a total of 2^N Riemann sheets exist. For each matrix element S_{ij} where $(i, j = 1, 2, ..., N)$, two cuts are present: a right-hand cut originating from the threshold on the real energy axis of the relevant channel, and a left-hand cut representing the crossed channels. Resonances are associated with poles and zeros located on these Riemann sheets as shown in Fig. 4.18. Analytic continuation formulas of coupled process matrix elements to the unphysical sheets of the Riemann surface provide a representation for these resonances [86]. The diagonal elements of the

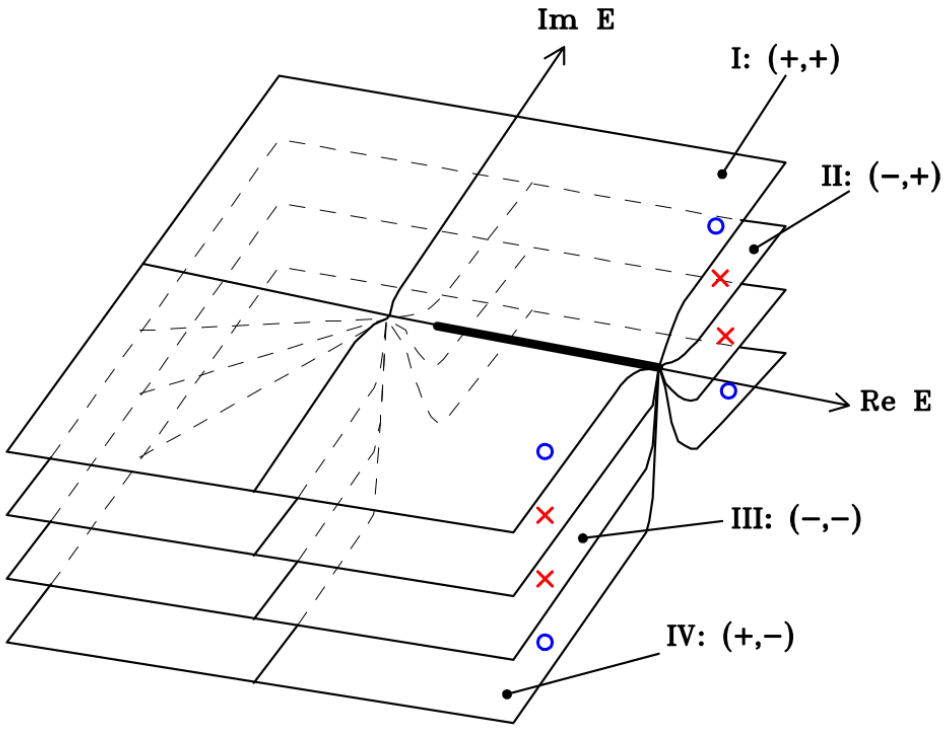

Figure 4.18: The four Riemann sheets of two channels. Figure from [85]

S-matrix of the N-coupled channels case are given by:

$$S_{ii} = \frac{d(k_1, .., k_{i-1}; -k_i, ..., k_{i+1}, ..., k_N)}{d(k_1, ..., k_N)}\,, \tag{4.49}$$

whereas the non-diagonal elements can be calculated using the following expression:

$$S_{ii}S_{jj} - S_{ij}^2 = \frac{d(k_1, .., k_{i-1}, -k_i, ..., k_{i+1}, k_{j-1}, -k_j, k_{j+1}, k_N)}{d(k_1, ..., k_N)}\,. \tag{4.50}$$

The Jost function $d(k)$ can be decomposed into two components: $d_{res}(k)$, representing the resonant part, and $d_{bgr}(k)$, representing the background part corresponding to neglected channels and resonances.

Chapter 5

P-wave elastic scattering analysis

Within this chapter, a comprehensive reexamination of historical data relating to $\pi\pi$ scattering has been carried out. Specifically, the focus has been on the elastic phase shifts and inelasticities up to an energy threshold of approximately 2 GeV. The central objective of this investigation is to shed light on the status of higher vector ρ excitations, particularly the ρ'. To achieve this purpose, an analytical model has been employed – a well-established three-channel S-matrix parametrization, as expounded in section 2.1. This model provides a clear representation of the complex pole locations of numerous ρ resonances, employing extended Breit-Wigner-type expressions. Moreover, the preservation of convenient crossing symmetry has been addressed by minimizing disparities between experimental and theoretical real amplitude components derived from dispersion relations, as detailed in section 5.2. The units employed throughout this analytical endeavor are in terms of energy/mass and expressed in MeV.
The analysis presented in this chapter has been published in September 2020 [87].

5.1 Introduction

The introductory section's discourse underscores the importance of achieving a more profound grasp of the masses attributed to ρ' and $K^{\star\prime}$ particles. The paradigms of quark models, underpinned by the conventional Coulomb-plus-linear interquark potential, propose an escalation in radial splittings for lighter quarks, concomitant with a dynamically evolving strong coupling constant in the Coulombic component [88]. Consequently, if the ρ' mass were to deviate considerably from the predictions established by models such as GI and similar counterparts, it would pose a formidable challenge to these theoretical frameworks. Hence, the ongoing exploration of these particles, coupled with the amelioration of our comprehension of their characteristics, remains a primary task.

The exact mass determination of a broad resonance, like ρ', significantly relies on the manner in which pertinent scattering data are treated. Notably, the conventional employment of Breit-Wigner (BW) parametrizations can render results uncertain, potentially leading to variations on the order of 10 MeV for $\rho(770)$ and surpassing 100 MeV for ρ' [89]. This

discrepancy could, to some extent, emanate from the intricacies of attaining unitarity in multi-BW parametrizations, particularly within the ambit of profoundly inelastic processes entailing ρ'.

Furthermore, the traditional static methodology applied to mesonic resonances in most quark models often treats them as stable composite states comprised of a quark and an antiquark. However, the potential impact of coupled-channel effects stemming from meson loops can be substantial. Illustratively, the unitarized multichannel quark model expounded in [90] underscores the influence of interconnected channels on the ρ' mass. This model effectively mitigates a bare mass of 1.48 GeV by approximately 190 MeV, yielding a realized mass of 1.29 GeV. It is important to note that the utilization of different confinement interactions within this model raises inquiries regarding the universality of unitarization effects in the realm of widely employed quark models. Furthermore, substantial shifts in mass may emerge within ground states and higher radial excitations, necessitating a comprehensive parameter recalibration upon the unitarization of any given model.

Recent insights from lattice-QCD simulations have further enriched the understanding of such topics. An unquenched simulation centered on antiquark interpolators exclusively culminated in a genuinely representative spectrum in [91], facilitating estimations of light and strange hadron masses. The primary radial excitation of $K^\star(892)$ was appraised to slightly surpass 1.6 GeV. In a complementary vein, the same lattice collaboration probed P-wave $K\pi$ scattering through the deployment of both quark-antiquark and meson-meson interpolators in [92]. Employing Lüscher's technique [93], discrete energy levels were discerned and subsequently utilized to derive $K\pi$ phase shifts for diverse lattice dimensions. Upon extrapolation to the actual pion mass, the inferred phases exhibited commendable agreement with empirical data, encompassing not only the $K^\star(892)$ mass but also its width. Notably, the revelation emerged that the initial radial excitation of $K^\star(892)$ exhibited a mass of $1.33\pm$ 0.02 GeV, notably lower by approximately 300 MeV than the earlier lattice simulation devoid of meson-meson interpolators. It is worth acknowledging that this computational approximation hinges on the portrayal of solely the $K\pi$ decay channel and, as such, treats the $K^{\star\prime}$ as a purely elastic resonance. The overarching significance of embracing unitarity as a pivotal aspect for achieving quantitatively precise spectroscopic outcomes is emphatically emphasized.

5.1.1 Channels of interest

The most recent confirmation of the $\rho(1250)$ resonance was achieved in [94] through a dispersive analysis of amplitudes in three interconnected P-wave decay channels. This analysis incorporated a built-in crossing-symmetry requirement within the $\pi\pi$ channel. This validation is strongly supported by both physical and mathematical considerations. In this investigation, the chosen channels were selected to replicate the main two-body decay processes of ρ excitations.

Alongside the $\pi\pi$ channel, which was a robust candidate for inclusion in the analysis due to the wealth of experimental data on phase shifts and inelasticities, two additional efficient channels were considered. The higher ρ resonances possess numerous observable

decay routes, which cannot be comprehensively accounted for using the S-matrix method due to the increasing complexity of Riemann sheets and complex poles. Consequently, for the higher ρ excitations, the decay modes listed in the PDG [81], channel couplings, and $\pi\pi$ phase shifts were closely examined to select the two supplementary channels from the multiple potential decay paths.

For the PDG entry $\rho(1450)$, the following modes were identified: $a_1(1260)\pi$, $h_1(1170)\pi$, $\pi(1300)\pi$, and $\rho(2\pi)$ in the S-wave configuration. All of these were encompassed in the 4π decays. Moreover, the first three channels primarily led to $\rho\pi$ decay, resulting in three relatively close decay channels for an excited ρ vector state. Consequently, all these channels yielded a quasifinal state of $\rho 2\pi$, with 4π serving as the ultimate final state. In contrast, the fourth decay channel, $\rho(2\pi)$ in the S-wave configuration, was dominated by the $f_0(500)$ resonance. To simulate these decays, a single $\rho 2\pi$ channel with a threshold of 1055 MeV was introduced. Despite the central thresholds for the aforementioned four channels being 195-385 MeV higher [81], considering the notably broad nature of the relevant resonances, opening the effective channel at the $\rho 2\pi$ threshold seemed appropriate.

Regarding the third effective channel in this study, it is observed that an isovector vector state strongly couples to a P-wave state through spin, isospin, and orbital angular momentum recoupling coefficients. The $\rho\rho$ decay mode is prominent among the $\rho 2\pi$ decays in the PDG $\rho(1700)$ entry, alongside the previously mentioned $a_1(1260)\pi$, $h_1(1170)\pi$, and $\pi(1300)\pi$ modes. While the PDG indicates a $\rho\rho$ threshold of 1550 MeV, a threshold value of 1512 MeV was reported in [95] through fitting P-wave phase shifts. This latter value is adopted as the threshold in this analysis, justifying the decision to open this channel at a lower energy level. Therefore, $\rho\rho$ is considered a more suitable designation for the third effective decay channel, replacing the previous $\rho\sigma$ designation used in [95, 96].

These three channels were previously examined in [95, 94, 96]. However, when investigating $\rho(1250)$ decays, particular attention must be paid to the $\omega\rho$ decay mechanism observed in various experiments [81]. As a result, two analyses will be conducted: the first utilizing the three channels $\pi\pi$, $\rho 2\pi$, and $\rho\rho$, and the second substituting the $\rho 2\pi$ channel with the $\omega\pi$ channel and setting the threshold at 922 MeV by fitting it to the data, leading to a more comprehensive assessment.

5.2 Methodology

The investigation involves a comprehensive examination of the S-matrix poles of various resonances on distinct Riemann sheets of the complex energy plane. The determination of the complex pole positions is achieved by fitting the amplitude's free parameters to the experimental data and the dispersion relations known as GKPY equations [97]. This results in model-independent outcomes. Furthermore, as the pole locations are established directly in the fits, the search for poles by analytically extending the amplitudes into the complex energy or momentum plane is not required. As a result, full unitary and analytical amplitudes

are utilized, which can be expressed as:

$$A_{ij}(s) = \frac{1}{2i}\frac{S_{ij}(s) - \delta_{ij}}{1 - \frac{4m_\pi^2}{s}}\,, \tag{5.1}$$

where s is the effective two-pion mass squared, S_{ij} denotes the S-matrix elements as mentioned before and δ_{ij} represents the Kronecker delta. Thus, in the case of the $\pi\pi$ channel, such an element reads

$$S_{11}(s) = \eta_{11}(s)e^{2i\delta_{11}(s)}\,, \tag{5.2}$$

with phase shift and inelasticity denoted by δ_{11} and η_{11} respectively.

In Section 4.7, it was mentioned that in the case of three coupled channels, the possible locations of poles are spread over eight Riemann sheets. To simplify this eight-sheeted Riemann surface, a uniformizing variable w is introduced, which can be expressed as:

$$w = \frac{\sqrt{s - s_2} + \sqrt{s - s_3}}{\sqrt{s_3 - s_2}}\,, \tag{5.3}$$

where s_2 and s_3 are the thresholds of the second and third channel, i.e. $\rho 2\pi$ and $\rho\rho$ respectively. The resonant pole can be determined using the following expression:

$$\sqrt{s_r} = E_r - i\frac{\Gamma_r}{2}\,, \tag{5.4}$$

with E_r as the resonance mass and Γ_r its full width.
So for $s = s_r$:

$$w_r = \frac{\sqrt{s_r - s_2} + \sqrt{s_r - s_3}}{\sqrt{s_3 - s_2}}\,. \tag{5.5}$$

Elements of an S-matrix are expressed as follows:

$$S = S^{res}S^{bgr}\,, \tag{5.6}$$

where S^{res} and S^{bgr} represents the resonant and background parts of the S-matrix respectively, and the $\pi\pi$ channel S-matrix element reads:

$$S_{11} = S_{11}^{res}S_{11}^{bgr} = \frac{d_{res}^*(-w^*)}{d_{res}(w)}\frac{d_{bgr}(-k_1, k_2, k_3)}{d_{bgr}(k_1, k_2, k_3)}\,, \tag{5.7}$$

note that d_{res} encodes all the dynamics of the interacting particles, both in individual channels and between them. The momenta in a given channel will be denoted by k_i, where k_1 represents the first channel which is $\pi\pi$, k_2 represents the second channel $\rho 2\pi$, and so on. The resonance contributions S^{res} are defined as:

$$d_{res}(w) = w^{\frac{-M}{2}}\prod_{r=1}^{M}(w + w_r^*)\,, \tag{5.8}$$

where M is the number of all poles. The background Jost function has the form:

$$d_{bgr}(k_1) = \exp\left[2ia - 2b\left(\frac{k_1}{m_1}\right)^3 \Theta(s, s_2)\right], \tag{5.9}$$

the mathematical framework outlined above involves the utilization of the Heaviside function $\Theta(s, s_2)$, which takes a value of 1 when $s \geq s_2$ and 0 when $s < s_2$, where s and s_2 are real numbers. Additionally, real numbers a and b are used in the framework. This entire mathematical approach was published in the research conducted by [95, 94], wherein the poles that correspond to a specific resonance and lie on distinct Riemann sheets were categorized into clusters. As mentioned in sec. 4.7 Riemann sheets are numbered according to the signs of the imaginary components of the momenta. As a result, the eight Riemann sheets of the studied three channels are numbered as: I $(+,+,+)$, II $(-,+,+)$, III $(-,-,+)$, IV $(+,-,+)$, V $(+,-,-)$, VI $(-,-,-)$, VII $(-,+,-)$ and VIII $(+,+,-)$.

Fits to data for phase shifts and inelasticities in the $\pi\pi$ channel below 2 GeV [95] revealed five resonances lying on different Riemann sheets, namely $\rho(770)$, $\rho(1250)$, $\rho(1450)$, $\rho(1600)$, and $\rho(1800)$.
These amplitudes were employed in association with three significant modifications in [94, 96]:

1. Removing the limits on pole movement as a function of channel coupling, resulting in large variations in pole locations for two of them, connected with the $\rho(770)$ cluster. These locations change by several hundred MeV, leading to extremely tiny phase shifts and inelasticity, as expected from a weak background. These would be referred to as "background poles". Two other $\rho(770)$ poles and all of the higher ρ states move by merely a few MeV or less.

2. Applying a threshold expansion with four parameters below 640 MeV.

3. The measured amplitudes in S, P, D, and F waves were restricted by satisfying crossing symmetry (which is briefly introduced in sec. 2.1.2) in the $\pi\pi$ channel up to roughly 1100 MeV. This was done by incorporating a χ^2_{CS} component in χ^2_{Total} which corresponds to the specified crossing symmetry (CS):

$$\chi^2_{\text{CS}} = \sum_i^N \frac{[\mathfrak{Re}A^{(\text{in})}(E_i) - \mathfrak{Re}A^{(\text{out})}(E_i)]^2}{\epsilon}. \tag{5.10}$$

The terms presented in Eq. (5.10) can be explored in greater detail:

- $N = 26$ represents the number of the chosen energies between the $\pi\pi$ threshold and 1100 MeV at which χ^2_{CS} is calculated,

- ϵ is normalization constant and is fixed at 0.01 in order to make the size of χ^2_{CS} comparable with χ^2_{data}, the other component of χ^2_{Tot}.

- $\mathfrak{Re}A^{(\text{in})}(E)$ corresponds to the real part of the amplitude used in the fitting of the data and the GKPY equations.
- $\mathfrak{Re}A^{(\text{out})}(E)$ is the same quantity to be calculated through the dispersion relation, as follows:

$$\mathfrak{Re}A_{\ell}^{I(\text{out})}(s) = \sum_{I'=0}^{2} C_{st}^{II'} a_0^{I'} + \sum_{I'=0}^{2}\sum_{\ell'=0}^{4} \int\!\!\!\!\!\!-_{4m_\pi^2}^{\infty} ds'\, K_{\ell\ell'}^{II'}(s,s')\, \mathfrak{Im}A_{\ell'}^{I'(\text{in})}(s') + d_{\ell}^{I}(s)\,. \tag{5.11}$$

Where

- $C_{st}^{II'}$ represents the crossing matrix between the $\pi\pi$ channels with isospin I and I',
- $a_0^{I'}$ is the S-wave scattering length vector for isospin I',
- $K_{\ell\ell'}^{II'}(s,s')$ are the kernels associated with once-subtracted dispersion relations with enforced crossing symmetry.

The first term of Eq. (5.11) called the "Subtraction term" in which it is a linear combination of the S-wave scattering length. While the second term is denoted by the "Kernel term" in which they are constructed for the partial wave projected amplitudes with $s \longleftrightarrow t$ crossing symmetry condition. Finally the third term called the "Driving term" in which they have the same structure as the second term except the fact that they are not related to the phenomenological input amplitude $A_{\ell'}^{I'(\text{in})}(s')$. The driving term is determined by Regge parametrization. Additionally, these dispersion relations create considerably less uncertainties in the calculated real parts of the amplitudes from Eq. (5.11) than the well-known Roy [98] dispersion relations with two subtractions, as proved in [97]. In reality, the integrals in Eq. (5.11) are performed from the threshold up to around 2 GeV because data at higher energies are absent and so-called driving terms are utilized thereabove.
Although the amplitudes yield inaccurate $\pi\pi$ scattering lengths in [95], resulting in poor threshold behavior, this did not prohibit getting very acceptable findings for the resonance pole locations of the distinct ρ mesons for lying much beyond the threshold. Whereas, the fits to the GKPY in [94, 96] are heavily reliant on the amplitude's threshold behavior (i.e. the threshold behavior of the amplitude became extremely relevant) as the integrals in Eq. (5.11) begin at threshold and the amplitudes there are least restricted by the kernels'[1] dependency on s.
To improve the amplitudes near-threshold behavior in [95], a polynomial was introduced below 640 MeV by modifying the original amplitudes in Eqs. (5.7)→(5.9) based on fits to the data and the GKPY equations, as discussed earlier in point 2. This polynomial is a generalized expansion in pion momentum k powers, specifically designed for near-threshold calculations for both $S0$ and $P1$ wave amplitudes.

$$\mathfrak{Re}A(s) = \frac{\sqrt{s}}{4k}\sin 2\delta = m_\pi k^2\left[a + bk^2 + ck^4 + dk^6 + O(k^8)\right]\,. \tag{5.12}$$

[1] for explicit formulae of the kernels, see the Appendix of Ref. [97]

In this study, the parameters a and b, commonly known as the scattering length and effective range, respectively, were employed. These parameters are referred to as the slope parameter and can be established or tailored to suit the data and dispersion relations. For the purpose of this calculation, a^2 was fixed at 0.0381 m_π^{-3} and b^3at 0.00523 m_π^{-5}. These particular values were chosen based on previous experimental data and theoretical calculations, and were further optimized through a fit to the data and dispersion relations to obtain the best possible agreement with the observed phase shifts. Furthermore, the values of c and d were permitted to vary during the fitting process for the data and GKPY equations. These parameters were employed to seamlessly integrate the polynomial-derived phase shifts, including their values and first derivatives, with the multichannel phase shifts defined by Eqs. (5.7)→(5.9). To achieve this, a matching energy of roughly 640 MeV was utilized, which was determined by fitting the free matching energy parameters for both the S and P waves to the phase shifts. The optimal value of 640 MeV was discovered to provide the most satisfactory description of the P wave data and is still lower than the pole mass of the $\rho(770)$, indicating that the effective range approximation may be employed. The $\pi\pi$ P-wave is therefore concurrently fitted to the dispersion relations and the experimental data. The $\chi^2_{\rm Total}$ is defined by:

$$\chi^2_{\rm Total} = \chi^2_{\rm CS} + \chi^2_{\rm Data}\,, \tag{5.13}$$

where $\chi^2_{\rm CS}$ defined in Eq. (5.10) includes input from all 6 important partial waves (JI: $S0$, $S2$, $P1$, $D0$, $D2$ and $F1$) while $\chi^2_{\rm Data}$ contains only phase-shifts and inelasticities of the $P1$-wave (will be denoted by P-wave) as follows:

$$\chi^2_{\rm Data} = \sum_{i=1}^{N^\ell_\delta} \frac{(\delta_i^{\rm exp} - \delta_i^{\rm th})^2}{(\Delta\delta_i^{\rm exp})^2} + \sum_{i=1}^{N^\ell_\eta} \frac{(\eta_i^{\rm exp} - \eta_i^{\rm th})^2}{(\Delta\eta_i^{\rm exp})^2}\,. \tag{5.14}$$

Where $\delta_i^{\rm exp}$ and $\delta_i^{\rm th}$ are the phase shifts experimental and theoretical (calculated) values in the considered channel of the different waves respectively. Similarly for $\eta_i^{\rm exp}$ and $\eta_i^{\rm th}$ which denotes the experimental and calculated inelasticity values. All the changes observed during the fits in $\mathfrak{Re}A_\ell^{I({\rm out})}(s)$ in Eq. (5.11) are caused by only modifying the P-wave.
The maximum number of the free parameters was set to be 50, and they can be demonstrated as:

- mass and width of all poles that contributes to each resonance of the P wave:
  - 8 parameters for $\rho(770)$,
  - 16 parameters for $\rho(1250)$,
  - 8 parameters for $\rho(1450)$,

[2]The scattering length a characterizes the low-energy behavior of the scattering process and describes the effective range of the interaction between particles. Previous experimental data and theoretical calculations have established the value of a for pion-pion scattering to be around 0.1 m_π^{-3}.

[3]The effective range b describes the short-range behavior of the interaction and is related to the curvature of the phase shift. The value of b is typically much smaller than that of a.

- 8 parameters for $\rho(1600)$,
- 8 parameters for $\rho(1800)$,

- the matching energy,
- the background parameter of Eq. (5.9) a, while the other parameter b was fixed at -0.85×10^{-4} to avoid violating unitarity above 1700 MeV for inelastisities.

The fitting process was conducted successively with an increasing number of free parameters to prevent convergence to local minima, rather than the global minimum. Subsequently, a detailed description of the fitting methods employed in this study is given below.

- First step: only matching energy, background parameter and $\rho(770)$ i.e 10 free parameters,
- Second step: like in the 1^{st} step plus $\rho(1250)$ i.e. 26 free parameters,
- Third step: like in the 2^{nd} step plus $\rho(1450)$ i.e. 34 free parameters,
- Fourth step: like in the 3^{rd} step plus $\rho(1600)$ i.e 42 free parameters,
- Fifth step: like in the 4^{th} step plus $\rho(1800)$ i.e. 50 parameters.

In this study, the fits were performed at each step with a changing number and value of the new pole's starting parameters. In each stage, the fitted parameters served as the starting parameters for the following step. The matching energy and background parameter a were also taken at varied beginning values in the first phase. The overall number of parameters used and their corresponding numbers for each resonance were the least, resulting in satisfactory values of χ^2_{Total}. However, further increasing their number no longer resulted in a noticeably better χ^2_{Total}.

As previously mentioned, in addition to the discussed $\rho 2\pi$ channel decay mode, there is another significant mode, $\omega\pi$, classified in the PDG [81] under $\rho(1450)$ and $\rho(1700)$ entries with resonance mass ranges of 1250–1624MeV and 1550–1800 MeV, respectively. Therefore, the study was rerun using the $\omega\pi$ instead of the $\rho\pi$, dropping the threshold value to 922 MeV from 1055 MeV. The fits to the experimental data and the GKPY equations were repeated, resulting in only slight variations in the masses of all resonances (i.e., the real parts of the poles), which were observed to be $\rho(770)$ by +0.1MeV, $\rho(1250)$ by +9.7MeV, $\rho(1450)$ by +6.5MeV, $\rho(1600)$ by +2.4MeV, and $\rho(1800)$ by -7.5MeV. However, the quality of the fits, as indicated by the values of χ^2, was nearly identical, as shown in Table5.1, indicating the stability and reliability of the obtained results. Note that the number of degrees of freedom (n.d.f) in the fits was 297 i.e.

$$\begin{aligned}(\text{n.d.f.}) &= \text{Exp. data points} + \text{ D.R. energy points} - \text{free parameters} \\ &= 191 + (6 \times 26) - 50\,. \end{aligned} \tag{5.15}$$

channel	χ^2_{total}	$\chi^2_{total}/n.d.f$	χ^2_{Data}	χ^2_{CS}
$\rho 2\pi$	403.1	1.357	294.1	109.0
$\omega\pi$	406.4	1.368	296.0	110.4

Table 5.1: Values of χ^2 for the fits with different second channel.

The expression 6×26 indicates that there are 6 partial waves with 26 energies each. The discussion was resumed with the consideration of $\rho 2\pi$ as the second channel. The adjustments made previously ensured that the amplitude satisfied the crossing-symmetry criterion from the threshold up to approximately 1100 MeV, while also maintaining its unitary and analytic character. The resulting modified amplitude was then used to fit the data in [94] as well as the GKPY equations, resulting in a set of pole clusters. Table 5.2 presents the resonance poles, which have the greatest influence on the overall amplitude, obtained from these pole clusters. In order to consider the impact of all higher ρ resonances that were not included in

Resonance	Riemann Sheet	E_r , $\Gamma_r/2$ (MeV)
$\rho(770)$	II	765.2 ± 0.4 , 73.1 ± 0.3
$\rho(1250)$	III	1264.1 ± 33 , 146.7 ± 12
$\rho(1450)$	III	1424.7 ± 26 , 104.9 ± 24
$\rho(1600)$	IV	1595.1 ± 5 , 69.5 ± 4
$\rho(1800)$	VI	1779.2 ± 14 , 121.9 ± 16

Table 5.2: Pole positions on various Riemann sheets, for $\sqrt{s_r} = E_r - i\Gamma_r/2$, of the unitary amplitude fitted to experimental data and GKPY equations.

$d_{res}(w)$ of Eq.(5.8), the background introduced in Eq.(5.9) was fitted to the data as well as the GKPY equations. The obtained results consisted of a constant with a relatively small phase shift of about 20°, and small inelasticity with a smooth increase (see Figs. 5.2 and 5.4).

5.3 Results and Discussion

The results presented in Figs. 5.1→5.5 are based on the fits carried out in [94, 96].

Discussion:

- **Figure 5.1:**
  From a thorough examination of both Fig.5.1 and Table5.1, it becomes apparent that the fitted curves closely replicate the experimental data, taking into account the phase shift errors, over the relevant energy ranges, up to approximately 2 GeV. It should be noted that the experimental data used for the phase shifts were obtained from[99, 100, 101, 102, 103, 104], while those for the inelasticity were taken from [99, 100, 101, 102, 104].

- **Figure 5.2:**
  Figure 5.2 clearly shows that $\rho(770)$ has the largest impact on the overall phase shift, as expected. The contributions from the ρ excitations are overpowered by $\rho(770)$. The second most influential resonance is $\rho(1250)$, while $\rho(1450)$ has the least effect. The plot effectively conveys the relative strengths of the different resonances in shaping the phase shift. It is worth noting that the expected threshold behavior, predicted by a polynomial with constant scattering length and effective range, is only observed in the overall phase shift and not in the individual resonances.

- **Figure 5.3:**
  In this figure, it is evident that $\rho(1250)$ has a greater impact than $\rho(1450)$, which is consistent with the previous analysis. The influence of $\rho(1250)$ is significant between 1.0 GeV and 1.5 GeV and is comparable to that of $\rho(1600)$ and $\rho(1800)$. On the other hand, the contribution of $\rho(1450)$ is relatively small throughout the entire energy range. This finding supports the previous conclusions about the importance of the different ρ resonances in the overall behavior of the amplitude.

- **Figure 5.4:**

  - One can observe by analyzing Fig. 5.4, that below 1.5 GeV i.e. near the $\rho\rho$ threshold the inelasticity of the $\rho(1250)$ amplitude considerably differs than 1, and that coupled with the part of the inelasticity due to the $\rho(770)$ nearly totally controls the inelasticity of the full amplitude.
    Between the $\rho 2\pi$ and $\rho\rho$ thresholds, contributions from $\rho(1450)$ and $\rho(1600)$ basically cancel each other out.
  - Above about 1.5 GeV, $\rho(1800)$ nearly fully controls the energy dependence of η, interfering with the still huge but already quite unstructured $\rho(1250)$ component equivalent in size to that of $\rho(770)$.
  - Above 1.5 GeV, the contribution of $\rho(1450)$ to η is negligible, also it exhibits a modest maximum at around 1.4 GeV, as predicted.

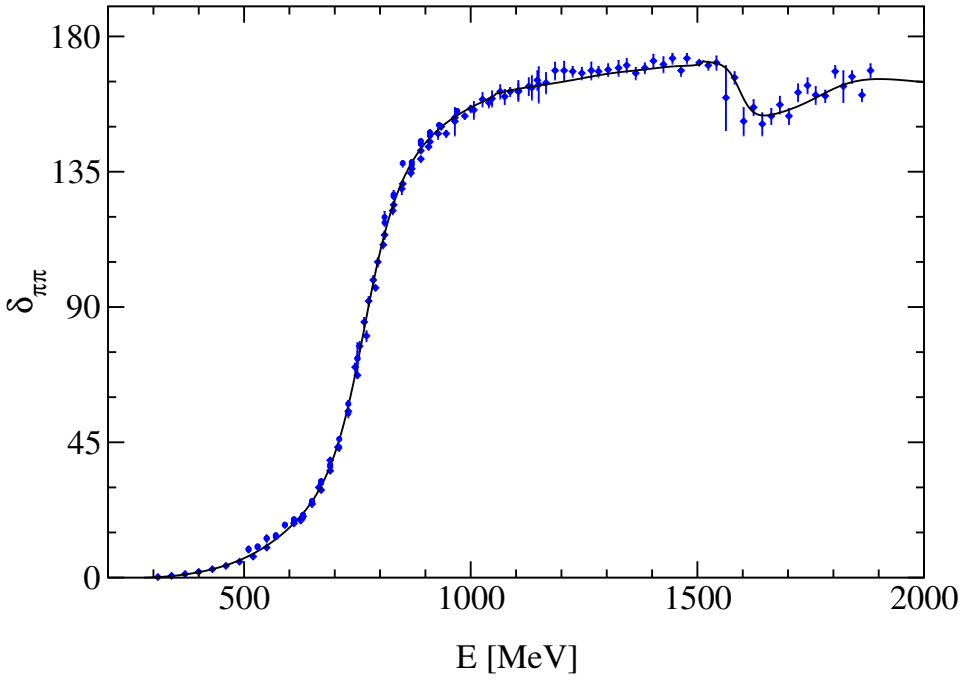

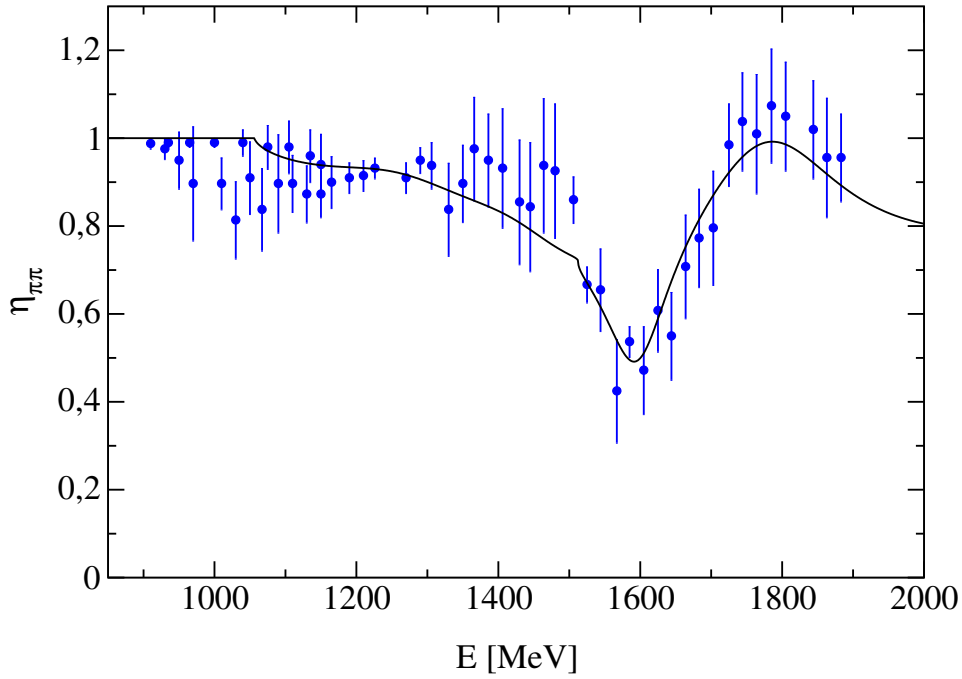

Figure 5.1: The $\pi\pi$ phase shifts and inelasticities fitted to the data and the GKPY dispersion relations.

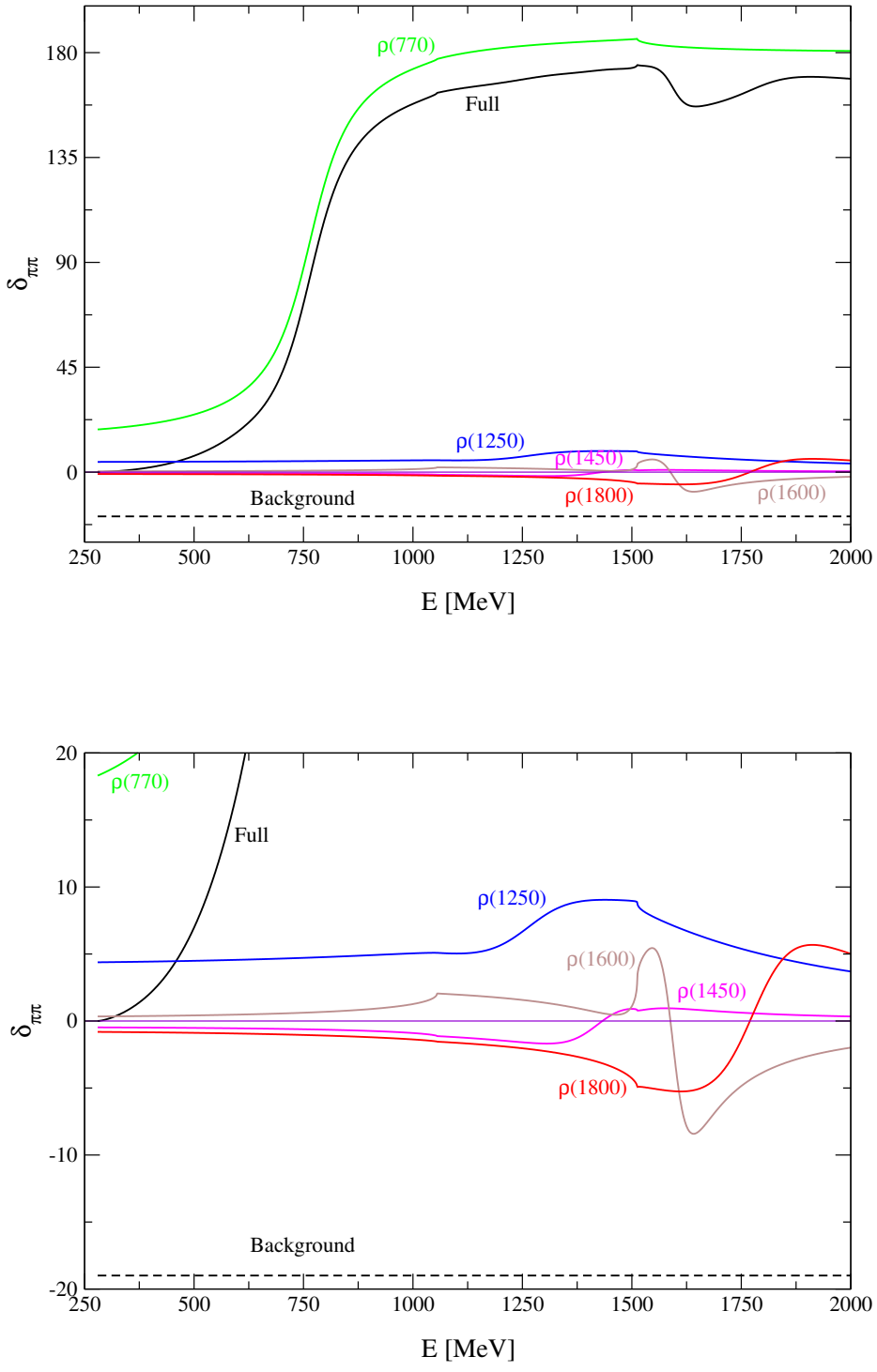

Figure 5.2: Upper figure: phase shift due to individual resonances, as well as full phase and background; lower figure: enlarged fragment from the upper figure.

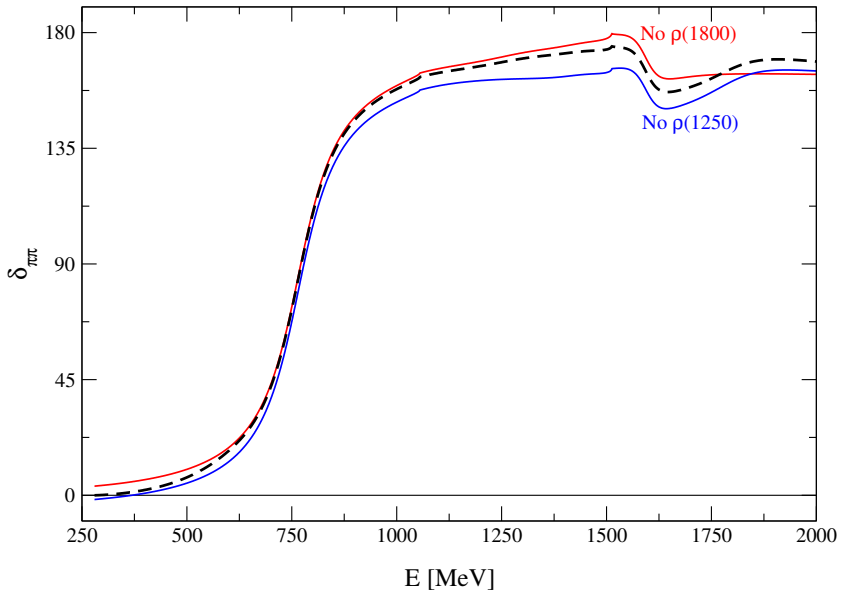

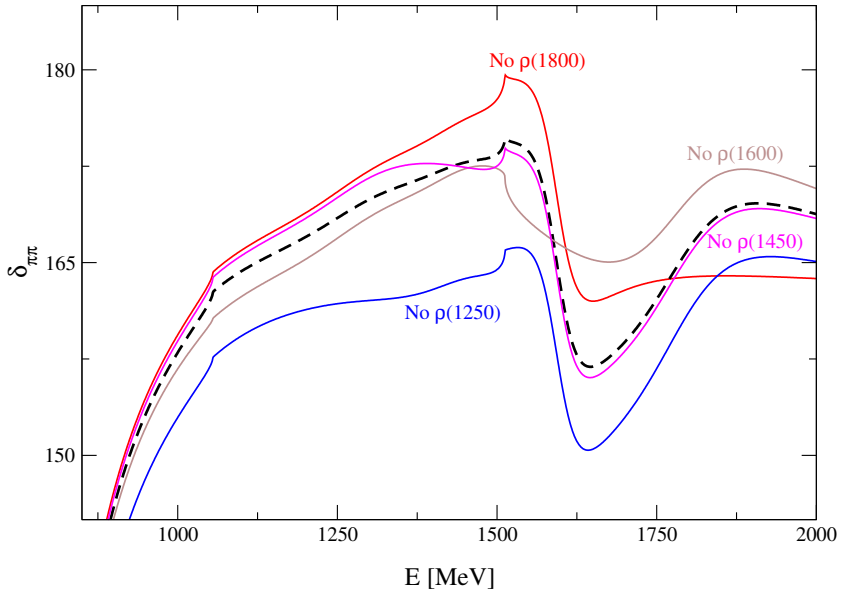

Figure 5.3: Upper figure: phase shift from full amplitude (dashed line) and the same but without $\rho(1250)$ and $\rho(1800)$; lower figure: as upper figure but enlarged over a reduced energy interval and also without $\rho(1450)$ and $\rho(1600)$.

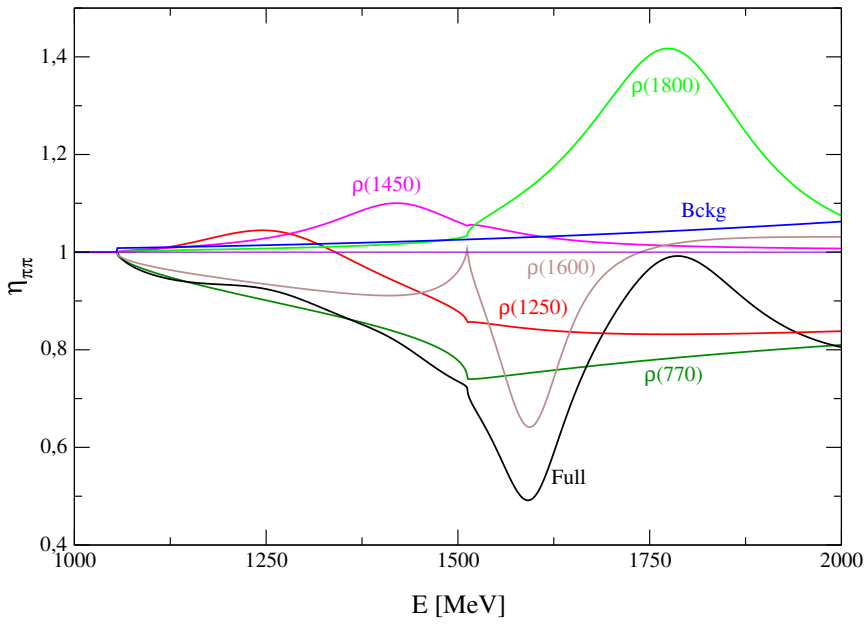

Figure 5.4: Inelasticity due to individual resonances, full amplitude, and background.

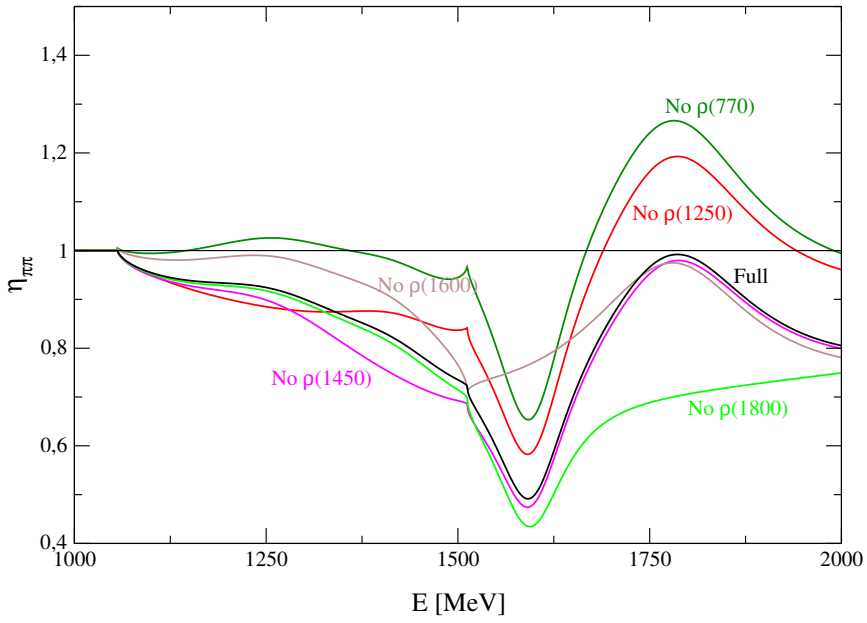

Figure 5.5: Inelasticity due to full amplitude and same without individual resonances.

- The considerable decline in complete inelasticity at roughly 1.6 GeV is mostly influenced by $\rho(1600)$, which occurs following the opening of the $\rho\rho$ channel. The background has a little part in the construction of η, resulting in a gradual and smooth ascent.

- **Figure 5.5:**
  In Fig.5.5, the inelasticity curve is shown after removing different ρ resonances from the amplitude. The largest shift is caused by eliminating $\rho(1250)$, followed by $\rho(770)$, compared to the curve generated by the entire amplitude. Omitting $\rho(1600)$ or $\rho(1800)$ results in a considerable change but only at 1600 MeV or above. Removing $\rho(1450)$ leads to only a slight shift in η over a narrow energy range below 1.5 GeV, with no impact on the form of the inelasticity curve. These findings demonstrate the varying contributions of the different ρ resonances to the behavior of the inelasticity curve.

5.4 Conclusion

The findings from the combined analysis provide compelling evidence for the inclusion of the ρ' resonance at approximately 1.26 GeV. Moreover, the stability of the fitted pole positions, as well as the demonstrated fulfillment of multichannel unitarity and optimal crossing symmetry, offer strong support for the reliability of the identified excited states, including those situated around 1.42 GeV, 1.60 GeV, and 1.78 GeV. In light of these results, it is recommended that $\rho(1250)$ be reinstated in the PDG tables as a distinct entry.

Chapter 6

Predictions for the $\omega\pi$ Channel

6.1 Introduction

The purpose of constructing and analyzing photoproduction amplitudes is to investigate resonances, specifically mesons, that appear in final state interactions. This analysis aims to complete and refine the spectroscopy of these states using the standard $q\bar{q}$ model or identify exotic states. To achieve this, it is essential to have amplitudes of final state interactions that are unitary and preferably available in multiple coupled channels across a wide range of effective mass.

In this chapter, the creation and analysis of such unitary amplitudes for interactions in three coupled channels in the P wave will be illustrated, spanning from the $\pi\pi$ threshold to approximately 1800 MeV. Referring back to the previous chapter, these channels will be $\pi\pi$, $\omega\pi$, and $\rho\rho$, and the analysis aims to:

1. Creating theoretical amplitudes that have not been experimentally tested in the $\omega\pi$ channel and analyzing their mass distributions while considering different positions of the $\rho(1450)$ meson (hereafter referred to as ρ').

2. Providing a fairly universal method that can be directly applied to various channels in the P wave, as well as adaptable to other partial waves.

In the future, the analysis described in point 1 will offer the opportunity to experimentally test the $\omega\pi$ amplitudes, providing irrefutable evidence of the true location of a pole of the amplitude associated with the ρ'.

However, calculating the $\omega\pi$ amplitudes is challenging due to the presence of at least two ρ mesons associated with several poles on different Riemann sheets [105, 87]. Additionally, this channel is coupled with other channels, such as the lower $\pi\pi$ and higher $\rho\rho$ channels, which further complicates the analysis. The latter is rather an effective channel representing basically several other channels that have thresholds around 1400-1600 MeV (e.g. $a_1(1260)\pi$, $\pi(1300)\pi$, $\eta\rho$). Nevertheless, by predicting the $\omega\pi$ phase shift and inelasticity, one can better understand the behavior of the scattering amplitude, which is a key quantity in describing

the photoproduction process. This can lead to more accurate predictions of the cross-sections and other observables that can be measured or extracted from experiments.

Furthermore, this analysis will help in identifying the resonances and their properties involved in the $\omega\pi$ photoproduction process. Such knowledge is fundamental for understanding the dynamics of strong interactions in the hadron spectrum and for testing different theoretical models.

The determination of amplitudes in all three aforementioned channels will be undertaken through the judicious employment of separable potentials featuring both non-relativistic and relativistic propagators. These potentials have been already successfully used many times as a valuable tool for studying, for example, the spectroscopy of scalar-isocalar mesons in the two coupled channels $\pi\pi$ and $K\bar{K}$ [106] as well as the three channels $\pi\pi$, $K\bar{K}$ and $2\pi2\pi$ [107]. They also work very well in the parameterization of two-body interactions in final states in heavy meson decays, where they replace the often used non-unitary isobar models [108] by one single unitary model.

The use of these potentials offers simplicity and requires a relatively small number of free parameters to describe multiple channels across a wide range of effective mass. For example, in the work on spectroscopy of scalar mesons [107], only 14 parameters were needed for three coupled channels in the energy range from the $\pi\pi$ threshold to 1800 MeV (representing four resonances). In contrast, unitarized isobar models would require more than 30 free parameters (including the number of poles on various Riemann sheets, multiplied by two for mass and width).

For further details on these potentials, refer to [106, 109]. The following sections will outline their most important general features and discuss their properties for the P wave in more detail.

6.2 Model of three coupled channels

The matrix of scattering amplitudes T satisfies a system of coupled Lippmann-Schwinger equations in the momentum space:

$$\langle \mathbf{p}| T |\mathbf{q}\rangle = \langle \mathbf{p}| V |\mathbf{q}\rangle + \int \frac{d\mathbf{u}}{(2\pi)^3} \langle \mathbf{p}| V |\mathbf{u}\rangle \langle \mathbf{u}| G |\mathbf{u}\rangle \langle \mathbf{u}| T |\mathbf{q}\rangle \ , \tag{6.1}$$

where, for the interactions considered here in three coupled channels, V and G are 3×3 matrices, that serve as the interaction (potential) matrix and the diagonal matrix of channel propagators respectively. Vectors $\mathbf{p}$, $\mathbf{q}$ and $\mathbf{u}$ are three-dimensional momenta ($\mathbf{u}$ is relative momentum between interacting particles in the center of mass). The diagonal matrix of these propagators is written as:

$$\langle \mathbf{u}| G_{\alpha\gamma} |\mathbf{u}\rangle = G_\alpha \delta_{\alpha\gamma} \quad (\text{where } \alpha, \gamma = 1, 2, 3 \text{ number the channels}) \, , \tag{6.2}$$

where

$$G_\alpha(E, \mathbf{u}) = \frac{1}{E_1(\mathbf{k}_\alpha) + E_2(\mathbf{k}_\alpha) - E_{\alpha 1}(\mathbf{u}) - E_{\alpha 2}(\mathbf{u}) + i\epsilon}, \quad \epsilon \to 0(+). \tag{6.3}$$

Here energy $E_l(\mathbf{k}_\alpha) = \sqrt{m_{\alpha l}^2 + \mathbf{k}_\alpha^2}$ ($l = 1, 2$ numbers the particles in given channel α) in relativistic approach and $E_l(\mathbf{k}_\alpha) = m_{\alpha l} + \frac{\mathbf{k}_\alpha^2}{2m_{\alpha l}}$ in nonrelativistic one[1] is the energy of a particle in given channel. The total energy of two interacting particles l is given by

$$E = 2E_\pi = E_\pi + E_\omega = 2E_\rho. \tag{6.4}$$

Energy $E_{\alpha l}(\mathbf{u}) = \sqrt{m_{\alpha l}^2 + \mathbf{u}^2}$ ($E_{\alpha l}(\mathbf{u}) = m_{\alpha l} + \frac{\mathbf{u}^2}{2m_{\alpha l}}$) is the energy of individual particle l with relative momentum $\mathbf{u}$ in a given two-body channel α. Of course for $\alpha = 1$ or 3 masses of interacting particles are identical so Eq. (6.3) reduces to

$$G_\alpha(E, \mathbf{u}) = \frac{1}{E - 2E_\alpha(\mathbf{u}) + i\epsilon}, \quad \epsilon \to 0(+)\,. \tag{6.5}$$

The on-shell momenta k_α in individual channels are connected with the total energy by

$$k_1 = \sqrt{\frac{E^2}{4} - m_\pi^2} \qquad (k_1 = \sqrt{2Em_\pi - 2m_\pi^2}),$$

$$k_2 = \frac{1}{2E}\sqrt{[E^2 - (m_\omega + m_\pi)^2][E^2 - (m_\omega - m_\pi)^2]} \quad (k_2 = \sqrt{\frac{2m_\omega m_\pi}{m_\omega + m_\pi}}\sqrt{E - m_\omega - m_\pi}),$$

$$k_3 = \sqrt{\frac{E^2}{4} - m_\rho^2} \qquad (k_3 = \sqrt{2Em_\rho - 2m_\rho^2}). \tag{6.6}$$

The general form of separable potential has the following form:

$$\langle \mathbf{p}|\, V_{\alpha\gamma}\, |\mathbf{q}\rangle = \sum_{j=1}^{n} \lambda_{\alpha\gamma,\,j}\; g_{\alpha,\,j}(\mathbf{p}) g_{\gamma,\,j}(\mathbf{q}), \quad \alpha, \gamma = 1, 2, 3\,, \tag{6.7}$$

where n is rank of the potential and $\lambda_{\alpha\gamma,\,j}$ are coupling constants in channels ($\alpha = \gamma$) and between channels ($\alpha \neq \gamma$).

Form factors that have the Yamaguchi form

$$g_{\alpha,\,j}(\mathbf{p}) = \sqrt{\frac{4\pi}{m_\alpha}} \frac{\mathbf{p}}{(\mathbf{p}^2 + (\beta_{\alpha,\,j})^2)^2}\,, \tag{6.8}$$

depend on the relative centre of mass meson momenta $\mathbf{p}$ in the final channel or $\mathbf{q}$ in the initial channel (see Eq. 6.1). Consequently, $\beta_{\alpha,\,j}$ are the range parameters and the reduced masses m_α are given as:

$$m_1 = \frac{m_\pi}{2}, \quad m_2 = \frac{m_\omega m_\pi}{m_\omega + m_\pi}, \quad m_3 = \frac{m_\rho}{2}\,. \tag{6.9}$$

As described in the upcoming section, in order to accurately represent the experimental data and generate a pole associated with ρ', it is necessary to use second-order potentials

[1]Hereafter expressions for approach with nonrelativistic propagator will be given in the text in paratheses

in the $\pi\pi$ and $\omega\pi$ channels. For a better distinction of indices in these potentials, in all subsequent formulas the index j will be numbered by a or b. In the channel $\rho\rho$ the first order potential is sufficient.

Thus the diagonal separable potentials for each channel are given as (for channel 3 the subscript j is unnecessary and has been omitted):

$$\begin{aligned}
\langle \mathbf{p}| \, V_{11} \, |\mathbf{q}\rangle &= \lambda_{11,a} g_{1,a}(p) g_{1,a}(q) + \lambda_{11,b} g_{1,b}(p) g_{1,b}(q), \\
\langle \mathbf{p}| \, V_{22} \, |\mathbf{q}\rangle &= \lambda_{22,a} g_{2,a}(p) g_{2,a}(q) + \lambda_{22,b} g_{2,b}(p) g_{2,b}(q), \\
\langle \mathbf{p}| \, V_{33} \, |\mathbf{q}\rangle &= \lambda_{33} g_3(p) g_3(q).
\end{aligned} \tag{6.10}$$

The transition potential matrix elements read (to indicate between which terms in the potentials of channels 1 and 2 there is a given coupling, the coupling constants are numbered with two indices $j = a, b$):

$$\begin{aligned}
\langle \mathbf{p}| \, V_{12} \, |\mathbf{q}\rangle &= \lambda_{12,aa} \; g_{1,a}(p) g_{2,a}(q) + \lambda_{12,bb} \; g_{1,b}(p) g_{2,b}(q) + \\
&\quad \lambda_{12,ab} \; g_{1,a}(p) g_{2,b}(q) + \lambda_{12,ba} \; g_{1,b}(p) g_{2,a}(q), \\
\langle \mathbf{p}| \, V_{13} \, |\mathbf{q}\rangle &= \lambda_{13,a} \; g_{1,a}(p) g_3(q) + \lambda_{13,b} \; g_{1,b}(p) g_3(q), \\
\langle \mathbf{p}| \, V_{23} \, |\mathbf{q}\rangle &= \lambda_{23,a} \; g_{2,a}(p) g_3(q) + \lambda_{23,b} \; g_{2,b}(p) g_3(q).
\end{aligned} \tag{6.11}$$

Following the formalism developed in [106, 110] the Jost function is defined as:

$$D(k_1, k_2, k_3) = det(\mathbf{1} - \boldsymbol{\lambda}\mathbf{I}), \tag{6.12}$$

where, in presented here analysis, $\boldsymbol{\lambda}$ is a symmetric 5×5 coupling constants matrix:

$$\boldsymbol{\lambda} = \begin{pmatrix}
\lambda_{11,a} & 0 & \lambda_{12,aa} & \lambda_{12,ab} & \lambda_{13,a} \\
0 & \lambda_{11,b} & \lambda_{12,ba} & \lambda_{12,bb} & \lambda_{13,b} \\
\lambda_{12,aa} & \lambda_{12,ba} & \lambda_{22,a} & 0 & \lambda_{23,a} \\
\lambda_{12,ab} & \lambda_{12,bb} & 0 & \lambda_{22,b} & \lambda_{23,b} \\
\lambda_{13,a} & \lambda_{13,b} & \lambda_{23,a} & \lambda_{23,b} & \lambda_3
\end{pmatrix} \tag{6.13}$$

and $\mathbf{I}$ is a symmetric 5×5 matrix

$$\mathbf{I} = \begin{pmatrix}
I_{1,aa} & I_{1,ab} & 0 & 0 & 0 \\
I_{1,ab} & I_{1,bb} & 0 & 0 & 0 \\
0 & 0 & I_{2,aa} & I_{2,ab} & 0 \\
0 & 0 & I_{2,ab} & I_{2,bb} & 0 \\
0 & 0 & 0 & 0 & I_3
\end{pmatrix} \tag{6.14}$$

consisting of the integrals:

$$I_{\alpha,ij}(k_\alpha) = \int \frac{d\mathbf{u}}{(2\pi)^3}\; g_{\alpha,i}(\mathbf{u})\; G_\alpha(E,\mathbf{u})\; g_{\alpha,\,j}(\mathbf{u}). \tag{6.15}$$

As in the previous expressions, here the symbol α represents the channel under consideration, while the variables i and j correspond to the specific second-order potential elements labeled as a and b, respectively. In the third channel, the explicit labeling of the potential elements is omitted when using integrals.

The form factors $g_{\alpha,i}(k_\alpha)$ appearing in the integral in the Eq. (6.15) and presented in the expresion (6.8), have a form different from that used to describe the interactions in a similar model for the S wave [106, 107, 110]. In the case of the P wave examined here, the denominator $(\mathbf{p}^2 + (\beta_{\alpha,\,j})^2)$ is squared and the numerator is multiplied by $\mathbf{p}$. The greater power in the denominator guarantees the convergence of the integrals 6.15 and the term in the numerator ensures the correct behavior of the amplitudes at the thresholds, which should be

$$\delta(k) = a_P k^3 + b_P k^5 + O(k^7), \tag{6.16}$$

where a_P is the $\pi\pi$ scattering length in the P-wave.

Model for the P wave presented here and defined by potentials (6.10),(6.11) and integrals (6.14) contains 18 parameters in total: 13 coupling constants $\lambda_{\alpha\gamma,\,j}$ and 5 parameters $\beta_{\alpha,\,j}$ For simplicity a dimensionless coupling constants in further calculations will be used:

$$\Lambda_{\alpha\alpha,\,j} = \frac{\lambda_{\alpha\alpha,\,j}}{2\,(\beta_{\alpha,\,j}\beta_{\alpha,\,j})^{5/2}}, \qquad \Lambda_{\alpha\gamma,\,ij} = \frac{\lambda_{\alpha\gamma,\,ij}}{2\,(\beta_{\alpha,\,i}\beta_{\gamma,\,j})^{5/2}}\,, \tag{6.17}$$

and the redefined integrals:

$$J_{\alpha,ij} = 2\,(\beta_{\alpha,\,i}\beta_{\alpha,\,j})^{5/2}\, I_{\alpha,ij}\,. \tag{6.18}$$

As previously mentioned in the preface of part two, the S-matrix elements $S_{\alpha\gamma}$ $(\alpha,\gamma = 1,2,3)$ can be written as a ratio of the same Jost functions but with different signs of some arguments in numerator and denominator, for example for the $\pi\pi$ channel it reads

$$S_{11} = \frac{D(-k_1,k_2,k_3)}{D(k_1,k_2,k_3)}. \tag{6.19}$$

Expressions for other elements can be found in [109]. The scattering matrix defined in this way satisfies the unitarity condition: $S^+S = 1$, which guarantees obtaining results without unnecessary contributions from e.g. the background, unnecessary interference between the amplitude components and which significantly increases the unambiguity and reliability of the results.

In Eq. (6.19), the full Jost function for three coupled channels is, in fact, a function of the product of three independent Jost functions that describe the dynamics in each channel separately, along with the Jost function $F(k_1,k_2,k_3)$ that describes the couplings between the channels:

$$D(k_1,k_2,k_3) = D_\pi(k_1)D_{\omega\pi}(k_2)D_\rho(k_3) - F(k_1,k_2,k_3)\,, \tag{6.20}$$

where

$$D_\pi(k_1) = 1 - \Lambda_{11,a} J_{1,aa}(k_1) - \Lambda_{11,b} J_{1,bb}(k_1) + \Lambda_{11,a}\Lambda_{11,b}\, d_1(k_1), \tag{6.21}$$

$$D_{\omega\pi}(k_2) = 1 - \Lambda_{22,a} J_{2,aa}(k_2) - \Lambda_{22,b} J_{2,bb}(k_2) + \Lambda_{22,a}\Lambda_{22,b}\, d_2(k_2), \tag{6.22}$$

$$D_\rho(k_3) = 1 - \Lambda_3 J_3(k_3), \tag{6.23}$$

and

$$d_\alpha(k_i) = J_{\alpha,aa} J_{\alpha,bb} - J^2_{\alpha,ab}\,. \tag{6.24}$$

All these Jost functions include all couplings within channels $\Lambda_{\alpha\alpha,j}$, between channels $\Lambda_{\alpha\gamma,ij}$, all the integrals $J_{\alpha,ij}$ and have a very long arithmetic form not presented in this thesis.[2]

All integrals in matrix (6.14) defined in Eq. (6.15) and redefined in Eq. (6.18) can be calculated analytically for nonrelativistic propagator. The analytical form of these integrals and their derivations are presented in Appendix E.

Integrals with relativistic propagator can be calculated analytically only for channels 1 and 3 where interacting particles have the same masses. Integrals for channel 2 with different masses m_ω and m_π have beed calculated numerically. Explicit expressions for the integrals in channels 1 and 3 and details of the method of calculating the integrals in channel 2 are presented in Appendix F

6.3 Analysis Method

According to the unitary condition of the scattering matrix S all matrix LB ~~element~~ elements can be parameterized in terms of the channel phase shift δ_α and inelasticity η_α. The simplest form have expressions for diagonal matrix elements:

$$S_{\alpha\alpha} = \eta_\alpha e^{2i\delta_\alpha}, \tag{6.25}$$

while others are determined by the unitarity condition. Thus, by definition of the S matrix in Eq. (6.19), δ_α and η_α can be directly related to all free potential parameters appearing in the Jost function $D(k_1, k_2, k_3)$.

In this analysis these parameters were fitted to the current experimental data on the $\pi\pi$ P-wave isovector phase shifts and inelasticity up to almost 1900 MeV. There is no data for interactions in the $\omega\pi$ and $\rho\rho$ channels, so the phase shifts and inelasticities in these channels were only determined theoretically. However, in order to impose greater constraints on the tested amplitudes (and thus better define them), limitations resulting from the occurrence of the ρ' resonance and the imposed, quite well-known, value of the scattering length in the $\pi\pi$ channel were introduced in the analysis. The fitting were performed using the χ^2 test and its components for the phase shitfs and inelasticites were of the form:

$$\chi^2_{\delta_j} = \sum_{l=1}^{N_\delta} \left| \frac{e^{2i\delta_j^{th}} - e^{2i\delta_j^{exp}}}{\Delta\delta_j} \right|^2, \tag{6.26}$$

[2]Available after prior inquiry to Nadine.Hammoud@ifj.edu.pl

$$\chi^2_{\eta_j} = \sum_{l=1}^{N_\eta} \left(\frac{\eta_j^{th} - \eta_j^{exp}}{\Delta\eta_j} \right)^2 . \tag{6.27}$$

Where δ_j, η_j are the phase shifts and inelasticity in channels $j = 1, 2, 3$ (in fits only $j = 1$), $\Delta\delta_j$, $\Delta\eta_j$ are the corresponding phase shifts and inelasticity experimental errors respectively and N_{δ_j} and N_{η_j} are the numbers of experimental points. Superscripts "th" and "exp" refer to theoretical (from presented model here) and experimental values. The third component related to the occurrence of the ρ' resonance (pole on a given Riemann sheet) had the form:

$$\chi^2_{res} = \left| 10^7 (D(k_1, k_2, k_3)) \right|^2 , \tag{6.28}$$

where the Jost function $D(k_1, k_2, k_3)$ is simply the denominator of all the S matrix elements (see for example Eq. (6.19)) and the factor 10^7 only served to increase the weight of this term and thus force the function χ^2_{res} to zero for a complex energy at the given pole position. The last fourth component contained information about the scattering length in the $\pi\pi$ channel, which, according to the results from [111], was assumed $a_P^{exp} = 38.5 \pm 1.2\, m_\pi^{-3}/1000$. This component had the form

$$\chi^2_{a_P} = \left(\frac{a_P^{th} - a_P^{exp}}{\Delta a_P^{exp}} \right)^2 . \tag{6.29}$$

The total χ^2 was the sum of all four of these components and the total number of free parameters was 18 (parameters of potentials). Number of degrees of freedom (hereafter ndf) was therefore 75 (for δ_π) + 47 (for η_π) + 1 (for a_P) + 1 (for pole ρ') - 18 = 106. The choice of the Riemann sheet for the assumed resonance pole was dictated by the indications in the work [87]. And so, if the resonance mass (real part of the pole) was lower than the threshold of the third channel (effective $\rho\rho$), then it was the $(-,-,+)$ sheet. Above this threshold, the $(-,-,-)$ sheet was selected. Parameters of the complex ρ' resonance pole at $E_r = Re(E_r) - i\Gamma_r/2$ were not free - they were either not used in the fits or fixed at given position. The pole on the $(+,-,+)$ sheet mentioned in the work [87] was not taken into account in this analysis as a sheet of the significant pole because, as shown by the fits, it has no significant contribution and above the $\rho\rho$ threshold, the physical momentum of the particles are real in all channels, so to guarantee the proximity of the pole to the physical region the complex momenta should have a negative imaginary part. However, in order to refer to this work and show that, in this analysis, there are no new poles in this sheet that are relevant to the description of the fitted amplitudes, information about analytical structure of Jost function on this sheet will be given below - together with information on sheets $(-,-,+)$ and $(-,-,-)$.

6.3.1 Fitting procedure

The initial investigations encompassed the entire energy spectrum, nearly reaching 1900 MeV, for both relativistic and nonrelativistic propagators denoted as $fit0_R$ and $fit0_{NR}$ respectively. These analyses were undertaken without imposing any constraints on the position of the resonance pole, resulting in a degrees of freedom value of 105. The optimization algorithm

utilized for this purpose was the CERN library program MINUIT, employing the SIMPLEX and MIGRAD methods to locate the global minima of the χ^2 function.

The cumulative value of χ^2 gives 84.2 with 0.8 per degree of freedom (pdf) for $fit0_R$, and correspondingly, 96.1 for $fit0_{NR}$ with a pdf of 0.9. The outcomes of these fitting procedures were acquired through an iterative process involving 31 iterations. The initial iteration began within the energy range commencing from the threshold of $\pi\pi$ interactions, extending up to 400 MeV, encompassing solely two potential parameters within the $\pi\pi$ channel - specifically, a potential of rank one in this energy domain.

Consecutive fits were executed, incrementing the energy range in increments of 50 MeV. Each of these fits was initialized using the parameter values obtained from the previous one. As the energy range expanded, additional terms and parameters were introduced into the potentials and subsequent channels. This sequential methodology was necessitated by the limited constraints imposed on the fitted potentials. In scenarios characterized by such constraints, meticulous guidance is imperative to navigate the fitting procedure toward the optimal minimum within the multidimensional parameter space.

In all instances of these fitting procedures, the term $\chi^2_{a_P}$, related to the scattering length, was consistently included.

The values associated with the 18 parameters comprising the fitted potentials for models denoted as $fit0_R$ and $fit0_{NR}$ are meticulously presented in Table 6.1. Notably, the β parameters characterizing the $fit0_R$ model exhibit a discernible range spanning from 300 to 7000 MeV. In contrast, the couplings observed within the various channels uniformly possess positive values that remain constrained below unity.

Remarkably, the cross-channel couplings manifest negligible magnitudes, consistent with theoretical predictions. This outcome finds its rationale in the intricate interplay of numerous couplings, where none is substantially favored due to the lack of data in channels 2 and 3. Turning attention to the parameters of the $fit0_{NR}$ model, it emerges that the β values fall within the interval of 300 to 21000 MeV. Unlike the uniformity seen in $fit0_R$, the coupling constants across channels in the $fit0_{NR}$ model exhibit variable signs, with the coupling strength in the third channel markedly surpassing others.

A noteworthy mathematical observation involves the reciprocal roles played by terms 1 and 2 relative to their counterparts in the $fit0_R$ model. This observation extends to the coupling constants between channels, which, in the $fit0_{NR}$ model, display distinctive signs and notably increases the magnitudes compared to those inherent in $fit0_R$.

The profound disparities between the parameter configurations of $fit0_R$ and $fit0_{NR}$ become evident upon closer inspection. This contrast becomes particularly salient when considering the associated χ^2 values and the loci of the poles. The pole positions were established employing an alternative FORTRAN program, leveraging the MINUIT library. The search for vanishing χ^2_{res} values, as defined in Eq. (6.28), discloses the pole positions as follows: for the $fit0_R$ model, $E_r = 1627.7 - i83.6$ on the $(-,-,-)$ Riemann sheet and $E_r = 1650.5 - i67.0$ on the $(-,-,+)$ Riemann sheet. In the context of the $fit0_{NR}$ model, these pole positions shift to $E_r = 1588.39 - i712.2$ on the $(-,-,-)$ Riemann sheet and $E_r = 1628.9 - i638.6$ on the $(-,-,+)$ Riemann sheet. The parameters characterizing the poles within the context

of the $fit0_R$ exhibit values that are deemed acceptable and possess a plausible association with observable physical resonant phenomena. In stark contrast, the poles encompassed by the $fit0_{NR}$ are situated at considerable distances, rendering them unsuitable as viable candidates for conceivable physical resonance manifestations.

It is important to highlight that all parameters inherent to the $fit0_R$ exhibit a higher degree of physical realism. Notably, the magnitudes of these parameters are consistent with those documented in prior investigations pertaining to interactions occurring in the S wave [107]. This serves to corroborate the assertion regarding the accuracy of the $fit0_R$.

The observed distinctions between the outcomes of $fit0_R$ and $fit0_{NR}$ could potentially stem from the energy regime under scrutiny, where energies surpassing 1000 MeV necessitate the relativistic treatment of light pions. Evidently, the mathematical formulations governing Jost functions, when predicated upon a relativistic propagator, exhibit an enhanced adaptability, thus affording a more extensive latitude for alignment with empirical data.

Given the substantial disparities between outcomes yielded by fits utilizing relativistic and non-relativistic propagators, the subsequent analysis within this section, as well as the succeeding sections, will exclusively revolve around outcomes derived from the utilization of the relativistic propagator.

Important step in the next fits was the inclusion of position of a pole for the ρ' resonance at a given complex energy and on a given Riemann sheet. The first such fits started with the final parameters of amplitudes for the $fit0_R$ (see Table 6.1) and with the pole on the sheet $-,-,+$ at energy $E_r = 1150.0 - 150.0$ MeV. Successive fits were performed for increasing value of $\mathrm{Re}(E_r)$ (i.e. resonance mass) with a step of 50 MeV and with the same value of $\mathrm{Im}(E_r) = -150.0$ MeV (i.e. half of the resonance width). As in the previous procedure, each fit started with the potential parameters from the previous fit. For $\mathrm{Re}(E_r)$ below the third threshold $2m_\rho \sim 1550$ MeV this pole was "manually" placed on the $(-,-,+)$ sheet and above this value on the $(-,-,-)$ sheet.

For the completeness of the examined fits, the influence of changes in the width of the fixed resonance (i.e. $\mathrm{Im}(E_r)$) on the values of the total χ^2 and on potential parameters was also examined. Both reducing and increasing the -150.0 MeV value adopted in the above-mentioned fits for relativistic propagator by a few MeV did not significantly affect χ^2 (the changes were about 5-10 i.e. 6-12%). On the other hand, larger changes (above 20 MeV), led to much larger increase in χ^2. Thus, the value $\mathrm{Im}(E_r) = -150.0$ MeV has been kept as physically real (comparable to the values in Table II in the work [87]) and as mathematicaly acceptable - corresponding to a fairly wide minimum.

6.3.2 Analysis of results from performed fits

Table 6.2 presents the dynamic variations of the aggregate χ^2 values as they correspond to the manipulation of the manually assigned $\mathrm{Re}(E_r)$ values. Within all of these fitting instances, the χ^2_{res} component concerning the resonance position (as expressed in Equation 6.28) amounted to approximately 10^{-3}. This conferred a precision of approximately 0.5 MeV for the resonance position subsequent to fitting, in contrast to its pre-fitting imposition.

parameter	$\beta_{1,a}$	$\beta_{1,b}$	$\beta_{2,a}$	$\beta_{2,b}$	β_3
value for $fit0_R$ (MeV)	276.4	6113.7	6632.0	1222.7	2334.7
value for $fit0_{NR}$ (MeV)	21005.6	278.4	5101.3	1927.1	1725.5

parameter	$\Lambda_{11,a}$	$\Lambda_{11,b}$	$\Lambda_{22,a}$	$\Lambda_{22,b}$	Λ_3
value for $fit0_R$	6.5×10^{-4}	0.931	0.709	0.154	0.973
value for $fit0_{NR}$	-0.994	-2.472×10^{-5}	-1.827	0.818	7.494

parameter	$\Lambda_{12,aa}$	$\Lambda_{12,bb}$	$\Lambda_{12,ab}$	$\Lambda_{12,ba}$	$\Lambda_{13,a}$	$\Lambda_{13,b}$	$\Lambda_{23,a}$	$\Lambda_{23,b}$
value for $fit0_R$ $\times 100$	6.72	-29.18	-5.30	30.21	2.64	3.99	1.70	-4.58
value for $fit0_{NR}$ $\times 100$	-84.16	16.59	71.62	-84.16	-27.51	-6.53	1363.96	-1132.93

parameter	Re(E_r)	Im(E_r)	Riemann sheet
value for $fit0_R$	1627.7 MeV (free)	-83.6 MeV(free)	$(-,-,-)$
value for $fit0_{NR}$	1588.39 MeV (free)	-712.2 MeV(free)	$(-,-,-)$

	χ^2_{total}	χ^2_δ	χ^2_η	$\chi^2_{a_P}$
value for $fit0_R$	84.2	51.4	32.8	0.06
value for $fit0_{NR}$	94.2	54.3	39.8	0.01

Table 6.1: Values of fitted parameters in first fits for relativistic and nonrelativisitc propagators ($fit0_R$ and $fit0_{NR}$ respectively).

As can be seen from the tabulated data, the χ^2 values exhibit minimal sensitivity to alterations in the resonance positions. This observation suggests that the ensemble of these positions are acceptable and aligns greatly with the data concerning phase shifts and inelasticity within the $\pi\pi$ channel.

Noteworthy is the observation that the distinctions between χ^2 values across individual fits are insufficient to definitively select the optimal outcome corresponding to the placement of the manually introduced pole. The only definite declaration that can be made is that the mass of ρ' should not fall below approximately 1250 MeV.

To probe which pole (and by extension, which Riemann sheet) should be proximate to the third threshold as enumerated in Table 6.2, two results emerge for the same predetermined resonance mass (1550 MeV), each corresponding to poles residing on distinct Riemann sheets. While the parameters characterizing the artifact poles exhibit similarity, a slightly superior χ^2 is achieved with the fitting that encompasses a manually inserted pole on the $(-,-,+)$ Riemann sheet. The 6.2 table also contains other important information - namely the position of another pole generated automatically in each fit. It is not a simple projection of a manually imposed pole onto another Riemann sheet but completely new pole which, in each obtained result, lies in such an energy range and on such a Riemann sheet that it has a significant impact on the fitted amplitudes. For each fit its position has been found after careful examination of the analytical structure of the obtained Jost function $D(k_1, k_2, k_3)$ in the complex energy plane for $1000 < Re(E_r) < 2000$ MeV and $0 < -Im(E_r) < 500$ MeV. Such new pole is necessary to describe the dynamics of interactions in the channels studied here above 1500 MeV what agrees very well with other detailed analyses. For example according to the data in the Tables of Elementary Particles [105] and according to the results of the work [87] there should be at least two ρ resonances in the energy range of 1200-1800 MeV (ρ' and ρ").

In addition to this new pole, there is one more pole lying on the same sheet as it, but in the energy range that it is far from the physical region. This pole just a projection of a manually imposed pole onto another sheet and does not play an important role in shaping the fitted amplitudes.

Due to the rich analytical structure of the Jost function, it is very instructive to study the three-dimensional distributions of its modulus for different positions of the assumed pole and on different Riemann sheets. Illustrated in Figure 6.1 is an array of such distributions, charting the course of fits incorporating a manually introduced ρ' on the $(-,-,+)$ sheet. This sequence spans a continuum of masses, ranging from 1150 MeV to 1550 MeV. Beyond this threshold, the same pole finds its placement on the $(-,-,-)$ sheet, as elucidated in the subsequent Figure 6.2. Distributions on three Riemann sheets $(-,-,+), (-,-,-)$ and $(+,-,+)$ are presented on these figures and clearly show two poles: of the imposed resonance and that new one being the artifact. That new one changes the parameters in accordance with the requirements imposed by the fits to experimental data for subsequent masses of manually inserted the pole. In each of the figures one can see two poles on a given Riemann sheet. Comparing them with those in the table 6.2 one can see that there is always one of them in this table and it is the one that significantly affects the fitted amplitudes (on the

Re(E_r) (MeV)	1150	1250	1350	1450	1550	1550	1650	1750	1850
χ^2	103.3	95.6	94.8	95.1	94.9	95.1	98.7	95.8	94.2
Riemann sheet	III	III	III	III	III	VI	VI	VI	VI
$Re(E_r)$ (MeV)	1643	1650	1651	1652	1690	1688	1670	1578	1614
$-Im(E_r)$ (MeV)	53	63	75	68	90	70	83	82	106
Riemann sheet	VI	VI	VI	VI	VI	III	III	III	III

Table 6.2: Values of the total χ^2 for various positions of imposed resonance pole on Riemann sheets III: $(-,-,+)$ and VI: $(-,-,-)$ and positions of poles - artifacts at E_r (rounded to 1 MeV) - with their Riemann sheets

$(-,-,+)$ sheet below 1500 MeV and on the sheet $(-,-,-)$ above 1500 MeV). The secondary pole, observed alongside the prominent one, represents a mere projection of the former onto an alternate Riemann sheet. This secondary pole, however, bears minimal significance in shaping the dynamics of the ascribed amplitudes. This phenomenon is starkly evident in the $(+,-,+)$ sheet, where both observable poles are veritable extensions of their counterparts in the $(-,-,+)$ and $(-,-,-)$ sheets, and they do not play a significant role in the dynamics of the amplitudes.

Hence, the current analysis unveils the complex mechanism through which a novel resonance emerges in response to the introduction of a primary one, accompanied by the intricate fitting of amplitudes involving numerous inter-channel couplings.

The existence of these dual resonances is a theoretical necessity, but a relevant question relates to the attributes of the lighter resonance (ρ'). This query is influenced by discussions in works like [87] and its cited references, suggesting a mass below 1300-1350 MeV for ρ', in contrast to the more prevalent utilization of 1450 MeV.

Although the disparities in χ^2 values between the diverse fits detailed here are subtle, they fall short of providing a conclusive response to this inquiry. Nevertheless, this answer might be furnished by predicted distributions of phase shifts and inelasticity within the yet unexplored $\omega\pi$ channel.

The distributions presented in Figure 6.3 lend themselves to comparison with outcomes from forthcoming experiments and analyses centered around $\omega\pi$ interactions. This comparison could serve as a foundation for deducing the parameters of the ρ' resonance.

Evidently, as the resonance mass undergoes modification, there is a discernible shift in the pitch of the phase shift. Furthermore, when fixed mass values are relatively small, the figures distinctly portray two isolated increments in phase shifts. This pattern arises due to the existence of two separate poles that considerably influence the adjusted amplitudes, as evidenced by the specific mass values, both fixed and pertaining to the artifact, within Table 6.2. For the fixed resonance mass of ρ' lying in the range of 1500-1700 MeV, the

real components of these two poles are closely aligned. Through positive interference, they combine to yield a singular elevation in phase shifts, wherein distinguishing two separate resonances (located on distinct Riemann sheets) becomes challenging.

The sole indicator suggesting the presence of more than one resonance within this interval is a phase shift increase exceeding 180 degrees. For fixed masses surpassing 1700 MeV, the reappearance of a phase shift curve featuring two distinct slopes emerges once more, corresponding to amplitudes associated with two more distinctly separated resonances.

Upon scrutinizing the manifestation of inelasticity, traces of dual resonances become apparent across all segments except the 1500-1700 MeV region. The pronounced dip around 1600 MeV results from the initiation of the third channel and the interplay of resonances.

Furthermore, the escalating curvature of the inelasticity beyond 1800 MeV in the latter figures is also attributed to the interaction between these two resonances. However, it necessitates meticulous analysis, given its occurrence at the boundary of the performed fits.

To validate the accuracy of the fitting process to $\pi\pi$ data, a comparison of phase shifts and inelasticity against empirical data is displayed in Figure 6.4. Above 970 MeV data are from experimental works [100, 99, 102, 103, 104]. Below this energy, the values with errors from work [111] are used. This was done in order to approximate the amplitudes fitted here to those fulfilling the crossing symmetry condition tested in that work. In addition, these values, as derived from the model, are more "smooth" ie. devoid of experimental fluctuations, which allowed the fits to focus on the area of over 1000 MeV, important for this analysis. This comparison corresponds to a fitting endeavor wherein the mass of ρ' is maintained at a constant value of 1350.0 MeV.

The fitting's notable efficacy is immediately discernible, even upon cursory inspection. This visual assessment is substantiated by the quantitatively small total χ^2 value, amounting to 94.8 (0.9 pdf).

From Eq. (6.20), it's evident that the complete Jost function is composed of two components: one arising from the individual Jost functions within each channel, and another originating from the function F that governs the inter-channel interactions.

The function's behavior, elucidated beneath this equation, reveals that resetting all inter-channel connections nullifies this function and effectively isolates the individual Jost functions where the operand sign in both the numerator and denominator of the scattering matrix elements remains consistent (refer to Eq. (6.19)).

This method offers the advantage of independently testing each individual Jost function within any given channel. Consequently, it becomes feasible to identify the source channel of a particular pole whether it's the manually introduced pole i.e "by hand" or an artifact. This identification involves identifying which individual Jost function in the denominator is nullified by a specific pole. It's important to note that due to the transition from the complete $D(k_1, k_2, k_3)$ to individual $D_\alpha(k_\alpha)$ by eliminating the F function, the pole's position will differ.

Moreover, a gradual reduction in inter-channel couplings allows for a systematic exploration of the trajectory that poles traverse in the complex energy plane as couplings decrease.

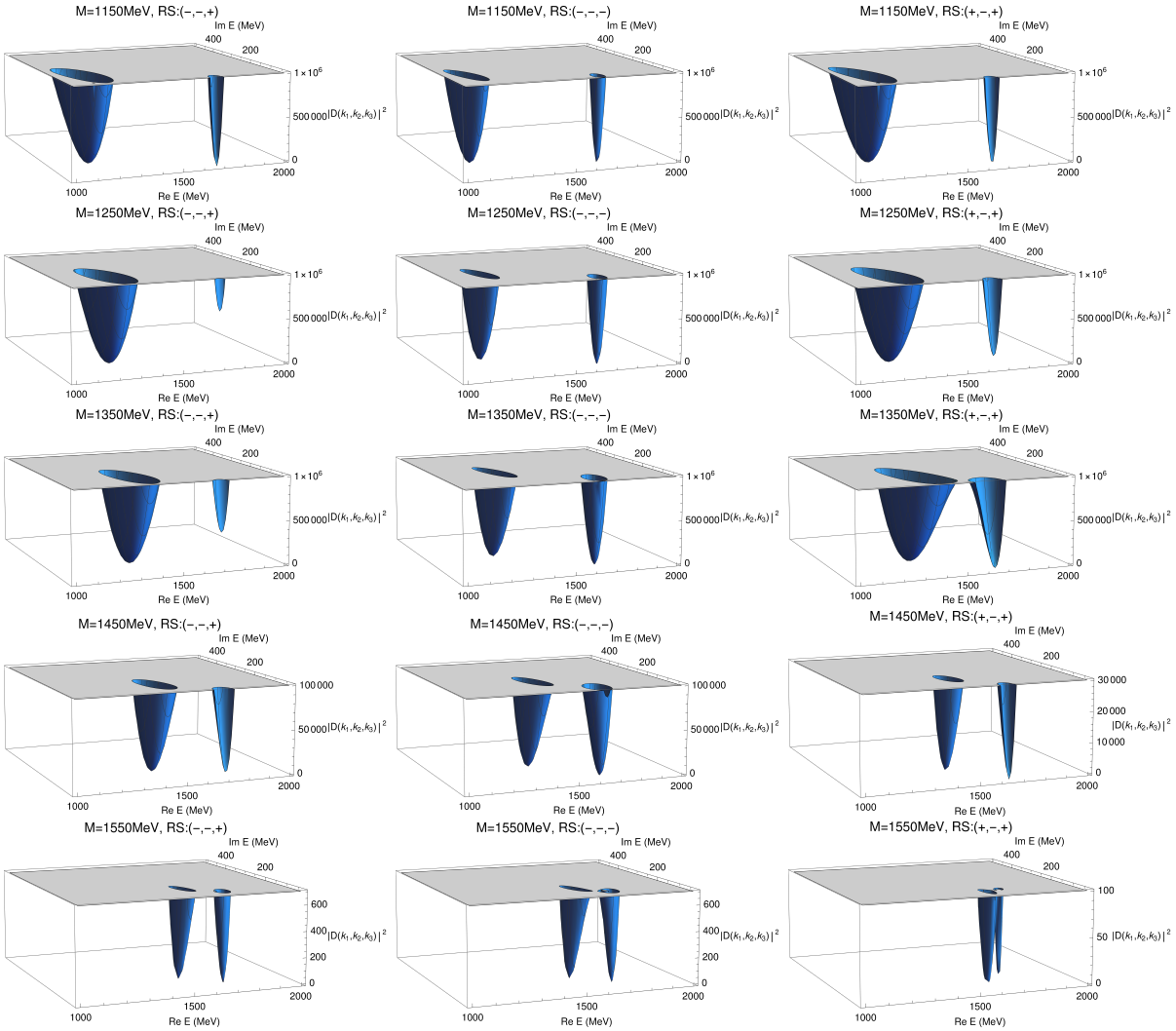

Figure 6.1: A series of three-dimensional distributions of the Jost function for various manually inserted pole masses on the $(-,-,+)$ Riemann sheet, up to 1550 MeV. Each mass is accompanied by distributions on three Riemann sheets: $(-,-,+)$, $(-,-,-)$, and $(+,-,+)$.

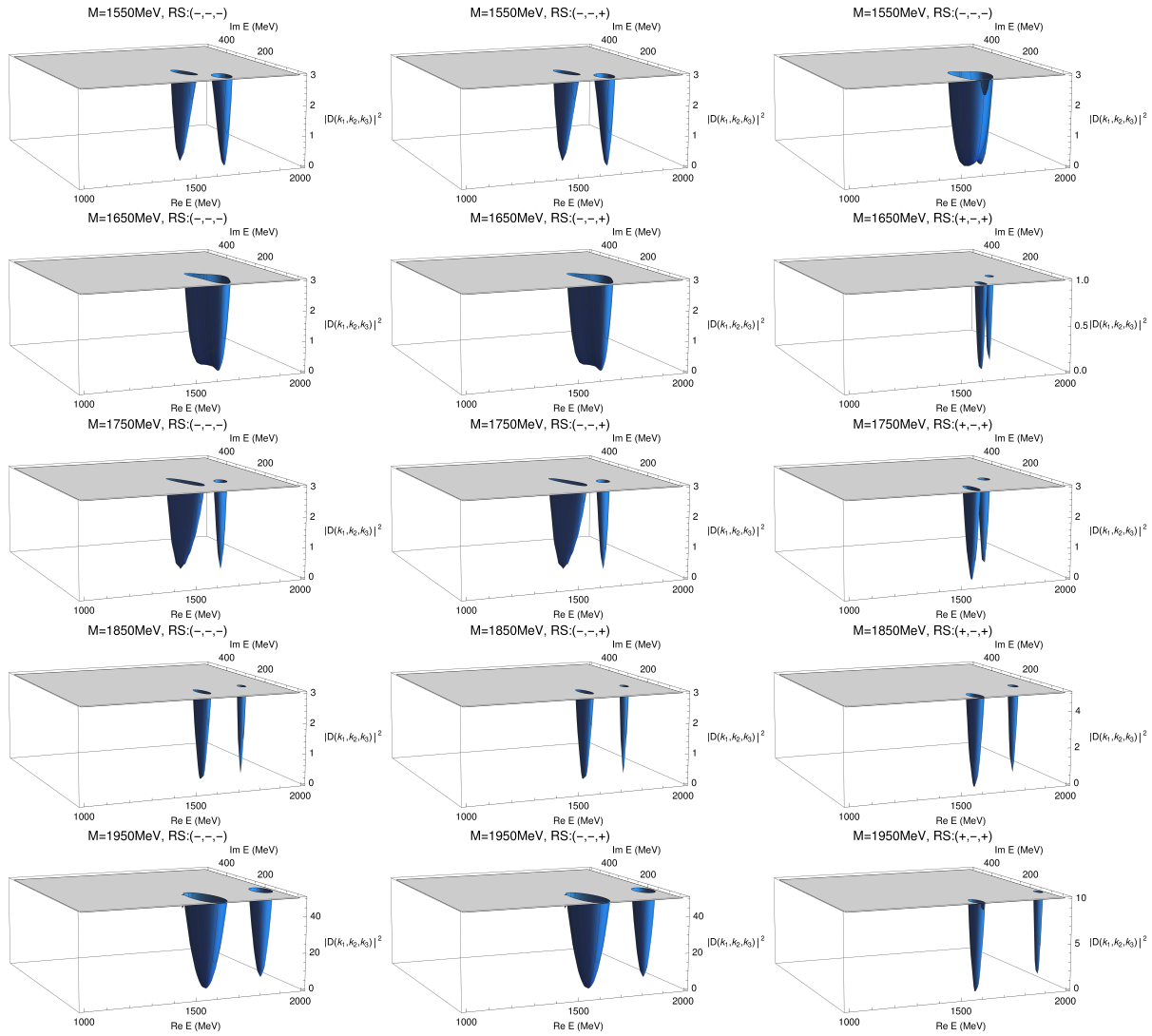

Figure 6.2: Sequence of three-dimensional distributions of the Jost function for successive masses of manually inserted the poles on the $(-,-,-)$ Riemann sheet above 1550 MeV. For each mass presented are distributions on three Riemann sheets: $(-,-,-)$,$(-,-,+)$ and $(+,-,+)$.

This methodology can be extended to the third resonance in the exhibited amplitudes—the lighter vector-isovector meson $\rho(770)$.

The trajectories for all three resonances are depicted in figures 6.5, 6.6, and 6.7. Evidently, changes in coupling between channels yield alterations in the real and imaginary components of the poles.

This observation underscores the substantial influence of channel couplings—sufficiently potent to provoke significant changes in pole parameters during coupling variations. The phenomenon of Riemann sheet transitions during inter-channel coupling shifts is well-documented and finds resonance in other analyses, as exemplified in [107] (Fig. 4).

As anticipated, the $\rho(770)$ resonance emerges within the $\pi\pi$ channel. The ρ' meson finds its origin in the $\omega\pi$ channel, while the ρ'' meson arises from the $\rho\rho$ channel.

Evidently, the incorporation of a third channel was imperative to enable the generation of the three essential singularities i.e. poles associated with the resonances. Analogous fittings conducted with only two channels yielded solely two resonances: $\rho(770)$ and an effective $\rho(1500)$. However, the latter presented a notably inferior description of experimental data beyond approximately 1000 MeV, as opposed to the more accurate portrayal facilitated by the three-resonance model expounded upon here.

It's noteworthy that the utilization of rank-two potentials in the $\pi\pi$ and $\omega\pi$ channels is substantiated by the considerable i.e. large energy ranges dominated by these channels, coupled with the complex data-energy variations observable within these regions.

Fittings employing rank-one potentials in all three channels, or with a rank-two potential exclusively in channel 1 or 2, failed to capture the essence of $\pi\pi$ data, leading to a total χ^2 value per degree of freedom surpassing 2 pdf. This underlines that the requirement for rank-two potentials in channels 1 and 2 is primarily rooted in mathematical necessities, although these mathematical requirements are inherently intertwined with the dynamics of interactions.

An interesting illustration concerning the $\rho(770)$ resonance pertains to the discrepancy in reported meson mass, which is nearly 10 MeV according to [105]. This variation finds comprehensive explanation in sources like [89], relating it to the interplay of poles and zeros on the left side of the imaginary axis within the complex momentum of interacting particles.

While these poles and zeros exert limited influence on the overall amplitude, they symmetrically mirror the leading poles and zeros positioned to the right of the imaginary axis. Nonetheless, their presence remains indispensable to uphold the unitarity of interaction amplitudes.

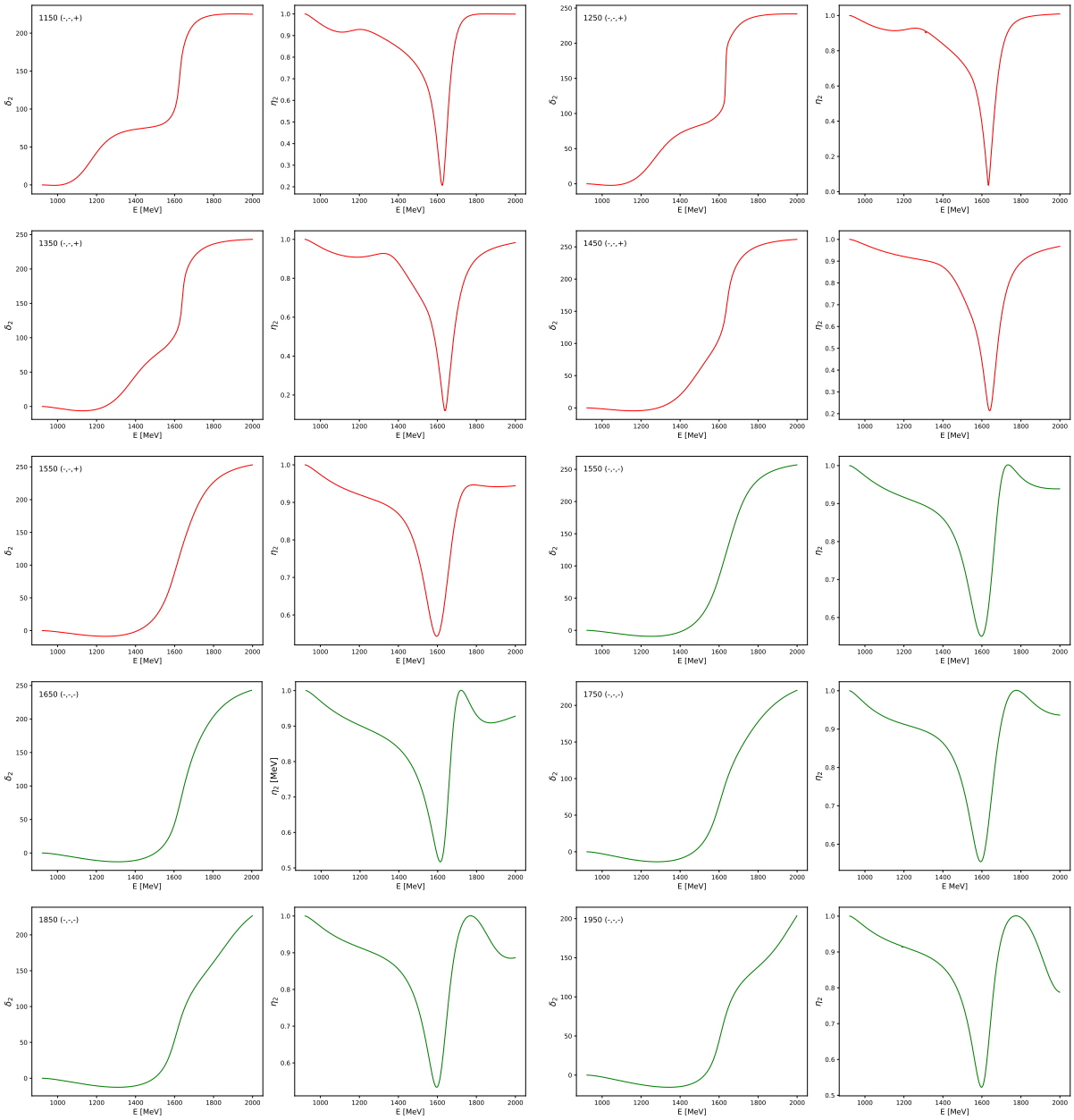

Figure 6.3: $\omega\pi$ phase shifts and inelasticities distributions for sequence of manually inserted ρ' pole. Numbers and names of the Riemann sheets on figures for the phase shift denote the mass of the ρ' resonance manually braced on the indicated Riemann sheet in fitted amplitudes. This information also applies to each inelasticity plot to the right of each phase shift plot. The red line was used for fits with fixed ρ' on the $(-,-,+)$ sheet and the green line on the $(-,-,-)$ sheet. The two figures with the same mass 1550 MeV show results from two fits with ρ' on different Riemann sheets.

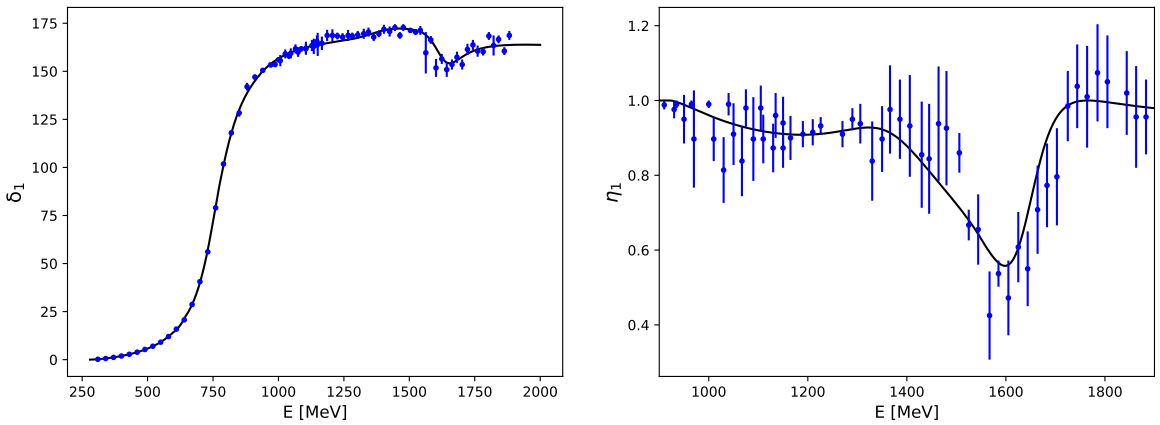

Figure 6.4: $\pi\pi$ phase shifts and inelasticities distributions for fit with manually inserted ρ' pole at 1350.0 MeV. Data are from [111, 100, 101, 102, 104]

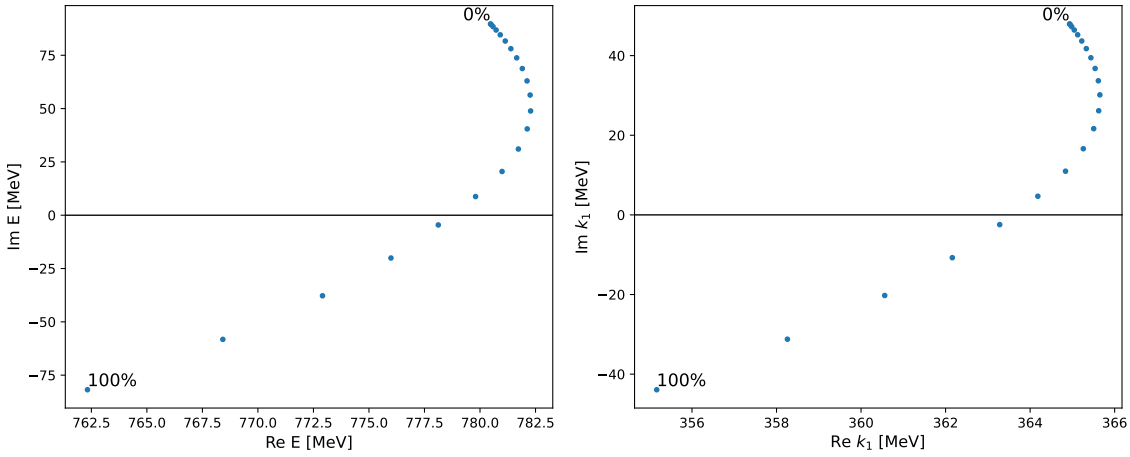

Figure 6.5: Trace of a pole associated with $\rho(770)$ for varying couplings between channels in fit with fixed mass of ρ' at 1350.0 MeV (changes in percentage of full coupling), left figure - trace for energy and right figure - trace for pion momentum.

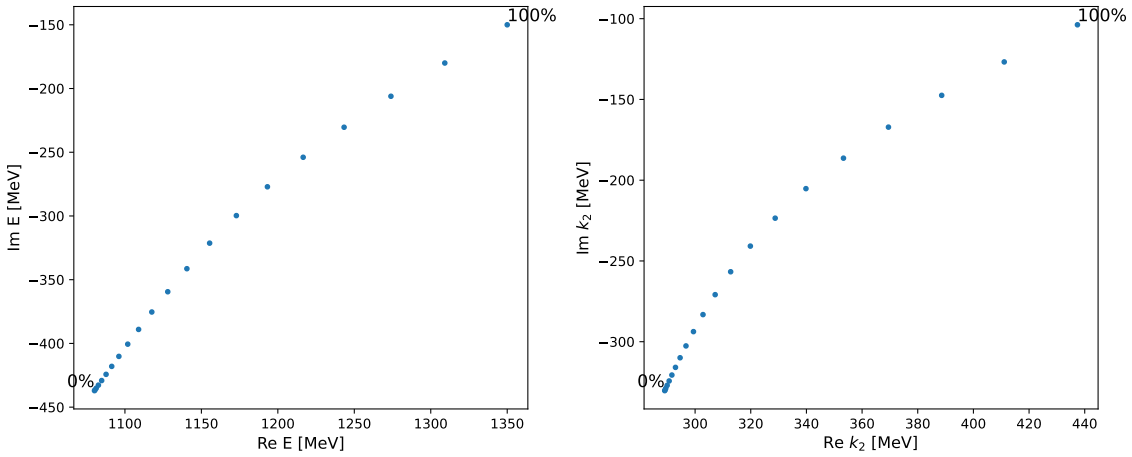

Figure 6.6: As in figure 6.5 but for a pole associated with ρ' and for relaive ω-π momentum

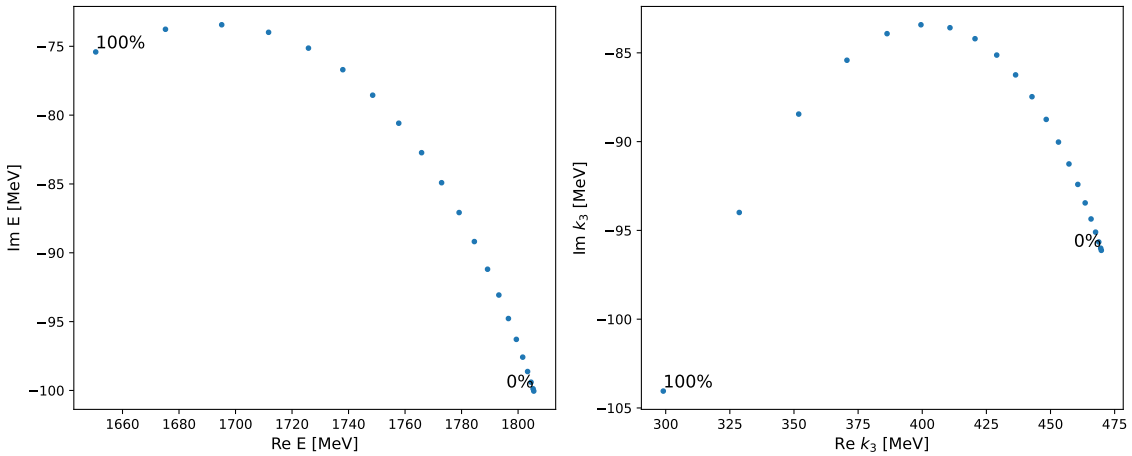

Figure 6.7: As in figure 6.5 but for a artifact pole associated with ρ" and for ρ momentum

Chapter 7

Summary and Outlook

7.1 Summary

This thesis embarks on a captivating journey through the intricate domain of hadron spectroscopy, skillfully unraveling the complexities of meson resonances. This comprehensive exploration revolves around in-depth analyses of photoproduction processes and meticulous spectroscopy evaluations, with the goal of providing a comprehensive description of various phenomena in exclusive particle production within hadron-hadron interactions.

The foundational principles underpinning the extensive analyses presented throughout this thesis are precisely established in its initial chapters. Chapter 1 delivers a comprehensive introduction to the theory of strong interactions, delving into the essentials of the Standard Model and Quantum Chromodynamics (QCD). This foundational journey not only imparts a profound understanding of mesons and their unique characteristics but also elucidates the motivations driving this academic endeavor.

Moreover, Chapter 2 lays out a robust theoretical framework for investigating resonances. By introducing the scattering S-matrix formalism within the context of quantum field theory, a pathway emerges for exploring the non-perturbative assessment of hadronic processes. This framework relies on dispersion theory and the encompassing Regge theory, Regge amplitudes, trajectories, and the central concept crucial to this investigation.

Advancing to the focal points of inquiry, "Part I - Photoproduction of Light Mesons" dedicates its focus to the exact exploration of two-pion photoproduction, with an emphasis on meson resonances within the $\pi\pi$ system. Chapter 3 leads this endeavor with a comprehensive investigation of double pion photoproduction, carefully examining scenarios involving virtual pion exchange. This chapter skillfully adapts classical relations to enhance the precision of analysis. Section 3.1 uncovers key components and kinematic notations, while Section 3.2 delves deeply into the non-resonant Deck model, successfully deriving a unitary and gauge-invariant Deck amplitude. This is achieved through a strategic combination of the Deck model with the SAID parametrization of πN scattering amplitudes, effectively probing the dominant exchange mechanism of the reaction at forward angles that is given by the one

virtual pion exchange in the $t_{\gamma\pi}$ channel. Notably, the analysis yields both vector and scalar resonance amplitudes, encompassing $\rho(770)$, $f_0(500)$, and $f_0(980)$, which play substantive roles in shaping the behaviors of P- and S-waves, correspondingly. This process entails a precise utilization of Regge theory, where the selection of specific trajectories was guided by the inherent nature of the exchanged Reggeon — such as the pomeron and f_2 trajectories for $\rho(770)$ resonance and ρ trajectory for both scalar resonances amplitudes.

This chapter's critical outcome lies in the comprehensive analysis of the double pion photoproduction process, achieved through the adoption of the Drell-Söding-Deck mechanism, which elucidates the involvement of resonances and interference effects, despite the Deck component's role as a background contributor.

Building upon the foundations established in the preceding chapter, Chapter 4 embarks on the crucial task of utilizing the derived physical relations and amplitudes to unveil the underlying physics of the process at hand. The primary focus here lies in the calculation of cross sections and the analysis of angular distribution moments. Sections 4.1 and 4.2 delve into the intricacies of the conventions employed for computing these angular moments. The overarching objective is to ensure that the model meticulously developed in the previous chapter possesses the capability to faithfully replicate the experimental data gathered by CLAS. In the subsequent Section 4.3, a pivotal realization emerges: the need to redefine the dependence on the momentum transfer variable. Specifically, this necessitates a reevaluation of the couplings within specific components of the model. The section expounds upon the methodology employed for this redefinition and presents the outcomes of the initial fitting procedure. Moreover, in Section 4.4 a fit encompasses the contributions of resonances below 1 GeV, most notably the involvement of $\rho(770)$ and $f_0(500)$ is presented. Following this, the narrative shifts to the exploration of non-resonance contributions originating from the various partial waves under scrutiny is discussed in Section 4.5. Where it becomes evident that each partial wave, no matter how seemingly minor its individual impact, plays a vital role in the overall dynamics of the process. Subsequently, in Section 4.6, a novel fitting approach is introduced, one that spans the entire energy range of interest. This extended model encompasses not only the Deck piece but also embraces the combined contributions of resonance and non-resonance components from both P and S waves. Notable among these contributions are those stemming from ρ, $f_0(500)$, and $f_0(980)$. The findings of this fitting procedure reveal an exceptional alignment with the experimental data, surpassing the performance of the initial fit.

In essence, the profound insight gained from this chapter is the recognition of the collective significance of all partial waves contributing to each moment. It becomes evident that both resonant and non-resonant contributions from these partial waves, no matter how seemingly marginal their individual effects, collectively they actively shapes the experimental data, ultimately extracting the underlying physics of the observed process. Their intricate interplay and interference yield a comprehensive understanding of the phenomenon in question,

underscoring their collective importance.

Transitioning to "Part II - Light Meson Spectroscopy", the exploration ascends to an extensive evaluation of light meson spectroscopy, navigating through the experimental landscape of mesonic resonances below 2 GeV. In Chapter 5, a comprehensive analysis of elastic $\pi\pi$ phase shifts and inelasticities is presented, discerningly identifying the $J^{PC} = 1^{--}$ excited ρ resonances while addressing the persistent debate surrounding $\rho(1450)$ versus $\rho(1250)$. A sophisticated parametrization approach utilizing a unitary and analytic three-channel S matrix forms the bedrock of this analysis, ensuring robust results. The selection criteria for effective channels are laid out in Section 5.1.1, while the enhanced parametrization approach is elaborated upon in Section 5.2, showcasing the method's adaptability to various channels and its contribution to the stability of fitted pole positions. The analysis reinforces the reliability of identified resonances, emphasizing the importance of $\rho(1250)$ and advocating for its distinct entry in the PDG tables.

Concluding this insightful journey, Chapter 6 offers a forward-looking perspective by forecasting insights within the $\pi\omega$ channel. This chapter embarks on uncharted territory, attentively crafting theoretical amplitudes for the $\omega\pi$ channel and scrutinizing their mass distributions. The methodology developed here is commendably universal, extending its adaptability to various partial waves and channels beyond the P wave. The analysis method, fitting procedures, and outcomes are robustly discussed in sections 6.3 6.3.1 6.3.2 respectively. Thus, shedding light on the significance of this exploration and its contribution to the broader understanding of particle interactions.

7.2 Outlook and Future Directions

In this journey through the intricate realm of meson spectroscopy, the exploration of the subatomic world has unearthed profound insights and illuminated uncharted territories. Standing at these crossroads, it becomes evident that this odyssey has only just begun.

The discoveries presented in these pages challenge the boundaries of current understanding, beckoning towards unexplored realms of knowledge. The enigmatic breakdown of SCHC at higher momentum transfers hints at the need for innovative theoretical paradigms, opening the door to forging new intellectual frontiers.

The ongoing pursuit of unraveling the mysteries of double pion photoproduction remains a captivating endeavor. As additional contributions from other partial waves are incorporated, and as correlations between the fitted parameters are analyzed, the final pieces of the puzzle are falling into place. This evolving model will serve as the bedrock for the study of even more intricate and complicated photoproduction processes.

The resounding success of the methodology in locating resonances not only validates the approach but also inspires further expansion. The promise of additional investigations into meson systems and diverse categories of hadrons extends the horizon of discovery.

As the environment of hadron spectroscopy burgeons, the landscape becomes ripe for

exploration. Pioneering experimental techniques, coupled with evolving theoretical frameworks, tantalizingly hint at the untold secrets concealed within the meson spectrum. The delicate interplay between spectroscopy, lattice QCD computations, and chiral effective field theories promises to enrich the comprehension of the enigmatic realm of strong interactions.

In closing, this thesis serves as more than a culmination of knowledge; it acts as a stepping stone towards a profound understanding of the universe's most fundamental forces. It is part of an unbroken chain of exploration and discovery, and the insights gathered here shall guide the ongoing quest to decipher the cosmos' deepest mysteries.

In the words of Albert Einstein,"The most beautiful thing that can be experienced is the mysterious. It is the source of all true art and science." May the continued pursuit of knowledge in the domain of meson spectroscopy forever be a testament to the beauty of the mysterious, and may it lead to ever greater revelations about the universe we call home.

Appendix A

Dirac Matrices

A.1 Representations of Gamma Matrices in Quantum Field Theory

In quantum field theory, gamma matrices are commonly represented in several ways, including the Dirac, Weyl, and Majorana representations. Here's a brief overview of each:

1. Dirac Representation

In the Dirac representation, the gamma matrices are 4×4 matrices. They can be written as:

$$\gamma^0 = \begin{pmatrix} I & 0 \\ 0 & -I \end{pmatrix}, \quad \gamma^i = \begin{pmatrix} 0 & \sigma^i \\ -\sigma^i & 0 \end{pmatrix},$$

where I and 0 are the 2×2 identity and null matrices respectively, σ^i are the Pauli matrices, and i runs over spatial indices.

2. Weyl Representation

In the Weyl representation, the gamma matrices are 2×2 matrices, and they can be written as:

$$\gamma^0 = \begin{pmatrix} 0 & I \\ I & 0 \end{pmatrix}, \quad \gamma^i = \begin{pmatrix} 0 & \sigma^i \\ -\sigma^i & 0 \end{pmatrix}.$$

This representation is useful when dealing with chiral or left- and right-handed components of spinors.

3. Majorana Representation

The Majorana representation is used in the context of Majorana spinors, which are self-conjugate and real. The gamma matrices in this representation are also 2×2 matrices, and they can be written as:

$$\gamma^0 = \begin{pmatrix} 0 & \sigma^2 \\ -\sigma^2 & 0 \end{pmatrix}, \quad \gamma^i = \begin{pmatrix} \sigma^i & 0 \\ 0 & -\sigma^i \end{pmatrix}.$$

In this representation, the gamma matrices are all imaginary and antisymmetric. These representations are related to each other through unitary transformations. The choice of representation depends on the specific context and the convenience for performing calculations in a particular problem. In this thesis, the gamma matrices were consistently represented using the Dirac representation. Consequently, the Pauli spin matrices σ^i are:

$$\sigma_x = \begin{pmatrix} 0 & 1 \\ 1 & 0 \end{pmatrix}, \quad \sigma_y = \begin{pmatrix} 0 & -i \\ i & 0 \end{pmatrix}, \quad \sigma_z = \begin{pmatrix} 1 & 0 \\ 0 & -1 \end{pmatrix}. \tag{A.1}$$

Here are the complete gamma matrices used:

$$\gamma^0 = \begin{pmatrix} 1 & 0 & 0 & 0 \\ 0 & 1 & 0 & 0 \\ 0 & 0 & -1 & 0 \\ 0 & 0 & 0 & -1 \end{pmatrix}, \quad \gamma^1 = \begin{pmatrix} 0 & 0 & 0 & 1 \\ 0 & 0 & 1 & 0 \\ 0 & -1 & 0 & 0 \\ -1 & 0 & 0 & 0 \end{pmatrix}, \tag{A.2}$$

(A.3)

$$\gamma^2 = \begin{pmatrix} 0 & 0 & 0 & -i \\ 0 & 0 & i & 0 \\ 0 & i & 0 & 0 \\ -i & 0 & 0 & 0 \end{pmatrix}, \quad \gamma^3 = \begin{pmatrix} 0 & 0 & 1 & 0 \\ 0 & 0 & 0 & -1 \\ -1 & 0 & 0 & 0 \\ 0 & 1 & 0 & 0 \end{pmatrix}. \tag{A.4}$$

These matrices satisfies the following anti-commutation relation:

$$\{\gamma^\mu, \gamma^\nu\} = \gamma^\mu\gamma^\nu + \gamma^\nu\gamma^\mu = 2g^{\mu\nu}. \tag{A.5}$$

We can summarize the Gamma matrices trace identities as:

$$Tr[\gamma^\mu] = 0, \tag{A.6}$$
$$Tr[\gamma^\mu\gamma^\nu] = 4g^{\mu\nu}, \tag{A.7}$$
$$Tr[\gamma^\mu\gamma^\nu\gamma^\rho\gamma^\sigma] = 4(g^{\mu\nu}g^{\rho\sigma} + g^{\mu\sigma}g^{\nu\rho} - g^{\mu\rho}g^{\nu\sigma}), \tag{A.8}$$
$$Tr[\text{ odd number of Dirac matrices}] = 0. \tag{A.9}$$

The chirality matrix is defined to be:

$$\gamma^5 = \gamma_5 = i\gamma^0\gamma^1\gamma^2\gamma^3 = -\frac{i}{4!}\epsilon_{\mu\nu\rho\sigma}\gamma^\mu\gamma^\nu\gamma^\rho\gamma^\sigma, \tag{A.10}$$

and it obeys the following properties:

$$\gamma_5^2 = 1, \tag{A.11}$$
$$\{\gamma_5\gamma_\mu\} = 0. \tag{A.12}$$

Furthermore, the traces involving the chirality matrix yield:

$$Tr[\gamma^5] = 0, \tag{A.13}$$
$$Tr[\gamma^\mu\gamma^\nu\gamma^5] = 0, \tag{A.14}$$
$$Tr[\gamma^\mu\gamma^\nu\gamma^\rho\gamma^\sigma] = -4i\epsilon^{\mu\nu\rho\sigma}. \tag{A.15}$$

Two useful identities relating γ^5 with the Levi-Cevita tensor are:

$$\gamma^5[\gamma_\mu, \gamma_\nu] = i\epsilon_{\mu\nu\rho\sigma}\gamma^\rho\gamma^\sigma, \tag{A.16}$$
$$\frac{1}{2}\gamma^5[\gamma^\delta, [\gamma_\mu, \gamma_\nu]] = i\epsilon_{\mu\nu\rho\sigma}\gamma^\sigma\gamma^\delta\gamma^\rho, \tag{A.17}$$

where $\epsilon^{0123} = -\epsilon_{0123} = 1$.

Appendix B

Wigner D-matrix

The Wigner D-matrix was proposed by Eugene Wigner in 1927, and it can be defined as an irreducible unitary matrix representing the groups SU(2) and SO(3). This matrix plays an important role in quantum mechanical theory of angular momentum, where its complex conjugate represents the an eigenfunction of the Hamiltonian of spherical and symmetric rigid rotors.
To define the D matrix [112, 113, 114], one can begin with the three components of the angular momentum operator J: J_x, J_y, and J_z, also referred to as the generators of the Lie algebra of SU(2) and SO(3). These operators adhere to the following commutation relations:

$$[J_x, J_y] = i\hbar J_z \qquad [J_y, J_z] = i\hbar J_x \qquad [J_z, J_x] = i\hbar J_y \,, \tag{B.1}$$

where i is the pure imaginary and $\hbar = \frac{h}{2\pi}$ is the Plank's constant which will be taken equal to one for simplicity. Then:

$$J^2 = J_x^2 + J_y^2 + J_z^2 \,, \tag{B.2}$$

which is known as Casimir operator of the SU(2) group. The eigenfunction and the eigenvalues of both operators J^2 and J_z defines:

$$J^2 \left|jm\right\rangle = j(j+1) \left|jm\right\rangle \,, \tag{B.3}$$

$$J_z \left|jm\right\rangle = m \left|jm\right\rangle \,, \tag{B.4}$$

where $j = 0, 1/2, 1, 3/2..$ and $m \in [-j, j]$. We define the rotation operator as:

$$\mathcal{R}(\alpha, \beta, \gamma) = e^{-i\alpha J_z} e^{-i\beta J_y} e^{-i\gamma J_z} \,, \tag{B.5}$$

with α,β, and γ defines the Euler angles.
Consequently one can say that the Wigner D matrix is a square matrix of dimension $(2j+1)$ and has the following general element:

$$D^j_{m'm}(\alpha, \beta, \gamma) \equiv \left\langle jm'\right| \mathcal{R}(\alpha, \beta, \gamma) \left|jm\right\rangle \,, \tag{B.6}$$

$$\text{where} \quad D^j_{m'm}(0, \beta, 0) = \left\langle jm'\right| e^{i\beta J_y} \left|jm\right\rangle = d^j_{m'm}(\beta) \,, \tag{B.7}$$

known as Wigner's small d-matrix.

B.1 Some properties of the *D*-matrix:

- Orthogonality relations:
  The Wigner D-matrix elements represents a special case of the Schur orthogonality relations, in which they form a set of orthogonal functions of the Euler angles:

$$\int_0^{2\pi} d\alpha \int_0^{\pi} d\beta \sin(\beta) \int_0^{2\pi} d\gamma D^{j'}_{m'k'}(\alpha,\beta,\gamma)^* D^{j}_{mk}(\alpha,\beta,\gamma) = \frac{8\pi^2}{2j+1}\delta_{m'm}\delta_{k'k}\delta_{j'j} \quad \text{(B.8)}$$

  Moreover, these matrix elements represents a unitary transformation from one spherical basis i.e. $|lm\rangle$ to another one i.e. $\mathcal{R}(\alpha,\beta,\gamma)\,|lm\rangle$. This property could be represented by the following relations:

$$\sum_k D^{j}_{m'k}(\alpha,\beta,\gamma)^* D^{j}_{mk}(\alpha,\beta,\gamma) = \delta_{mm'}\,, \quad \text{(B.9)}$$

$$\sum_k D^{j}_{km'}(\alpha,\beta,\gamma)^* D^{j}_{km}(\alpha,\beta,\gamma) = \delta_{mm'}\,. \quad \text{(B.10)}$$

- Relation to spherical harmonics and Legendre polynomials:
  The D-matrix element with zero second index is proportional to both the spherical harmonics and the Legendre polynomials in which it satisfies the following relation:

$$D^{l}_{m0}(\alpha,\beta,\gamma) = \sqrt{\frac{4\pi}{2l+1}} Y_l^{m*}(\beta,\alpha)\,, \quad \text{(B.11)}$$

$$D^{l}_{m0}(\alpha,\beta,\gamma) = \sqrt{\frac{(l-m)!}{(l+m)!}} P^l_m(\cos\beta) e^{-im\alpha}\,. \quad \text{(B.12)}$$

  The small d-matrix elements can be also linked to the Legendre polynomials as defined in the following expressions:

$$d^{l}_{m0}(\beta) = \sqrt{\frac{(l-m)!}{(l+m)!}} P^l_m(\cos\beta)\,, \quad \text{(B.13)}$$

$$d^{l}_{00}(\beta) = P_l(\cos\beta) = D^{l}_{00}(\alpha,\beta,\gamma) \quad \text{(B.14)}$$

- Symmetries and special cases of d matrix:

$$d^{j}_{m',m}(\pi) = (-1)^{j-m}\delta_{m',-m}\,, \quad \text{(B.15)}$$

$$d^{j}_{m',m}(\pi-\beta) = (-1)^{j+m} d^{j}_{m',-m}(\beta)\,, \quad \text{(B.16)}$$

$$d^{j}_{m',m}(\pi+\beta) = (-1)^{j-m} d^{j}_{m',-m}(\beta)\,, \quad \text{(B.17)}$$

$$d^{j}_{m',m}(2\pi+\beta) = (-1)^{2j} d^{j}_{m',m}(\beta)\,, \quad \text{(B.18)}$$

$$d^{j}_{m',m}(-\beta) = d^{j}_{m,m'}(\beta) = (-1)^{m'-m} d^{j}_{m',m}(\beta)\,. \quad \text{(B.19)}$$

A list of the d-matrix elements is available in [115].

Appendix C

Threshold Behavior of PW

In Section 3.2.1, a discussion emerged regarding the necessity of a threshold correction factor for managing divergences in the amplitude as it approaches the threshold. Two distinct correction approaches were introduced:

$$R_1 = \left(\frac{|p_1|^{\text{off-shell}}}{|p_1|^{\text{on-shell}}} \right)^{l}, \tag{C.1}$$

$$R_2 = \left(\frac{|p_1|^{\text{off-shell}}}{|p_1|^{\text{on-shell}}} \right)^{l+\frac{1}{2}}. \tag{C.2}$$

In Figs.3.5 and 3.6, the P-wave results for both the real and imaginary components of the A^+ and A^- amplitudes were presented. These figures focused on a pion virtuality of $t_\pi = -0.1\text{GeV}^2$. Upon analyzing these results, it was concluded that the second approach appeared to be more effective. However, the absence of divergences in the pure off-shell scenario suggested that the off-shell model could proceed without the need for additional correction elements.

To provide additional support for this conclusion, supplementary figures, namely Figures C.1,C.2,C.3, and C.4, were prepared. These figures employed a color scheme where thick and dashed lines represented the real ($\mathbb{R}$) and imaginary ($\mathbb{IM}$) components, respectively, for each case:

- Green indicated the on-shell case at $t_\pi = m_\pi^2$.
- **Black** designated the pure off-shell scenario with no additional terms at $t_\pi = -0.1$ GeV^2.
- Blue corresponded to the off-shell case with the inclusion of R_1 as a correction factor.
- Red represented the off-shell case with the presence of R_2 as an additional correction factor.

The analysis of these results yields the following insights:

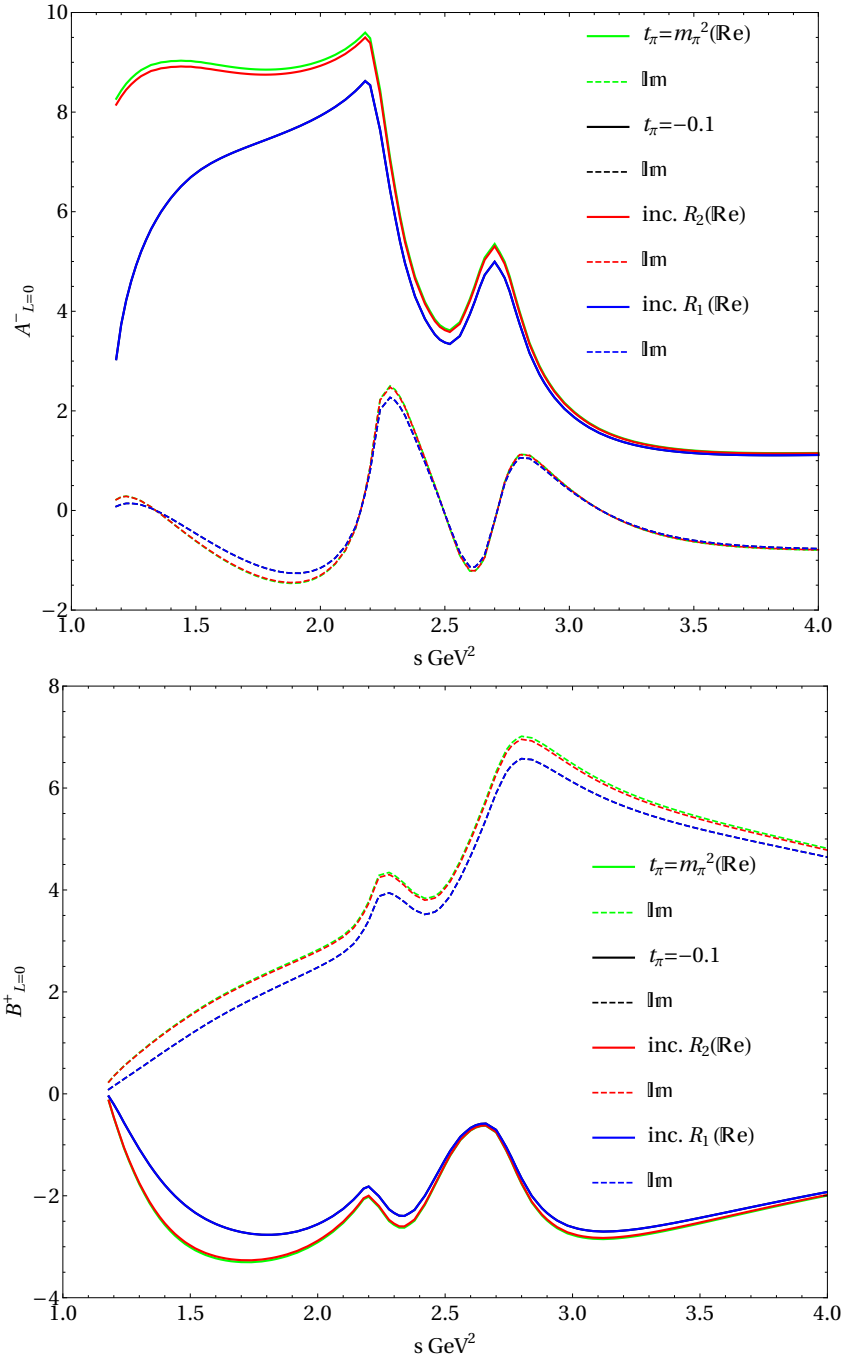

Figure C.1: S-wave results for A^- and B^+ at $t = -0.1$ GeV^2 and for $t_\pi = -0.1$ GeV^2

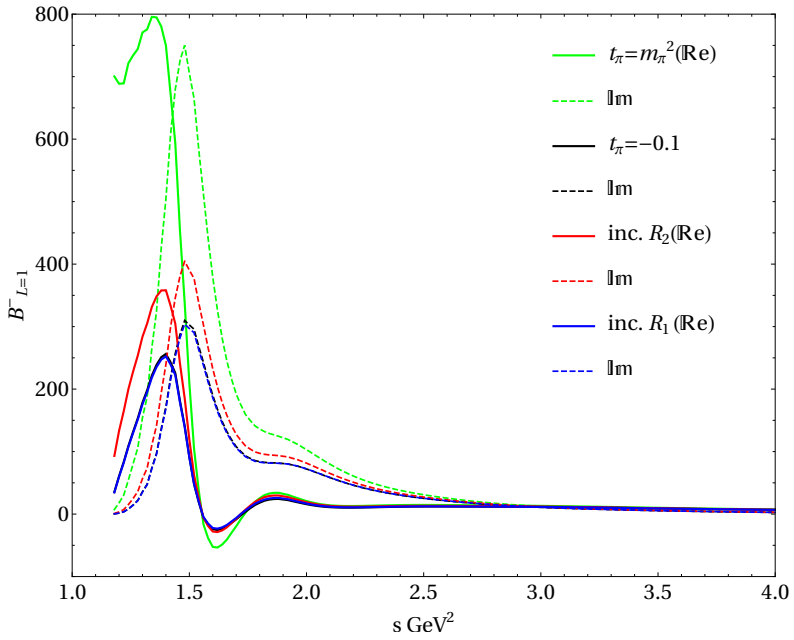

Figure C.2: P-wave results for B^- at $t = -0.1$ GeV^2 and $t_\pi = -0.1$ GeV^2

✓ For $L = 0$, the addition of R_1 to the partial waves has no discernible impact on the off-shell results, which remain nearly identical. In contrast, using R_2 tends to emulate the behavior of the on-shell case.

✓ Similarly, for $L = 1$, the introduction of R_1 does not alter the off-shell values significantly, while R_2 brings them closer to the on-shell behavior.

✓ In the cases of both S and P waves, the outcomes from all scenarios appear to coincide for energies above $s = 2.5$ GeV^2.

✓ Both correction factors demonstrate efficiency for $L = 2$. However, it is worth noting that across the entire energy range, the pure off-shell case closely approximates the on-shell behavior.

✓ Likewise, akin to the D-wave, the results from all cases exhibit close alignment across the entire energy spectrum.

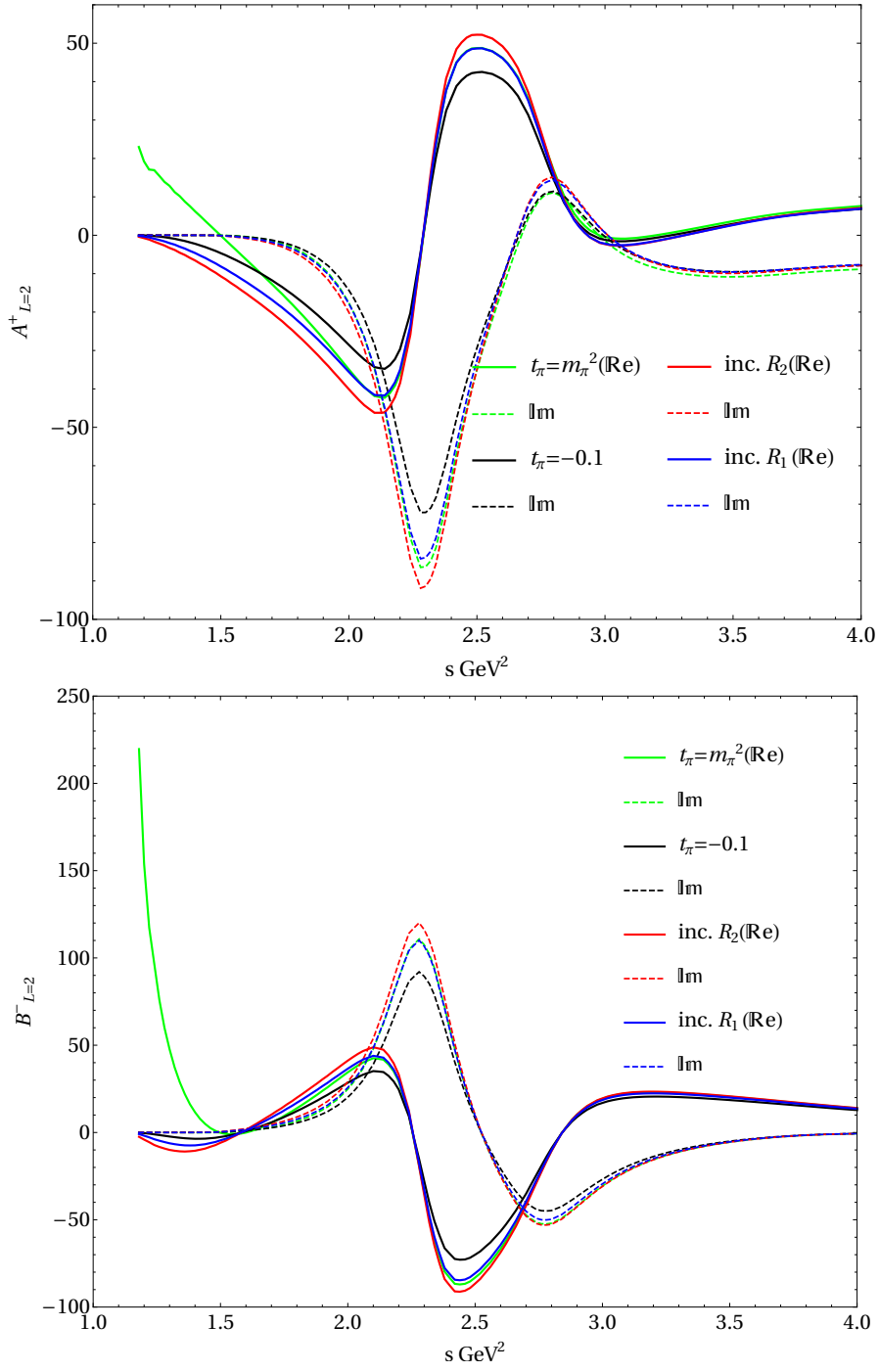

Figure C.3: D-wave results for A^+ and B^- at $t = -0.1$ GeV^2 and for $t_\pi = -0.1$ GeV^2

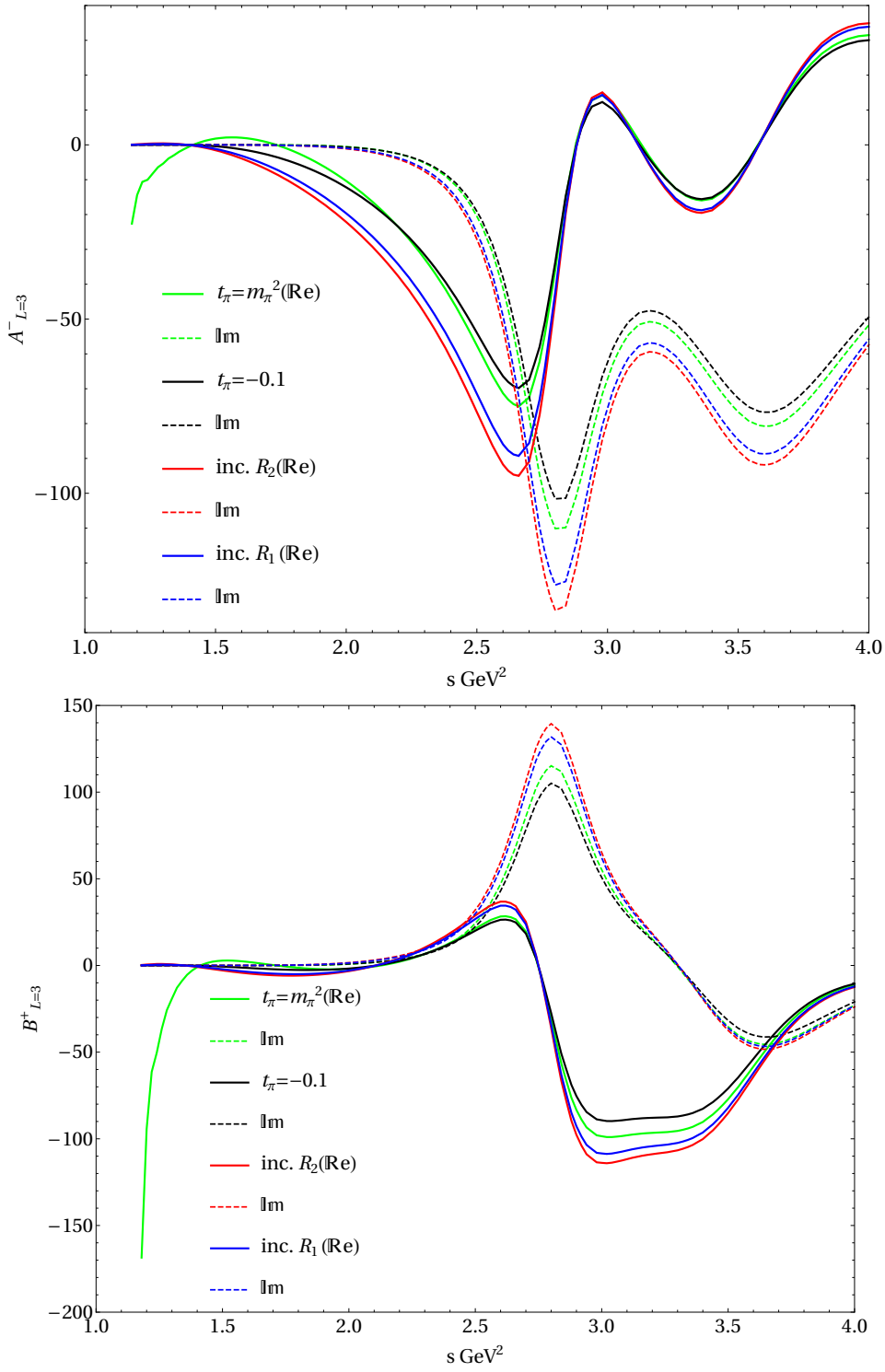

Figure C.4: F-wave results for A^- and B^+ at $t = -0.1$ GeV^2 and for $t_\pi = -0.1$ GeV^2

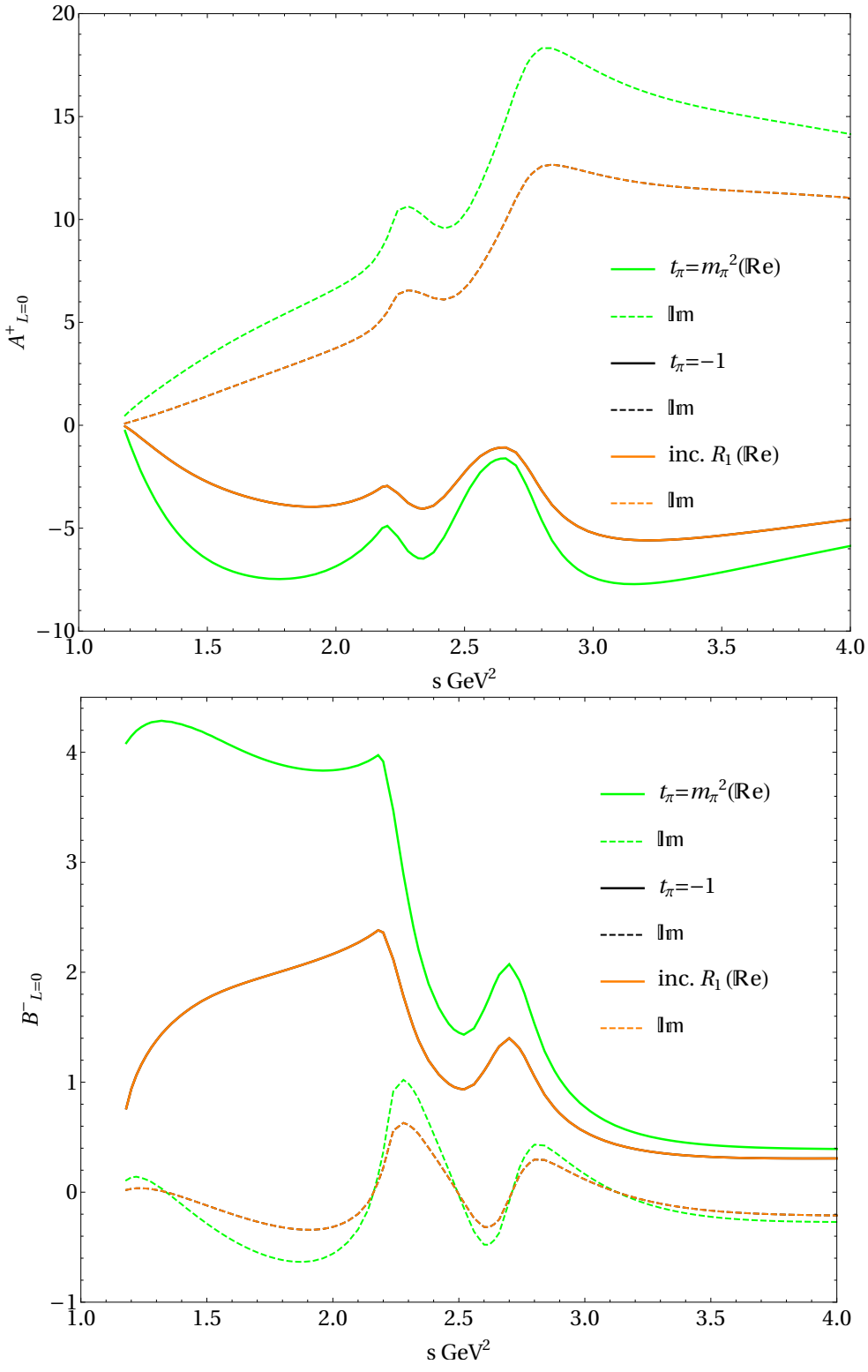

Figure C.5: S-wave results for A^+ and B^- at $t = -0.1$ GeV^2 and $t_\pi = -1$ GeV^2

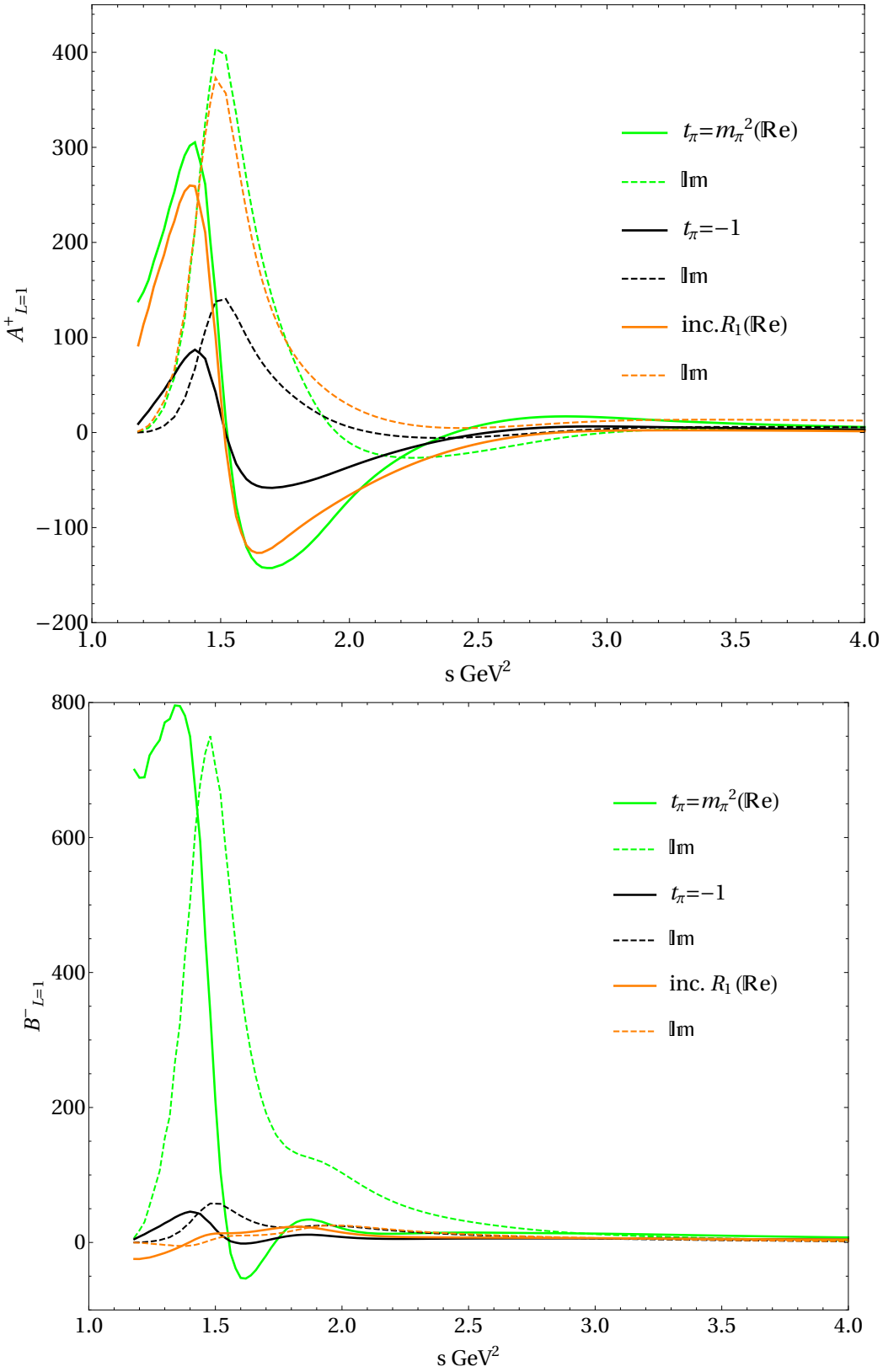

Figure C.6: P-wave results for A^+ and B^- at $t = -0.1$ GeV^2 and $t_\pi = -1$ GeV^2

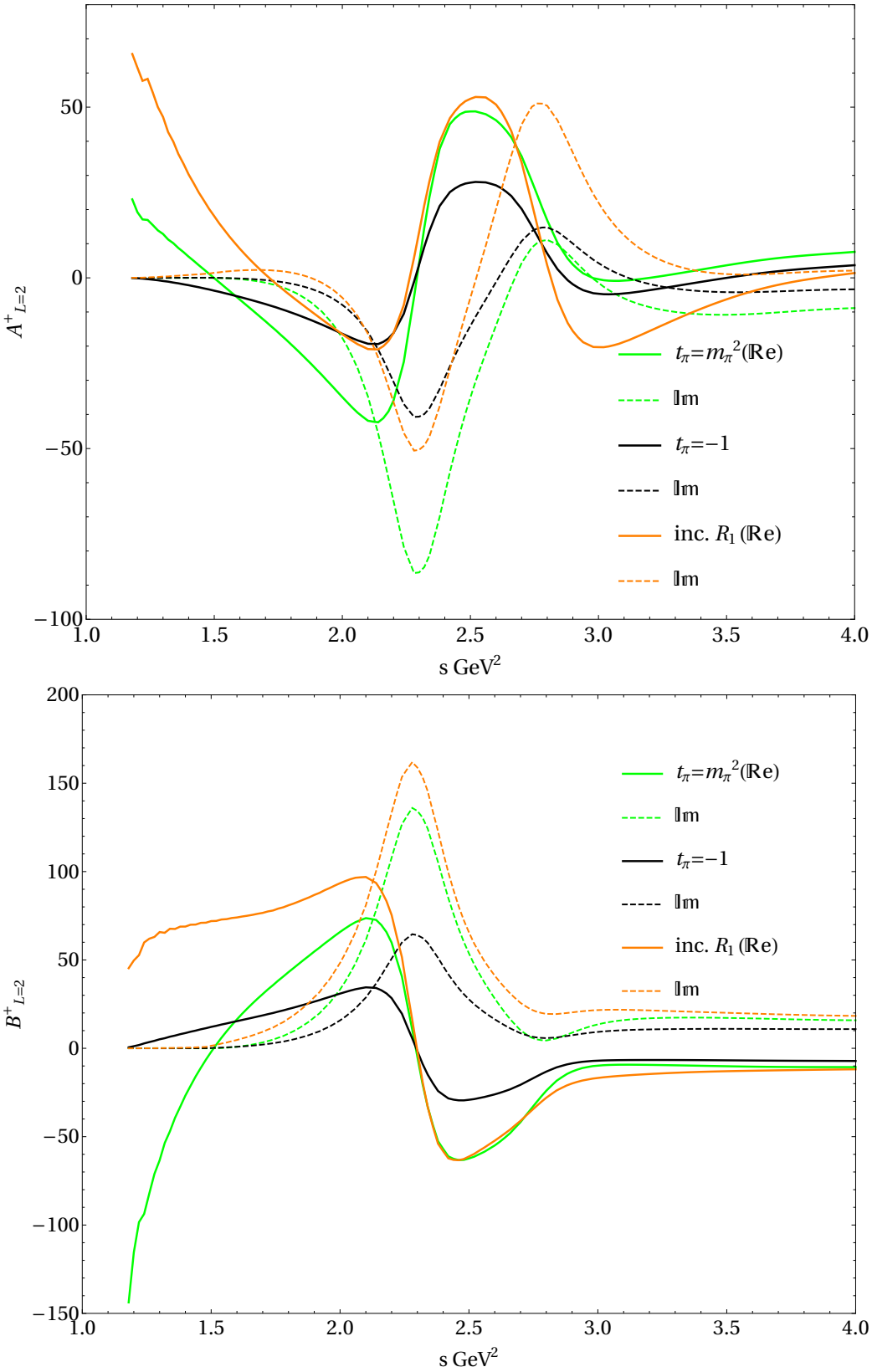

Figure C.7: D-wave results for A^+ and B^+ at $t = -0.1$ GeV^2 and $t_\pi = -1$ GeV^2

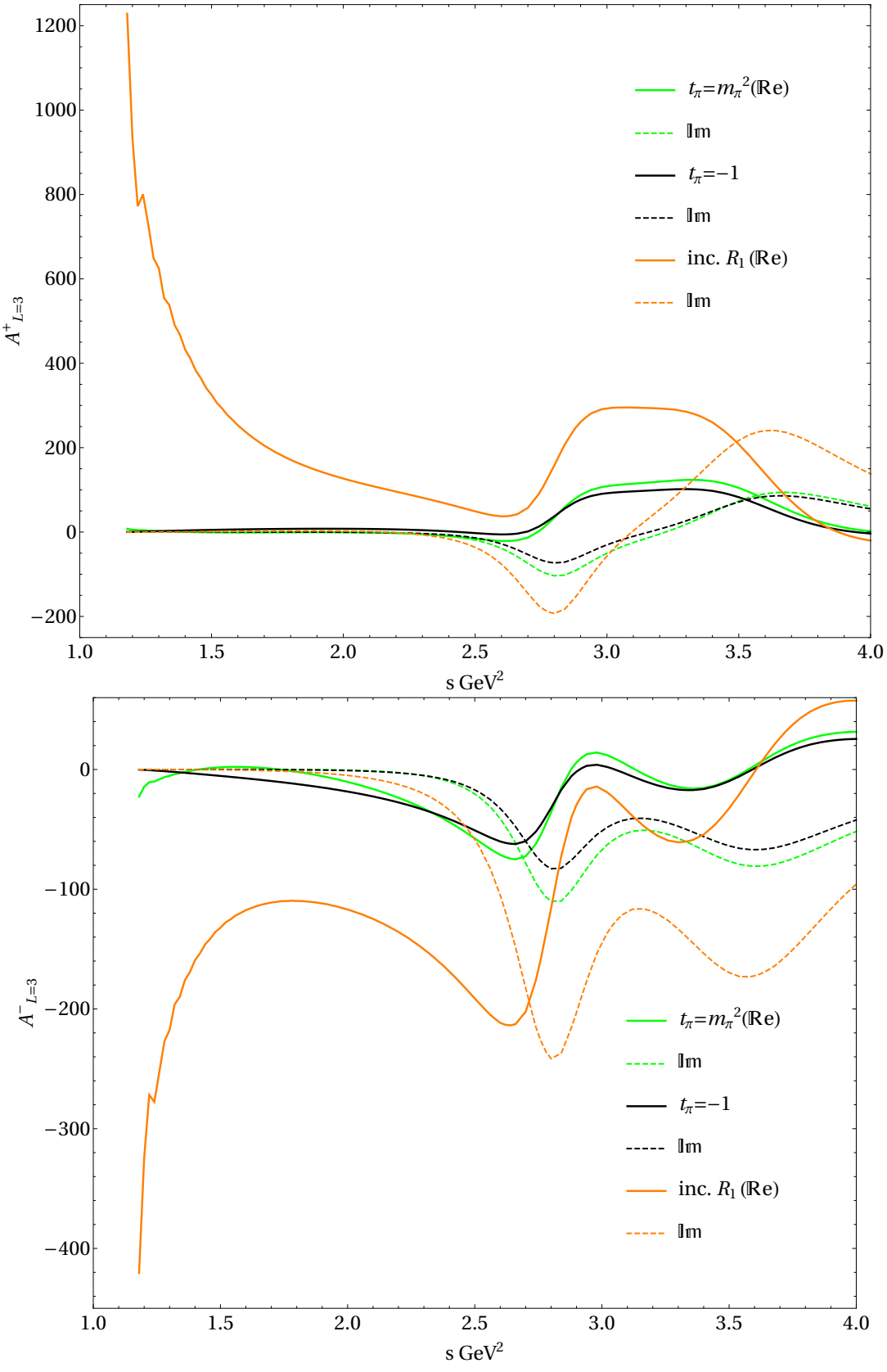

Figure C.8: F-wave results for $A^\pm_{L=3}$ at $t = -0.1$ GeV^2 and $t_\pi = -1$ GeV^2

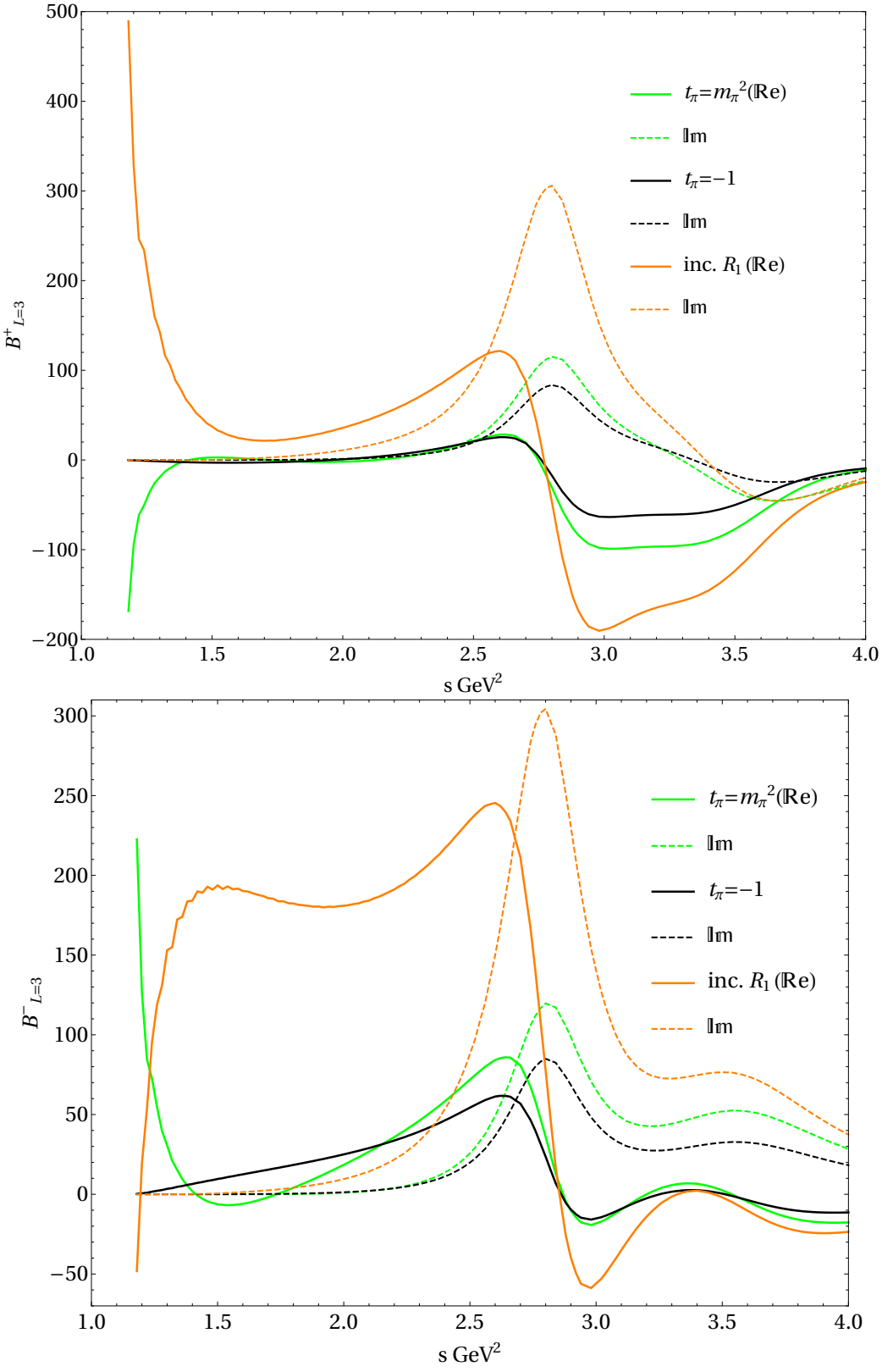

Figure C.9: F-wave results for $B^{\pm}$ at $t = -0.1$ GeV^2 and $t_\pi = -1$ GeV^2

This preliminary analysis focused on a small t_π. Now, an investigation into the impact of a larger pion virtuality is undertaken. To this end, Figures C.5, C.6, C.7, C.8, and C.9 present the A and B amplitudes for S, P, D, and F waves at $t = -0.1$ GeV^2 with $t_\pi = -1$ GeV^2. In these figures, a color scheme is employed, with thick lines representing the real ($\mathbb{R}$) parts and dashed lines denoting the imaginary ($\mathbb{IM}$) parts, with the following color codes:

- Green: On-shell case at $t_\pi = m_\pi^2$.
- **Black**: Pure off-shell scenario with no additional terms at $t_\pi = -1$ GeV^2.
- Orange: Off-shell case with the addition of R_1 as a correction factor.

These figures offer a comprehensive overview of how various factors influence amplitude behavior under conditions of higher pion virtuality. Observing this data leads to several key observations:

✓ Similar to the scenario with small virtuality, the utilization of R_1 for the S wave appears unnecessary, as it yields results similar to those without it.

✓ In the case of the P wave, the introduction of R_1 enhances the A values, but it has negligible effects on the B amplitude.

✓ Interestingly, for high virtuality, all scenarios exhibit convergence in both S and P waves for energies exceeding $s = 2.5$ GeV^2.

✓ Notably, the introduction of a threshold correction factor leads to peculiar behavior in the D wave amplitude below 2 GeV^2, whereas the pure off-shell case maintains a more stable behavior across the entire energy spectrum.

✓ The unconventional behavior of the amplitudes with the extended correction factor is vividly demonstrated in Figures C.8 and C.9 for the F wave. In contrast, the pure off-shell outcomes closely resemble the on-shell ones. Consequently, this discovery underscores the considerable risks associated with the incorporation of an additional term, particularly at high pion virtuality.

$\Rightarrow$ Therefore, it is advisable to proceed with the off-shell case without introducing any supplementary terms, as this approach appears to yield more stable and reliable results, especially under conditions of elevated pion virtuality.

Appendix D

Moments and Partial Waves

This appendix offers a detailed presentation of the explicit expressions for the moments sourced from the reference [cite source]. These moments, as defined in Eq.(4.12), are expressed in the context of partial waves truncated to the $L = 3$ (F) wave:

$$
\begin{aligned}
\langle Y_{00} \rangle &= |S|^2 + |P_-|^2 + |P_0|^2 + |P_+|^2 + |D_-|^2 + |D_0|^2 + |D_+|^2 + |F_-|^2 + |F_0|^2 + |F_+|^2 \\
\langle Y_{10} \rangle &= SP_0^* + P_0 S^* + \sqrt{\frac{3}{5}} \left(P_- D_-^* + P_-^* D_- + P_+ D_+^* + D_+ P_+^* \right) + \sqrt{\frac{4}{5}} \left(P_0 D_0^* + D_0 P_0^* \right) \\
&+ \sqrt{\frac{24}{35}} \left(D_- F_-^* + F_- D_-^* + D_+ F_+^* + F_+ D_+^* \right) + \sqrt{\frac{216}{280}} \left(D_0 F_0^* + F_0 D_0^* \right) \\
\langle Y_{11} \rangle &= \left(-P_- S^* - S P_-^* + P_+ S^* + S P_+^* \right) + \sqrt{\frac{1}{20}} \left(P_- D_0^* + D_0 P_-^* - P_+ D_0^* - D_0 P_+^* \right) \\
&+ \sqrt{\frac{3}{20}} \left(-P_0 D_-^* - D_- P_0^* + P_0 D_+^* + D_+ P_0^* \right) \\
&+ \sqrt{\frac{9}{140}} \left(D_- F_0^* + F_0 D_-^* - D_+ F_0^* - F_0 D_+^* \right) \\
&+ \sqrt{\frac{9}{70}} \left(-D_0 F_-^* - F_- D_0^* + D_0 F_+^* + F_+ D_0^* \right)
\end{aligned}
$$

$$
\begin{aligned}
\langle Y_{20}\rangle &= SD_0^* + D_0S^* + \sqrt{\frac{1}{5}}\left(2|P_0|^2 - |P_-|^2 - |P_+|^2 + |F_-|^2 + |F_+|^2\right) \\
&+ \sqrt{\frac{18}{35}}\left(P_-F_-^* + F_-P_-^* + P_+F_+^* + F_+P_+^*\right) \\
&+ \sqrt{\frac{27}{35}}\left(P_0F_0^* + F_0P_0^*\right) + \sqrt{\frac{5}{49}}\left(|D_-|^2 + |D_+|^2\right) + \sqrt{\frac{20}{49}}|D_0|^2 + \sqrt{\frac{16}{45}}|F_0|^2 \\
\langle Y_{21}\rangle &= \frac{1}{2}\left(SD_+^* + D_+S^* - SD_-^* - D_-S^*\right) \\
&+ \sqrt{\frac{3}{20}}\left(P_0P_+^* + P_+P_0^* - P_-P_0^* - P_0P_-^*\right) \\
&+ \sqrt{\frac{9}{140}}\left(P_-F_0^* + F_0P_-^* - P_+F_0^* - F_0P_+^*\right) \\
&+ \sqrt{\frac{6}{35}}\left(P_0F_+^* + F_+P_0^* - P_0F_-^* - F_-P_0^*\right) \\
&+ \sqrt{\frac{5}{196}}\left(D_0D_+^* + D_+D_0^* - D_0D_-^* - D_-D_0^*\right) \\
&+ \sqrt{\frac{1}{90}}\left(F_0F_+^* + F_+F_0^* - F_0F_-^* - F_-F_0^*\right) \\
\langle Y_{22}\rangle &= \sqrt{\frac{3}{10}}\left(P_-P_+^* + P_+P_-^*\right) + \sqrt{\frac{3}{140}}\left(P_-F_+^* + F_+P_-^* + P_+F_-^* + F_-P_+^*\right) \\
&+ \sqrt{\frac{4}{30}}\left(-F_+F_-^* - F_-F_+^*\right) + \sqrt{\frac{3}{196}}\left(-D_-D_+^* - D_+D_-^*\right) \\
\langle Y_{30}\rangle &= SF_0^* + F_0S^* + \sqrt{\frac{18}{70}}\left(-P_-D_-^* - D_-P_-^* - P_+D_+^* - D_+P_+^*\right) \\
&+ \sqrt{\frac{108}{140}}\left(P_0D_0^* + D_0P_0^*\right) + \sqrt{\frac{2}{45}}\left(D_-F_-^* + F_-D_-^* + D_+F_+^* + F_+D_+^*\right) \\
&+ \sqrt{\frac{16}{45}}\left(D_0F_0^* + F_0D_0^*\right) \\
\langle Y_{31}\rangle &= \frac{1}{2}\left(SF_+^* + F_+S^* - SF_-^* - F_-S^*\right) \\
&+ \sqrt{\frac{18}{140}}\left(P_+D_0^* + D_0P_+^* - P_-D_0^* - D_0P_-^*\right) \\
&+ \sqrt{\frac{6}{35}}\left(P_0D_+^* + D_+P_0^* - P_0D_-^* - D_-P_0^*\right) \\
&+ \sqrt{\frac{1}{90}}\left(D_+F_0^* + F_0D_+^* - D_-F_0^* - F_0D_-^*\right) \\
&+ \sqrt{\frac{1}{20}}\left(D_0F_+^* + F_+D_0^* - D_0F_-^* - F_-D_0^*\right)
\end{aligned}
$$

$$
\begin{aligned}
\langle Y_{32}\rangle &= \sqrt{\frac{3}{14}}\left(-P_+D_-^* - D_-P_+^* - P_-D_+^* - D_+P_-^*\right)\\
&+ \sqrt{\frac{1}{12}}\left(-D_+F_-^* - F_-D_+^* - D_-F_+^* - F_+D_-^*\right)\\
\langle Y_{40}\rangle &= \sqrt{\frac{2}{7}}\left(-P_+F_+^* - F_+P_+^* - P_-F_-^* - F_-P_-^*\right) + \sqrt{\frac{16}{21}}\left(P_0F_0^* + F_0P_0^*\right)\\
&+ \sqrt{\frac{16}{49}}\left(-|D_+|^2 - |D_-|^2\right) + \sqrt{\frac{36}{49}}|D_0|^2\\
&+ \sqrt{\frac{36}{121}}|F_0|^2 + \sqrt{\frac{1}{121}}\left(|F_+|^2 + |F_-|^2\right)\\
\langle Y_{41}\rangle &= \sqrt{\frac{5}{42}}\left(P_+F_0^* + F_0P_+^* - P_-F_0^* - F_0P_-^*\right)\\
&+ \sqrt{\frac{5}{28}}\left(P_0F_+^* + F_+P_0^* - P_0F_-^* - F_-P_0^*\right)\\
&+ \cdot\sqrt{\frac{30}{196}}\left(D_0D_+^* + D_+D_0^* - D_-D_0^* - D_0D_-^*\right)\\
&+ \sqrt{\frac{30}{968}}\left(F_0F_+^* + F_+F_0^* - F_0F_-^* - F_-F_0^*\right)\\
\langle Y_{42}\rangle &= \sqrt{\frac{5}{28}}\left(-P_+F_-^* - F_-P_+^* - P_-F_+^* - F_+P_-^*\right) + \sqrt{\frac{10}{49}}\left(-D_-D_+^* - D_+D_-^*\right)\\
&+ \sqrt{\frac{10}{121}}\left(-F_-F_+^* - F_+F_-^*\right)
\end{aligned}
$$

Appendix E

J_{NonRel}

Form factors used in this analysis have form

$$g_{\alpha,j}(p) = c\sqrt{\frac{4\pi}{m_\alpha}}\frac{p}{(p^2+(\beta_{\alpha,j})^2)^2} \tag{E.1}$$

where α denotes the channel under consideration, j term in multi-order potentials and c is constant used for normalization of the Jost function (after integration) to 1 at $k_\alpha = 0$. Using formalism presented in Section 6.2 for norelativistic energies in propagator one gets expression for the Jost function:

$$J_{\alpha,aa}(k_\alpha) = 4\,c^2\,\pi\int_0^\infty \frac{dp\,p^4}{(k_\alpha^2-p^2)(\beta_{\alpha,a}^2+p^2)^4} \tag{E.2}$$

which after integration and after inserting the value of the constant c gives:

$$J_{\alpha,aa}(k_\alpha) = \frac{-1+\frac{4ik_\alpha}{\beta_a}+\frac{k_\alpha^2}{\beta_a^2}}{(1-\frac{ik_\alpha}{\beta_a})^4}\,, \tag{E.3}$$

Analogous calculations give the result on the integral for the second-order potential (in Eq. 6.24):

$$J_{\alpha,ab}(k) = \frac{-1+\frac{2i(\beta_a+\beta_b)k_\alpha}{\beta_a\beta_b}+\frac{k_\alpha^2}{\beta_a\beta_b}}{\left(1-\frac{ik_\alpha}{\beta_a}\right)^2\left(1-\frac{ik_\alpha}{\beta_b}\right)^2}. \tag{E.4}$$

Scattering length for rank-one potential can be calculated analytically and reads:

$$a_P = \frac{-16\Lambda_\alpha}{\beta_\alpha^3(1+\Lambda_\alpha)} \tag{E.5}$$

and for the rank-two potential has the form[1]:

$$a_P = -4\frac{4\beta_{\alpha,b}^3\Lambda_{\alpha,a}+4\beta_{\alpha,a}^3\Lambda_{\alpha,b}+3\Lambda_{\alpha,a}\Lambda_{\alpha,b}(\beta_{\alpha,a}^3-\beta_{\alpha,a}^2\beta_{\alpha,b}-\beta_{\alpha,a}\beta_{\alpha,b}^2+\beta_{\alpha,b}^3)}{\beta_{\alpha,a}^3\beta_{\alpha,b}^3(1+\Lambda_{\alpha,a}+\Lambda_{\alpha,b})}. \tag{E.6}$$

[1]analytical expressions for the three-channel model described in this paper are very long but can be obtained after prior inquiry to Nadine.Hammoud@ifj.edu.pl

Appendix F

J_{Rel}

The formula below is for the diagonal element of the Jost function matrix (Eq. 6.14) and for a channel with two identical particle masses (channels 1 and 3 in this analysis). To increase the readability of the formula, the channel and term indicator in the rank-two potential are omitted. This formula takes into account redefinition (6.18) and normalization to 1 for $k = 0$.

$$
\begin{aligned}
J = & \frac{(1+a^2)^{-4}}{3b\sqrt{(1-b^2)}\pi + s\Big(8(1-b^2) + 3b^3(2b - 2\pi + b^2\pi)\Big) - 3(2-b^2)b^4 Ld} \times \\
& \Big[3(-2+b^2)b^4 Lg + \Big(8 - 8b^2 + 6b^4 + 3\pi E(1 - 2b^2 + b^4)\Big)s + \\
& a^6 s\Big(-16 + 28b^2 - 6b^4 - 3\pi E(1-b^2)^2\Big) - 3a^4\Big((-16 + 40b^2 - 30b^4 + 9b^6)Lg + \\
& s\Big(-8 + 16b^2 - 14b^4 + 9\pi E(1-b^2)^2\Big)\Big) + 3a^2\Big(Lg\, b^2(8 - 20b^2 + 9b^4) + \\
& s\Big(16 - 28b^2 + 18b^4 + 9\pi E(1-b^2)^2\Big)\Big) + 24a^3 E\Big((1-b^2)^2 2sL + 2i\pi(1-b^2)^{5/2}\Big)\Big] \qquad \text{(F.1)}
\end{aligned}
$$

where

$$
\begin{aligned}
a =& k/\beta, \\
b =& m/\beta, \\
s =& \sqrt{1-b^2}, \\
L =& \log\left(\frac{a-\sqrt{a^2+b^2}}{a+\sqrt{a^2+b^2}}\right), \\
E =& \sqrt{a^2+b^2}, \\
Lg =& \log\left(\frac{1+s}{1-s}\right), \\
Ld =& \log\left(\frac{1-b^2+s}{-1+b^2+s}\right).
\end{aligned}
\tag{F.2}
$$

The formula below is for the non-diagonal element of the Jost function matrix (Eq. 6.14) and for a channel with two identical particle masses. This formula takes into account redefinition 6.18 and normalization to 1 for $k = 0$.

In order to shorten the expression for the Jost functions, the $\alpha = 1$ index denoting the tested channel has been omitted. Here indices 1 and 2 numer the term in the rank-two potiential in the $\pi\pi$ channel.

$$
\begin{aligned}
J_{12} = &\Bigg\{(a_1a_2+r)^2(1+a_1a_2r)^2\Big[iL_c\Big(b_1(b_2+3b_2r^2)-2(r+r^3)\Big)s_b - iL_br\Big(-2(1+r^2)+ \\
&b_1b_2r(3+r^2)\Big)s_c - (1-r)\sqrt{r}\Big(\sqrt{b_1b_2}\pi(1-r)^2+4\sqrt{r}(1+r)\Big)s_bs_c\Big]\Bigg\}^{-1}\times \\
&r\Bigg\{iL_cr\Big(b_1(b_2+3b_2r^2)-2(r+r^3)\Big)s_b - iL_br^2\Big(-2(1+r^2)+b_1b_2r(3+r^2)\Big)s_c+ \\
&2(a_1a_2)^{3/2}(L+i\pi)(1-r^2)^3s_as_bs_c-(1-r)r^{3/2}(4\sqrt{r}+4r^{3/2}-\pi s_a+2\pi rs_a-\pi r^2s_a)s_bs_c+ \\
&a_1^2a_2^2\Big[iL_cr\Big(3b_1b_2(2+r^2+r^4)-2r(4+r^2+r^4)\Big)s_b+iL_b\Big(2+2r^2+8r^4-3b_1b_2r(1+r^2+2r^4)\Big)s_c+ \\
&(-1+r)(2+2r+8r^2+8r^3+2r^4+2r^5+3\pi\sqrt{r}s_a-3\pi r^{3/2}s_a-3\pi r^{7/3}s_a+3\pi r^{9/2}s_a)s_bs_c\Big]+ \\
&a_1a_2\Big[iL_c\Big(3b_1b_2(1+r^2+2r^4)-4(r+r^3+r^5)\Big)s_b+iL_br\Big(4(1+r^2+r^4)-3b_1b_2r(2+r^2+r^4)\Big)s_c- \\
&3\sqrt{r}(2\sqrt{r}-2r^{9/2}-\pi s_a+2\pi rs_a-\pi r^2s_a+\pi r^3s_a-2\pi r^4s_a+\pi r^5s_a)s_bs_c\Big]+ \\
&a_1^3a_2^3r\Big[-4iL_cr^2s_b+4iL_br^2s_c+\Big(-2+2r^4+\pi(-1+r)^3\sqrt{r}s_a\Big)s_bs_c+ \\
&ib_1b_2r\Big(L_c(3+r^2)s_b-L_b(1+3r^2)s_c\Big)\Big]\Bigg\}
\end{aligned}
\tag{F.3}
$$

where

$$
\begin{aligned}
a_1 =& k/\beta_1, \quad a_2 = k/\beta_2, \\
b_1 =& m/\beta_1, \quad b_2 = m/\beta_2, \\
r =& \beta_1/\beta_2, \\
s_a =& \sqrt{a_1 a_2 + b_1 b_2}, \\
s_b =& \sqrt{-1 + b_1 b_2 r}, \\
s_c =& \sqrt{-1 + \frac{b_1 b_2}{r}}, \\
L =& \log\Big[\frac{\sqrt{a_1 a_2} - \sqrt{a_1 a_2 + b_1 b_2}}{\sqrt{a_1 a_2} + \sqrt{a_1 a_2 + b_1 b_2}}\Big], \\
L_c =& \log\Big[\frac{1 - i s_c}{1 + i s_c}\Big], \\
L_b =& \log\Big[\frac{1 - i s_b}{1 + i s_b}\Big].
\end{aligned}
\tag{F.4}
$$

Procedure of calculation of the Jost function matrix elements (Eq. 6.14) for the case of potential with different masses (for this analysis it is channel 2 - $\omega\pi$) is presented below. The integrals can not be expressed by analytical formulae and numerical method has been applied.

Derivation of the expression for the diagonal elements for real k momentum:

Substitution

$$y = \sqrt{\frac{p^2}{p^2 + 4m_2^2}} \tag{F.5}$$

gives

$$p = \frac{2 m_\omega m_\pi y}{\sqrt{(m_\omega + m_\pi)^2 (y^2 - 1)}} \tag{F.6}$$

where $m_2 = \frac{m_\omega m_\pi}{m_\omega + m_\pi}$.

Thanks to this substitution, the integration in Eq. (6.15) reduces to the area of y: $(0, 1)$ instead of $(0, \infty)$ for p. Due to the singularity in this region (for some real k), however, it must be a Cauchy integral. This singularity appears at

$$sing = \frac{k\sqrt{m_1 - m_2}(m_1 + m_2)}{\sqrt{(m_1 - m_2)(4m_1^2 m_2^2 + k^2(m_1 + m_2)^2)}}\,. \tag{F.7}$$

The residue resulting from the omission of this pole has the form (for readability, the normalisation coefficient for $k = 0$ has been omitted)

$$\text{Residue} = -\frac{k^3\sqrt{k^2+m_1^2}\sqrt{k^2+m_2^2}}{(b^2+k^2)^4(\sqrt{k^2+m_1^2}+\sqrt{k^2+m_2^2})}\,. \tag{F.8}$$

For the non-diagonal element of the matrix of the Jost function, the singularity is in the same place as for the diagonal element (does not depend on β parameter), while the residue is given by

$$\text{Residue} = -\frac{k^3\sqrt{(k^2+m_1^2)}\sqrt{(k^2+m_2^2)}}{(b_1^2+k^2)^2(b_2^2+k^2)^2(\sqrt{k^2+m_1^2}+\sqrt{k^2+m_2^2})}\,. \tag{F.9}$$

After determining the real parts of integrals (Cauchy($sing$)) and imaginary parts (Residue), the complex value of the Jost function is expressed by the sum of these terms.

$$J = \text{Cauchy}(sing) + i\pi\text{Residue} \tag{F.10}$$

For complex values of momentum k, one can compute the real and imaginary parts of the elements of the Jost function matrix, integrate them over y, and add them.

All integrals have been normalized to 1 at k = 0.

In the presented analysis, the scattering length was not calculated analytically due to the need to numerically count the Jost function in channel 2[1].

To check procedures of derivations and formulea for singularities and Residues presented above for real k (for fits to phase shifts and inelasticities) and algoritm for complex k (for analyses of poles of amplitudes) the same method has been applied for potentials with two identical masses (channel 1 and 3 in this analysis). Results obtained using analytical expressions in Eqs (F.1)-(F.4) and numerical values obtained using Cauchy theorem with residues described above were identical.

[1] Analytical expressions for rank one potential available after prior inquiry to Nadine.Hammoud@ifj.edu.pl

Bibliography

[1] Robert T. Deck,
"Kinematical interpretation of the first $\pi - \rho$ resonance",
Phys. Rev. Lett. **13**, 169 (1964)

[2] G. Aad et al., Phys. Lett. B **716** (2012)

[3] S. Chatrchyan et al., Phys. Lett. B **716** (2012)

[4] Ahmed Marwan Abdelrahman Foda,
"Photoproduction of the $b_1(1235)$ Meson off the proton at E_γ= 6-12 GeV",
Ph.D. thesis, University of Regina, January (2021)

[5] M. Gell-Mann,
"A Schematic Model of Baryons and Mesons",
Physics Letters. **8**, 214 (1964)

[6] G. Zweig, *"An SU(3) Model for Strong Interaction Symmetry and its Breaking"*, CERN Report No.8182/TH.401

[7] M. Gell-Mann,
"The Eightfold Way: A Theory of strong interaction symmetry",
(No. TID-12608; CTSL-20). California Inst. of Tech., Pasadena. Synchrotron Lab, (1961)

[8] M. Gell-Mann,
"Symmetries of baryons and mesons",
Physical Review **125**: 3, 1067, (1962)

[9] O.W. Greenberg, Phys. Rev. Lett. **13** (1964), 598–602

[10] J.M. Richard, *"An intriduction to the quark model"*, arXiv:1205.4326 [hep-ph]

[11] H. Kastrup, P. Zerwas, eds., QCD 20 Years Later, World Scientific , Singapore (1993)

[12] F. Yndurain, *"The Theory of Quark and Gluon Interactions"*,
Springer, (2006)

[13] R. Feynman, *QED: The Strange Theory of Light and Matter Princeton University Press*, Princeton, N. J. (1985)

[14] G. Leibbrandt, Rev. Mod. Phys. **59**, 1067 (1987)

[15] L. D. Faddeev and V. N. Popov, Phys. Lett. B **25**, 29 (1967)

[16] D. J. Gross and F. Wilczek, Phys. Rev. D **8**, 3633 (1973)

[17] D. J. Gross and F. Wilczek, Phys. Rev. D **9**, 980 (1974)

[18] D. J. Gross and F. Wilczek, Phys. Rev. Lett. **30**, 1343 (1973)

[19] H. D. Politzer,Phys. Rev. Lett. **30**, 1346 (1973)

[20] Jason Ho,
"Beyond the Conventional Quark Model: Using QCD Sum Rules to Explore the Spectrum of Exotic Hadrons",
Ph.D. thesis, Department of Physics and Engineering Physics, University of Saskatchewan, June (2020)

[21] S. Dinter,
"Analysis of Final States with π^0 and η Mesons produced in $\pi - p$ interactions and Studies of the Electromagnetic Calorimeters at COMPASS",
Diploma thesis, Ludwig-Maximilians-Universität München, (2010)

[22] J. Hedditch,
"1^{+-} exotic meson at light quark masses",
Phys. Rev.D **72**: 1-17, (2005)

[23] T. Manke,
"Hybrid quarkonia on asymmetric lattices",
Phys. Rev.Lett. **82**: 4396-4399, (1999)

[24] C. Morningstar und M. Peardon,
"The Glueball spectrum from an anisotropic lattice study",
Phys. Rev. D **60**: 1-13, (1999)

[25] P. Lacocket al.(UKQCD), Phys. Lett.B **401**, 308 (1997), [hep-lat/9611011]

[26] Colin J. Morningstar, Mike Peardon,
"The glueball spectrum from an anisotropic lattice study",
Phys.Rev.D **60**: 034509, (1999), [arXiv:hep-lat/9901004]

[27] C. A. Meyer and E. S. Swanson, Prog. Part. Nucl. Phys. **82**, 21-58 (2015).

[28] E. Klempt and A. Zaitsev, Phys. Rept. **454**, 1-202 (2007).

[29] J. J. Dudek, R. G. Edwards, M. J. Peardon, D. G. Richards, and C. E. Thomas, *"Toward the excited meson spectrum of dynamical QCD"*, Phys. Rev., vol. D **82**, p. 034508, (2010)

[30] BESIII Collaboration, M. Ablikim et al., Phys. Rev. Lett. **110**, 252001 (2013)

[31] Belle Collaboration, Z. Q. Liu et al., Phys. Rev. Lett. **110**, 252002 (2013)

[32] LHCb Collaboration, R. Aaij et al., Phys. Rev. Lett. **115**, 072001 (2015)

[33] LHCb Collaboration, R. Aaij et al., Phys. Rev. Lett. **117**, 152003 (2016)

[34] GlueX Collaboration, H. Al Ghoul et al., AIP Conf. Proc. 1735, 20001 (2016)

[35] Curtis A. Meyer, *"Light and exotic mesons"*, Carnegie Mellon University, Pittsburgh, PA 15213

[36] Daniel Alberto Stanischesk Molnar, *"The Role of Exotic Mesons and Final State Interactions in e^+e^- Collisions"*, Ph.D. thesis, Department of Physics, Mathematics and Computer Science at the Johannes Gutenberg University of Mainz, (2022)

[37] J. A. Wheeler, *"On the mathematical description of light nuclei by the method of resonating group structure"*, Phys. Rev. **52**, 1107–1122 (1937)

[38] W. Heisenberg, *"The observable quantities in the theory of elementary particles"*, magazine for physics **120**, 513–538 (1943)

[39] S. Mandelstam, *"Determination of the pion - nucleon scattering amplitude from dispersion relations and unitarity. General theory"*, Phys. Rev., **112**, pp. 1344– 1360, (1958)

[40] S. Mandelstam, *"Analytic properties of transition amplitudes in perturbation theory"*, Phys. Rev., **115**, pp. 1741–1751, (1959)

[41] M. Tanabashi et al. (Particle Data Group), *"Review of Particle Physics"*, Phys. Rev. D **98**, 030001 (2018)

[42] T. Regge, *"Introduction to complex orbital momenta"*, Nuovo Cim. 14 (1959) 951

[43] T. Regge, *"Bound states, shadow states and Mandelstam representation"*, Nuovo Cim.18 (1960) 947–956

[44] A. Sommerfeld,
"Partial Differential Equations in Physics",
Academic Press (1949), G.N.Watson, Proc, Roy, Soc 95(1918) 83

[45] A. Martin and T. Spearman, Elementary particle theory. North-Holland Pub.Co., 1970.

[46] P. D. B. Collins,
"An Introduction to Regge Theory and High-Energy Physics",
Cambridge Monographs on Mathematical Physics, Cambridge, UK: Cambridge Univ. Press, (2009)

[47] V. N. Gribov,
"The theory of complex angular momenta: Gribov lectures on theoretical physics",
Cambridge Monographs on Mathematical Physics, Cambridge University Press, (2007)

[48] L. B. Okun, *"The life and legacy of Pomeranchuk"*,
"International Conference: I.Ya. Pomeranchuk and Physics at the Turn of Centuries" ,
Moscow, Russia, January 24-28, (2003), pp. 3–20. 2003. arXiv:physics/0307123

[49] A. Donnachie and P. V. Landshoff,
"pp and anti-pp Elastic Scattering",
Nucl. Phys. B **231** (1984) 189–204

[50] A. Donnachie and P. V. Landshoff,
"Total cross-sections",
Phys. Lett. B **296** (1992) 227–232, arXiv:hep-ph/9209205

[51] V. Mathieu et al.
"Vector meson photoproduction with a linearly polarized beam",
Phys. Rev.D **97**, 094003 (2018), doi:PHYSICAL REVIEW D 97, 094003

[52] C. Amsler and N. A. Tornqvist,
"Mesons beyond the naive quark model",
Phys. Rept. **389** (2004) 61–117

[53] H. B. Meyer and M. J. Teper,
"Glueball Regge trajectories and the pomeron: A Lattice study",
Phys. Lett. B **605** (2005) 344–354, arXiv:hep-ph/0409183

[54] F. J. Llanes-Estrada, S. R. Cotanch, P. J. de A. Bicudo, J. E. F. T. Ribeiro, and A. P.Szczepaniak,
"QCD glueball Regge trajectories and the Pomeron",
Nucl. Phys. A **710** (2002) 45–54, arXiv:hep-ph/0008212

[55] M. N. Sergeenko,
"Glueballs and the Pomeron",
EPL 89 (2010), no. 1, 11001, arXiv:1107.1671

[56] K. Schilling, P. Seyboth and G.E. Wolf,
"On the Analysis of Vector Meson Production by Polarized Photons",
Nucl.Phys., B **15**:397–412, (1970)

[57] K. Blum, *"Density Matrix Theory and Applications"*, Springer, (2012)

[58] J.J. Sakurai, *" Theory of strong interactions"*, Ann. Phys.(NY), 11:1, (1960)

[59] T.H. Bauer et al.,
" The hadronic properties of the photon in high-energy interactions",
Reviews of Modern Physics, **50**(2):261, (1978)

[60] J. J. Sakurai,
"Vector meson dominance and high-energy electron proton inelastic scattering",
Phys. Rev. Lett. **22** (1969) 981–984

[61] A. P. Szczepaniak,
"Role of photo production in exotic meson searches", Phys. Lett. B **516**:72–76, (2001)

[62] T. Skorodumina et al.,
"Observation of new structure in the $\eta\pi$ system produced in $\gamma p \to \eta\pi^+ n$ reaction",
Physical Review C **93**, no. 6, 065201, (2016)

[63] S. D. Drell, Rev. Mod. Phys. **33**, 458 (1961)

[64] P. Söding, Phys. Lett. **19**, 702 (1966)

[65] J. Pumplin, Phys. Rev. D **2** (1970) 1859

[66] G. Chew, M. Goldberger, F. Low, and Y. Nambu, Phys. Rev. **106**, 1337 (1957)

[67] M. Jacob and G. Wick, Annals Phys. **7**, 404 (1959)

[68] R. Workman, R. Arndt, W. Briscoe, M. Paris, and I. Strakovsky, Phys.Rev. C **86**, 035202 (2012), 1204.2277

[69] R. Höhler,
"Pion-nucleon scattering",
Landolt-Bornstein, New Series, Vol. I/9b2, ed. H. Schopper, Springer-Verlag, Berlin, (1983)

[70] M. Tanabashi et al. (Particle Data Group),
"48. Resonances",
Phys. Rev. D **98**, 030001 (2018) and updated on 6th December,(2019)

[71] F. E. Close and G. A. Schuler,
"Central production of mesons: Exotic states versus pomeron structure",
Phys.Lett., B **458**, pp. 127–136, (1999)

[72] T. Arens, O. Nachtmann, M. Diehl, and P. V. Landshoff,
"Some tests for the helicity structure of the pomeron in ep collisions", Z.Phys., vol. C **74**, pp. 651–669, (1997)

[73] P. Lebiedowicz, O. Nachtmann, and A. Szczurek,
"Exclusive central diffractive production of scalar and pseudoscalar mesons tensorial vs. vectorial pomeron",
Annals Phys., vol. **344**, pp. 301–339, (2014).

[74] P. Lebiedowicz, O. Nachtmann, and A. Szczurek,
"Central exclusive diffractive production of $\pi^+\pi^-$ continuum, scalar and tensor resonances in pp and $p\bar{p}$ scattering within tensor pomeron approach",
Phys. Rev., vol. D **93**, no. 5, p. 054015, (2016).

[75] C. Bromberg et al.,
"Study of A 2 production in the reaction $\pi^- p \to K^0 K^- p$ at 50 GeV/c, 100 GeV/c, 175 GeV/c",
Phys.Rev., D **27**, pp. 1–11, (1983)

[76] L. Lesniak, A.P. Szczepaniak,
"Theoretical model of the phi meson photoproduction amplitudes",
ACTA PHYSICA POLONICA B **34**(2003), https://doi.org/10.48550/arXiv.hep-ph/0304007

[77] V. Mathieu, J. Nys, C. Fernández-Ramiréz, A. Jackura, A. Pilloni, N. Sherrill, A. P. Szczepaniak, and G. Fox,
"Vector Meson Photoproduction with a Linearly Polarized Beam",
https://doi.org/10.1103/PhysRevD.97.094003

[78] A. Donnachie and Yu. S. Kalashnikova,
"Photoproduction of $a_0(980)$ and $f_0(980)$",
Phys. Rev. C **93**, 025203 – Published 16 February (2016)

[79] V. Mathieu, and Albaladejo, M. and Fernández-Ramírez, C. and Jackura, A. W. and Mikhasenko, M. and Pilloni, A. and Szczepaniak, A. P.,
"Moments of angular distribution and beam asymmetries in $\eta\pi^0$ photoproduction at GlueX",
https://doi.org/10.48550/arXiv.1906.04841

[80] M. Battaglieri et al, (CLAS collaboration), *"Photoproduction of pi+ pi- meson pairs on the proton"*,
Phys. Rev. D **80**, 072005, (2009)

[81] P. A. Zyla et al. (Particle Data Group), *"Review of Particle Physics"*, PTEP, 083C01 (2020)

[82] S. Godfrey and N. Isgur,
"Mesons In A Relativized Quark Model With Chromodynamics",
Phys. Rev. D **32**, 189 (1985)

[83] G. Rupp, S. Coito, and E. van Beveren,
"Meson spectroscopy: too much excitement and too few excitations",
Acta Phys. Polon. Supp. 5, 1007 (2012) arXiv:1209.1475 [hep-ph]

[84] Srijit Paul,
"Scattering meson and baryon resonances in lattice QCD",
PhD thesis, The Cyprus Institute and University of Wuppertal, June (2019)

[85] Robert Kaminski,
"Parameterization of amplitudes, finding resonances and unitarity, peculiarities and traps",
talk at "Matter To The Deepest" conference, Katowice IX (2019)

[86] D. Krupa, V. A. Meshcheryakov, and Yu. S. Surovtsev, Nuovo Cimento A **109**, 281, (1996).

[87] N. Hammoud, R. Kamiński, V. Nazari and G. Rupp,
" Strong evidence of the $\rho(1250)$ from a unitary multichannel reanalysis of elastic scattering data with crossing-symmetry constraints",
Phys. Rev. D **102**, no.5, 054029 (2020), https://doi.org/10.1103/PhysRevD.102.054029

[88] J. L. Rosner,
"Experimental tests of models of hadrons containing heavy quarks",
Reports on Progress in Physics, **64**, no. 3, pp. 327-381, (2001)

[89] E. Bartoš, S. Dubnička, A. Liptaj, A. Z. Dubničková and R. Kamiński,
" What are the correct $\rho^0(770)$ meson mass and width values?",
Phys. Rev. D **96**, no.11, 113004 (2017), https://doi.org/10.1103/PhysRevD.96.113004

[90] E. van Beveren, G. Rupp, T. A. Rijken, and C. Dullemond,
"Radial Spectra and Hadronic Decay Widths of Light and Heavy Mesons",
Phys. Rev. D **27**, 1527 (1983)

[91] G. P. Engel, C. B. Lang, D. Mohler, and A. Schäfer,
"Excited light and strange hadrons from the lattice with two Chirally Improved quarks",
PoS Hadron 2013, 118 (2013), arXiv:1311.6579 [hep-ph].

[92] S. Prelovsek, L. Leskovec, C. B. Lang, and D. Mohler,
"K π scattering and the K decay width from lattice QCD"*,
Phys. Rev. D **88**, 054508 (2013), arXiv:1307.0736 [hep-lat]

[93] M. Luscher,
"Two particle states on a torus and their relation to the scattering matrix",
Nucl. Phys. B **354**, 531 (1991)

[94] P. Bydzovsky, R. Kaminski, and V. Nazari,
"Dispersive analysis of the S-, P-, D-, and F-wave $\pi\pi$ amplitudes",
Phys. Rev. D **94**, 116013, (2016), arXiv:1611.10070 [hep-ph]

[95] Y. S. Surovtsev, P. Bydzovsky, R. Kaminski, and M. Nagy,
"Light-meson spectroscopy and combined analysis of processes with pseudoscalar mesons",
Phys.Rev. D **81**, 016001 (2010), doi:10.1103/PhysRevD.81.016001

[96] V. Nazari,
"Study on Spectroscopy of Light Mesons",
PhD thesis, Institute of Nuclear Physics, Polish Academy of Sciences, February (2017)
In order to obtain an electronic copy, please send an email to vahabnazari@gmail.com

[97] R. Garcia-Martin, R. Kaminski, J. R. Pelaez, J. Ruiz de Elvira, and F. J. Yndurain,
"The Pion-pion scattering amplitude. IV: Improved analysis with once subtracted Roy-like equations up to 1100 MeV",
Phys. Rev. D **83**, 074004 (2011), arXiv:1102.2183 [hep-ph]

[98] S. M. Roy,
"Exact integral equation for pion pion scattering involving only physical region partial waves",
Phys. Lett. B **36**, 353 (1971)

[99] J. R. Batley et al. (NA48/2 Collaboration), Eur. Phys. J. C **54**, 411, (2008)

[100] S. Pislak et al. (BNL-E865 Collaboration), Phys. Rev. Lett. **87**, 221801 (2011)

[101] S. D. Protopopescu, M. Alston-Garnjost, A. Barbaro- Galtieri, S. M. Flatté, J. H. Friedman, T. A. Lasinski, G. R. Lynch, M. S. Rabin, and F. T. Solmitz,
Phys. Rev. D **7**, 1279 (1973)

[102] B. Hyams et al., Nucl. Phys. B **64**, 134 (1973)

[103] P. Estabrooks and A. D. Martin, Nucl. Phys. B **79**, 301 (1974)

[104] B. Hyams et al., Nucl. Phys. B **100**, 205 (1975)

[105] R.L. Workman et al. (Particle Data Group), Prog. Theor. Exp. Phys. 2022, 083C01 (2022)

[106] R. Kamiński, L. Leśniak and J. P. Maillet,
"*Relativistic effects in the scalar meson dynamics*",
Phys. Rev. D **50**, 3145-3157 (1994), https://doi.org/10.1103/PhysRevD.50.3145

[107] R. Kamiński, L. Leśniak and B. Loiseau,
"*Scalar mesons and multichannel amplitudes*",
Eur. Phys. J. C **9**, 141-158 (1999), https://doi.org/10.1007/s100530050414

[108] J. P. Dedonder, R. Kamiński, L. Leśniak and B. Loiseau,
"*Dalitz plot studies of $D^0 \to K^0_S K^+ K^-$ decays in a factorization approach*",
Phys. Rev. D **103**, no.11, 114028 (2021), https://doi.org/10.1103/PhysRevD.103.114028

[109] L. Leśniak,
"*Meson spectroscopy and separable potentials*",
Acta Physica Polonica B **27**, 1835 (1966)

[110] R. Kamiński, L. Leśniak and B. Loiseau,
"*Three channel model of meson meson scattering and scalar meson spectroscopy*",
Phys. Lett. B **413**, 130-136 (1997), https://doi.org/10.1016/S0370-2693(97)01090-3

[111] R. Garcia-Martin, R. Kamiński, J. R. Pelaez, J. Ruiz de Elvira and F. J. Yndurain,
"*The Pion-pion scattering amplitude. IV: Improved analysis with once subtracted Roy-like equations up to 1100 MeV*",
Phys. Rev. D **83**, 074004 (2011), https://doi.org/10.1103/PhysRevD.83.074004

[112] Wigner, E. P.,
"Gruppentheorie und ihre Anwendungen auf die Quantenmechanik der Atomspektren. Braunschweig: Vieweg Verlag",(1931)
Translated into English by Griffin, J. J. "Group Theory and its Application to the Quantum Mechanics of Atomic Spectra",(1959)

[113] Biedenharn, L. C.; Louck, J. D, *"Angular Momentum in Quantum Physics"*,(1981)

[114] Rose, Morris Edgar, *"Elementary theory of angular momentum"*, (1995)

[115] PDG Table of Clebsch-Gordan Coefficients, Spherical Harmonics, and d-Functions, http://pdg.lbl.gov/2008/reviews/clebrpp.pdf